

AN EXPERIMENTAL-COMPUTATIONAL STUDY ON THE PLASTIC DEFORMATION
BEHAVIOR OF BODY-CENTERED CUBIC TITANIUM ALLOYS

By

Vahid Khademi

A DISSERTATION

Submitted to
Michigan State University
in partial fulfillment of the requirements
for the degree of

Mechanical Engineering–Doctor of Philosophy
Materials Science and Engineering–Dual Major

2018

ABSTRACT

AN EXPERIMENTAL-COMPUTATIONAL STUDY ON THE PLASTIC DEFORMATION BEHAVIOR OF BODY-CENTERED CUBIC TITANIUM ALLOYS

By

Vahid Khademi

A combined experimental-computational investigation was performed in the first part of this work to quantify the relationship between plastic strain and crystallographic misorientation. Several material characterization techniques including tensile testing, Scanning Electron Microscopy (SEM), Digital Image Correlation (DIC), and Electron Backscatter Diffraction (EBSD) were combined to study the correlation between plastic strain and crystallographic misorientation at the microscale for two body-centered cubic (bcc) titanium (Ti) alloys, namely Ti-13Cr-1Fe-3Al (wt.%) and TIMETAL-21S [Ti 15Mo-3Nb-3Al-0.2Si (wt.%)]. The results revealed that larger grains experienced more misorientation dispersion compared to smaller grains. An empirical equation was proposed to estimate the crystallographic misorientation at the grain scale as a function of plastic strain and grain size. Furthermore, the effects of crystallographic orientation and loading history on the misorientation were investigated. It was observed that {100} oriented grains (with respect to the tensile axis) exhibited more of a tendency for orientation change than {110} and {111} oriented grains. Interrupted loading resulted in higher crystallographic misorientation than monotonic (uninterrupted) loading. A qualitative comparison between the DIC-SEM strain field map and the misorientation maps revealed that there is a better correlation between the hot spots in the KAM map and the DIC-SEM strain field map compared with the correlation between the hot spots in the MD maps and the DIC-SEM strain field map. Some of the metrics, developed in the misorientation analysis, were implemented by EDAX-TSL, Inc. (Mahwah, NJ) in their latest orientation imaging microscopy (OIM) commercial software.

Slip trace analysis was performed to characterize the distribution of the plastic deformation modes at RT, 200 °C, and 300 °C on three bcc Ti alloys: Ti-13Cr-1Fe-3Al (wt.%), TIMETAL-21S, and Ti-29Nb-13Ta-4.6Zr-xO (wt.%), where x is 0.1, 0.3, and 0.7 (wt.%). The results revealed that dislocation slip was the dominant plastic deformation mechanism for Ti-13Cr-1Fe-3Al (wt.%), TIMETAL-21S, Ti-29Nb-13Ta-4.6Zr-0.3O (wt.%), and Ti-29Nb-13Ta-4.6Zr-0.7O (wt.%). The {123}<111> slip systems exhibited the highest contribution, while the {110}<111> showed the least contribution of the observed traces. However, the normalized slip activity (according to the possible slip planes of each system) suggested that the activity of all the systems were relatively equal for the TCFA, while the activity of the {110}<111> was slightly greater than other two slip systems for the TIMETAL-21S. Three deformation mechanisms, i.e., stress-induced martensitic (SIM) transformation (β phase to α' phase), the {332}<113> mechanical twinning, and the slip activity activated and cooperated for the Ti-29Nb-13Ta-4.6Zr-0.1O (wt.%).

In the second part of this work, the room temperature (RT) and elevated temperature strength of a low-cost Ti alloy were enhanced through thermomechanical processing (TMP). In-situ and ex-situ TMP treatments were systematically designed and conducted to increase the strength of a low-cost bcc Ti alloy. By performing heat treatments in the range of 300 °C to 600 °C, it was found that nanoscale and microscale precipitates formed in the bcc matrix, which led to enhance the strength. With an applied mechanical load, the phase transformation process was accelerated. The resulting mechanical properties depended on the type and duration of the TMP treatments. The maximum tensile strength of Ti-13Cr-1Fe-3Al (wt.%) reached approximately 1500 MPa at 410 °C. The TMP and alloy composition range was patented internationally.

Copyright by
VAHID KHADEMI

2018

To my parents, Mohtaram and Ghader, and my sister, Sara,
for their endless and unconditional love and support

ACKNOWLEDGEMENTS

First of all, I would like to express my sincere thanks to my advisor, Prof. Carl J. Boehlert, for the opportunity to work in his research group. He has given me tremendous support and encouragement over the course of my studies at Michigan State University (MSU). I learned a lot from his advice and priceless feedback. Prof. Boehlert was always available to discuss and resolve any technical aspects of my research and also other personal issues. I am grateful for him providing me many opportunities to present my work at technical conferences and meetings. I do appreciate his understanding and caring personality, which will remain in my mind.

I would like to express my gratitude to Prof. Thomas R. Bieler for his valuable feedback throughout my journey at MSU. I am very grateful for many occasions that he spent to discuss my research with me and provide me precious feedback and ideas. I learned a lot from his scientific expertise and he was always eager to help. I will never forget that he stayed up until midnight to help me to make a better presentation at a conference, which means a lot to me.

My sincere gratitude goes to Prof. Philip Eisenlohr for his invaluable comments and guidance. His enthusiasm and passion, and also his precise and keen insight and ideas inspired me throughout my time at MSU. I also would like to thank Prof. Thomas J. Pence, a member of my doctoral committee, for his time and valuable feedback. I would like to thank Prof. Martin Crimp for his comments during the group meetings.

Furthermore, I would like to express my gratitude to Prof. Ahmed Naguib, graduate program director of mechanical engineering department, Prof. Xinran Xiao, my former advisor. Also, I would like to thank Dr. Per Askeland for his assistance with the operation and trouble-shooting of

the electron microscopes and other materials analysis equipment. I would like to thank Prof. Masahiko Ikeda from Kansai University and Prof. Mitsuo Niinomi from Tohoku University, Japan for their comments and providing titanium alloys for our research. Also, I am thankful to Dr. Huihong Liu, Osaka University, Japan, for performing TEM on some of the samples. Furthermore, I would like to thank you Prof. Samantha Daly, formerly faculty at the University of Michigan and now at the University of California, Santa Barbara, and Dr. Zhe Chen for their help to perform digital image correlation experiment.

Finally, I would like to thank the current and former members of the “metals group”, who have directly and indirectly helped me in my research, including Dr. Chen Zhang, Mr. Harsha Phukan, Mr. Yang Su, Mr. Quan Zhou, Mr. Di Kang, Ms. Aida Amroussia, Ms. JoAnn Ballor, Ms. Uchechi Okeke, Mr. Aritra Chakraborty, and Mr. Zhuowen Zhao. Also, I would like to thank my friends, Dr. Ehsan Masoumi Khalil abad and Dr. Ata Babazadeh.

TABLE OF CONTENTS

LIST OF TABLES	xii
LIST OF FIGURES	xiii
LIST OF ABBREVIATIONS.....	xxviii
CHAPTER 1	1
1 RATIONALE AND RESEARCH OBJECTIVE.....	1
1.1 Microscale study of polycrystalline materials.....	1
1.2 Justification for studying the deformation behavior of Ti alloys.....	2
1.3 Work performed	6
CHAPTER 2	9
2 BACKGROUND AND LITERATURE REVIEW	9
2.1 Misorientation	10
2.2 DIC.....	14
2.3 Strain aging and Cottrell atmosphere.....	15
2.4 Fundamentals of Ti and Ti alloys.....	16
2.4.1 Crystal structure	16
2.4.2 Deformation mechanism.....	19
2.4.3 The effect of substitutional alloying elements on the strength of Ti alloys.....	22
2.4.4 The effect of precipitation on the strength of Ti alloys	24
2.4.5 The effect of oxygen content on the strength of Ti alloys	27
2.4.6 The effect of heat treatment on the strength of Ti alloys.....	29
2.5 Critical assessment of the state of the art	31
CHAPTER 3	33
3 EQUIPMENT AND MATERIALS.....	33

3.1	Equipment	33
3.1.1	Scanning electron microscopy (SEM)	33
3.1.2	Electron Backscatter Diffraction.....	33
3.1.3	In-situ tensile stage	34
3.1.4	Universal test machine	35
3.1.5	Hardness.....	36
3.1.6	Oven and vacuum tube.....	36
3.1.7	Thermocouples.....	37
3.1.8	Dynamic mechanical analysis.....	38
3.2	Materials.....	38
3.3	Specimen geometry and sample preparation.....	40
CHAPTER 4		41
4	MISORIENTATION ANALYSIS.....	41
4.1	Experiments performed	41
4.2	Reference orientation	43
4.2.1	Reference orientation criteria.....	44
4.3	Results	50
4.3.1	Evolution of orientation gradient as function of plastic strain.....	50
4.3.2	The relationship between misorientation and plastic strain	55
4.3.3	The effect of orientation on MD_{min}	58
4.3.4	The influence of grain Size on $MD(min)$	62
4.3.5	The influence of distance from grain boundary on $MD(min)$	65
4.3.6	The effect of loading history on misorientation value	67
4.3.7	Digital Image Correlation	67
4.3.7.1	DIC strain field map	72
4.4	Discussion	74
4.4.1	Evolution of orientation change.....	74
4.4.2	Misorientation and plastic strain.....	76
4.4.3	On the orientation	80
4.4.4	Grain size	84
4.4.5	Distance from grain boundary	89
4.4.6	Interrupted vs Monotonic tensile test.....	90
4.4.7	DIC.....	91

4.5	Summary and Conclusion	97
CHAPTER 5		99
5	DEFORMATION BEHAVIOR OF BCC TI ALLOYS	99
5.1	Slip trace analysis procedure.....	99
5.2	Deformation behavior of TCFA.....	103
5.2.1	Microstructure and texture.....	103
5.2.2	In situ tensile test of TCFA.....	106
5.2.3	RT tensile test of TCFA.....	108
5.2.4	200 °C tensile test of TCFA.....	111
5.2.5	300 °C tensile test of TCFA.....	114
5.3	Deformation behavior of TIMETAL-21S.....	118
5.3.1	Microstructure and texture of TIMETAL-21S	118
5.3.2	In situ tensile test of TIMETAL-21S.....	122
5.3.3	RT tensile test of TIMETAL-21S.....	124
5.3.4	230 °C tensile test of TIMETAL-21S.....	127
5.3.5	300 °C tensile test of TIMETAL-21S.....	130
5.4	Deformation behavior of TNTZ-xO.....	133
5.4.1	RT tensile test of TNTZ-0.1O.....	135
5.4.2	RT tensile test of TNTZ-0.3O.....	139
5.4.3	RT tensile test of TNTZ-0.7O (Sample20-lhs).....	143
5.5	Discussion	146
5.5.1	Microstructure.....	146
5.5.2	Mechanical proprieties.....	146
5.5.3	Deformation mechanism.....	150
5.5.3.1	TCFA and TIMETAL-21S	151
5.5.3.2	TNTZ-xO.....	156
5.6	Summary and Conclusion	162
CHAPTER 6		164
6	ENHANCING THE STRENGTH OF TCFA.....	164
6.1	Determining the temperature range of phase transformation.....	164
6.2	Heat treatment	166

6.3	In-situ tensile test at 400 °C.....	169
6.3.1	Interrupted tensile test at 410 °C.....	172
6.3.2	Monotonic tensile test at 410 °C.....	176
6.3.3	The effect of preloading on UTS at 410 °C	180
6.3.4	Interrupted tensile test at 410 °C.....	184
6.4	In-situ TCFA tensile test at 450 °C	186
6.5	In-situ tensile test at 475 °C.....	190
6.6	Discussion	193
6.7	Summary and conclusions.....	200
CHAPTER 7		201
7	SUMMARY AND CONCLUSIONS	201
7.1	Summary and outcomes of this work.....	201
7.2	Summary and conclusions.....	202
7.2.1	Misorientation analysis	202
7.2.2	Deformation behavior of TCFA and TIMETAL-21S.....	205
7.2.3	Deformation behavior of TNTZ-xO	206
7.2.4	Enhancing the UTS of TCFA	207
7.3	Recommendations for future work.....	209
BIBLIOGRAPHY.....		211

LIST OF TABLES

Table 1-1 Some of the basic characteristics of Ti alloys as compared with Fe, Ni, and Al alloys (Lütjering and Williams, 2003).....	4
Table 2-1 The mechanical properties of CP-Ti and Ti-6Al-4V alloys (Lütjering and Williams, 2003).	23
Table 2-2 Electronegativity of O, Ti and Ti substitutional alloying elements in the Pauling scale (Rohrer, 2001).....	28
Table 3-1 The compositions and type of analysis performed for each alloy	39
Table 4-1 The calculated MD_G values at each level of plastic strain and the associated parameters for TCFA.....	57
Table 4-2 The number of possible slip directions (S.D) and the Schmid factors of the $\{110\}\langle 111\rangle$ and $\{112\}\langle 111\rangle$ slip systems (presented by S.S1 and S.S2, respectively) for the $\{100\}$, $\{111\}$, $\{110\}$ orientation with respect to the tensile direction for a bcc structure	84
Table 4-3 The constant values determined from equation (4.15) for each alloy. The least square estimator was acquired on the experimental data to obtain the constants and R^2	88
Table 5-1 The analyzed chemical compositions of TNTZ-0.1O, TNTZ-0.3O, and TNTZ-0.7O (Geng et al., 2011)	133
Table 5-2 Schmid factor for the RT deformed TNTZ-0.1O sample. The strain was 5.8%.	138
Table 5-3 Summary of the distribution of the alloying elements	146
Table 6-1 The Summary of in situ tensile tests on TCFA alloy from RT to 475 °C	198

LIST OF FIGURES

Figure 1.1 Some Ti alloy applications: (a) Hip and knee implant, (b) Fukuoka Yahuoku Dome’s roof, (c) Oil and gas drilling riser (Geetha et al., 2009; Lütjering and Williams, 2003) 5

Figure 1.2 Approximate breakdown of the USA market of Ti and its alloys in 1998 (Lütjering and Williams, 2003)..... 6

Figure 2.1 The misorientation distribution maps obtained based on the average orientation: (a) before deformation and (b) after deformation (Buchheit et al., 2015)..... 13

Figure 2.2 (a) a subset of random particles before deformation and (b) the subset of same area at deformed state. The displacement field is determined by comparing these two subsets with an image processing algorithm (Kammers and Daly, 2013a)..... 15

Figure 2.3 Typical stress (y-axis) versus strain (x-axis) behavior in materials exhibiting upper and lower yield points. A sudden decrease in the stress may occur after reaching the YS in some metallic materials (see points A, A’, B, and B’). The stress at which the sudden drop occurs is called the upper yield point (point A and B), while the lower stress is known as lower yield point. $\Delta Y1$ = increase in stress produced by pre-strain, $\Delta Y2$ = increase in stress produced by aging, $\Delta Y3$ = increase in stress produced by pre-straining and aging= $\Delta Y1+\Delta Y2$, ΔU = Change in UTS due to pre-straining and aging, Δe =Change in elongation due to pre-straining and aging (Bülbül et al., 2017) 17

Figure 2.4 Interstitial atom diffuses to the dislocation core to form a Cottrell atmosphere 17

Figure 2.5 The unit cell of (a) the α phase and (b) the β phase of pure Ti. The corresponding lattice parameters are also provided. 18

Figure 2.6 Alloying elements classified into three groups based on their effect on the β transus temperature (Geetha et al., 2009; Lütjering and Williams, 2003). 19

Figure 2.7 Illustration of three slip systems in bcc materials highlighted by a shaded plane and a direction depicted by the red arrows: (a) one variant of the six {110} slip planes, (b) one variant of the twelve {211} slip planes, (c) one variant of the twenty-four {321} slip planes. All the systems have a common Burgers vector of $\langle 111 \rangle$ 21

Figure 2.8 (a) SEM photomicrograph taken at $N = 2300$ cycles, activated slip systems and associated Schmid factors (μ) in ferritic grains, (b) accumulated frequencies of the highest Schmid factors for 230 ferritic grains of which the slip systems are identified (area of $600 \times 500 \mu\text{m}^2$) (El Bartali et al., 2008)..... 22

Figure 2.9 Different precipitate sizes and morphologies formed in Ti-12Mo-6Zr-2Fe; (a) grain boundary and primary α precipitates formed in homogenized sample; (b) and (c): an aged sample exhibited fine secondary α phase particles, which resulted in an increase in the strength (Banerjee et al., 2004) 25

Figure 2.10 Dark field TEM photomicrographs of (a) ellipsoidal ω precipitates in Ti-16Mo aged for 48 hr at 450°C , (b) cuboidal ω precipitates in Ti-8Fe aged for 4 hr at 400°C (Lütjering and Williams, 2003)..... 26

Figure 2.11 Temperature versus time diagram for Ti-20V, where the ω phase formed at lower temperatures and longer times (Hickman, 1969)..... 26

Figure 2.12 The effect of O content on microstructure of Ti-35-Nb-5Ta-7Zr after aging at 538°C for 8 hr, (a): 0.06, (b):0.46, (c):0.68 O wt.%. The α phase was inhomogeneously distributed at the higher O contents (Qazi et al., 2005). 28

Figure 2.13 The effect of aging temperature on YS of Ti-35Nb-7Zr-5Ta-xO, where x was 0.06 wt.% for low O content, 0.46 wt.% for medium O content, and 0.68 wt.% for high O content. All the samples were aged for 8 hr (Qazi et al., 2005) 30

Figure 3.1 The in-situ testing setup inside the Tescan Mira3 SEM chamber. The heater is located underneath the sample. A thermocouple was spot-welded to the side of the gage section for the elevated-temperature tests..... 35

Figure 3.2 An image of the test machine used for the tensile tests performed outside the SEM. For the elevated temperature tests, quartz heater elements were used. Thermocouples were spot-welded to the surface in the middle of the gage section of the test specimens. 36

Figure 3.3 Image of the furnace used for the heat treatments. The real-time sample temperature was measured during the heat treatment..... 37

Figure 3.4 A schematic showing the geometry of the test specimens used in the tensile experiments. The dimensions are in millimeters. The thickness was ~ 0.6 and ~ 0.8 mm for the TIMETAL-21S and TCFA specimens, respectively..... 40

Figure 4.1 The Global Misorientation Deviation (*MDG*) values for three reference orientations (*RO*) metrics for (a) TCFA and (b) TIMETAL-21S at different levels of plastic strain. Linear lines were fit to the data for each metric. All R^2 values were higher than 0.87. 48

Figure 4.2. One grain, which contained 804 data points, was selected from a TCFA sample deformed to 12.5% plastic strain to depict the misorientation distribution with respect to the *RO*. (a) The orientation map and assisted color code, the misorientation distribution of (b) *MDMin*, (c) *MDMax*, (d) *MDGeo. C.*, (e) *MDAvg. Ori.*, (f) *MDPt*. The *RO* position was colored in red at each map. 49

Figure 4.3 EBSD IPF maps obtained after different levels of plastic strain for TCFA. (a) 0%, (b) 2.7%, (c) 6.6%, (d) 9.4%, and (e) 12.3% plastic strain. At 0% plastic strain, the material exhibited a relatively uniform orientation distribution for almost all the grains. With an increase in the plastic strain level, the evolution of the orientation gradient within the grains became more pronounced. The inverse pole figure (IPF) color code is included along with the loading direction as a reference. 51

Figure 4.4 EBSD IPF maps obtained after different levels of plastic strain for TIMETAL-21S. (a) 0%, (b) 3.3%, (c) 5.4%, (d) 9.2%, and (e) 11.7% plastic strain. At 0% plastic strain, the material exhibited a relatively uniform orientation distribution for almost all the grains. With an increase in the plastic strain level, the evolution of the orientation gradient within the grains became more pronounced. The IPF color code is included along with the loading direction as a reference. 52

Figure 4.5 IPF maps with respect to $\langle 010 \rangle$ at different levels of plastic strain for TCFA. (a) 0%, (b) 2.7%, (c) 6.6%, (d) 9.4%, and (e) 12.3% plastic strain. In (a), three clouds, that were magnified highlighted by the red circle, represent the orientation spread of three TCFA grains at 0%. The orientation spread became larger as the level of plastic strain increased. Fewer clouds can be seen at 12.3% plastic strain, which indicates the orientation spread increased with increasing plastic strain. 53

Figure 4.6 IPF maps with respect to $\langle 010 \rangle$ at different levels of plastic strain for TIMETAL-21S. (a) 0%, (b) 3.3%, (c) 5.4%, (d) 9.2%, and (e) 11.7% plastic strain. The orientation spread became larger as the level of plastic strain increased. Fewer clustered areas can be seen at 11.7% plastic strain, which indicates the orientation spread increased with increasing plastic strain. 54

Figure 4.7 The *MDG(Min)* versus plastic strain for TCFA and TIMETAL-21S. (a) The linear regression satisfactorily describes the relationship between global plastic strain and *MDG(Min)*. (b) The *MDG(Min)* versus plastic strain for TIMETAL-21S at ~12% exhibited an upward curvature. 56

Figure 4.8 The cumulative distribution of MD_{Min} values at different levels of plastic strain for TCFA. With increasing plastic strain, the MD_{Min} shifted to the right. 57

Figure 4.9 IPF (with respect to the loading direction) of MD values. This plot represents the distribution of the MD values of 444 grains from a TCFA sample tensile deformed to 12.3% plastic strain (posttest MD values). The grains located close to the [101] corner exhibited lower MD values compared to other regions, which indicates a lower tendency for orientation change. For a better visualization, the three studied groups, i.e. {100}, {110}, and {111} were separated by three arcs. There was a small common area between {110} and {111} groups. 58

Figure 4.10 Partitioned EBSD maps highlighting the three crystallographic orientations with a tolerance angle of 20° with respect to the loading direction: (a) $\langle 100 \rangle$, (b) $\langle 101 \rangle$, and (c) $\langle 111 \rangle$, and their corresponding IPF for a TCFA sample, which was subjected to tensile loading to 12.3% plastic strain. There is a small common area between {110} and {111} groups, where the threshold angle was 20° 60

Figure 4.11 The MD values as a function of grain orientation and plastic strain for (a) TCFA and (b) TIMETAL-21S. The {100} group exhibited a higher MD value than other groups, while the {101} exhibited a lower MD value. The population fraction percent of each group is provided in front of the corresponding legend. 61

Figure 4.12 The cumulative distribution of grain size for (a) TCFA and (b) TIMETAL-21S samples tensile tested to different strain levels. Although the tensile tests were performed on different samples, the data indicate a similar grain size distribution for all the samples. 63

Figure 4.13 The $MD(\min)$ versus D/D_{avg} for different plastic strain levels for (a) TCFA and (b) TIMETAL-21S. The $MD(\min)$ values were almost constant for the undeformed materials. With increasing plastic strain level, the larger grains exhibited a higher $MD(\min)$ values. This was more pronounced at the high plastic strain levels. 64

Figure 4.14 The distribution of MD values at grain boundaries for 200 grains of a TCFA sample loaded to 12.3% plastic strain at RT. The points in which the MD values were greater than 3 $MDG(\min)$ are shown in yellow and the points where MD values was less than half $MDG(\min)$ are colored in dark blue. There were some regions where the MD values were 4 times greater than $MDG(\min)$ on both sides of the grain boundaries. 66

Figure 4.15 The influence of distance from the grain boundary on MD for a TCFA sample that was deformed to 12.3% plastic strain at RT. The larger the distance from the grain boundary, the lower the MD value was. 66

Figure 4.16 The $MDG(Min)$ versus global plastic strain for monotonic tensile tests for (a) TCFA and (b) TIMETAL-21S. The linear regression indicates a linear relationship between global plastic strain and $MDG(Min)$ with a relatively high R^2 value. The triangular points represent the $MDG(Min)$ values of interrupted tensile tests..... 68

Figure 4.17 The surface of the sample that was coated with gold nanoparticles (AuNP)..... 69

Figure 4.18 The stress versus displacement curve for the TCFA sample that was coated with AuNP. The test was paused nine times to acquire SE SEM photomicrographs for calculating the strain through DIC characterization. Each drop in stress indicates the position of each pause..... 70

Figure 4.19 SE SEM photomicrographs of the selected area of the TCFA sample, (a) before the test and before the coating was applied to the surface, (b) before the test and after the coating was applied to the surface, (c) after the test with coating, and (d) after the test, after slight polishing (to remove the coating for performing posttest EBSD analysis)..... 71

Figure 4.20 EBSD IPF maps from the selected area of the TCFA sample, (a) before the test, before coating and (b) after the test, the coating was removed by slight polishing. Black points indicate where the confidence index was less than 0.05. A substantial orientation change was observed in some of the grains. 72

Figure 4.21 (a) The equivalent plastic strain map after 10.8% strain. This map was generated by combining 30 subareas. The areas, where the equivalent strain was more than three times the global strain, are exhibited in black. A local strain concentration was observed in most of the grains. (b) The posttest EBSD IPF map [Figure 4.20(b)] was overlaid on the equivalent plastic strain map. The IPF color code is similar to the color code in Figure 4.20..... 73

Figure 4.22 (a) (a) Square lattices before deformation and (b) lattices after shear deformation where SSDs formed and where (c) no dislocations formed. (d) Square lattices before deformation and after bending deformation, where GNDs formed.. 74

Figure 4.23 The MD versus plastic strain. The plastic strain was measured according to three cases, (I) according to the plastic region in the stress-displacement curves, which is shown as “Stress-displacement curves”, (II) by a caliber, according to the total length of the specimen before and after the test, which is shown as “Sample measurement”, and (III) by using the pretest and posttest SE SEM photomicrographs, which is shown as “SEM measurement”. The local plastic strain was measured by using the pretest and posttest SE SEM photomicrographs of the areas (case III), where the EBSD scans were performed. The local plastic strain was ~6% higher than the global plastic strain (case II), where the global plastic strain was ~12%..... 78

Figure 4.24 The Md versus true plastic strain using the plastic strain values measured by the SE SEM photomicrographs, for two cases: (I) assuming that necking did not occur. (The equation 4.16 was used to calculate the true plastic strain for all the points.), and (II) assuming that necking occurred at the highest level of plastic strain (the value of true strain for that highest plastic strain was calculated by equation 4.17, which resulted in a lower R^2 value. 79

Figure 4.25 A schematic of the change in the width (in mm) of the sample that was subjected to ~12% global plastic strain. The local plastic strain at the center of the gage length was ~18%. The initial thickness of the sample was ~0.6 mm, and it was ~0.45 mm throughout the gage length after the loading..... 80

Figure 4.26 The orientation dispersion after tensile loading for a bcc single crystal Fe, where the initial orientation was close to (a) [100], (b) [111], and (c) [011], with respect to the tensile direction. The red points indicate the undeformed orientation state. The [001] exhibited an orientation tendency toward [111]. The [011] did not spread significantly, while the [111] rotated toward [011] (Franciosi et al., 2015). 81

Figure 4.27 The orientation change tendency for a bcc structure tensile loaded in regions A and B is toward the [111] and [110], respectively. The [110] is considered as the stable orientation for the bcc structures (Hosford, 2009)..... 81

Figure 4.28 Slip can only occur in a_1b_3 and b_1a_3 directions in the $\{110\}\langle 111\rangle$ slip system with respect to tensile loading, y axis. The other two slip directions are perpendicular to the y axis (a_2b_4 and b_2a_4 directions). For each possible slip plane, there is a symmetrical slip plane with respect to the loading direction, e.g., $a_1a_2b_3b_4$ and $b_1b_2a_3a_4$ planes are symmetrical with respect to y axis. Hence, the orientation change will be relatively small in the single crystal because the symmetrical systems activity equally contributes to accommodate plastic deformation. 83

Figure 4.29 Theoretical MD values (obtained using equation [4.15]) versus the experimental MD values for TCFA (in blue) and TIMETAL-21S (in red). Almost 3000 grains were analyzed for each alloy. 88

Figure 4.30 (a) Stress-displacement curve of TCFA interrupted test and (b) the upper yield point (UYP), lower yield point (LYP), and stress relaxation (SR) for TCFA sample. (c) Stress-displacement curve of TIMETAL-21S interrupted test and (d) the UYP and LYP and SR for TIMETAL-21S sample 91

Figure 4.31 The misorientation distribution maps for the (a) $MD_{Avg, Before}$, (b) the $MD_{Avg, After}$, and (c) the strain field map at 0.11 strain. Some grains (green stars) showed better correlation in the $MD_{Avg, Before}$ map (the RO was the average orientation before the deformation), while some other grains (black circles) exhibited better correlation in

MDAvg, After map (the RO was the average orientation after the deformation was considered), (comparing with strain field map). The grains, with blue rhombuses inside, exhibited similar misorientation distribution in both maps. However, poor correlation was observed in other grains (black triangles). 93

Figure 4.32 (a) The DIC-SEM strain field map at 0.11 strain and (b) the 3rd nearest KAM map from similar area at 0.11 strain. The $KAM_{Avg.}$ was 1.4°. The corresponding hot spots at the grain boundaries in the DIC-SEM strain map exhibited higher values in the KAM map for most of the grains. There was not good correlation between hot spots in two maps for the grains that are highlighted with black circles. The areas, where the CI was less than 0.1, were colored in green. 94

Figure 5.1 Example of the slip trace analysis provided for a RT test of a TCFA tensile deformed to ~8% strain. (a) The slip trace was indicated by the solid line on the SE SEM micrograph in the highlighted grain. (b) Corresponding EBSD IPF map. (c) All possible trace lines, which were calculated by a MATLAB code, are shown. A black solid line was drawn parallel to the observed slip trace in (a). The 2 black dashed lines were drawn with a tolerance angle of 4 degrees from the black solid line. The system 32 with Schmid factor of 0.48 was chosen as the active slip system because it exhibited the highest Schmid factor and was located between the two dashed lines (Khademi et al., 2016). 102

Figure 5.2 SE SEM photomicrographs of the microstructure of an as-received TCFA: (a) high magnification and (b) low magnification..... 103

Figure 5.3 The cumulative distribution of the equivalent grain diameter for seven different microstructure patches for the as-received TCFA. 104

Figure 5.4 EBSD data of an undeformed TCFA tensile-tested specimen: (a) EBSD IPF map in the tensile direction and (b) The representative texture of the TCFA microstructure in the form of {100} and {110} pole figures in the normal direction. The pole figures suggest that the alloy was not strongly textured. 105

Figure 5.5 Engineering stress vs. displacement for TCFA samples tensile tested at RT, 200 °C, and 300 °C. The stress drops indicate that stress relaxation occurred when the tests were interrupted for SEM imaging. None of the tests were taken to failure..... 107

Figure 5.6 Low-magnification SE SEM photomicrograph of a RT deformed TCFA sample tested to 940 MPa and 8.4% strain. Uniform plastic strain was observed throughout the gage section. The center line, scribed on the sample using a razor blade before the test, was used as a fiducial marker. The tensile axis was horizontal. 108

Figure 5.7 Sequential SE SEM photomicrographs acquired during the RT TCFA test: (a) 1.3% strain, (b) 3.4% strain, (c) 4.4% strain, (d) 8.4% strain, (e) posttest EBSD IPF map, and (f) EBSD color code and scale bar. Each of these images represents the same microstructural patch. The tensile axis was horizontal. 109

Figure 5.8 A histogram of the Schmid factor distribution of the slip systems for TCFA samples tested at RT to 8.4% strain. 111

Figure 5.9 Low-magnification SE SEM micrograph of the 200 °C tensile deformed TCFA sample, which was taken ~8% strain. The heater location is specified by the yellow circle. Local plastic strain occurred in the heated area of the gage section. The center line, scribed on the sample before the test, was used as a fiducial marker. The tensile axis was horizontal. 112

Figure 5.10 Sequential SE SEM photomicrographs acquired during the 200 °C TCFA test at (a) 0% strain, (b) 1.2% strain, (c) 2% strain, (d) 8% strain, and (e) posttest EBSD IPF map. Each of these images represents the same microstructural patch. The tensile axis was horizontal. 113

Figure 5.11 A histogram of the Schmid factor distribution of the observed slip systems for the TCFA sample tensile tested at 200 °C to ~8% strain. 114

Figure 5.12 Low-magnification SE SEM micrograph of the 300 °C tensile deformed TCFA sample after achieving 2.2% strain. The heater location was specified by the yellow circle. Local plastic strain occurred at the center of the heated area of the gage section. The center line, scribed on the sample before the test, was used as a fiducial marker. The tensile axis was horizontal. The temperature of second thermocouple (T_2), which was spot-welded outside of the heater, was ~ 220 °C during the test, while the temperature of the test thermocouple (T_1) was 300 °C. This indicated the nature of the temperature gradient in the sample. 115

Figure 5.13 Sequential SE SEM photomicrographs acquired during the 300 °C TCFA test: (a) 0% strain, (b) 1% strain, (c) 2.2% strain, (d) 12% strain, and (e) Pretest EBSD IPF map. Each of these images represents the same microstructural patch. The tensile axis was horizontal. 116

Figure 5.14 A histogram of the Schmid factor distribution of the slip systems for the TCFA sample tested at 300 °C at ~2.2% strain. 117

Figure 5.15 SE SEM photomicrographs from the microstructure of the as-received TIMETAL-21S (a) high magnification and (b) low magnification. 119

Figure 5.16 The cumulative grain size distribution for TIMETAL-21S of separated microstructural patches. 120

Figure 5.17 EBSD data of the undeformed TIMETAL-21S: (a) EBSD IPF map in the tensile direction and (b) The representative texture of TIMETAL-21S microstructure in the form of {100} and {110} pole figures in the normal direction. 121

Figure 5.18 Engineering stress vs. displacement for TIMETAL-21S samples tensile tested at RT, 230 °C, and 300 °C. The stress drops indicate that stress relaxation occurred when the tests were interrupted for SEM imaging. None of the tests were taken to failure. 123

Figure 5.19 Low-magnification SE SEM micrograph of a RT deformed TIMETAL-21S sample. Uniform plastic strain was observed throughout the gage section. The small Vickers hardness indents, made before the test, were used as fiducial markers to help measure the strain. The tensile axis was horizontal..... 124

Figure 5.20. Sequential SE SEM photomicrographs of a TIMETAL-21S sample tested at RT: (a) 0%, (b) at 1.2% strain, (c) at 6.5% strain, and (d) posttest EBSD IPF map. Each of these images represents the same microstructural patch. The tensile axis was horizontal..... 125

Figure 5.21 A histogram of the Schmid factor distribution of the slip systems for the TIMETAL-21S sample tensile tested at RT to ~6.5% strain..... 126

Figure 5.22 Low-magnification SE SEM micrograph of a 230 °C deformed TIMETAL-21S sample. Localized plastic strain was observed in the heated area of the gage section. The Vickers hardness indents, made before the test, were used as fiducial markers to measure the local strain. The tensile axis was horizontal. The features that are shown inside the red ovals are spot-welding artifacts that occurred before the test. 127

Figure 5.23 Sequential SE SEM photomicrographs of the TIMETAL-21S sample tested at 230 °C acquired during the test at (a) 0% strain, (b) at 0.9% strain, (c) at 2% strain, (d) at 5.5% strain, (e) at 8.2% strain, (f) at 10.8% strain, (g) at 18.4% strain, and (h) pretest EBSD IPF map. Each of these images represents the same microstructural patch. The tensile axis was horizontal..... 128

Figure 5.24 Low-magnification SE SEM micrograph of a 300 °C deformed TIMETAL-21S sample after 11% strain. Local plastic strain was observed at the center of the heated area of the gage section. The Vickers hardness indents, made before the test, were used as fiducial markers to measure the local strain. The tensile axis was horizontal. 130

Figure 5.25 (a) before test EBSD IPF map. Sequential SE SEM photomicrographs of TIMETAL-21S sample tested at 300 °C: (a) 0%, (b) at 0.8% strain, (c) at 1.6% strain, and (d) at 11% strain. Each of these images represents the same microstructural patch. The tensile axis was horizontal. 131

Figure 5.26 The histogram of Schmid factor distribution of slip systems for the TIMETAL-21S sample tested at 300 °C, after ~11% strain. 132

Figure 5.27 Engineering stress vs. displacement curve for each of the TNTZ-xO samples tensile tested at RT. The stress drops indicate that stress relaxation occurred when the tests were paused for acquiring the SE SEM photomicrographs. None of the tests were taken to failure. The slope variation was due to slipping of the sample during loading in the grips. 134

Figure 5.28 Sequential SE SEM photomicrographs acquired during the RT TNTZ-0.1-O test at (a) 1.7% strain, (b) 3.1% strain, (c) 5.2% strain, and (d) 8.4% strain. Each of these images represents the same microstructural patch. (e) Pretest EBSD IPF map, and (f) Posttest EBSD IPF map. The tensile axis was horizontal. 136

Figure 5.29 (a) EBSD IPF map from the gage section of the TNTZ-0.1O tensile tested sample after 8.4% strain. (b), (c), and (d) mechanical twins were observed in some grains. The misorientation angle between the $\{332\}\langle 113\rangle$ and the matrix was approximately 50.5 degrees along the $\langle 110\rangle\beta$ direction. 137

Figure 5.30 (a) high-magnification SE SEM micrograph of a TNTZ-0.1O sample tensile tested at 5.8% strain at RT. Fine slip traces are evident in some grains. (b) Posttest EBSD IPF map. 138

Figure 5.31 Low-magnification SE SEM micrograph of a RT deformed TNTZ-0.3O sample. Some boundary cracks were observed throughout the gage section. The tensile axis was horizontal. 139

Figure 5.32 Sequential SE SEM photomicrographs acquired during the RT TNTZ-0.3O test: (a) 0.9% strain, (b) 1.8% strain, (c) 2.9% strain, (d) 4.6% strain, and (e) Pretest EBSD IPF map. Each of these images represents the same microstructural patch. The tensile axis was horizontal. 140

Figure 5.33 SE SEM photomicrographs indicating that the grain boundary cracks formed after 4.6% strain for the TNTZ-0.3O sample deformed at RT. Few slip trace lines were observed in the grains next to cracks. The cracks usually formed perpendicular to the tensile axis. 141

Figure 5.34 The histogram of Schmid factor distribution of slip systems for the TNTZ-0.3O at RT, tension experiment after ~2.9% strain. 142

Figure 5.35 Low-magnification SE SEM micrograph of a RT deformed TNTZ-0.7O sample. Uniform plastic strain was observed throughout the gage section. The tensile axis was horizontal. 143

Figure 5.36 The sequential SE SEM photomicrographs acquired during the RT TNTZ-0.7O test (a) elastic region, (b) 1.4%, (c) 6.1% strain, and (d) Pretest EBSD IPF map, (e) posttest EBSD IPF map. Each of these images represents the same microstructural patch. The tensile axis was horizontal. 144

Figure 5.37 A histogram of Schmid factor distribution of slip systems for the TNTZ-0.7O sample tested to 6.1% strain at RT 145

Figure 5.38 Approximate UTS values of the studied alloys as a function of test temperature .. 149

Figure 5.39 Tensile stress–strain curves of TNTZ–0.1O, TNTZ–0.3O, and TNTZ–0.7O (Geng et al., 2011) 149

Figure 5.40 The observed activity of the different families of slip systems for each of the test temperatures. (a) The analyzed data show that Family (3) exhibited the highest activity at each temperature. (b) The total observed traces for each Family was divided by the total number of possible slip planes for the corresponding Family and this represented the normalized data. The normalized data illustrate that the contribution of Family (2) was slightly higher than that for the other two Families for TCFA. However, the contribution of Family (1) was the most and the contribution for Family (3) was the least for the TIMETAL-21S. 154

Figure 5.41 A histogram of the Schmid factor distribution of the slip systems for TCFA samples tested at RT to 8.4% strain for 485 observed traces. (a) only ~20% of the observed traces were matched when the $\{110\}\langle 111\rangle$ slip system was considered, (b) ~70% of the observed traces were matched when the $\{110\}\langle 111\rangle$ and the $\{112\}\langle 111\rangle$ slip systems were considered, and (c) ~95% of the observed traces were matched when all three slip systems were considered. 155

Figure 5.42 (a) SE SEM micrograph of a TNTZ-0.3O sample after ~5% strain. Some intergranular cracks observed, where some of them initiated in vicinity of a grain close to the hard orientation, the $\{111\}$ with respect to tensile direction, as indicated with dashed-lines in (b) EBSD IPF maps. Two areas, where the observed slip activity was relatively low, are indicated by white ovals. The non-homogenous O distribution might be the reason for heterogenous slip activity. The scratch was scribed before the test as a fiducial marker. 160

Figure 5.43 Some cracks initiated at relatively small strains in a tensile tested TNTZ-0.3O sample. One crack initiated at (a) ~2% strain and then (b) propagated both upward and downwards throughout other grain boundaries (3% strain), and (c) started to open at 5% strain 160

Figure 5.44 (a) TNTZ-0.3O after ~5% strain, the red ovals indicate that some grains exhibited few traces (the scratch was scribed before the test as marker for measuring the strain) and (b) TNTZ-0.7O at ~ 6% strain (the Vickers indents were made before the test for measuring the strain). 161

Figure 6.1 The storage Modulus (E') and Tan (δ) versus temperature for the TCFA alloy, obtained by a DMA test. The local maximum and minimum of Tan (δ) represents the temperature range of the phase transformation, which occurred between ~ 385 °C and ~ 450 °C..... 165

Figure 6.2 A slight change in slope of heat flux versus temperature is seen at ~ 380 °C for the TCFA alloy, which indicates a phase transformation occurred. 166

Figure 6.3 The effect of heat treatment on the Vickers hardness of TCFA. The samples were heated for 2 hours at the target temperature and then air-cooled. 167

Figure 6.4 The microstructure of the TCFA after heat treatment for 2 hours at (a) 500 °C and (b) 550 °C. The microscale precipitates were observed in both samples, and are believed to be the α platelets. Also, the continuous layers at the grain boundaries in (b) might be α layers (Lütjering and Williams, 2003)..... 168

Figure 6.5 The effect of heat treatment temperature and duration on the Vickers hardness for temperatures between 300 °C and 450 °C, aged for 24 hr. The maximum hardness (506 Hv) was obtained after the heat treatment at 410 °C for 24 hours. The measured hardness as a function of aging time at 410 °C (blue curve). No significant change was observed in the hardness of the samples aged for 24 hours and 48 hours..... 169

Figure 6.6 The stress-displacement curve for a TCFA sample tested at 410 °C. Stress relaxation occurred when the test was paused for acquiring SE SEM photomicrographs. The test lasted for ~ 1.5 hrs. 170

Figure 6.7 (a) Low-magnification SE SEM photomicrographs of the TCFA sample tested at 410 °C to 850 MPa. The test was interrupted for acquiring SE SEM photomicrographs. (b) Severe plastic deformation and many trace lines were observed outside the heated area, (c) The SE SEM photomicrographs of the heated area showed fewer trace lines. The hardness of the central region was ~ 500 Hv, while the hardness of outside of the heater (where the severe plastic deformation was observed) was ~ 340 Hv. The as-received hardness was ~ 320 Hv..... 171

Figure 6.8 A schematic of the modified sample geometry used for the elevated temperature tensile tests on TCFA. The blue circle shows the relative location of the heater. All dimensions are provided in mm. 173

Figure 6.9 The relative location of the heater and the sample for a tensile test performed at 410 °C. Two thermocouples were spot welded to the sample to measure the temperature in the heated area and outside of the heater. The temperature difference between these two locations ranged between 60 °C to 100 °C during the test..... 173

Figure 6.10 The stress-displacement curve for a TCFA sample that was tensile tested at 410 °C. Stress relaxation occurred as a result of pausing the test for acquiring SEM photomicrographs. The UTS was 1400 MPa. The ‘×’ indicates when the fracture occurred..... 174

Figure 6.11 Sequential SE SEM photomicrographs acquired from a selected area at the center of a TCFA sample tested at 410 °C. (a) first pause at 0.25 mm, 202 MPa, (b) second pause at 0.36 mm, 612 MPa, (c) third pause at 0.5 mm, 740 MPa, (d) fourth pause at 0.74 mm, 886 MPa, (e) fifth pause at 1.16 mm, 1150 MPa, (f) sixth pause at 1.6 mm, 1359 MPa. The sample fractured at ~ 1400 MPa..... 175

Figure 6.12 Low-magnification SE SEM photomicrograph of the fractured area of a TCFA sample, tensile tested at 410 °C. The stress was 1400 MPa when the fracture occurred..... 177

Figure 6.13 Dimples were observed in the high-magnification SE SEM photomicrograph of the fractured area for a TCFA sample that was tested in 410 °C (Figure 6.14). The central scratch was scribed before the test and used as a reference marker..... 177

Figure 6.15 The stress-displacement curve for a 410 °C tensile experiment of TCFA. This test was performed monotonically. The ‘×’ indicates when the fracture occurred. 178

Figure 6.16 (a) The gage section of a TCFA sample that was tested at 410 °C, monotonically (i.e., without pausing). The sample fractured near the shoulder. (b) High-magnification SE SEM photomicrograph taken at the center of the gage section [area I in (a)]. (c) More slip traces were observed next to the fractured area at the shoulder [area II in (a)]. 179

Figure 6.17 A schematic of the modified sample geometry used for the elevated temperature tests. The blue circle shows the relative location of the heater. All displacements are provided in mm. 180

Figure 6.18 The effect of preloading on the UTS. A TCFA sample was heat treated at 410 °C for 3 hours, while the sample was subjected to a stress of 600 MPa. Then, due to stress relaxation, the stress dropped to ~520 MPa. After 3 hours, the sample was monotonically loaded until fracture (see the point X)..... 181

Figure 6.19 Prior to tensile loading, the sample was aged for 3 hrs at 410 °C while also being subjected to a stress of 600 MPa. The UTS was ~1130 MPa. The fracture occurred at the center of the sample in the heated area. Evidence of plastic deformation was observed close to the fracture surface..... 182

Figure 6.20 SE SEM photographs taken for the TCFA sample illustrated in Figure 6.19. (a) Low-magnification SE SEM photomicrograph of the fractured area, (b) high-magnification SE SEM photomicrograph of fractured area. Many slip traces observed close to the fracture surface, (c) Many dimples were observed in the fracture surfaces..... 183

Figure 6.21 The stress-displacement curve for TCFA sample at 410 °C. The test was paused 17 times during the test, which lasted ~5 hrs. The UTS was 1435 MPa. “X” indicates where the sample fractured. 184

Figure 6.22 Many slip traces and cracks were observed near the fracture surface for the sample depicted in Figure 6.21. (a) Low-magnification SE SEM photomicrographs near the fracture surface and (b) high-magnification SE SEM photomicrograph near the fracture surface..... 185

Figure 6.23 Stress-displacement of a TCFA sample tensile tested at 450 °C 186

Figure 6.24 Low-magnification SE SEM photomicrograph of a TCFA sample tensile tested at 450 °C. After the 4th pause at 1201 MPa, a crack initiated in the area close to the spot-welded thermocouple. To prevent significant crack propagation, the test was stopped. 187

Figure 6.25 Sequential SE SEM photomicrographs taken from the same microstructural patch for a TCFA sample tensile tested at 450 °C. (a) Before the test, (b) 1st pause at 0.6 mm (700 MPa), (b) at 2nd pause, 0.8 mm (830 MPa), (c) at 3rd pause, 1.1 mm (1000 MPa), (d) at 4th pause, 1.54 mm, 1200 MPa, (e) at 5th pause (the test was stopped at this point due to crack propagation), (f) A crack started to propagate from the bottom of the sample in the area close to the spot-welded thermocouple. A low-magnification SE SEM photomicrograph of this area is shown in Figure 6.24..... 188

Figure 6.26 The stress-displacement curve for a TCFA sample that was tensile tested at 475 °C inside the SEM chamber. 190

Figure 6.27 Sequential SE SEM photomicrographs of the same area taken at different intervals during the tensile experiment. (a) before the test at 475 °C, (b) 1st pause at 617 MPa, 0.43 mm displacement, no evidence of plastic deformation was observed, (c) 2nd pause, 747 MPa, 0.66 mm displacement, surface cracks occurred in some grains, (d) 3rd pause at 1.28 mm displacement, 928 MPa, (e) 4th pause at 1.5 mm displacement, 970 MPa, several slip traces and surface cracks were observed. 191

Figure 6.28 (a) Bright field TEM photomicrograph and (b) TEM SADPs of the <111>, (c) <100> zone axis of β phase for the as-received TCFA alloy. 195

Figure 6.29 An X-ray diffraction pattern of the 400 °C heat treated TCFA sample, which exhibited an ω peak at $\sim 63^\circ$ 195

Figure 6.30 TEM photomicrographs of a TCFA sample that was tensile tested at 410°C. Some of the β phase transformed into the ω phase. (a) Bright field TEM image, (b) TEM SADP, (c) TEM Dark field image highlighting the ω phase variant associated with the diffraction spot highlighted by the red circle in (b), and (d) TEM dark field image highlighting the ω phase variant associated with the diffraction spot highlighted by the yellow circle in (b). 196

Figure 6.31 The stress-displacement curves for TCFA samples, tensile tested at RT, 410 °C, 450 °C, and 475 °C 199

LIST OF ABBREVIATIONS

2D	Two-dimensional
3D	Three-dimensional
Al	Aluminum
ASTM	American society for testing and materials
bcc	Body-centered cubic
BSE	Backscattered electron
CP	Commercially pure
Cr	Chromium
Cu	Copper
EBSD	Electron backscattered diffraction
EDM	Electro-discharge machining
ε_f	Elongation-to-failure
ε_{tot}	Total strain
Fe	Iron
fcc	Face centered cubic

hcp Hexagonal closed-packed

IPF Inverse pole figure

Mg Magnesium

Mo Molybdenum

N Nitrogen

Nb Niobium

Ni Nickel

RD Rolling or reference direction

RT Room temperature

O Oxygen

pct. Percent

σ stress

SE Secondary electron

SEM Scanning electron microscopy

SiC Silicon carbide

TD Transverse direction

TEM Transmission electron microscopy

Ti Titanium

V Vanadium

wt.% Weight percent

XRD X-ray diffraction

YS Yield strength

UTS Ultimate tensile strength

Zr Zirconium

TCFA Ti-13Cr-1Fe-3Al

TNTZ Ti-29Nb-13Ta-4.6Zr

CHAPTER 1

1 RATIONALE AND RESEARCH OBJECTIVE

1.1 Microscale study of polycrystalline materials

Component failure is a common problem in many industries. Metallic failure due to applied load is typically the result of damage accumulation, which starts from nanoscale and microscale events and extends to the macroscale. The deformation heterogeneity in polycrystalline materials leads to stress concentrations, which causes damage initiation. Studying the microstructure provides us a better understanding of the heterogeneous response of polycrystalline materials. Crystallographic orientation change occurs within the grains when polycrystalline materials are subjected to deformation. One methodology to investigate the heterogeneous deformation behavior is to study the local crystallographic orientation change within polycrystalline microstructures.

Electron backscatter diffraction (EBSD) is a commonly used characterization technique to measure the crystallographic orientations in polycrystalline materials. The first fully automated EBSD system was developed by Wright and Adams in 1992 (Wright and Adams, 1992), which was later termed Orientation Imaging Microscopy (OIM) (Adams et al., 1993). EBSD systems have been used to capture the evolving microstructural changes due to mechanical deformation and/or study the recrystallization behavior of metallic materials during in-situ heat treatment experiments (Adams et al., 1993; Boehlert et al., 2013; Chakkedath et al., 2016; El-Dasher et al., 2003; Khorashadizadeh et al., 2011; Rohrer et al., 2010; Wright and Adams, 1992; Wright et al., 2011).

The crystallographic orientation change has been correlated to plastic strain to estimate the level of plastic strain (Kamaya et al., 2005; Wright et al., 2016). In general, two methods have been used for quantifying the misorientation. The first method is based on the local variation of crystallographic orientation change between individual points. The Kernel Average Misorientation (KAM) has been used to quantify the local misorientation (Calcagnotto et al., 2010; Demir and Raabe, 2010). In the KAM approach, the average misorientation between the center point and its surrounding points is measured. In this method, the results are dependent on step size and the nearest neighboring points, e.g. the first nearest neighbor KAM exhibited higher values than the third nearest neighbors at all the measured strain levels (Wright et al., 2011; Wright et al., 2016). In the second method, a reference orientation, which will be explained in section 4.2, is defined for each grain and then the average misorientation is calculated for each individual grain based on reference orientation. The advantage of the second method over the first one is that the step size is not as influential (Kamaya et al., 2005). Until now, the effect of the chosen reference orientation has not been extensively studied. In the first part of this work, the effect of reference orientation was investigated at both the grain scale and also at the mesoscale. Furthermore, the effect of grain size, crystallographic orientation, and loading history on misorientation was studied. Another goal of this work was to qualitatively investigate the correlation between the hot spots from the DIC-SEM strain field map with EBSD crystallographic misorientation maps.

1.2 Justification for studying the deformation behavior of Ti alloys

Ti alloys have been used in the chemical processing, desalination, biomedical, oil and gas, power energy, sports, and automotive industries due to their high strength, high stiffness, high toughness, low density, excellent corrosion resistance, high melting point, and good biocompatibility (Lütjering and Williams, 2003). Figure 1.1 shows some examples of Ti alloy

applications in the biomedical, structural, and oil and gas industries. Ti is the fourth most abundant structural metal (after aluminum (Al), iron (Fe), and magnesium (Mg)) in the earth's crust. Although Ti was discovered in 1791 by William Gregor, it did not come into industrial use until the late 1940s and early 1950s (Lütjering and Williams, 2003). In Table 1.1 some important characteristics of Ti alloys are compared with other commonly used structural alloys based on Fe, Al, and nickel (Ni). High specific strength (the strength over weight ratio) is a factor that makes Ti alloys attractive for applications where weight saving is important, e.g. in the aerospace industry.

Ti alloys are divided into four groups based on their composition and equilibrium constituent phase(s) at room temperature (RT): α Ti, near- α Ti alloys, $\alpha+\beta$ Ti alloys, and β Ti alloys (Donachie, 2000). As provided in Figure 1.2, commercially-pure Ti (CP-Ti) and Ti-6Al-4V (Ti64) are the most widely used, while the β Ti alloys only had 4% of the total Ti market in 1998. The relatively high cost of Ti alloys is one of the major limitations of expanding their use in many other industries. To overcome this obstacle, many researches have been performed to develop and fabricate low-cost Ti alloys (Esteban et al., 2011; Gunawarman et al., 2005; Hartman et al., 1998; Santos et al., 2015, 2016). Furthermore, the low elastic modulus, high strength, and good biocompatible properties of Ti alloys make them suitable for biomedical implant applications (Akahori et al., 2005; Niinomi, 1998, 2003, 2008; Rack and Qazi, 2006; Zhou et al., 2004). In the past two decades many efforts have been made to introduce new biomedical Ti alloys, with low elastic moduli, for implant applications (Geetha et al., 2009; Kuroda et al., 1998; Long and Rack, 1998; Mohammed et al., 2014).

Considering that Ti alloys are relatively new materials (compared to steel and Al alloys for example), there is still room for research and development to gain a better understanding of the

deformation behavior of Ti alloys under service conditions. Therefore, it is essential to provide a detailed characterization of their microstructures, mechanical properties and deformation behavior. One of the objectives of this research was to characterize the microstructure and deformation behavior of three bcc Ti alloys:

- I. Ti-13Cr-1Fe-3Al (wt.%)¹, which is a relatively new low-cost Ti alloy that has potential for structural and biomedical applications
- II. TIMETAL-21S, which is a commercially established β Ti alloy
- III. Ti-29Nb-13Ta-4.6Zr-xO alloys (where x is 0.1, 0.3, and 0.7 wt.%), which were developed in Japan mainly for biomedical applications

Table 1-1 Some of the basic characteristics of Ti alloys as compared with Fe, Ni, and Al alloys (Lütjering and Williams, 2003)

	Ti	Fe	Ni	Al
Melting Temperature (°C)	1670	1538	1455	660
RT E (GPa)	115	215	200	72
Yield Stress Level (MPa)	1000	1000	1000	500
Density (g/cm ³)	4.5	7.9	8.9	2.7
Comparative Corrosion Resistance	Very High	Low	Medium	High
Comparative Reactivity with Oxygen	Very High	Low	Low	High
Comparative Price of Metal	Very High	Low	High	Medium

¹ Henceforth in this dissertation, all alloy compositions are provided in weight percent unless otherwise noted.

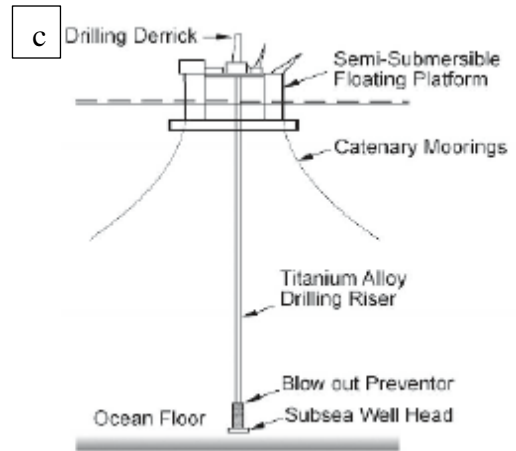
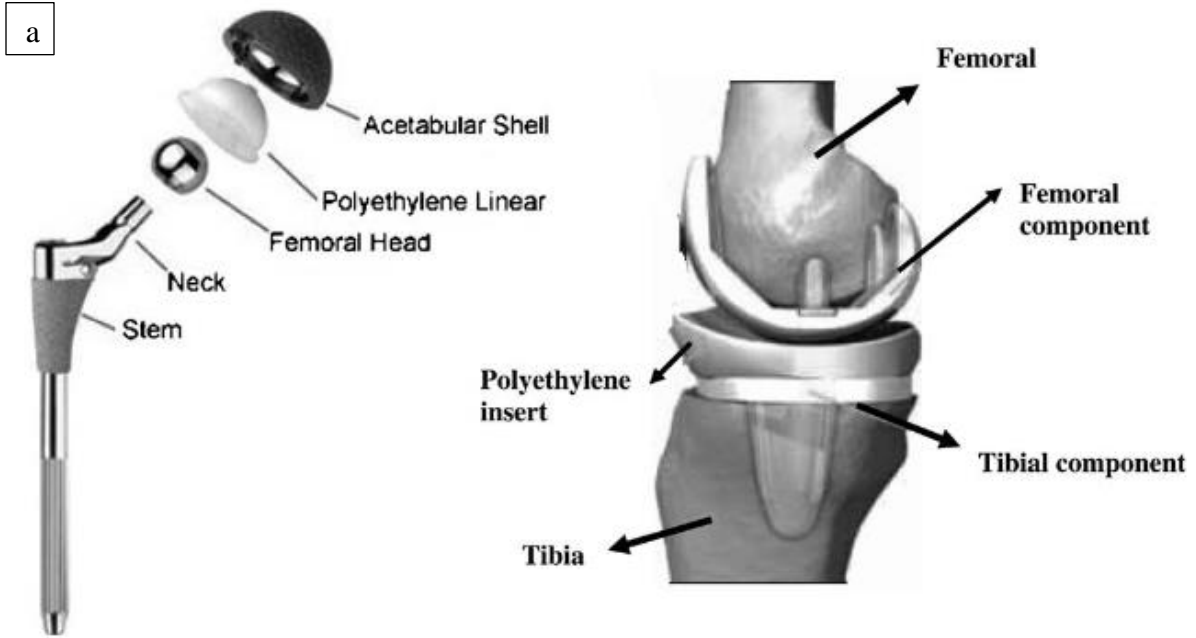


Figure 1.1 Some Ti alloy applications: (a) Hip and knee implant, (b) Fukuoka Yahuoku Dome's roof, (c) Oil and gas drilling riser (Geetha et al., 2009; Lütjering and Williams, 2003)

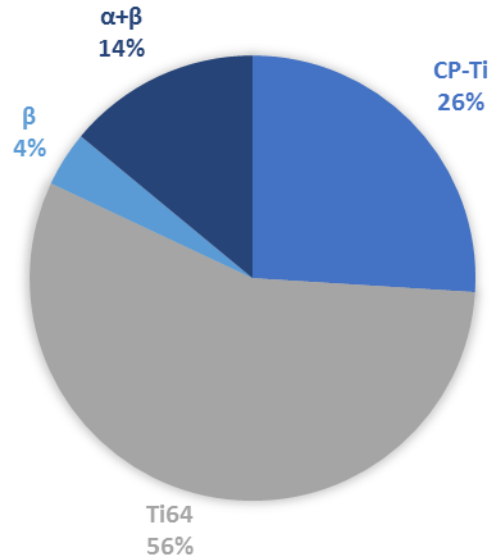


Figure 1.2 Approximate breakdown of the USA market of Ti and its alloys in 1998 (Lütjering and Williams, 2003)

1.3 Work performed

In the first part of this dissertation research, two approaches were used to characterize the deformation behavior of bcc Ti alloys at the microscale, namely misorientation analysis and slip trace analysis. In addition, the effect of oxygen (O) content on the deformation mode of Ti-29Nb-13Ta-4.6Zr-xO (where x is 0.1, 0.3, and 0.7 wt.%) was investigated. In the second part, the strength of a low-cost Ti alloy, Ti-13Cr-1Fe-3Al (TCFA), was enhanced by thermomechanical processing (TMP), which led to exceptionally high tensile strength in the temperature range of 385 °C to 450 °C.

In Chapter 2, a literature review is presented on misorientation analysis and slip trace analysis. A background on Ti and Ti alloys, including their crystal structure and alloying elements is

provided. The effect of interstitial elements on mechanical properties of Ti alloys is also presented, and the influence of heat treatment on bcc Ti alloys is discussed.

In Chapter 3, the experimental procedures and the equipment used in this research are presented. The measured alloy compositions are provided for each material. The techniques used for microstructural characterization and in-situ specimen preparation are described. Details of the in-situ mechanical tests and the heat treatment conditions are presented. A summary of the performed tests is also provided.

In Chapter 4, the results of the microstructure, texture, grain size, and in-situ tensile tests are presented. The influence of reference orientation on the crystallographic misorientation distribution at the grain scale and mesoscale for two Ti alloys (TCFA and TIMETAL-21S) is described. The corresponding crystallographic misorientation maps are provided. The relationship between global misorientation and plastic strain and the effects of grain size and crystallographic orientation on the misorientation level are discussed. An empirical equation is proposed to predict the misorientation at the grain scale as a function of global plastic strain and grain size. The influence of loading history on the misorientation is also described. The plastic strain field map, obtained from an in-situ SEM DIC experiment, is compared against five misorientation maps at the end of Chapter 4.

In Chapter 5, the slip trace analysis performed in this work is explained. In-situ tensile experiments, which were performed at RT, 200 °C and 300 °C for TCFA and TIMETAL-21S, are presented. The deformation evolution, captured by secondary electron (SE) SEM photomicrographs, is presented. The EBSD IPF maps for each test, both before and after deformation, are provided. The results of the slip trace analysis and the active deformation systems

for each testing condition of each material (TCFA, TIMETAL-21S, and TNTZ-xO) are presented and discussed. The distribution of the deformation modes is presented. Also, the effect of O content on the distribution of the deformation modes for TNTZ-xO is presented.

In Chapter 6, the TMP that was performed on TCFA is described. The temperature range of the phase transformation of TCFA was determined by two methods: Dynamic Mechanical Analyzer (DMA) and Differential Scanning Calorimetry (DSC). Based on those results, heat treatments were performed in the temperature range of 300 °C to 600 °C. The photomicrographs of the microstructures are provided for such heat-treated samples. The hardness test results for the heat-treated samples are presented. The results of the in-situ SEM tension experiments are also provided. The details of the TMP, which led to achieving the high strength of TCFA, are presented and discussed. In addition, the SE SEM photomicrographs of the surfaces of the deformed samples and their fracture surfaces are also provided and discussed.

In Chapter 7, the research summary and conclusions of this work are provided, and future work is suggested to guide further progress in this area.

CHAPTER 2

2 BACKGROUND AND LITERATURE REVIEW

The elastic and plastic responses of polycrystalline materials to applied load is generally heterogeneous especially at the microscale. Anisotropy has been proposed as a driving force for this behavior. During plastic deformation, the composition, crystallographic orientation, and loading condition can lead to activation of the following deformation mechanisms (Callister and Rethwisch, 2013):

- Dislocation slip
- Twinning
- Phase transformation
- Grain boundary sliding
- Diffusion

More than one of the above-mentioned deformation mechanisms can be activated simultaneously. When dislocation slip occurs, the crystal lattice rotates within the grains, which is affected by the neighboring grains. Otherwise, voids and cracks may form, which usually are the precursor to failure. Therefore, to gain a better understanding of the materials' behavior, it is essential to characterize the microstructural changes when the materials are subjected to plastic deformation. Microscale study of deformation provides us with details of the deformation mechanisms and also the damage initiation and propagation events.

EBSD and Transmission Electron Microscopy (TEM) have opened a window for better understanding of the nanoscale and microscale deformation behavior of polycrystalline materials.

Although TEM has been frequently used for characterization of the deformation behavior of materials, EBSD is now more widely used due to the following advantages over TEM (Humphreys, 2004):

- Easier sample preparation
- Large areas and volumes of material can be studied in less time.
- Relative ease of identifying an area of interest to study, such as a particular grain boundary, or grains with specific orientation and size, etc.
- More rapid and automated data acquisition
- Less expensive equipment

During plastic deformation, the density of geometrically necessary dislocations (GNDs) increases locally to accommodate local strain compatibilities, especially in neighboring grain boundaries. This results in orientation gradients within the grains (Schwartz et al., 2009).

2.1 Misorientation

The EBSD has been widely used for acquiring the crystallographic orientations of polycrystalline materials. The data obtained have been used to quantify the relationship between the crystallographic orientation and the plastic strain distribution (Brewer et al., 2006, 2009; Britton et al., 2010; Kamaya et al., 2005; Wilkinson and Britton, 2012; Wilkinson et al., 2014; Wright et al., 2011). Subedi et al. (2015) studied the variation of crystallographic orientation gradients by measuring the Kernel Average Misorientation (KAM) on polycrystalline pure copper at different regions of a tensile sample loaded to failure. For the region with low strains (~2%), the KAM values were higher at grain boundaries compared with the grain interiors, regardless of the EBSD step size. However, they observed that at a higher strain level (13%), the KAM values depended

on the step size. That is, for fine data point spacing (small step size), they reported that KAM values were higher at grain boundaries than within the grain, while for coarse data point spacing, the opposite was observed (Subedi et al., 2015). Their hypothesis was that the orientation change is larger in the perpendicular direction to the grain boundaries than in the parallel direction to the grain boundaries.

The following might be the reason for this behavior. Consider the 1st nearest KAM distribution in the vicinity of a grain boundary in a polycrystalline microstructure patch in two scenarios. If the spatial distance during data acquisition is very small, for example on the order of a few nanometers, the orientation change between neighboring points is very small, which results in very small KAM values, even though the materials were subjected to a relatively high plastic strain. This concern becomes more evident by considering the error of the data acquisition system, i.e. if the local change in orientation is less than the accuracy of the measurement system, the results are not repeatable. Hence, the KAM distribution depends on the spatial distance of the data acquisition.

Kamaya et al. [2005, 2006, 2009, 2011, 2012] quantified the relationship between plastic strain and crystal orientation for stainless steel and nickel-based alloys. They introduced a parameter, called Crystal Deformation (CD), which quantified the misorientation dispersion within each grain. The CD was independent of data density and the EBSD data acquisition system. The CD exhibited a linear relationship with plastic strain. Furthermore, the local average orientation gradient was measured with respect to a reference orientation. This methodology qualitatively suggested that the local average orientation gradient was higher in the neighborhood of grain boundaries and triple points (Kamaya et al., 2005). Later, the Modified Crystal Deformation Parameter (MCD) was introduced by the same research group. The MCD results also suggested a linear relationship between misorientation and plastic strain. However, the slope of the linear trend

between the plastic strain and the MCD was different than the slope of the CD versus the plastic strain for the same material (Kamaya et al., 2006). Kamaya proposed an average local misorientation measurement, which was a function of step size (Kamaya, 2009). For validation of this methodology, Type 316 austenitic stainless steel was tensile tested to plastic strains up to 19.7%. The results revealed that the relationship between plastic strain and misorientation was not linear for strains greater than 10%, especially for coarse step sizes. The results indicated that the plastic strain could be 15% locally when the global plastic strain was 4.9%. They also reported that the plastic deformation is locally higher near grain boundaries (Kamaya, 2009). Later, they introduced another parameter, local gradient (G_L). The G_L was defined as the slope of the average local misorientation² versus the distance from a reference point (Kamaya, 2011). They carried out a G_L sensitivity analysis. The results indicated that G_L was hardly affected by grid pattern and step size, and it was not affected by the measurement accuracy. This method was examined for Type 316 austenitic stainless steel using the notch root test, which showed that the strain gradient near the notch root could be estimated by the EBSD measurements (Kamaya, 2011).

EBSD, in conjunction with SEM imaging, was used to capture the localized plastic deformation at grain boundaries³ for Type 316 stainless steel. It was observed that the localized misorientation at the grain boundaries was more than three times that of the misorientation averaged over the entire area. It should be noted that the grain boundary misorientation was the average taken from data within 3 μm of the grain boundaries and the step size was 0.5 μm (Kamaya, 2012).

² The local misorientation was defined similar to the KAM, with a slight difference in definition of the neighboring points.

³ The localized plastic deformation at grain boundaries was defined as the average misorientation of the points, which their distance was less than a threshold from a particular grain boundary.

Buchheit et al. evaluated the misorientation evolution in annealed tantalum (Ta), which was tensile deformed inside a SEM to 20% strain (Buchheit et al., 2015). The misorientation distribution maps of selected areas were obtained based on the average orientation before deformation and the average orientation after deformation for corresponding strain levels as shown in Figure 2.1.

The results revealed that the relative misorientations was as high as 20° at 15% strain in some locations. In addition, the local misorientation was relatively high near grain boundaries, and such locations were the preferred locations for the initiation of new subgrains (Buchheit et al., 2015). Wright et al. carried out a uniaxial tensile test inside a SEM in conjunction with EBSD on a steel specimen. It was observed that both the KAM and the grain orientation spread increased with increasing strain (Wright et al., 2016).

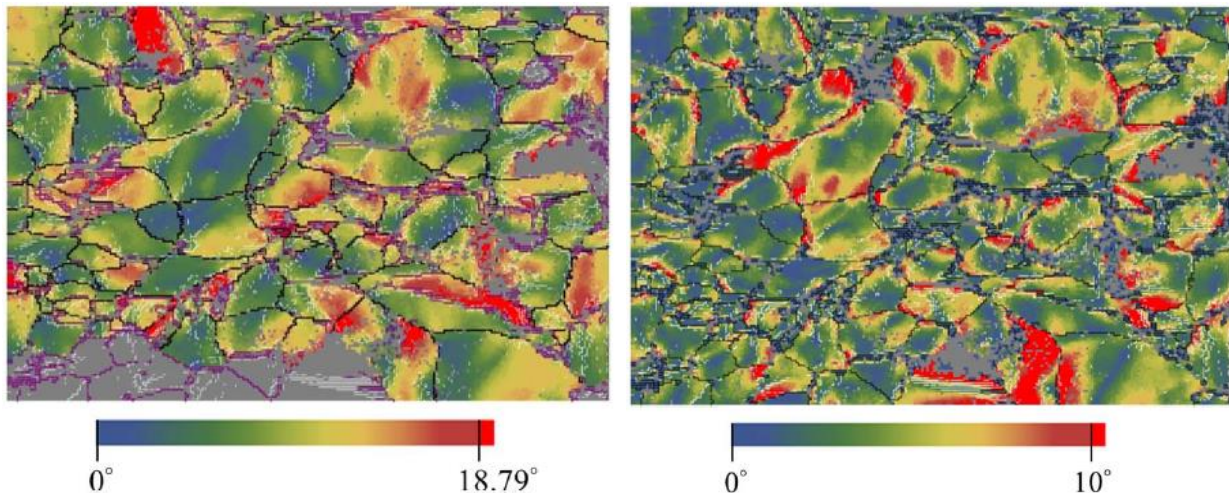


Figure 2.1 The misorientation distribution maps obtained based on the average orientation: (a) before deformation and (b) after deformation (Buchheit et al., 2015).

2.2 DIC

Digital Image correlation (DIC) was developed in the early 1980s to capture and track the full-field displacements and thus the strains in 2D and 3D space (Peters and Ranson, 1982; Sutton et al., 1983). Due to relatively easy use and existence of commercial and user-friendly software, such as Vic2D, the DIC has been used in a variety of fields from material characterization to biomedical applications. Compared to the conventional measurement tools, such as extensometers and strain gages, the DIC provides more detailed information during the deformation, such as local strain measurements, which highlight strain concentrations and local heterogeneous deformation. Such information is critical for understanding the deformation behavior, especially heterogeneous deformation. In addition, the full-field strain maps acquired through DIC at the microscale are important for the validation (or improvement) of theoretical models (e.g., crystal plasticity models). Recently, high resolution DIC (which can be used in conjunction with in-situ SEM experiments) has been developed to investigate and characterize the mechanical behavior of the metallic materials at the microscale (Sutton et al., 2006, 2007a, 2007b). This technique allows for direct quantification of the local strain concentrations at the microscale of the polycrystalline materials (Abuzaid et al., 2012a, 2012b; Carroll et al., 2013a; Chen and Daly, 2017; Ghadbeigi et al., 2010; Kang et al., 2007).

The DIC procedure at the microscale is briefly explained here. After polishing to a mirror finish, the sample is coated with high contrast nanoscale particles. The coated interest area is divided into subsets. Each individual subset has a unique grayscale value (due to the randomized pattern). The displacement field is determined by comparing the reference image (usually from the undeformed

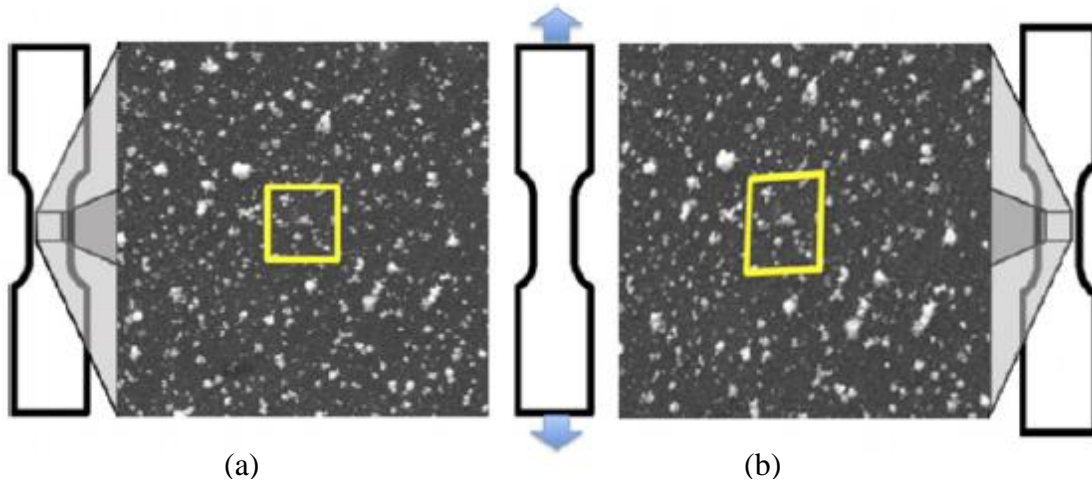


Figure 2.2 (a) a subset of random particles before deformation and (b) the subset of same area at deformed state. The displacement field is determined by comparing these two subsets with an image processing algorithm (Kammers and Daly, 2013a).

material) to the image of the deformed sample through an image processing algorithm. Then, the strain field is calculated from the displacement field. For the 2D DIC measurement, only one camera is required. However, two cameras are required for the 3D DIC measurement. For illustration, an area is highlighted before and after deformation in Figure 2.2 (Sutton et al., 2009).

2.3 Strain aging and Cottrell atmosphere

After reloading a sample, which was partially or totally unloaded, with the same loading rate, the YS may increase. This phenomenon is called static strain aging (Kubin et al., 1992). As presented in Figure 2.3, the UTS increases (compare point A and B in Figure 2.3), while the elongation-to-failure (ϵ_f) decreases. It is generally accepted that the interstitial atoms diffuse to dislocation cores during the aging and form the Cottrell atmosphere, which results in a greater YS. With increasing strain in the elastic region, the stress increases continually. However, a sudden decrease in stress may occur after reaching the YS in some of the metallic materials. The stress at

which the sudden drop occurs is called the upper yield point (point A in Figure 2.3), and the lower stress is known as the lower yield point (point A' in Figure 2.3). This phenomenon is mainly associated with interstitial impurities and has been explained by the Cottrell atmosphere (Cottrell and Bilby, 1949). The Cottrell atmosphere occurs in bcc and fcc materials with small interstitial atoms. In this process, the lattice is slightly distorted by interstitial atoms, which results in a residual stress field surrounding the interstitial atoms. In attempt to reduce the residual stress field, the interstitial atoms diffuse towards dislocation cores and pin the dislocations (see Figure 2.4). To unpin the dislocation, a small extra force is required to initiate the dislocation motion (upper yield point). Immediately after the unpinning, the dislocations are free to move, which requires a lower force (i.e., a lower yield point).

2.4 Fundamentals of Ti and Ti alloys

2.4.1 Crystal structure

Ti is a transition metal with an atomic number of 22, an atomic weight of 47.9, and an electron configuration of $[\text{Ar}]3d^24s^2$. Pure Ti has a hexagonal crystal structure (termed α phase) with lattice parameters of $a=0.295$ nm, and $c=0.466$ nm at RT. The c/a ratio is 1.587, which is smaller than ideal value (1.633) for hexagonal close packed (hcp) structure. Ti exhibits an allotropic phase transformation from hcp to bcc with a lattice parameter of $a=0.332$ nm. The Ti bcc phase is called the beta phase (β). Figure 2.5 represents a schematic of the α and β unit cells for pure Ti. The Ti alloying elements are classified into three groups: α stabilizing, β stabilizing, and neutral based on their effect on the β transus temperature. The lowest temperature at which a 100% β phase can exist is called the β transus temperature. The β transus temperature increases with increasing solute

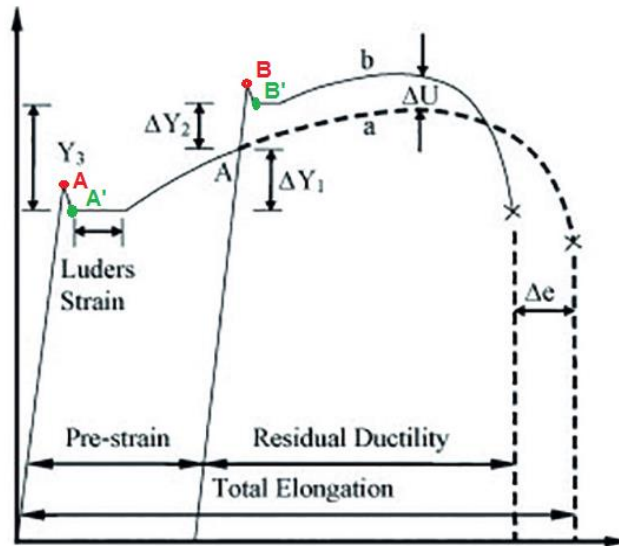


Figure 2.3 Typical stress (y-axis) versus strain (x-axis) behavior in materials exhibiting upper and lower yield points. A sudden decrease in the stress may occur after reaching the YS in some metallic materials (see points A, A', B, and B'). The stress at which the sudden drop occurs is called the upper yield point (point A and B), while the lower stress is known as lower yield point. ΔY_1 = increase in stress produced by pre-strain, ΔY_2 = increase in stress produced by aging, ΔY_3 = increase in stress produced by pre-straining and aging= $\Delta Y_1 + \Delta Y_2$, ΔU = Change in UTS due to pre-straining and aging, Δe =Change in elongation due to pre-straining and aging (Bülbul et al., 2017)

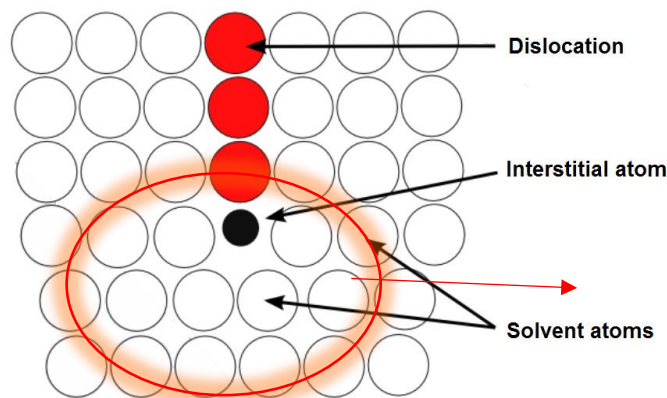


Figure 2.4 Interstitial atom diffuses to the dislocation core to form a Cottrell atmosphere⁴

⁴ https://en.wikipedia.org/wiki/Cottrell_atmosphere, the figure was modified.

content of α stabilizers. The substitutional element Al and the interstitial elements O, N, and C are strong α stabilizers. Al is the most commonly used element in Ti alloys. It is the only element in Ti alloys which raises the β transus temperature and has solubilities in both the α and β phases. β stabilizing elements are classified into β isomorphous elements and β eutectoid elements, based on the binary phase diagrams. V, Mo, and Nb are the most commonly used β isomorphous elements in Ti alloys. Adequate contents of these elements make it possible to stabilize the β phase at RT. The Cr, Fe, and Si are the most frequently used β eutectoid elements in Ti alloys. The effect of the α and β and neutral alloying elements are schematically represented in the corresponding phase diagrams provided in Figure 2.6. The most important alloying elements are provided for each group in Figure 2.6 (Brunette et al., 2012; Donachie, 2000; Leyens and Peters, 2006; Lütjering and Williams, 2003).

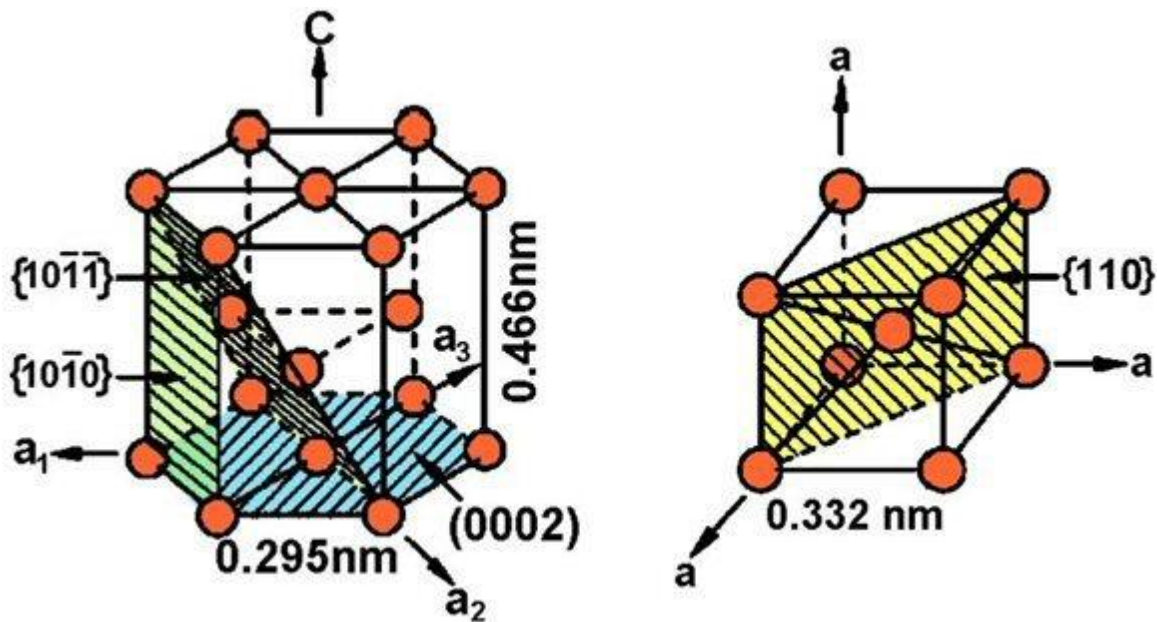


Figure 2.5 The unit cell of (a) the α phase and (b) the β phase of pure Ti. The corresponding lattice parameters are also provided⁵.

⁵ <http://www.dierk-raabe.com/titanium-alloys/>

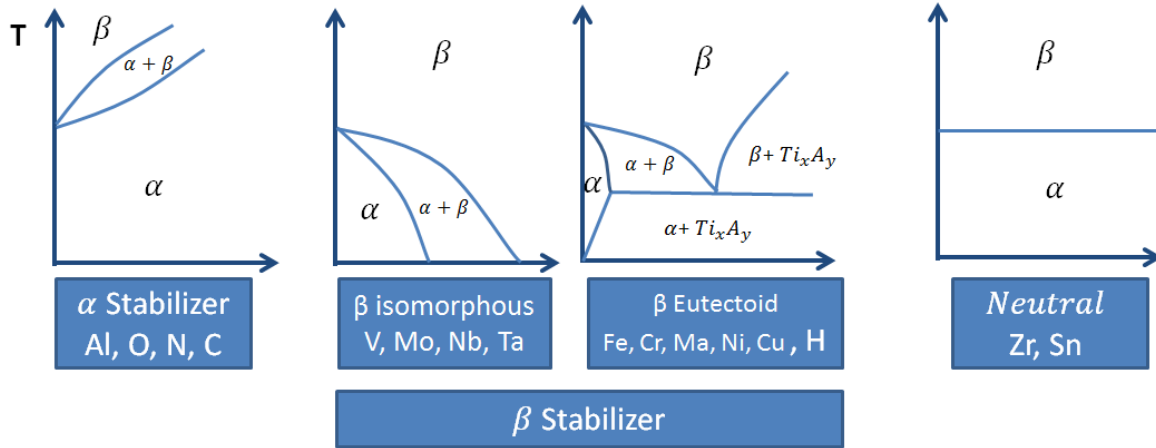


Figure 2.6 Alloying elements classified into three groups based on their effect on the β transus temperature (Geetha et al., 2009; Lütjering and Williams, 2003).

2.4.2 Deformation mechanism

Permanent deformation of Ti alloys is mostly attributed to the activation of slip systems and twinning. However, mechanical twinning and stress-induced martensitic (SIM) transformation have been observed during plastic deformation in some Ti alloys. For characterization of the deformation mode of Ti alloys, slip trace analysis has been extensively performed on α and α - β Ti alloys to investigate and characterize the deformation behavior (Boehlert et al., 2013; Li et al., 2012, 2013; Yin et al., 2016). 24 slip systems are usually considered for slip trace analysis of α Ti alloys (3 basal, 3 prismatic, 6 pyramidal $\langle a \rangle$, and 12 1st order pyramidal $\langle c+a \rangle$). Li et al. investigated the deformation behavior of near- α Ti-3Al-2.5V from RT to 455 °C (Li et al., 2014). The results revealed that prismatic slip was the dominant slip mode, independent of test temperature. In addition, it was observed that the extent of twinning decreased with increasing temperature. In tension-creep experiments, it was reported that grain boundary sliding played a significant role in the deformation. The deformation behavior of α - β Ti-6Al-4V was studied at RT and 455 °C (Li et al., 2015). The basal and prismatic slip played a major role in the tensile

deformation at RT and 455 °C, while twinning was observed in 4% of the total deformation systems. Prismatic slip was more active than basal slip at RT, which was in agreement with the results of Bridier et al. on the same alloy, while basal slip was more active than prismatic slip at 455 °C (Bridier et al., 2005).

Similar to α and α - β Ti alloys, the permanent deformation of β Ti alloys is mostly attributed to the activation of slip systems, especially when the β phase is stable (Hanada and Izumi, 1987). However, mechanical twinning and SIM transformation are more likely in the Ti alloys with relatively unstable β phase (Hanada and Izumi, 1987). The bcc materials exhibit a greater number of slip systems than fcc and hcp materials. 48 slip systems are distinguished in the bcc structure, while the fcc and hcp crystals have 12 and 24 slip systems, respectively. The high number of slip systems makes slip trace analysis of the bcc materials more complicated than the fcc and hcp materials. This complexity becomes more apparent considering the fact that unlike the fcc and hcp structures, there is no close packed plane for bcc crystals. In bcc materials, slip occurs in the close packed direction of the $\langle 111 \rangle$. Hence, slip may occur in the maximum resolved shear stress plane (MRSSP) in the $\langle 111 \rangle$ direction, even though the MRSSP may not even be one of the crystallographic planes [Pencil glide] (Gilormini et al., 1988; Taylor and Elam, 1926).

The common slip families in bcc materials are $\{110\}$, $\{112\}$, and $\{123\}$, all of which have a Burgers vector of $\langle 111 \rangle$. Figure 2.7 schematically represents the slip systems in bcc materials (Lütjering and Williams, 2003):

- I. Slip system $\{110\}\langle 111 \rangle$ has 6 slip planes, where each plane has 2 Burgers vectors.
- II. Slip system $\{211\}\langle 111 \rangle$ has 12 slip planes, where each plane has 1 Burgers vector.
- III. Slip system $\{321\}\langle 111 \rangle$ has 24 slip planes, where each plane has 1 Burgers vector.

With respect to the deformation of bcc metals such as Molybdenum, Tungsten, Tantalum, and Vanadium, slip appears planar and almost always occurs on $\{110\} \langle 111 \rangle$ systems at low temperatures. However, by increasing the temperature, there is an increase in the propensity for diffuse, wavy slip, and the activation of the $\{110\}$, $\{112\}$, and $\{123\}$ slip systems (Weinberger et al., 2013). However, in some studies, only the activation of the $\{110\} \langle 111 \rangle$, $\{112\} \langle 111 \rangle$, or/and the pencil glide have been observed at RT (Franciosi et al., 2015; Gilormini et al., 1988; Hsiung, 2010; Taylor and Elam, 1926; Weinberger et al., 2013). On the other hand, the activation and cooperation of all three slip systems have been identified in some other studies. For example, dislocation activity has been observed in all three slip systems ($\{110\}$, $\{112\}$, and $\{123\}$) at RT tensile tests on a β Ti alloy and a pure polycrystalline bcc Ta (Castany et al., 2012; Carroll et al., 2013a). In another study, the slip activity of 230 ferrite grains (bcc structure) were analyzed in a duplex stainless steel subjected to low-cycle fatigue (El Bartali et al., 2008). The results confirmed the activation of all the slip systems with a Schmid factor greater than 0.39. The typical slip features at 2300 cycles is present in Figure 2.8.

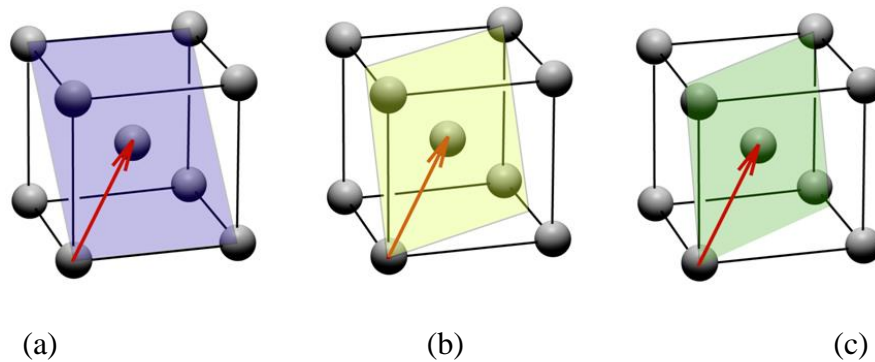


Figure 2.7 Illustration of three slip systems in bcc materials highlighted by a shaded plane and a direction depicted by the red arrows: (a) one variant of the six $\{110\}$ slip planes, (b) one variant of the twelve $\{211\}$ slip planes, (c) one variant of the twenty-four $\{321\}$ slip planes. All the systems have a common Burgers vector of $\langle 111 \rangle$.

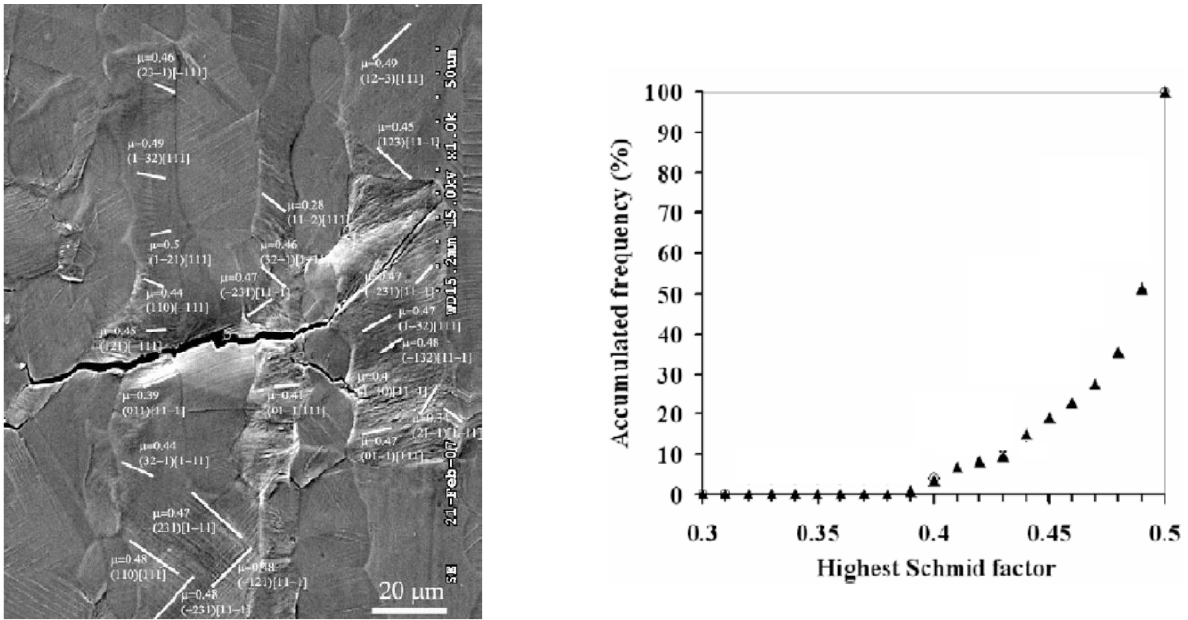


Figure 2.8 (a) SEM photomicrograph taken at $N = 2300$ cycles, activated slip systems and associated Schmid factors (μ) in ferritic grains, (b) accumulated frequencies of the highest Schmid factors for 230 ferritic grains of which the slip systems are identified (area of $600 \times 500 \mu\text{m}^2$) (El Bartali et al., 2008).

2.4.3 The effect of substitutional alloying elements on the strength of Ti alloys

Table 2.1 provides the tensile properties of CP-Ti and Ti-6Al-4V, which are the most frequently used materials in the Ti industry. For enhancing the mechanical properties of Ti alloys, the use of substitutional alloying elements is common. The different alloying contents and processing conditions result in different grain sizes and therefore influence the yield stress (YS).

The strengthening mechanisms of Ti alloys can be classified into: solid solution strengthening, dislocation density hardening, boundary strengthening, precipitate hardening, grain refinement (Lütjering and Williams, 2003) . The amount of substitutional alloying elements influence precipitation, which accordingly influences the strength of Ti alloys (Hwang et al., 2005; Lee et al., 2002; Li et al., 2002; Sakaguchi et al., 2005a, 2005b).

Table 2-1 The mechanical properties of CP-Ti and Ti-6Al-4V alloys (Lütjering and Williams, 2003).

Alloy	YS (MPa)	UTS (MPa)	Elongation %	E (GPa)	O content (wt.%)	Phase(s) In microstructure
CP Ti, Grade 1	170	240	24	100	0.18	α
CP Ti, Grade 2	275	345	20	100	0.25	α
CP Ti, Grade 3	380	450	18	100	0.35	α
CP Ti, Grade 4	485	550	15	100	0.5	α
Ti-6Al-4V (Standard)	780	860	10	110	0.2	$\alpha + \beta$
Ti-6Al-4V (ELI)	795	860	10	110	0.13	$\alpha + \beta$

The effect of Ta content (ranged from 0 to 20 (wt.)) was investigated in the Ti-30Nb-xTa-5Zr system (Sakaguchi et al., 2005a). The results revealed that both YS and elastic modulus (E) decreased with increasing Ta content from 0 wt.% to 10 wt.%. However, the YS increased with increasing Ta content from 15 wt.% and 20 wt.%. It was reported that the deformation mechanism was stress-induced martensitic transformation when the Ta content was less than 10 wt.%, while slip was the dominant deformation mechanism when the Ta content was 20 wt.%.

Lee et al. investigated the effect of Nb content on the mechanical properties of Ti-xNb alloys, where x was between 5 to 35 wt.% (Lee et al., 2002). They observed that the amount of Nb affects the crystal structure and morphology of Ti-xNb alloys. The alloy microstructure was dominated by the hexagonal phase when the Nb content was less than 15 wt.%. The alloy microstructure was dominated by the orthorhombic phase when the Nb content was between 17.5 to 25 wt.%. The alloy microstructure was dominated by the β phase when Nb content was higher than 25 wt.%. The highest strengths were achieved in Ti-10Nb and Ti-27.5Nb, where the dominant phases were orthorhombic and β , respectively. The effect of Nb content on the properties of Ti-xNb-10Ta-5Zr (where x was between 20 to 35) has also been investigated (Sakaguchi et al., 2005b). The maximum proof strength was achieved when the Nb content was 20 wt.%. The XRD profile

indicated the existence of the ω phase in Ti-20Nb-10Ta-5Zr, and stress-induced martensite transformation was the dominant deformation mechanism.

2.4.4 The effect of precipitation on the strength of Ti alloys

Precipitation hardening is the most effective mechanism for enhancing the strength of β Ti alloys (Lütjering and Williams, 2003). The precipitate volume fraction, size, and type can significantly affect the strength of β Ti alloys by hindering dislocation motion, which strongly depends on alloying contents, thermal treatment, and TMP (Ankem and Greene, 1999; Ivasishin et al., 2003; Liu and Welsch, 1988; Nag et al., 2009; Qazi et al., 2005; Rohrer, 2001). Banerjee et al. observed an increase in the hardness of Ti-13Mo-7Zr-3Fe after aging due to a refined scale of the α phase as shown in Figure 2.9. In another alloy, Ti-34Nb-9Zr-8Ta, the strength decreased for the same thermal treatment due to destroying the ordering of the B2 phase in the matrix (Banerjee et al., 2004).

The nanometer scale ω precipitates, which exhibit a hexagonal crystal structure, form by three mechanisms in Ti alloys (Dubinskiy et al., 2016; Lütjering and Williams, 2003; Liu et al., 2017b; Kuan et al., 1975):

- Martensitic transformation during quenching, which is called athermal ω (ω_{ath})
- Transformation during aging by a diffusion-controlled process, which is called isothermal ω (ω_{iso})
- Deformation-induced ω phase transformation

The isothermal ω phase has an ellipsoidal or a cuboidal shape as presented in Figure 2.10 (Lütjering and Williams, 2003). The ω phase can form during quenching, during aging at temperatures between 100 °C and 500 °C, or during mechanical deformation (Hickman, 1969).

The ω phase formed at lower temperatures and longer aging times for Ti-20V as presented in the temperature versus aging time diagram (see Figure 2.11). The ω phase results in an increase in both the strength and hardness, while decreasing the elongation-to-failure (ϵ_f) (Hickman, 1969). The maximum strength in Ti-35Nb-7Zr-5Ta-0.06O was found after aging at 427 °C due to ω phase precipitation. The highest YS in Ti-35Nb-7Zr-5Ta-0.68O was observed after aging at 482 °C, which was the result of α precipitation formation (Qazi et al., 2005). Aging Ti-2Al-16V at 350 °C for 100 hr resulted in an increase in the hardness due to the formation of α and ω phase precipitates. After aging Ti-2Al-16V at 550 °C for 50 hr, the increase in hardness was less than for a Ti-2Al-16V sample that was aged at 350 °C for 100 hr. This was because at 550 °C only α precipitation occurred for Ti-2Al-16V (Liu and Welsch, 1988).

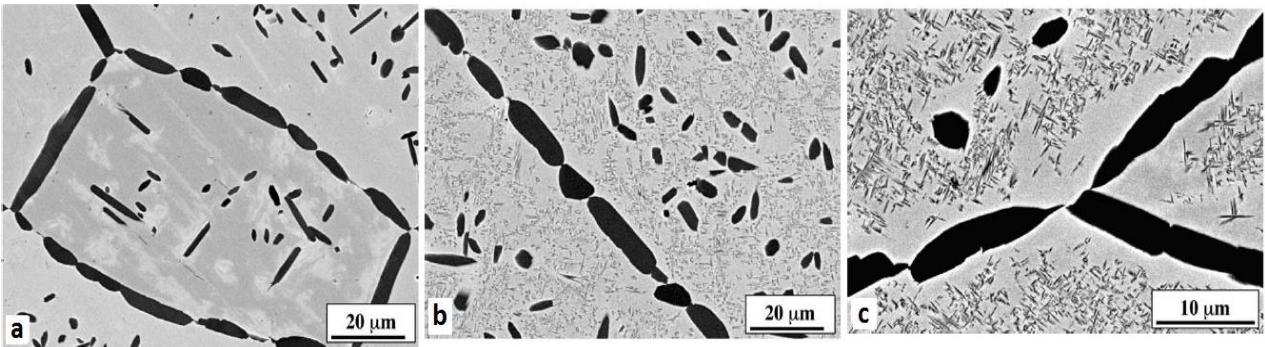


Figure 2.9 Different precipitate sizes and morphologies formed in Ti-12Mo-6Zr-2Fe; (a) grain boundary and primary α precipitates formed in homogenized sample; (b) and (c): an aged sample exhibited fine secondary α phase particles, which resulted in an increase in the strength (Banerjee et al., 2004)

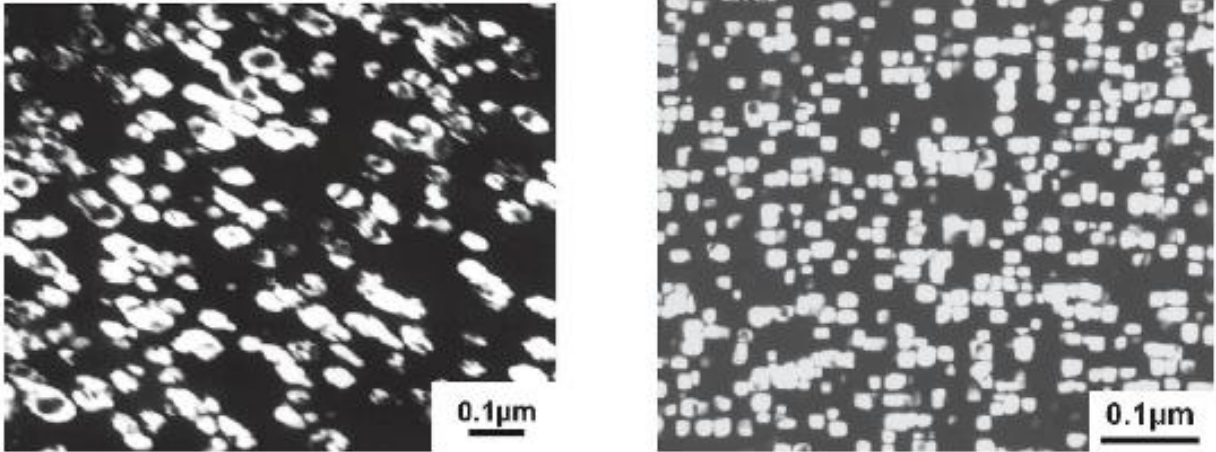


Figure 2.10 Dark field TEM photomicrographs of (a) ellipsoidal ω precipitates in Ti-16Mo aged for 48 hr at 450 °C, (b) cuboidal ω precipitates in Ti-8Fe aged for 4 hr at 400 °C (Lütjering and Williams, 2003).

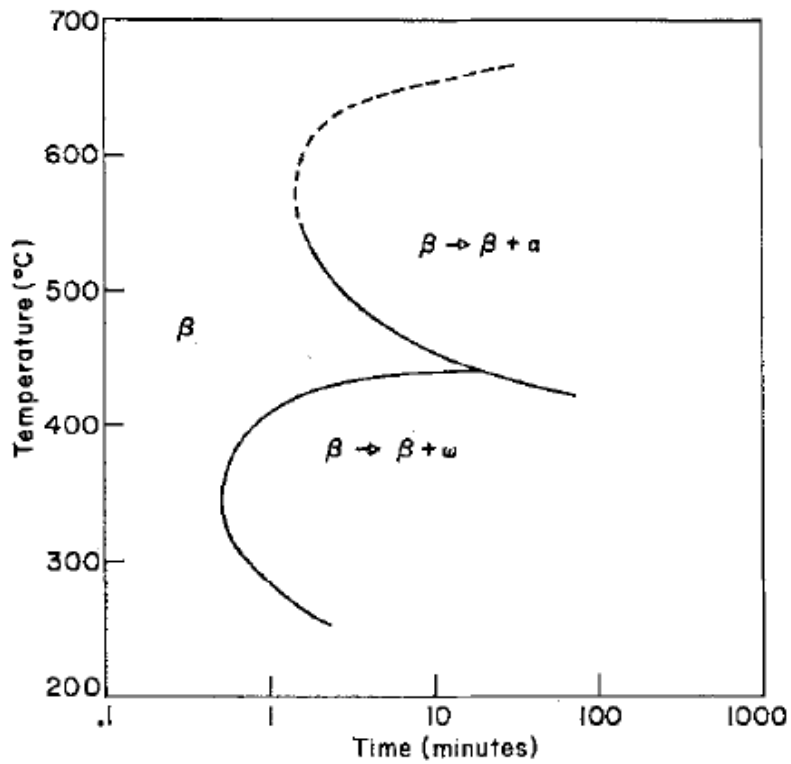


Figure 2.11 Temperature versus time diagram for Ti-20V, where the ω phase formed at lower temperatures and longer times (Hickman, 1969).

2.4.5 The effect of oxygen content on the strength of Ti alloys

Interstitial elements can strengthen Ti alloys by solid solution strengthening. Interstitial elements impose strain on neighboring host atoms (Callister and Rethwisch, 2013). O is the most influential interstitial element for Ti alloys. A small change in O content in Ti alloys results in significant changes in the strength (Geng et al., 2011; Qazi et al., 2005). It was reported that the amount of O content has a significant effect on the microstructure, the formation and coarsening of precipitates, and also the deformation mechanisms (Geng et al., 2011; Liu and Welsch, 1988; Qazi et al., 2005). Low O is known to enhance twinning. It was reported that Ti with 1000ppm (0.1 wt.%) O exhibits more twinning activity than Ti with 2000ppm (0.2 wt.%) O (Zaefferer, 2003). In addition, the volume fraction and morphology of precipitates depends on O content. The YS of grade I CP-Ti to grade IV CP-Ti increases from 170 MPa to 485 MPa, mainly due to the increase in their O content from 0.18 to 0.50 wt.% (see Table 2.1) (Lütjering and Williams, 2003). Figure 2.12 presents the effect of O content on precipitates formation in Ti-35Nb-5Ta-7Zr after aging for 8 hr (Qazi et al., 2005). Liu, et al. investigated the effect of O on Ti-6Al-2V (wt.%) and Ti-2Al-16V, which are the typical equilibrium α and β phase compositions in Ti-6Al-4V, respectively (Liu and Welsch, 1988). It was observed that the YS of the β Ti alloy increased from 311 MPa to 690 MPa with increasing O content from 0.13 to 0.59 wt.%.

Although increasing the O content results in increasing the strength, the ϵ_f usually decreases. However, both strength and ϵ_f increased in some β Ti alloys with an increase in O content (Geng et al., 2011; Qazi et al., 2005). For example, in the Ti-Nb-Zr-Ta system, Geng et al. (2011) observed that by increasing O from 0.3 to 0.7 wt.%, the YS increased from ~800 MPa to ~1000 MPa in the solution-treated condition, while the ϵ_f exhibited a 10% increase. Also, the YS of solution-treated Ti-35Nb-7Zr-5Ta increased from 530 MPa to 1081 MPa when the O content

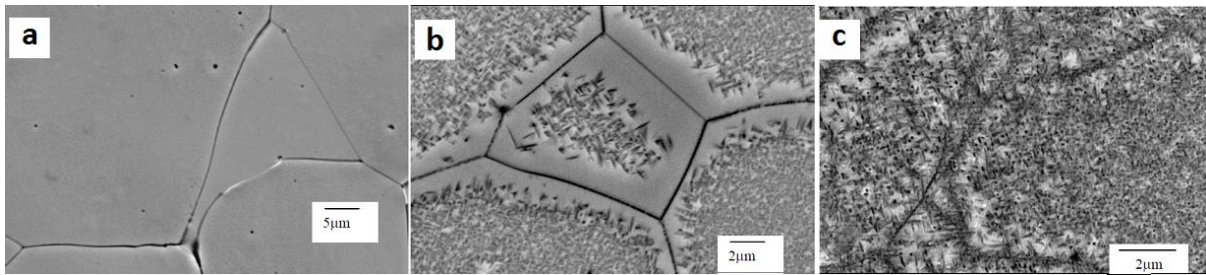


Figure 2.12 The effect of O content on microstructure of Ti-35-Nb-5Ta-7Zr after aging at 538 °C for 8 hr, (a): 0.06, (b):0.46, (c):0.68 O wt.%. The α phase was inhomogeneously distributed at the higher O contents (Qazi et al., 2005).

increased from 0.06 to 0.68 wt.% (Qazi et al., 2005). In single phase β microstructures, O may strengthen the crystal structure by increasing the bond strength. This phenomenon may be explained by noting the difference between the electronegativity of O and the other alloying elements. It is known that if the difference between the electronegativity of two different atoms is more than 1.7 (in the Pauling scale), ionic bonding is likely. The ionicity increases as this difference increases (Rohrer, 2001). As shown in Table 2.2, the difference between the electronegativity of O and Ti and its alloying elements is usually greater than or equal to 1.7. Therefore, localized ionic bonding is likely. The localized ionic bonding between O and Ti and the other alloying elements can hinder the motion of dislocations which results in strength enhancement (Geng et al., 2011).

Table 2-2 Electronegativity of O, Ti and Ti substitutional alloying elements in the Pauling scale (Rohrer, 2001).

Ti	Al	V	Cr	Zr	Nb	Mo	Ta	O
1.54	1.61	1.63	1.66	1.33	1.6	2.16	1.5	3.44

2.4.6 The effect of heat treatment on the strength of Ti alloys

Thermal treatment has a significant effect on the strength of Ti alloys due to precipitation formation by diffusion (Lütjering and Williams, 2003). Aging treatments affect the strength by creating precipitates and changing their size, geometry, and volume fraction (Chen et al., 2014; Dehghan-Manshadi and Dippenaar, 2011; Donachie, 2000; Ivasishin et al., 2005; Kobayashi et al., 1998; Lütjering and Williams, 2003). Solution treatment above the β transus temperature, followed by aging, is the most common thermal treatment for metastable β Ti alloys. Qazi et al. investigated the effect of aging temperature on strength of Ti-35Nb-7Zr-5Ta-xO, where x was between 0.06 to 0.69 wt.% (Qazi et al., 2005). As presented in Figure 2.13, the aging temperature has a substantial effect on the strength of Ti-35Nb-7Zr-5Ta-xO. The maximum strength was achieved at an aging temperature of 427 °C because of ω phase formation for 0.06O wt.%, while the maximum strength occurred at aging temperature of 482 °C for 0.46O wt.% due to the formation of both the α and ω precipitates. At 0.68 wt.% O, only α precipitation was observed and the α phase coarsened with increasing aging temperature. The highest strength was achieved by aging at 482 °C. Li et al. studied the effect of Nb in Ti-xNb-13Ta-4.6Zr alloys where the x was between 30 to 39 wt.%. Their results revealed that the α and ω phases formed only for lower Nb contents after aging at temperatures ranging between 300 °C and 600 °C for 48 hr (Li et al., 2002). The α and ω precipitation resulted in an increase in the strength. It was observed that isothermal aging of Ti-29Nb-13Ta-4.6Zr at 300 °C and 400 °C for 48 h resulted in the formation of ω precipitates, while aging between 350 °C and 600 °C resulted in α -phase precipitation (Li et al., 2002). It was reported that only α phase particles formed after 12 days at both 400 °C and 500 °C in Ti-39Nb-13Ta-4.6Zr.

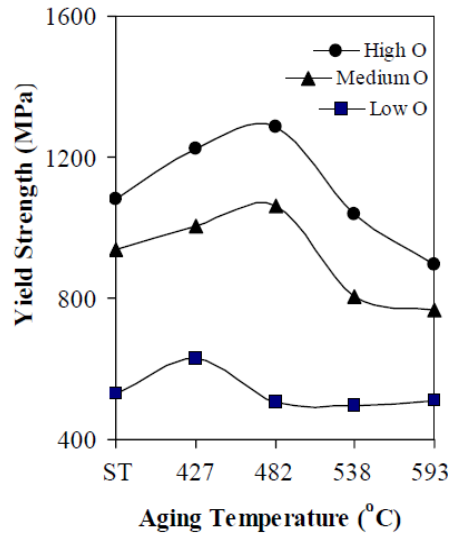


Figure 2.13 The effect of aging temperature on YS of Ti-35Nb-7Zr-5Ta-xO, where x was 0.06 wt.% for low O content, 0.46 wt.% for medium O content, and 0.68 wt.% for high O content. All the samples were aged for 8 hr (Qazi et al., 2005)

2.5 Critical assessment of the state of the art

Studying the plastic deformation behavior at the microscale is essential for understating the deformation mechanisms and failure modes and also for improving the forming processes of metallic materials. Knowing the plastic strain level is vital to estimate the remaining life of a metallic part. However, it is a challenging task to measure the plastic strain of a part during its operating conditions. Many researchers have correlated the level of plastic strain to the crystallographic misorientation of polycrystalline materials (Buchheit et al., 2015; Kamaya et al., 2005, 2006; Subedi et al., 2015; Wilkinson et al., 2014; Wright et al., 2011, 2016) . Furthermore, exploring the heterogeneity of the plastic deformation at the microscale may provide information regarding the crack initiation and propagation. With these aims, some experimental techniques have been developed and applied to characterize the plastic deformation at the microscale and nanoscale such as in-situ TEM and SEM experiments, which may be used to validate theoretical models (e.g. crystal plasticity models).

Although the TEM provides precise and detailed information, it is impractical to study a sufficiently large area to statistically analyze the influential parameters of the heterogenous plastic deformation. With advancement in SEM technology and the arrival of the automated EBSD in the early 1990s, studying the large scale (on the order of several hundred micrometers, which may contain hundreds of grains) plastic deformation opened new avenues for understanding deformation mechanisms and behavior. Such capability inspired the rapid development technologies for a variety of loading conditions inside a SEM so that the evolution of surface microstructures could be investigated in-situ. Furthermore, easy sample preparation and rapid data acquisition made the automated EBSD system more popular. In this chapter, the use of such

techniques to study slip activity and also the correlation between misorientation and plastic deformation at the microscale have been highlighted.

Several techniques have been developed to quantify the orientation change and correlate it with the plastic strain and GNDs. Some of the investigations have incorporated KAM as well as the misorientation dispersion. The latter method is independent of the step size, which is an advantage over the KAM approach. Although extensive research has been conducted on quantifying the orientation change according to misorientation dispersion and its correlation with global plastic strain, there are evident gaps in the correlation between misorientation and plastic strain at the grain scale, in particular for bcc Ti alloys. The work in this dissertation set out to fill in some of these gaps. Specifically, the influence of grain size, orientation, and loading history on misorientation dispersion have been investigated in two bcc Ti alloys,

Furthermore, as discussed in this chapter, the slip activity of bcc materials is still not very well understood, mainly due to the lack of close packed planes in the bcc crystalline structures. In addition to the crystallographic slip systems, pencil glide has also been suggested as another mechanism of the slip activity in bcc materials. For example, only the activity of the $\{110\}\langle 111\rangle$, $\{112\}\langle 111\rangle$, and/or Pencil glide have been reported in some studies, while the activity of the $\{123\}\langle 111\rangle$ slip systems have been also observed in other bcc alloys, in addition to the above-mentioned systems. Moreover, a relatively high number of slip systems (48 slip systems) in bcc structures, makes the characterization of the slip activity more challenging compared to fcc and hcp materials. In this work, the slip activity of three bcc Ti alloys have been investigated by conducting the slip trace analysis based on surface traces identified in the photomicrographs. Finally, a series of in-situ and ex-situ TMP treatments were systematically designed and conducted with the aim of enhancing the strength of a low-cost bcc Ti alloy.

CHAPTER 3

3 EQUIPMENT AND MATERIALS

The equipment utilized for performing the experimental part of this work is explained in this chapter. At the end of this chapter, the alloying components of the as-received Ti alloys is provided. The type of characterization work and analysis performed on each alloy is also specified.

3.1 Equipment

3.1.1 Scanning electron microscopy (SEM)

A field emission gun (FEG) Tescan Mira3 SEM was used for capturing the microscale images for studying the microstructures. This SEM was equipped with a back-scatter electron (BSE) detector. The combination of a SEM with an in-situ tensile stage enabled the identification of the slip trace evolution. Secondary electron (SE) and back-scatter electron (BSE) SEM photomicrographs were acquired before, during, and after the tensile experiments. The electron beam voltage was between 15 kV to 25 kV for different samples. The working distance was around 15 mm when the tensile stage was not used. Due to the in-situ tensile stage configuration, the working distance was around 20 mm when the tensile stage was used. For the provided SEM photomicrographs, the tensile axis was always horizontal.

3.1.2 Electron Backscatter Diffraction

The crystallographic orientation of selected areas of samples was obtained prior and after the deformation by an EBSD detector attached to the SEM. This EBSD detector was manufactured by EDAX-TSL (Mahwah, NJ, USA). Patterns were collected using a beam voltage of either 15 kV or 20 kV and a working distance of approximately 20 mm. The EBSD scans were performed at a step

size approximately one-tenth of the grain size for each alloy. A 2×2 binning setting was used for all the EBSD scans. All EBSD IPF maps were acquired on samples tilted 70 degrees about the tensile axis. After acquiring the EBSD data, EDAX-TSL OIM Analysis 6.1 software was used to specify the grains and crystallographic texture. For the slip trace analysis, the data was cleaned by using a grain tolerance angle of 5 degree. The average grain orientation generated by this software was used to obtain the Euler angles of each grain.

3.1.3 In-situ tensile stage

Tensile tests were performed inside a Tescan Mira3 SEM (see Figure 3.1). The screw-driven tensile stage was manufactured by Ernest F. Fullam, Inc. (originally located in Lantham, NY and later acquired by MTI Instruments, Albany, NY). Tensile tests were conducted at a constant displacement rate which corresponded to an approximate strain rate of 10^{-3} s^{-1} . Displacement, load, and time data were recorded during the experiments using the MTESTW version F 8.8e data acquisition and control software (Admet, Inc., Norwood, MA, USA). The tests were paused several times for acquiring the SEM images. During these pauses, stress relaxation occurred. After each pause, loading was continued at the same displacement rate. For the elevated temperature tests, the sample was heated at an approximate rate of 5 °C/min to the test temperature. The heater diameter was about 7 mm, which was located at the center of the gage section of the sample. The temperature was monitored using a K-type thermocouple spot-welded to the side of the gage section.

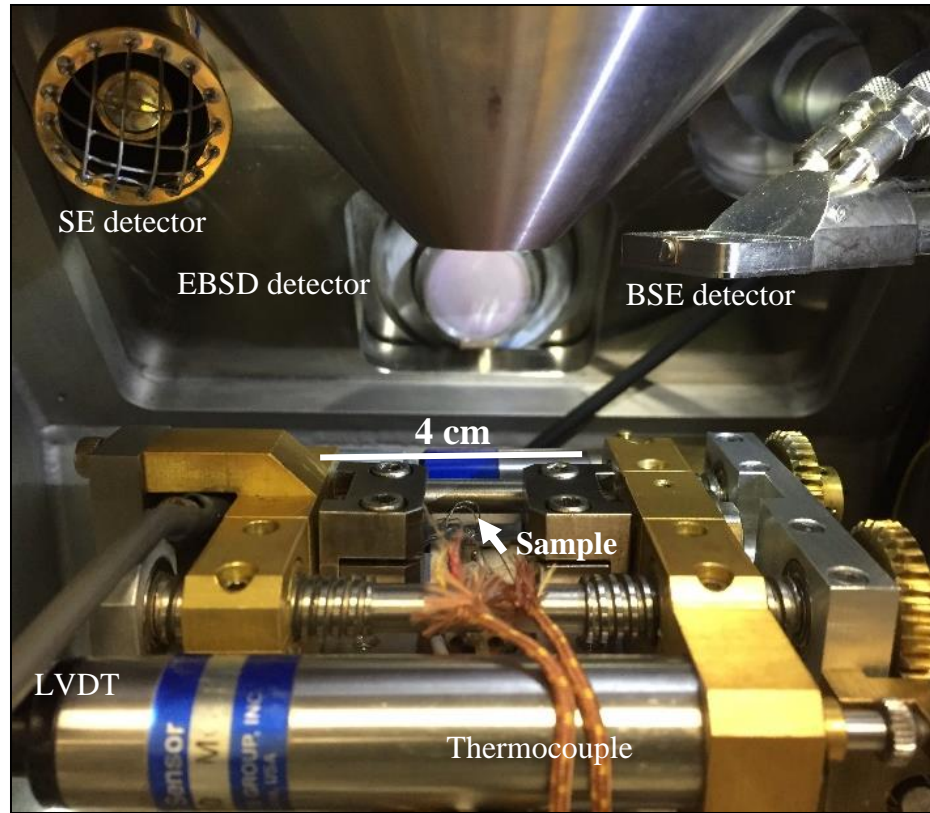


Figure 3.1 The in-situ testing setup inside the Tescan Mira3 SEM chamber. The heater is located underneath the sample. A thermocouple was spot-welded to the side of the gage section for the elevated-temperature tests.

3.1.4 Universal test machine

A hydraulic universal test machine was used to perform tensile tests outside the SEM chamber at RT and elevated temperatures (see Figure 3.2). Displacement, load, time, and temperature were recorded during the experiments using a material testing systems (MTS) data acquisition software package. All the tests were performed at a constant displacement rate of 2 mm/min. For the elevated temperature tests, the sample was heated to the target temperature, and the tests were started after the samples were soaked at the target temperature for a minimum of 15 minutes.

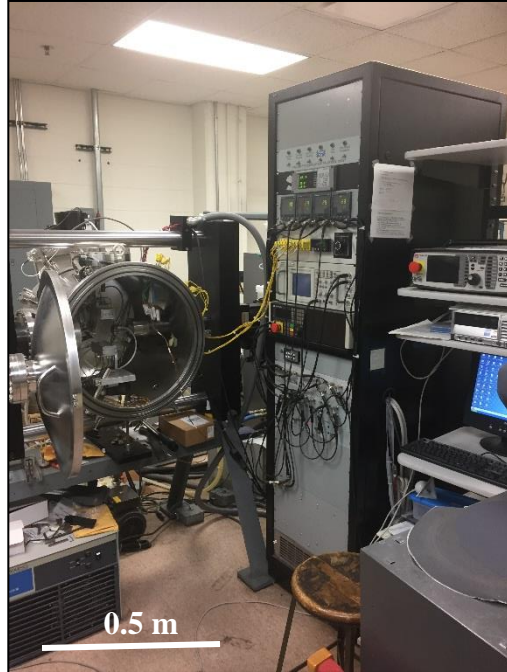


Figure 3.2 An image of the test machine used for the tensile tests performed outside the SEM. For the elevated temperature tests, quartz heater elements were used. Thermocouples were spot-welded to the surface in the middle of the gage section of the test specimens.

3.1.5 Hardness

Vickers hardness indents, input with a load of 500 gr for 15 seconds, were used for determining the hardness of samples. In addition, for the in-situ SEM tensile samples, Vickers hardness indents were used as fiducial markers to measure the strain during the test.

3.1.6 Oven and vacuum tube

An electrical oven and a vacuum tube were used to perform the heat treatments in this work. To measure the real-time sample temperature during the heat treatment process, a glass vacuum tube was designed and fabricated. The samples were covered with a thin tantalum (Ta) foil (0.2 mm) to

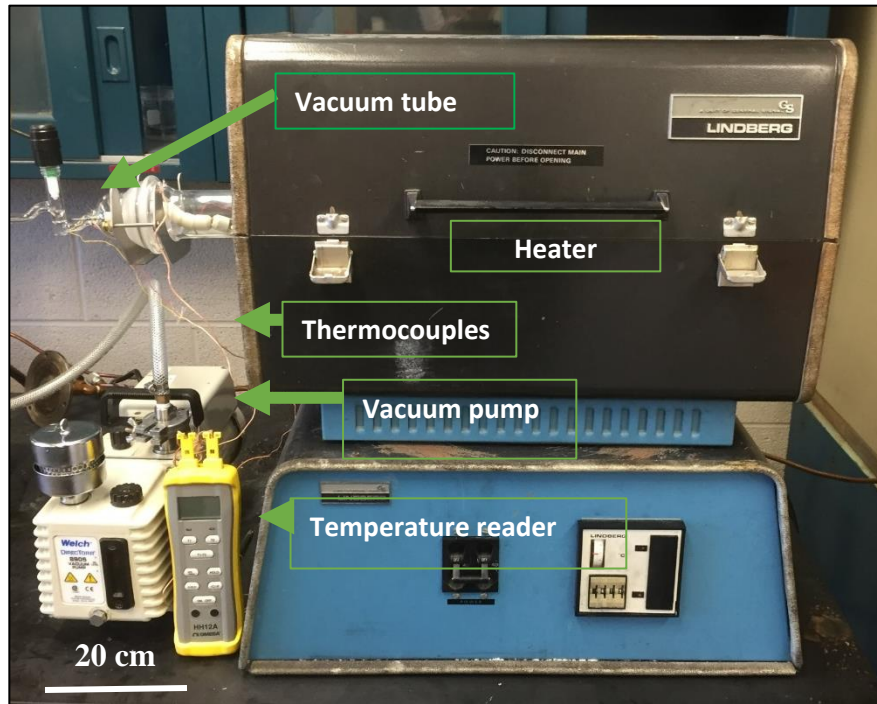


Figure 3.3 Image of the furnace used for the heat treatments. The real-time sample temperature was measured during the heat treatment.

decrease the oxidation intake of the samples. Figure 3.3 exhibits the heat treatment set up that was used.

3.1.7 Thermocouples

K-type thermocouples were used to measure the temperature of the samples during the heat treatments and the elevated temperature tensile tests. A spot-welding machine was used to attach the thermocouples to the samples. The voltage used to attach the thermocouples to the samples, was to ~35 volts. Up to five thermocouples were spot-welded to the surface of the gage section of the samples tested outside of the SEM chamber.

3.1.8 Dynamic mechanical analysis

Dynamic Mechanical Analysis (DMA) is a characterization method, mainly for studying the viscoelastic behavior of polymer. A sinusoidal force is applied, and the corresponding strain is measured as a function of the temperature or load frequency. The principle of this technique is based on measuring the phase lag (δ) between applied stress and strain. The storage modulus and loss modulus are defined as follows:

$$\text{Stress: } \sigma = \sigma_0 \sin(t\omega + \delta) \quad \& \quad \text{Strain: } \varepsilon = \varepsilon_0 \sin(t\omega + \delta)$$

$$\text{Storage modulus: } E' = \frac{\sigma_0}{\varepsilon_0} \cos(\delta) \quad \& \quad \text{Loss modulus: } E'' = \frac{\sigma_0}{\varepsilon_0} \sin(\delta)$$

$$\text{Phase angle: } \delta = \arctan\left(\frac{E''}{E'}\right)$$

In this work, DMA was used to determine the temperature range of the phase transformation for the TCFA alloy. The sample was heated at a rate of 5 degrees per minute. The rectangular sample measured $7 \times 0.7 \times 50 \text{ mm}^3$.

3.2 Materials

Five β Ti alloys were studied in this work. The compositions of these alloys are provided in Table 3.1. TCFA and TIMETAL-21S were received as solution-treated rolled plates with thicknesses of ~ 0.8 and ~ 0.7 mm, respectively. The thickness of the TNTZ-xO solution-treated samples was ~ 3 mm.

The slip trace analysis was performed on TCFA, TNTZ-xO, and TIMETAL-21S deformed at RT. The effect of elevated temperature on the deformation behavior was also investigated for TCFA and TIMETAL-21S.

Table 3-1 The compositions and type of analysis performed for each alloy

Abbreviation	Analysis	Compositions (wt.%)
TCFA	<ul style="list-style-type: none"> • Tensile test • Slip Trace Analysis • Misorientation Analysis • Heat treatment 	<p>Ti (Balance)</p> <p>Cr (13), Fe (1), Al (3)</p>
TIMETAL-21S	<ul style="list-style-type: none"> • Tensile test • Slip Trace Analysis • Misorientation Analysis • Heat treatment 	<p>Ti (Balance)</p> <p>Mo (15), Nb (3), Al (3), Si (0.2)</p>
TNTZ-0.10	<ul style="list-style-type: none"> • Tensile test • Slip Trace Analysis 	<p>Ti (Balance)</p> <p>Nb (29), Ta (13), Zr (4.6), O (0.1)</p>
TNTZ-0.30	<ul style="list-style-type: none"> • Tensile test • Slip Trace Analysis 	<p>Ti (Balance)</p> <p>Nb (29), Ta (13), Zr (4.6), O (0.3)</p>
TNTZ-0.70	<ul style="list-style-type: none"> • Tensile test • Slip Trace Analysis 	<p>Ti (Balance)</p> <p>Nb (29), Ta (13), Zr (4.6), O (0.7)</p>

3.3 Specimen geometry and sample preparation

The geometry of the test sample, used for the in-situ experiments performed inside the SEM, is presented in Figure 3.4. The samples were machined using electro-discharge machining. The specimens were mechanically polished prior to testing. The specimens were first ground using silicon carbide (SiC) papers through 400, 600, 1200, 2400, and 4000 grits sequentially. Each polishing step took 5 to 10 minutes. Water was used to rinse the specimens before moving to the next grinding step. A solution of five parts colloidal silica (with $0.06\mu\text{m}$ particle size) and one part 30% hydrogen peroxide was used as the finish polish. This usually required more than 30 minutes of polishing time. The polishing cloth used in this step was purchased from Buehler (catalog No. M500-12PS). After polishing, water was used to rinse away the colloidal silica. Finally, the specimens were ultrasonically cleaned in acetone and methanol, respectively, to remove the residual colloidal silica.

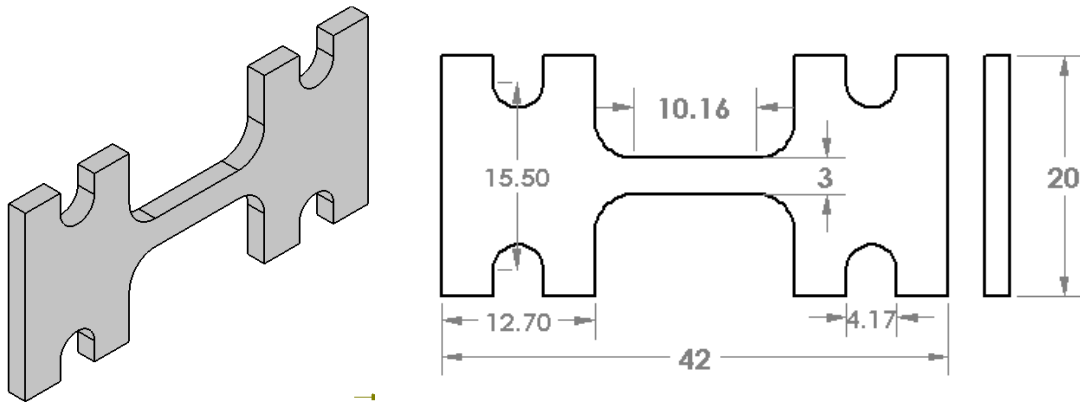


Figure 3.4 A schematic showing the geometry of the test specimens used in the tensile experiments. The dimensions are in millimeters. The thickness was ~ 0.6 and ~ 0.8 mm for the TIMETAL-21S and TCFA specimens, respectively.

CHAPTER 4

4 MISORIENTATION ANALYSIS

It is essential to know the level of the plastic strain to estimate the remaining life of a metallic component. However, it is a challenging task to measure the plastic strain for a part under its operating condition. In this chapter, the level of plastic strain has been estimated by quantifying the misorientation of the deformed microstructure, i.e., no information from undeformed state was used, for two bcc Ti alloys. The procedure of calculating the misorientation between two crystalline orientations is provided. The framework of the misorientation analysis is also presented. The evolution of the orientation change as a function of the plastic strain level is provided. Then, the global relationship between the plastic strain and crystallographic misorientation is provided. The effect of grain size and grain average orientation on the misorientation values are discussed at the grain scale. In addition, the results of two tensile loading conditions (uninterrupted [monotonic] and interrupted) are compared and discussed. At the end of this chapter, an experimental strain field map, obtained from a test in which DIC characterization was performed on a sample tested inside a SEM, is compared with misorientation distribution maps.

4.1 Experiments performed

The samples were cut from rolled sheets of both TCFA and TIMETAL-21S, using electrical discharge machining, with the tensile axis either parallel or perpendicular to the rolling direction. Both alloys exhibited a metastable bcc structure. The average grain diameters, measured using EBSD, were $\sim 50 \mu\text{m}$ and $\sim 15 \mu\text{m}$ for TCFA and TIMETAL-21S, respectively. The YS values were $\sim 940 \text{ MPa}$ and $\sim 840 \text{ MPa}$ for TCFA and TIMETAL-21S, respectively. Both alloys exhibited very little strain hardening. The specimens had a thickness of $\sim 0.7 \text{ mm}$, and a gage length of 10

mm. A schematic drawing of the sample geometry is provided in Figure 3.4. Five monotonic tensile tests were performed for TCFA and four tests were carried out for TIMETAL-21S (where the tensile axis was parallel the rolling direction). The tests were stopped at approximately 3%, 6%, 9%, and 12% global plastic strain. One monotonic tensile test was performed perpendicular to the rolling direction to investigate the effect of texture for TCFA. One sample of each alloy was subjected to an interrupted test to study the influence of the loading history on the misorientation values. The tensile tests were conducted at a constant displacement rate of 0.004 mm/s, which corresponded to a strain rate of $4 \times 10^{-4} \text{ s}^{-1}$. Displacement, load, and time data were recorded during the experiments using the MTESTW version F8.8e data acquisition and control software (Admet, Inc., Norwood, MA, USA). The SEM photomicrographs were acquired from areas deformed at the center of the gage section. EBSD was performed both before and after the deformation. For achieving high-quality posttest EBSD data of deformed samples, the specimens were polished after the test, using the same procedure as described previously. Posttest EBSD IPF maps were obtained from the center of the gage section under the following conditions: working distance of ~18 mm, acceleration voltage of 15 kV, beam intensity of 18, and tilt angle of 70° . The data were collected using a hexagonal grid with step sizes of 4 μm and 1 μm for TCFA and TIMETAL-21S, respectively. The EBSD IPF map consisted of ~ 100,000 data points for each tested sample. For quantifying the misorientation and investigating its relationship with the plastic strain, several algorithms were developed and implemented into MATLAB codes, which are described in the following sections.

4.2 Reference orientation

The misorientation in crystalline materials is measured by the difference between two crystalline orientations. By considering g_A and g_B as orientation matrices of orientation A and B, the misorientation operator Δg_{AB} can be defined as (<https://en.wikipedia.org/wiki/Misorientation>):

$$\Delta g_{AB} = g_B \times g_A^{-1} \quad (4.1)$$

To measure all possible misorientations, the number of total orientation spaces should be calculated by crystal symmetry. bcc materials have 24 symmetric operations. As a result, $24 \times 24 \times 2$ (1152) different misorientations can be identified in BCC materials with equation (4.2):

$$\Delta g_{AB} = (O_B^{cr} g_B) \times (O_A^{cr} g_A)^{-1} \text{ and } \Delta g_{AB} = (O_B^{cr} g_B) \times (O_B^{cr} g_B)^{-1} \quad (4.2)$$

where O^{cr} is one of the symmetric operators among all 24 possible operators for bcc materials.

The rotation angle (θ) and rotation axis (r) can be calculated for each case by following equations:

$$\cos \theta = \frac{\Delta g_{11}^{AB} + \Delta g_{22}^{AB} + \Delta g_{33}^{AB} - 1}{2} \quad (4.3)$$

$$r_1 = \frac{\Delta g_{23}^{AB} - \Delta g_{32}^{AB}}{2 \sin \theta} \quad (4.4)$$

$$r_2 = \frac{\Delta g_{13}^{AB} - \Delta g_{31}^{AB}}{2 \sin \theta} \quad (4.5)$$

$$r_3 = \frac{\Delta g_{12}^{AB} - \Delta g_{21}^{AB}}{2 \sin \theta} \quad (4.6)$$

It was proven that the absolute maximum angle of misorientation is 62.8° for a cubic crystal.

However, if one is only interested in measuring the misorientation angle between two crystalline

orientations, the total number of iterations can be reduced to 24, i.e., only one symmetric operation is needed as follows:

$$\Delta g_{AB} = g_B \times (O_A^{cr} g_A)^{-1} \quad (4.7)$$

The minimum orientation angle of 24 symmetric orientations between two given crystallographic orientations is called disorientation and can be determined by

$$D_{(A,B)} = \min \left(\arccos \frac{\Delta g_{11}^{AB} + \Delta g_{22}^{AB} + \Delta g_{33}^{AB} - 1}{2} \right) \quad (4.8)$$

In the following sections of this work, the disorientation angles were desirable. Therefore, only 24 iterations were performed to measure the disorientation between two orientations. In most of the literature, ‘misorientation’ is frequently used to describe the ‘disorientation’. In the rest of this work, ‘misorientation’ is used for ‘disorientation’.

4.2.1 Reference orientation criteria

The average Local Misorientation Deviation (MD_L) was calculated by the following equation at the grain scale:

$$MD_{L(i)} = \frac{\sum_{j=1}^{n(i)} D_{(RO_i, P_j)}}{n(i)} \quad (4.9)$$

where, i represents the grain ID, and j identifies point (j) in grain (i), RO_i is the reference orientation of grain (i), $n(i)$ is the total number of points within a grain (i), and $D_{(RO_i, P_j)}$ is the misorientation between crystallographic orientations of point P_j and RO_i within the grain (i). For quantifying the misorientation deviation for the entire map (all data points within the EBSD scan), the following formula was used:

$$MD_G = \frac{\sum_{i=1}^N \sum_{j=1}^{n(i)} D_{(RO_i, P_j)}}{\sum_{i=1}^N n(i)} \quad (4.10)$$

where, MD_G is Global Misorientation Deviation (a value that presents the misorientation deviation for the entire map data), N is the number of the total grains in the entire map, $n(i)$ presents the total data point inside the grain (i), RO_i is the reference orientation of grain (i), and P_j is the point (j) inside the grain (i).

In this work, a reference orientation (RO) was assigned for each individual grain, which describes the relative misorientation of the other data points with respect to the RO. The effect of the RO on the MD value and distribution was investigated for the following metrics:

- I. $MD_{Min, RO}$: The orientation that resulted in the Minimum MD value
- II. $MD_{Max, RO}$: The orientation that resulted in the Maximum MD value
- III. $MD_{Geo. C., RO}$: The orientation of Geometrical Center of the grain
- IV. $MD_{Avg. After., RO}$: The orientation of Average Orientation after deformation
- V. MD_{Pt} : In order to calculate the MD_{Pt} , one must calculate the misorientation values with respect to all the points within the grain. Then, the summation of all the misorientation values should be divided by the total number of points inside the grain. In other words, for a grain that contains n points, a total of n misorientation deviations (MD_L) is calculated. MD_{Pt} is the average of these n misorientation deviations, which was obtained with respect to each individual point.

For determining the average of all $MD_{G(Pt)}$ values (Metric V), the following equation was used:

$$MD_{G(Pt)} = \frac{\sum_{i=1}^N \sum_{j=1}^{n(i)} MD_{L(ij)}}{\sum_{i=1}^N n(i)} \quad (4.11)$$

where $MD_{L(ij)}$ is the MD_L of the grain (i), while the RO used was taken from point (j). The grains with 18 data points or less were excluded from the analysis. The effect of the following RO on the MD value and distribution was also investigated by other researchers:

- The average grain orientation prior to deformation (Buchheit et al., 2015)
- The orientation of the point in the grain with (Schwartz et al., 2009; Wright et al., 2016)
 - The lowest nearest neighbor KAM value
 - The highest pattern Quality
 - The highest confidence index
 - The smallest fit

It has been reported that KAM values significantly depend on the step size and EBSD condition (i.e., sample preparation procedure, surface quality, working distance, beam intensity, binning, and pattern resolution) (Signorelli et al., 2017). The last metrics for specifying RO , mentioned above, are also dependent on the EBSD conditions.

Figure 4.1 presents the MD_G for three studied metrics as a function of the plastic strain level for both alloys. Both alloys exhibited a similar trend, i.e., the MD_G increased with increasing the plastic strain level for both alloys. For quantifying the relationship between MD_G and global plastic strain, linear lines were fit by linear regression. The correlation coefficients (R^2) were higher for TCFA compared with TIMETAL-21S. The R^2 values were higher than 0.87 for all fit lines. Although, the EBSD IPF maps did not indicate significant orientation gradients inside the grains

at 0% plastic strain, as the MD_G was between ~ 0.5 to 3 at 0% strain (see Figure 4.1). This might be due to following reasons:

1. The as-received materials were subjected to a heat treatment after rolling to homogenize the material.
2. The error in measurement due to the accuracy of EBSD system is between 0.1 to 1 degree (Kamaya, 2009; Wilkinson and Britton, 2012)

To illustrate the effect of the RO on the local misorientation distribution at the grain scale, an arbitrary grain (which had 804 indexed EBSD points) was chosen from the EBSD IPF map of a TCFA sample, which was loaded to 12.3% plastic strain. Figure 4.2(a) illustrates the EBSD IPF map of the selected grain. The normalized misorientation distribution (the misorientation values were divided by the average for each metric) and the location of the RO for the studied criteria are presented in Figure 4.2(b) to Figure 4.2 (f). As can be seen in Figure 4.2, the MD_L for the selected grain varied between 2.94 and 13.34, depending on the RO metric. The RO was located at the grain boundary for criteria II (MD_{Max}), while for other metrics, the RO was positioned inside the grain close to the grain center. Although the MD_L value varied, the trend of the misorientation distribution was similar for all the metrics throughout the grain, i.e., relatively high values at the grain boundary and low values within the grain. The exception was for MD_{Max} metric, which exhibited high values in the core of the grain.

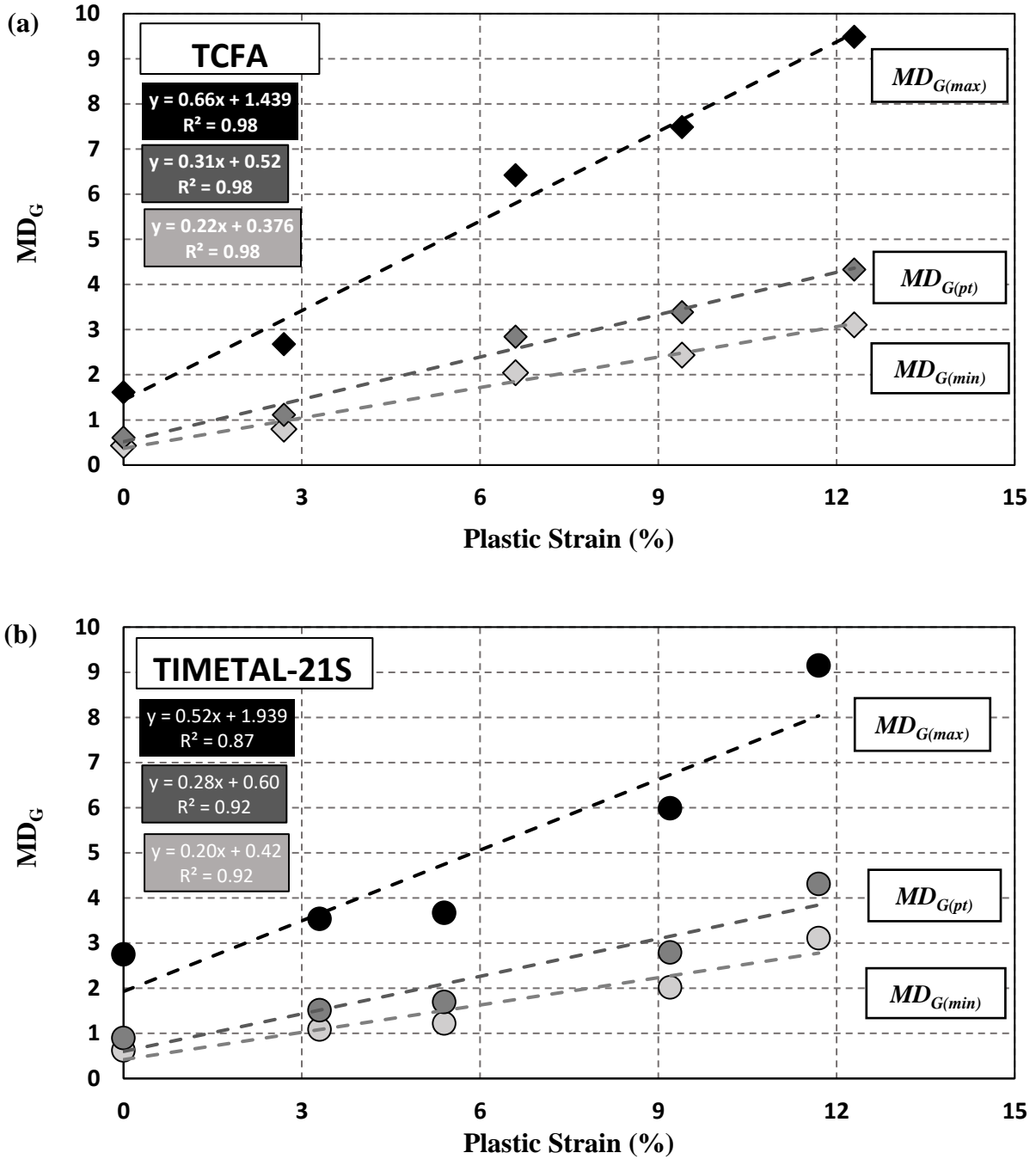


Figure 4.1 The Global Misorientation Deviation (MD_G) values for three reference orientations (RO) metrics for (a) TCFA and (b) TIMETAL-21S at different levels of plastic strain. Linear lines were fit to the data for each metric. All R^2 values were higher than 0.87.

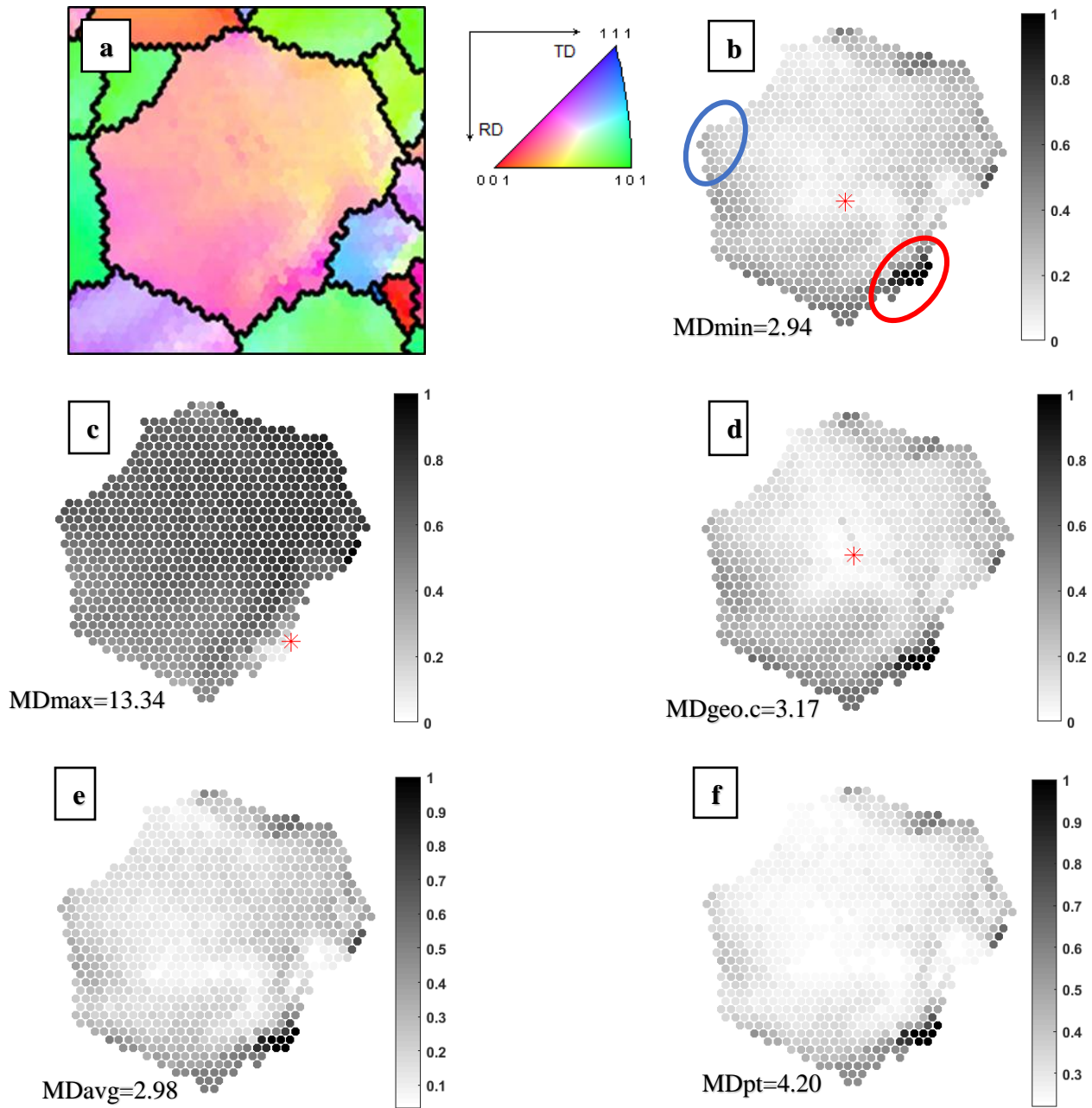


Figure 4.2. One grain, which contained 804 data points, was selected from a TCFA sample deformed to 12.5% plastic strain to depict the misorientation distribution with respect to the RO . (a) The orientation map and assisted color code, the misorientation distribution of (b) MD_{Min} , (c) MD_{Max} , (d) $MD_{Geo. C.}$, (e) $MD_{Avg. Ori.}$, (f) MD_{Pt} . The RO position was colored in red at each map.

Previous studies showed that the geometrically necessary dislocations (GND) and orientation gradient are higher in regions near the grain boundaries compared with the regions close to grain center, which might be due to the occurrence of a local plastic strain concentration (Schwartz et al., 2009). As shown in Figure 4.2(c), the MD distribution shows low MD values near the RO, which was located on the grain boundary, and high values close to the grain center for the MD_{Max} . Among the other metrics, which the MD distribution was similar, the MD_{Min} was chosen for determining the RO in the rest of this dissertation. It is important to note that the chosen RO for these maps were obtained from the deformed state. Therefore, these maps do not provide direct indication of how the orientation changed during the deformation.

4.3 Results

4.3.1 Evolution of orientation gradient as function of plastic strain

EBSD IPF maps are presented at different plastic strain levels for TCFA and TIMETAL-21S in Figure 4.3 and Figure 4.4, respectively. No significant orientation gradient was exhibited in the undeformed condition (0% plastic strain). With increasing plastic strain, the orientation gradient became more pronounced in each individual grain. This was apparent in the corresponding IPF (see Figure 4.5 and Figure 4.6). Each clustered area represents one grain at 0% plastic strain. For more clarification, three clustered areas, which represent three grains, are highlighted in Figure 4.5 (a). It should be noted that if points have similar crystallographic orientations, they are placed near each other in Figure 4.5 and Figure 4.6. The area of each cluster increased with increasing strain level. For example, only a few visible clustered areas were distinguished at 12% plastic strain in the IPF presented in Figure 4.5 (e) and Figure 4.6 (e).

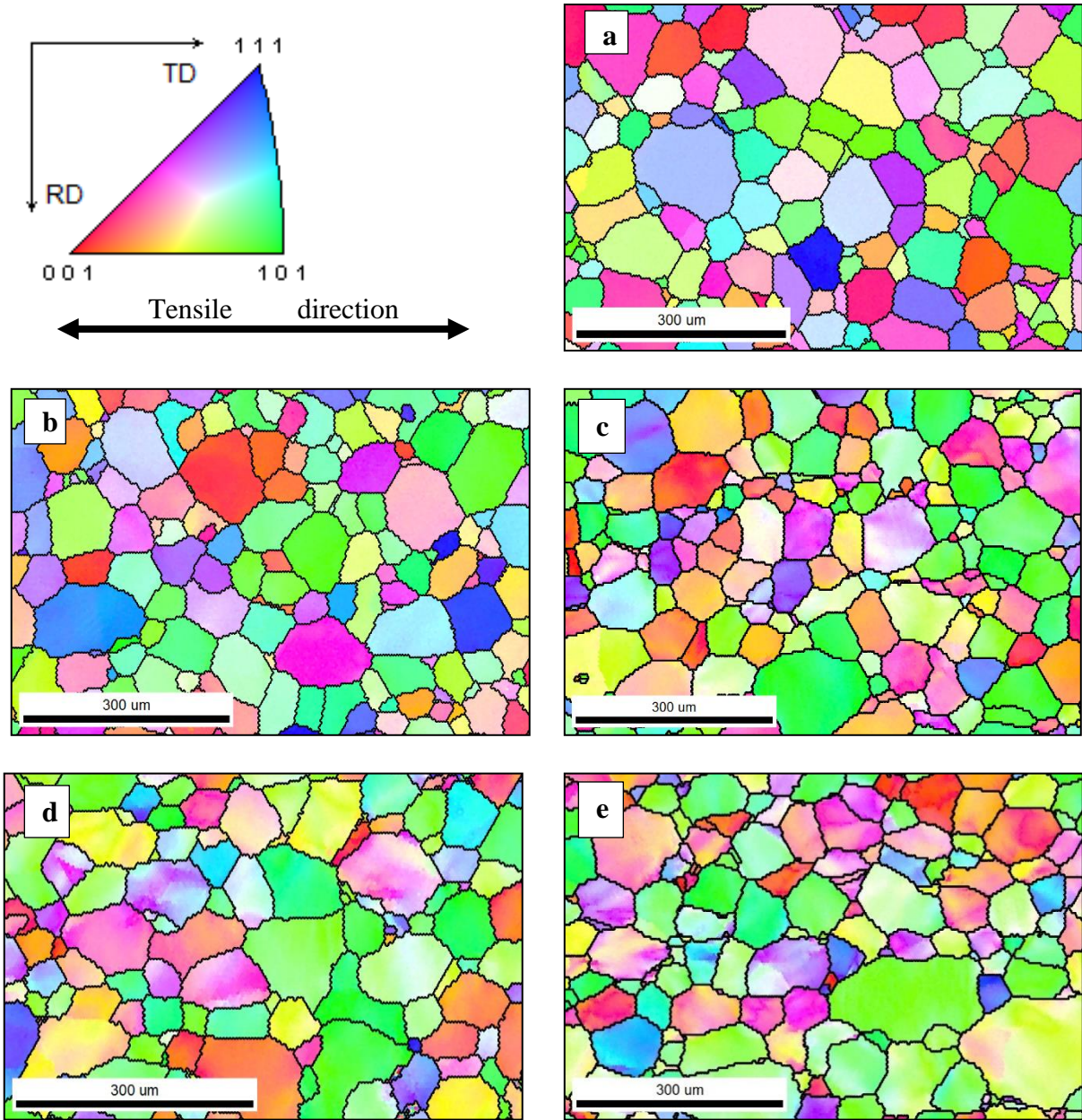


Figure 4.3 EBSD IPF maps obtained after different levels of plastic strain for TCFA. (a) 0%, (b) 2.7%, (c) 6.6%, (d) 9.4%, and (e) 12.3% plastic strain. At 0% plastic strain, the material exhibited a relatively uniform orientation distribution for almost all the grains. With an increase in the plastic strain level, the evolution of the orientation gradient within the grains became more pronounced. The inverse pole figure (IPF) color code is included along with the loading direction as a reference.

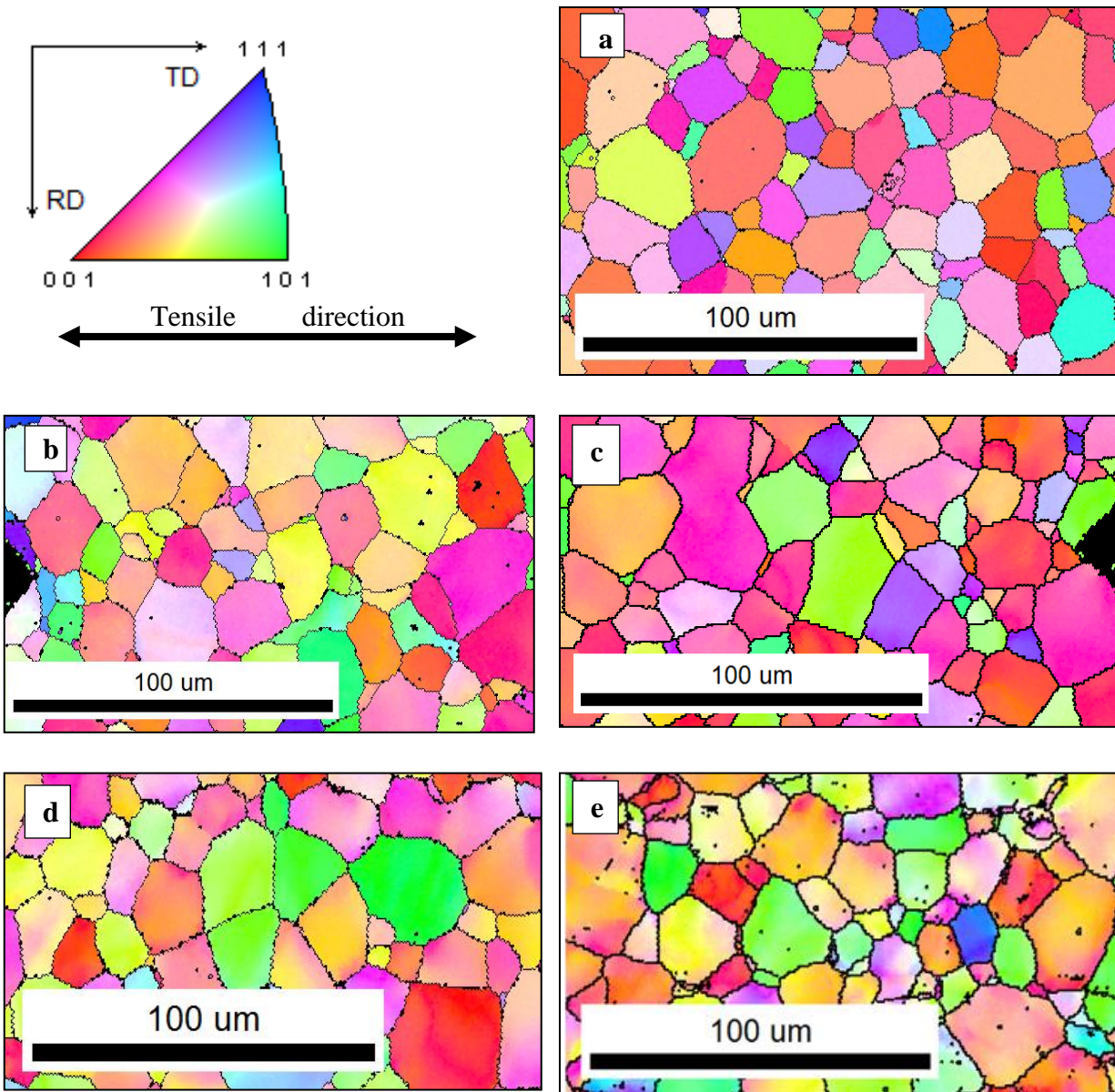


Figure 4.4 EBSD IPF maps obtained after different levels of plastic strain for TIMETAL-21S. (a) 0%, (b) 3.3%, (c) 5.4%, (d) 9.2%, and (e) 11.7% plastic strain. At 0% plastic strain, the material exhibited a relatively uniform orientation distribution for almost all the grains. With an increase in the plastic strain level, the evolution of the orientation gradient within the grains became more pronounced. The IPF color code is included along with the loading direction as a reference.

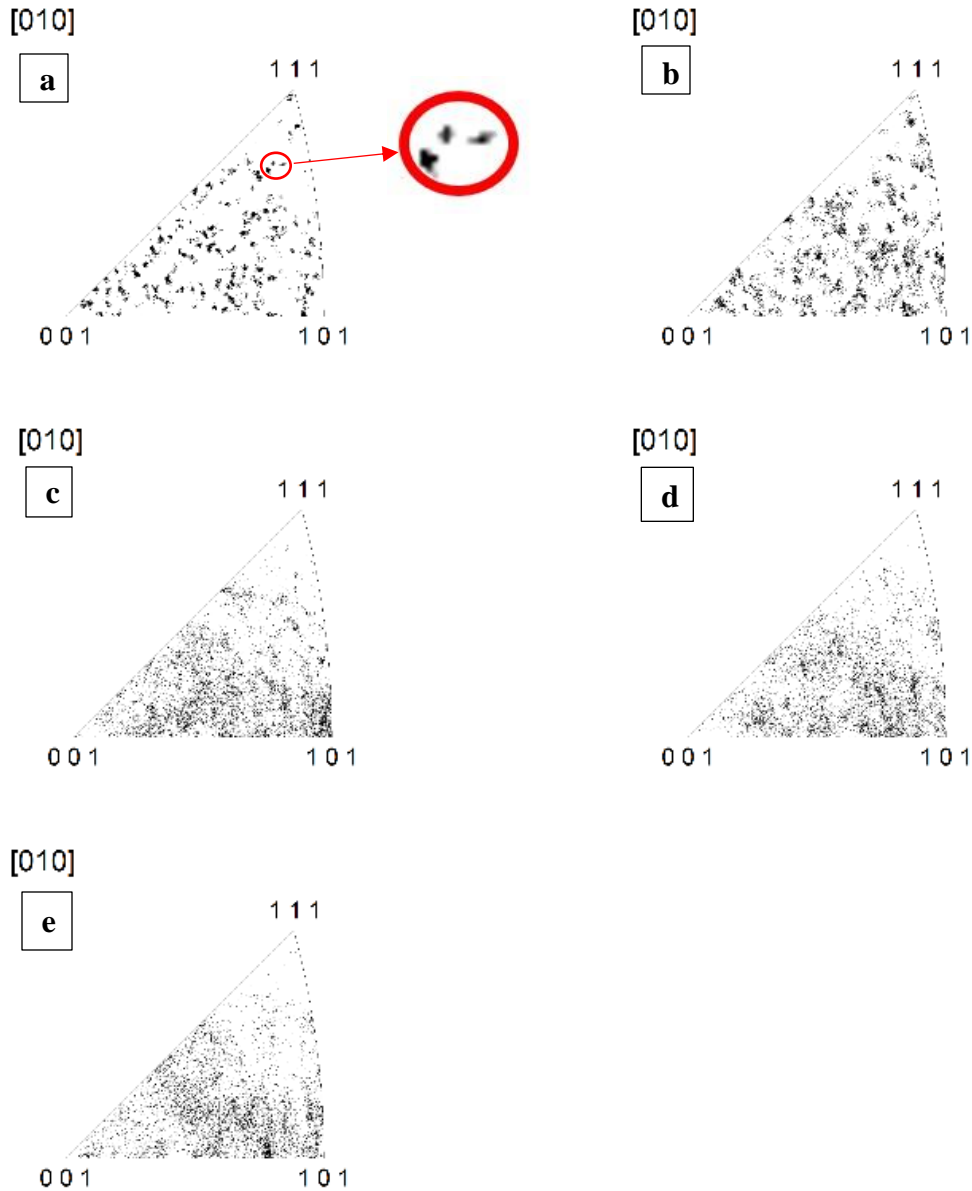


Figure 4.5 IPF maps with respect to $\langle 010 \rangle$ at different levels of plastic strain for TCFA. (a) 0%, (b) 2.7%, (c) 6.6%, (d) 9.4%, and (e) 12.3% plastic strain. In (a), three clouds, that were magnified highlighted by the red circle, represent the orientation spread of three TCFA grains at 0%. The orientation spread became larger as the level of plastic strain increased. Fewer clouds can be seen at 12.3% plastic strain, which indicates the orientation spread increased with increasing plastic strain.

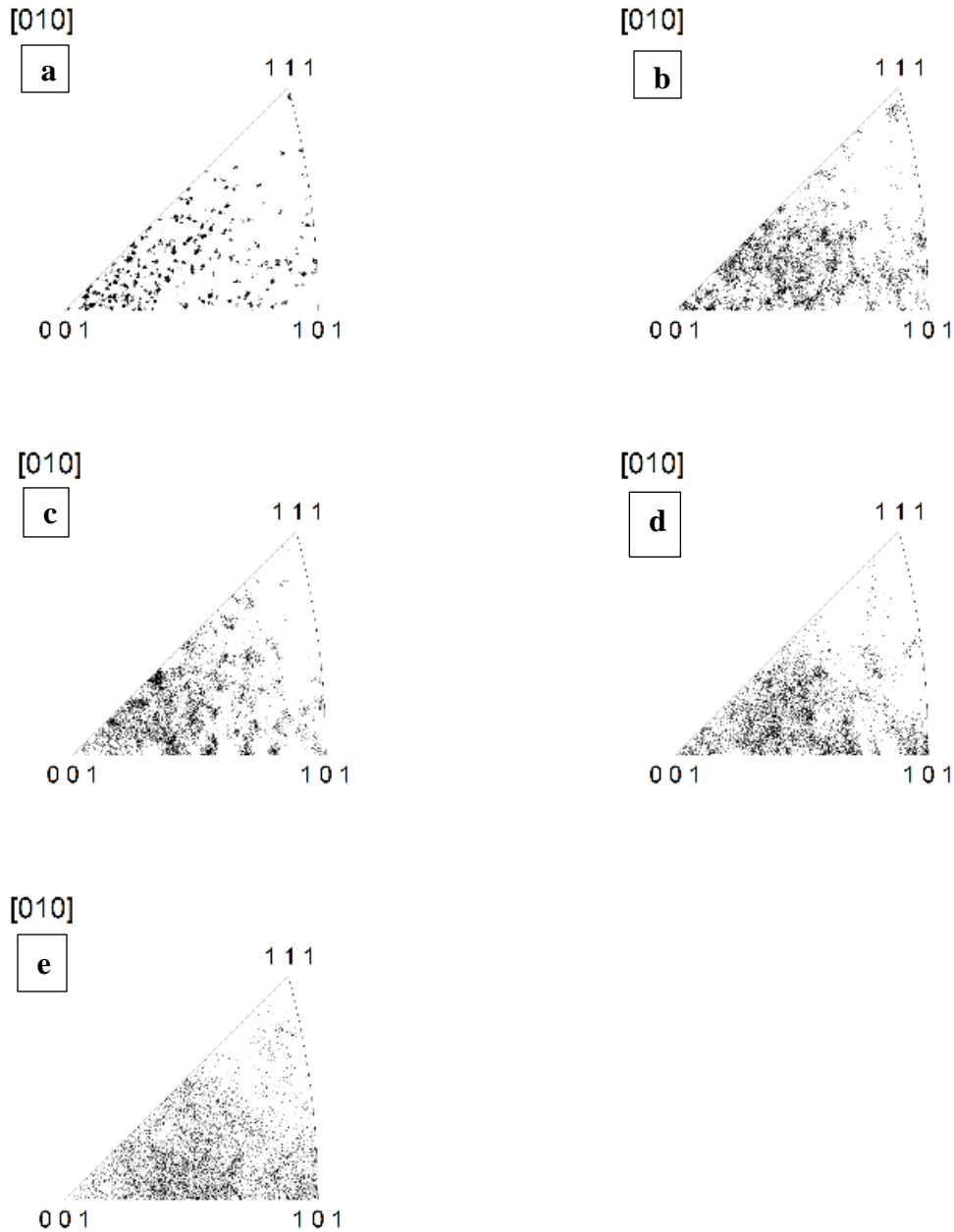


Figure 4.6 IPF maps with respect to $\langle 010 \rangle$ at different levels of plastic strain for TIMETAL-21S. (a) 0%, (b) 3.3%, (c) 5.4%, (d) 9.2%, and (e) 11.7% plastic strain. The orientation spread became larger as the level of plastic strain increased. Fewer clustered areas can be seen at 11.7% plastic strain, which indicates the orientation spread increased with increasing plastic strain.

4.3.2 The relationship between misorientation and plastic strain

The global minimum misorientation deviation ($MD_{G(\min)}$) was calculated using equation (4.10) for both alloys at each of the plastic strain levels attained. The reported plastic strain was calculated by measuring the difference between initial and final length of the samples. The $MD_{G(\min)}$ versus global plastic strain is plotted in Figure 4.7. A linear trend line was fit to the measured data points, from 0% to ~12% and ~9% for TCFA and TIMETAL-21S, respectively [see Figure 4.7(a)]. This suggests that linear regression (equations [4.12] and [4.13]) satisfactorily describes the relationship between the plastic strain and the $MD_{G(\min)}$ for both alloys.

$$MD_{G(\min),TCFA} = 0.22 \varepsilon_p + 0.37 (R^2 = 0.98) \text{ [degree]} \quad (4.12)$$

$$MD_{G(\min),TIMETAL} = 0.15 \varepsilon_p + 0.58 (R^2 = 0.97) \text{ [degree]} \quad (4.13)$$

However, an upward curvature was observed at ~12% plastic strain for TIMETAL-21S [see Figure 4.7(b)]. The cumulative distribution of $MD_{L(\min)}$ values at different levels of plastic strain for TCFA is shown in Figure 4.8. For the undeformed state, most of the grains exhibited similar $MD_{L(\min)}$ values. With increasing plastic strain, the $MD_{L(\min)}$ values increased. Furthermore, the range of each $MD_{L(\min)}$ curve increased with increasing plastic strain.

Table 4.1 summarizes the following relevant information for all the data points of the EBSD IPF maps: $MD_{G(\min)}$, SD: Standard deviation in grain scale ($MD_{L(\min)}$), the minimum and maximum $MD_{L(\min)}$, the difference between the minimum and maximum $MD_{L(\min)}$ (Δ), total data points, and the step size. The reported minimum and maximum MD were averaged from the 2% of grains with the lowest and highest $MD_{L(\min)}$, respectively. The minimum and maximum MD, the difference between them (Δ), and standard deviation (SD) increased with an increase in plastic strain.

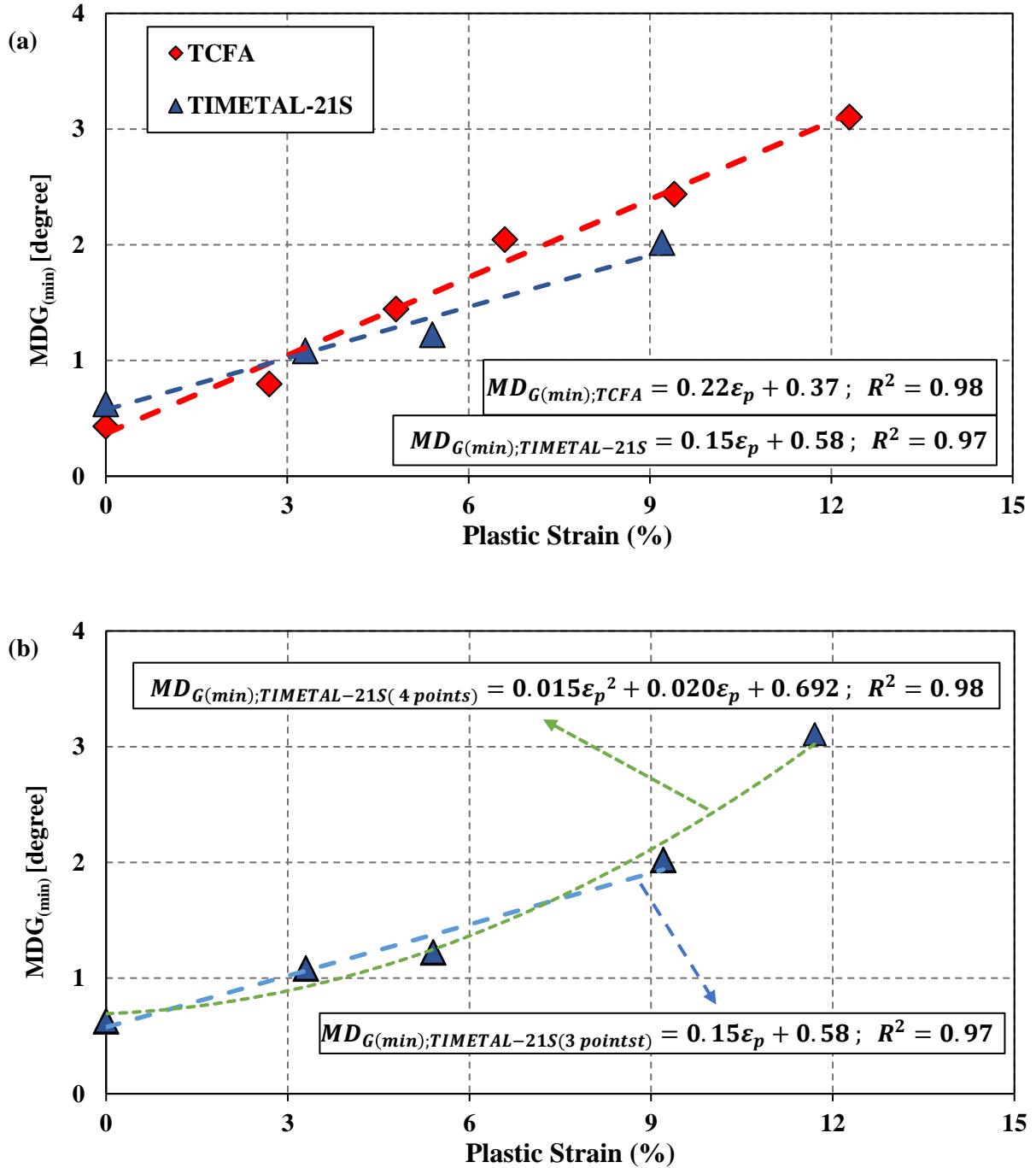


Figure 4.7 The $MDG_{(Min)}$ versus plastic strain for TCFA and TIMETAL-21S. (a) The linear regression satisfactorily describes the relationship between global plastic strain and $MDG_{(Min)}$. (b) The $MDG_{(Min)}$ versus plastic strain for TIMETAL-21S at ~12% exhibited an upward curvature.

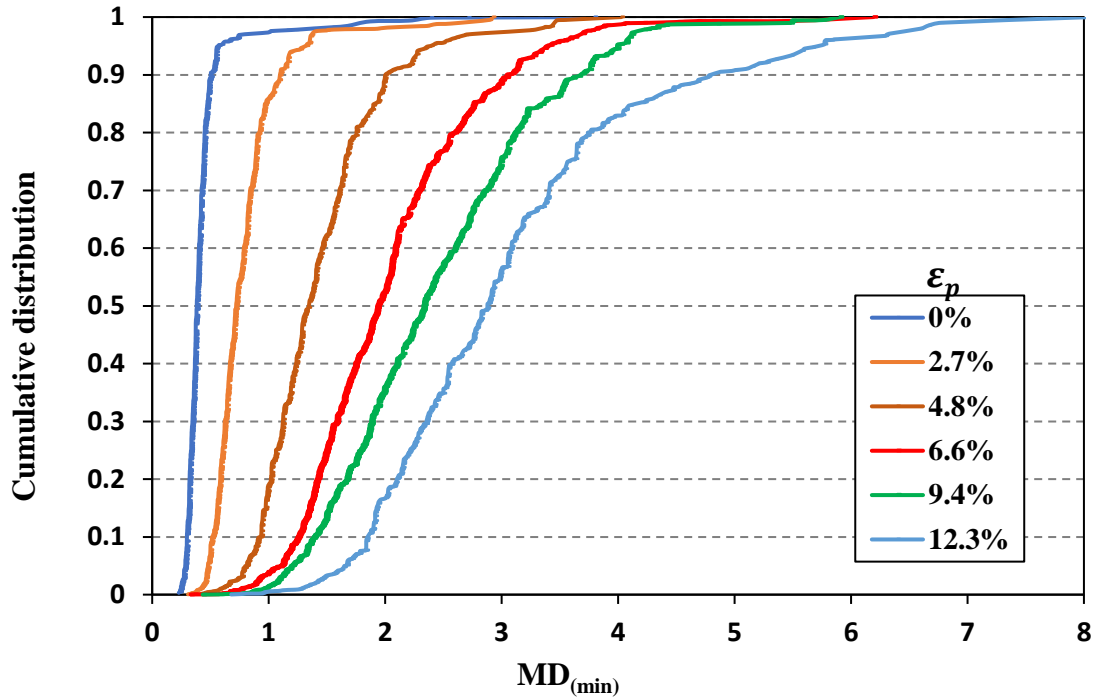


Figure 4.8 The cumulative distribution of MD_{Min} values at different levels of plastic strain for TCFA. With increasing plastic strain, the MD_{Min} shifted to the right.

Table 4-1 The calculated MD_G values at each level of plastic strain and the associated parameters for TCFA.

Plastic strain (%)	MD_G (SD)	Min(MD)	Max(MD)	$\Delta(MD_{max} - MD_{min})$	Total data points	Step size (um)
0	0.43 (0.26)	0.24	1.91	1.67	101865	4
2.7	0.8 (0.31)	0.36	2.3	1.94	90399	4
6.6	2.05 (0.72)	0.59	4.16	3.57	161095	4
9.4	2.44 (0.85)	0.75	4.76	4.01	141643	4
12.3	3.1 (1.14)	0.88	6.45	5.57	98425	4

4.3.3 The effect of orientation on $MD_{(\min)}$

In this section, the effect of crystallographic grain orientation on the misorientation was quantified at the grain scale. Figure 4.9 exhibits the color code IPF with respect to tensile direction of $MD_{L(\min)}$ for 444 grains for TCFA, which was deformed to 12.3% plastic strain. The grains close to the $\langle 101 \rangle$ corner have lower $MD_{L(\min)}$ values compared to other regions, i.e., the grains that are located in this area exhibited a lower tendency (lower $MD_{L(\min)}$ values) for orientation change compared to other orientations. To quantify the influence of the grain orientation on $MD_{(\min)}$, three crystalline orientations were chosen with respect to the loading direction: $\langle 100 \rangle$, $\langle 101 \rangle$, and $\langle 111 \rangle$. The grains with a less than 20° misorientation between the

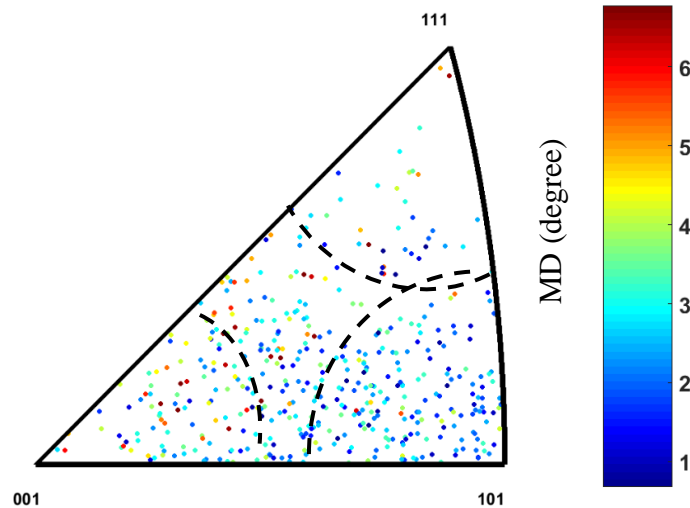


Figure 4.9 IPF (with respect to the loading direction) of MD values. This plot represents the distribution of the MD values of 444 grains from a TCFA sample tensile deformed to 12.3% plastic strain (posttest MD values). The grains located close to the $[101]$ corner exhibited lower MD values compared to other regions, which indicates a lower tendency for orientation change. For a better visualization, the three studied groups, i.e. $\{100\}$, $\{110\}$, and $\{111\}$ were separated by three arcs. There was a small common area between $\{110\}$ and $\{111\}$ groups.

reference orientation (RO) of the grain and one of the studied orientations were placed in the same group. For illustration, the EBSD IPF maps of the corresponding groups are presented for a portion of the TCFA sample deformed to 12.3% plastic strain in Figure 4.10. The $MD_{(min)}$ for each group strain is plotted as function of plastic strain in Figure 4.11. The total area fraction for each group is provided in front of the corresponding label. The fraction of each group showed a slight variation for each alloy due to the fact that the texture was not exactly the same throughout the as-received sheets. As can be seen, all groups exhibited almost the same $MD_{(min)}$ value in the undeformed state (0% plastic strain). At 3% plastic strain, all of the groups exhibited similar $MD_{(min)}$ values. With an increase in the plastic strain to ~6%, a slight variation was observed between the lowest and highest $MD_{(min)}$ groups for both alloys. However, at 9% plastic strain, the difference for each group became more notable and this could be easily distinguished at ~12% plastic strain for both alloys.

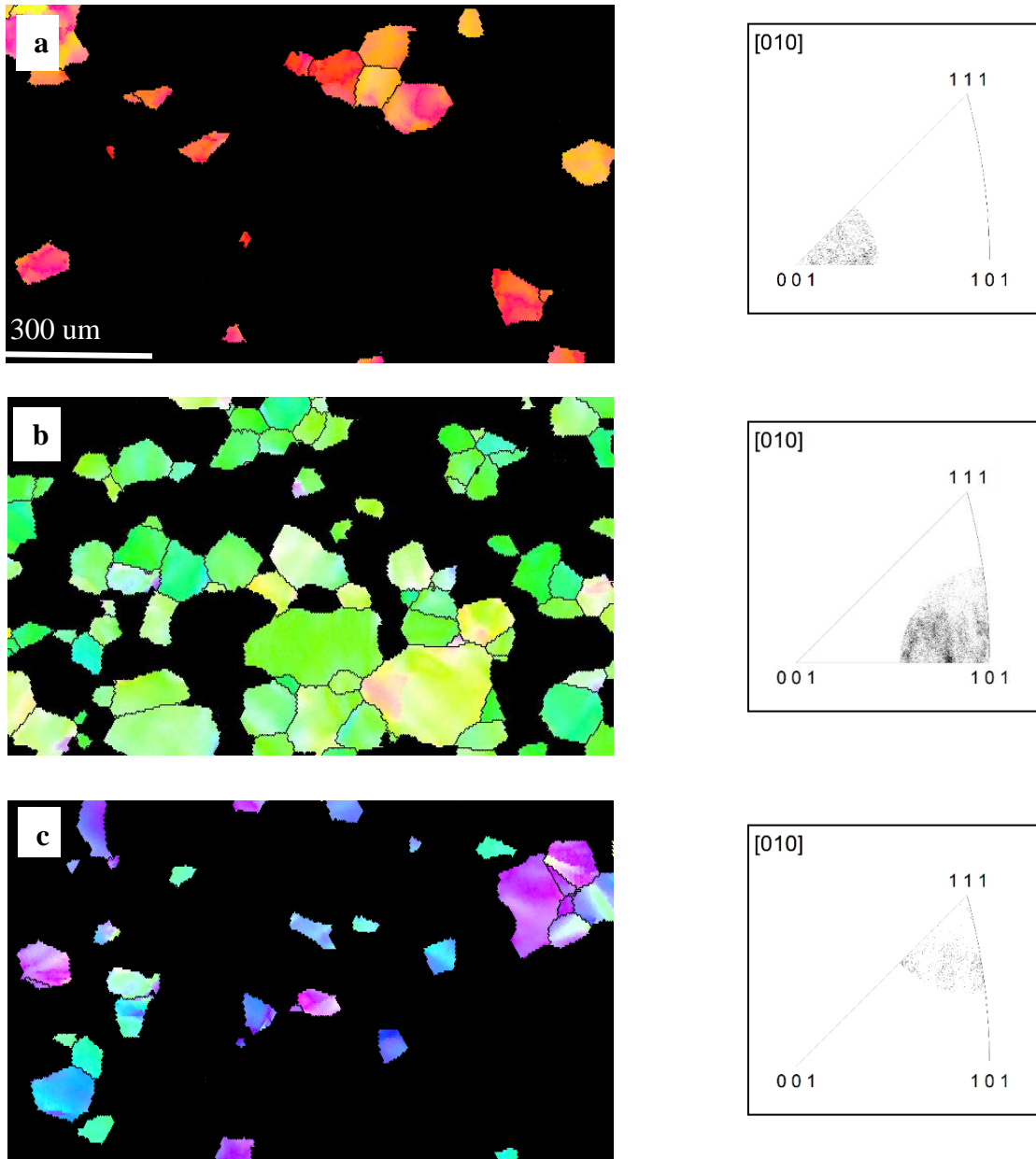


Figure 4.10 Partitioned EBSD maps highlighting the three crystallographic orientations with a tolerance angle of 20° with respect to the loading direction: (a) $\langle 100 \rangle$, (b) $\langle 101 \rangle$, and (c) $\langle 111 \rangle$, and their corresponding IPF for a TCFA sample, which was subjected to tensile loading to 12.3% plastic strain. There is a small common area between $\{110\}$ and $\{111\}$ groups, where the threshold angle was 20° .

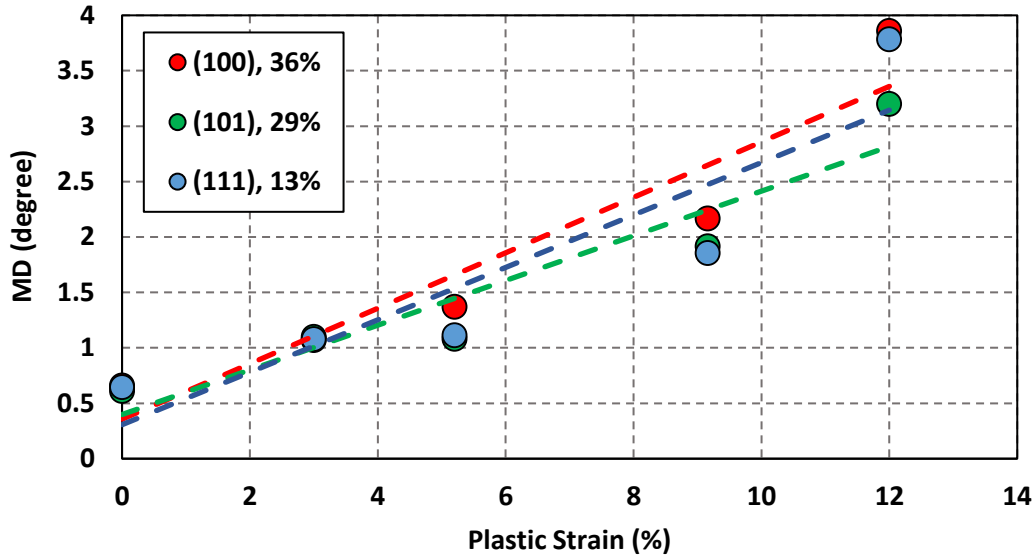
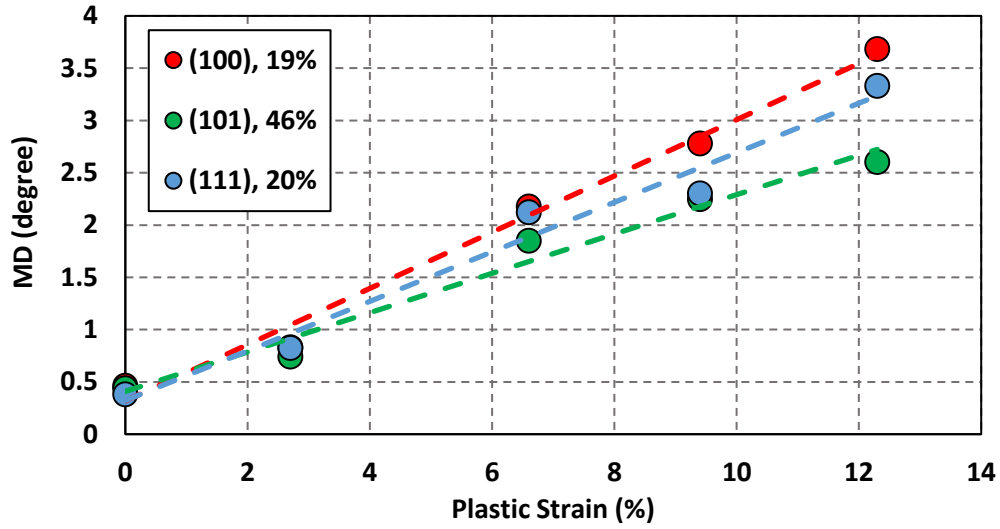


Figure 4.11 The MD values as a function of grain orientation and plastic strain for (a) TCFA and (b) TIMETA1-21S. The {100} group exhibited a higher MD value than other groups, while the {101} exhibited a lower MD value. The population fraction percent of each group is provided in front of the corresponding legend.

4.3.4 The influence of grain Size on $MD_{(min)}$

In the following, the relationship between the grain size and the $MD_{(min)}$ was quantified and characterized. The equivalent grain diameter was calculated based on EBSD data and following equation:

$$D = 2 \sqrt{\frac{n * l_1 * l_2}{\pi}} \quad (4.14)$$

where n is total number of data points within the grain, l_1 and l_2 are the vertical and horizontal step sizes of the EBSD scans, respectively. A total number of ~3000 grains were analyzed for each alloy. Approximately 600 grains were evaluated at each strain level. The cumulative equivalent grain diameter distribution is shown in Figure 4.12 for all the specimens examined. Almost, all the samples exhibited a similar grain size distribution. For quantifying the relationship between grain size and $MD_{(min)}$, the grains were grouped according to their equivalent diameters. The $MD_{(min)}$ versus $\frac{D}{D_{avg}}$ (D : equivalent diameters and D_{avg} : average grain size) is plotted as a function of plastic strain for TCFA and TIMETAL-21S in Figure 4.13. The grains with grain sizes less than 20 μm (due to low number of data points within the grains) and greater than 100 μm (due to low number of the grains within the microstructure patch) were excluded from the analysis for TCFA. Similarly, the grains with grain sizes less than 5 μm and greater than 30 μm were excluded from the analysis for TIMETAL-21S. The $MD_{(min)}$ versus $\frac{D}{D_{avg}}$ exhibited a linear trend at each level of plastic strain for both alloys, except the undeformed state where the $MD_{(min)}$ was almost constant for all the grain sizes. With an increase in plastic strain, the $MD_{(min)}$ variation between the subpopulation of small and large grain sizes became more significant.

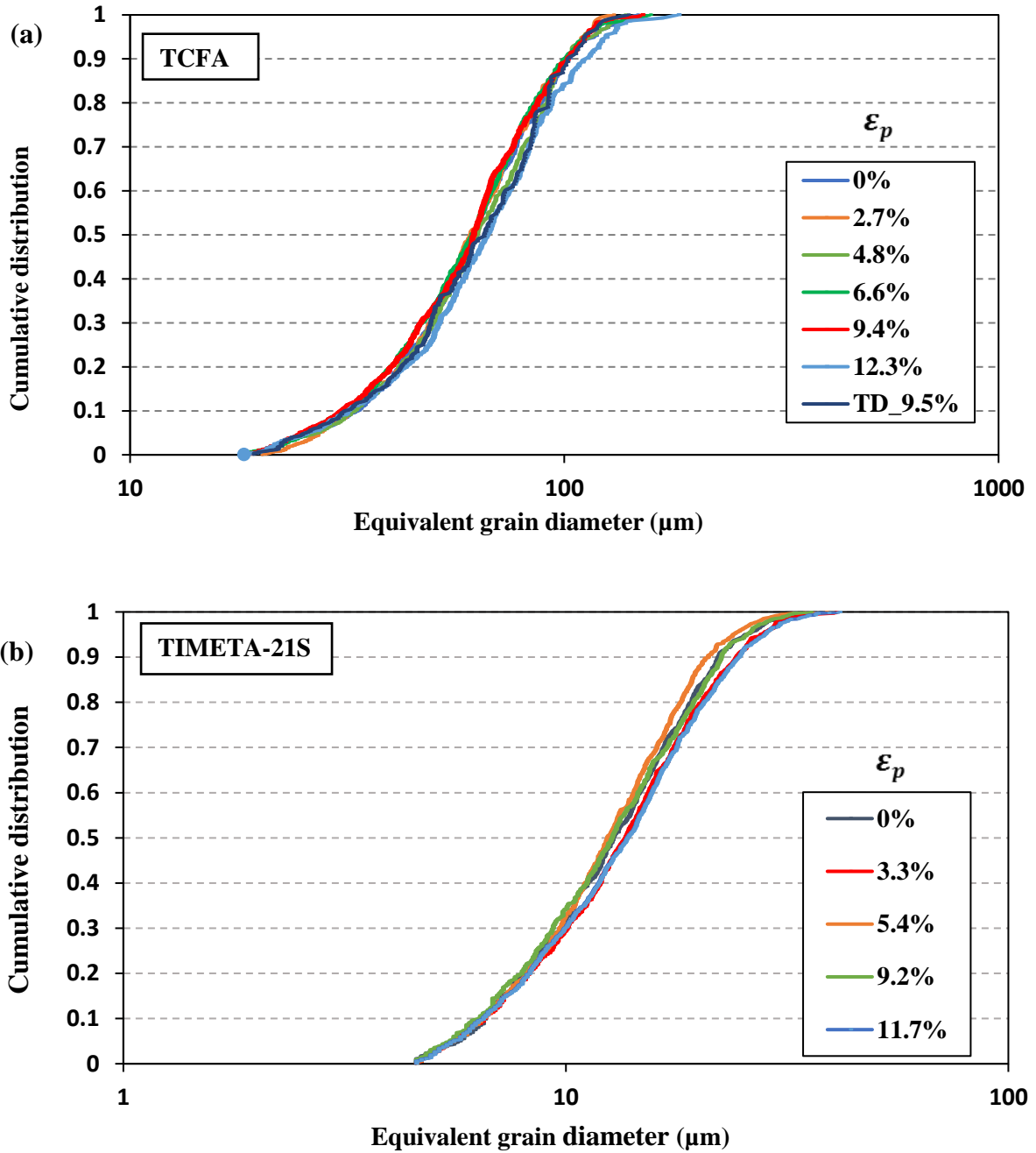


Figure 4.12 The cumulative distribution of grain size for (a) TCFA and (b) TIMETAL-21S samples tensile tested to different strain levels. Although the tensile tests were performed on different samples, the data indicate a similar grain size distribution for all the samples.

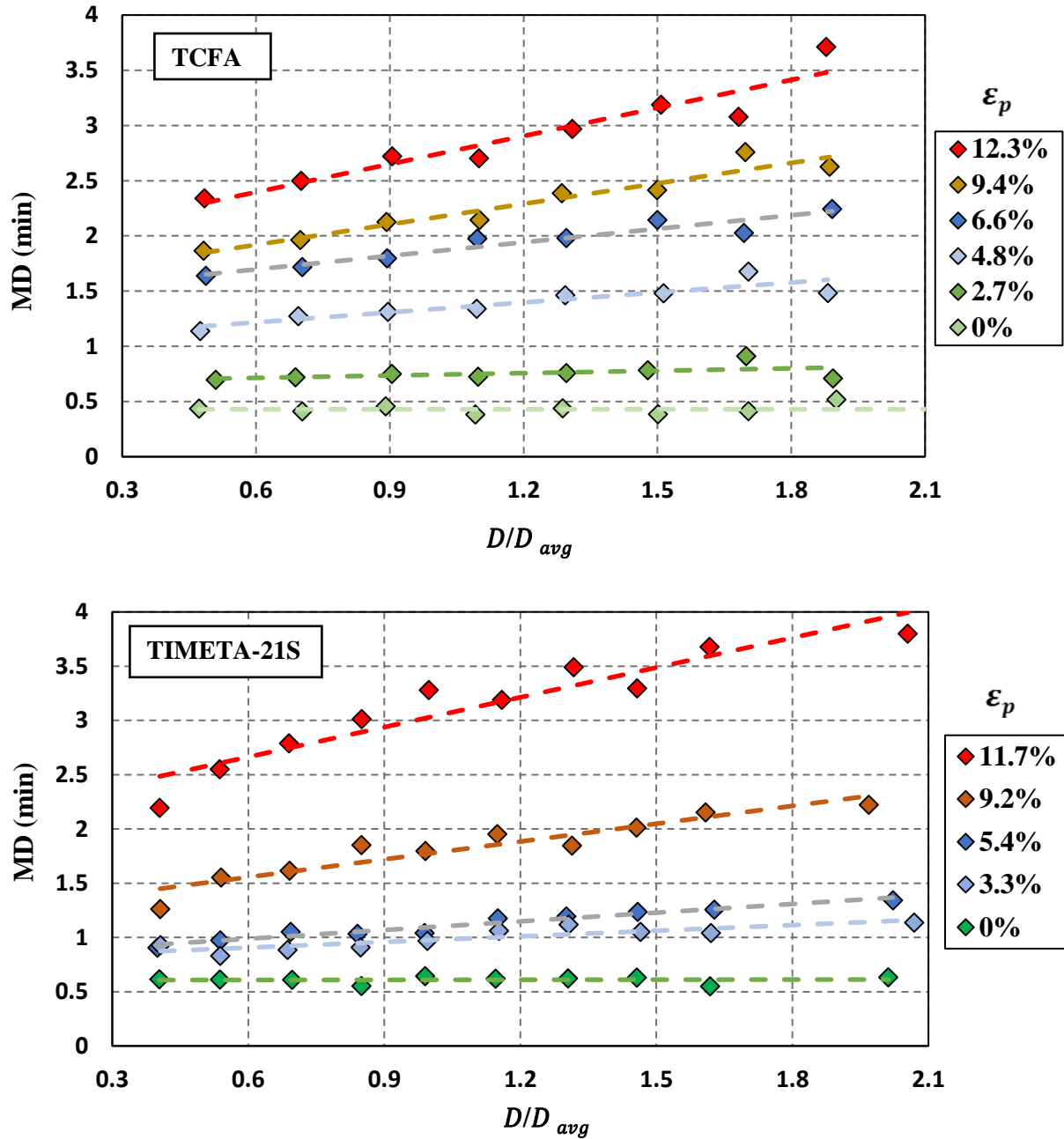


Figure 4.13 The $MD_{(min)}$ versus D/D_{avg} for different plastic strain levels for (a) TCFA and (b) TIMETA-21S. The $MD_{(min)}$ values were almost constant for the undeformed materials. With increasing plastic strain level, the larger grains exhibited a higher $MD_{(min)}$ values. This was more pronounced at the high plastic strain levels.

4.3.5 The influence of distance from grain boundary on $MD_{(\min)}$

In this section, the $MD_{(\min)}$ was used to quantify and evaluate the effect of distance from the grain boundary on the orientation change. Figure 4.14 presents the MD values distribution at the grain boundaries for 200 grains of a TCFA sample tensile tested to 12.3% plastic strain. For most of the grains, the MD was higher than $MD_{G(\min)}$ at the grain boundaries. In Figure 4.14, the points where MD values was 4 times greater than $MD_{G(\min)}$ are colored in yellow and the points where MD values was less than half $MD_{G(\min)}$ are colored in dark blue. There were some regions where the MD values were 4 times greater than $MD_{G(\min)}$ on both sides of the grain boundaries.

The data were grouped according to their distance from the closest grain boundary. Figure 4.15 exhibits the $MD_{(\min)}$ value versus the distance from grain boundary. It should be noted that the $MD_{(\min)}$ value at distance zero presents the data points that formed the grain boundary. The $MD_{(\min)}$ exhibited the greatest value at the perimeter of the grains and it decreased with an increase in the distance from the grain boundaries. The reported $MD_{(\min)}$ values were the averages from all the points at specific distances from the grain boundary. However, the local variation in MD was 3 times greater than the average $MD_{(\min)}$ for most of the grains (see Figure 4.14).

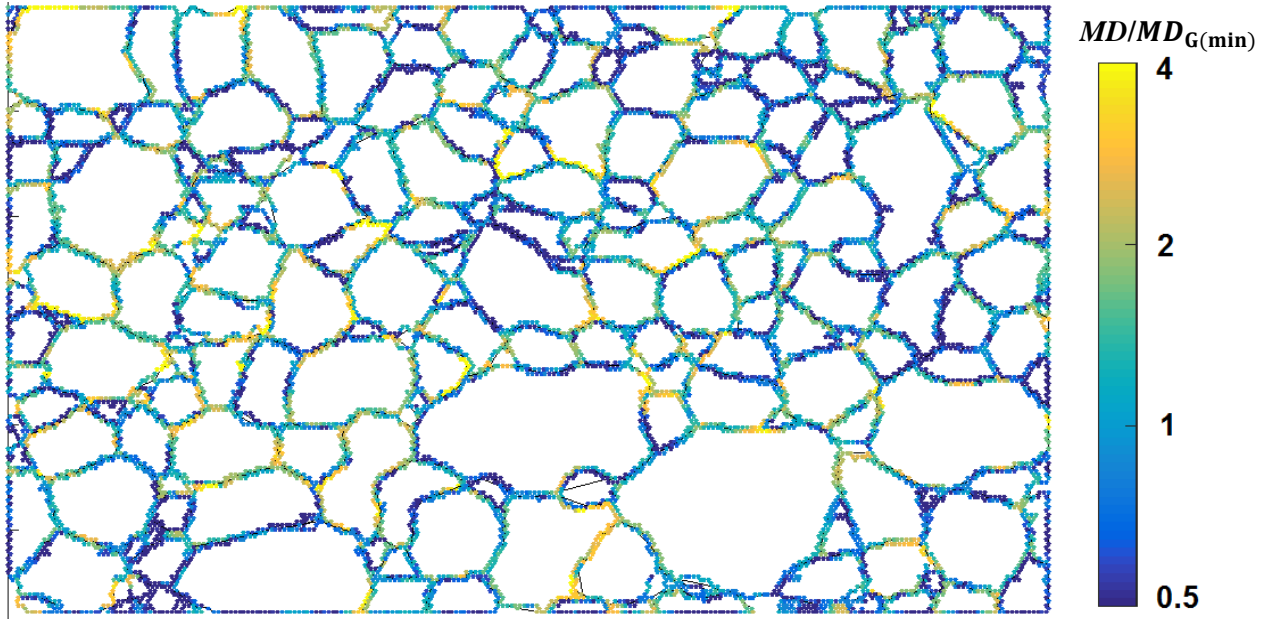


Figure 4.14 The distribution of MD values at grain boundaries for 200 grains of a TCFA sample loaded to 12.3% plastic strain at RT. The points in which the MD values were greater than $3 MD_{G(\min)}$ are shown in yellow and the points where MD values was less than half $MD_{G(\min)}$ are colored in dark blue. There were some regions where the MD values were 4 times greater than $MD_{G(\min)}$ on both sides of the grain boundaries.

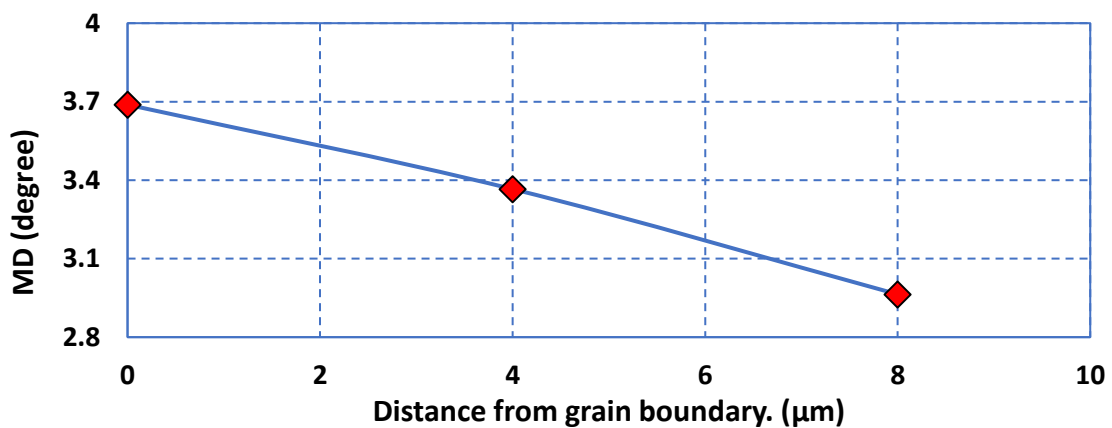


Figure 4.15 The influence of distance from the grain boundary on MD for a TCFA sample that was deformed to 12.3% plastic strain at RT. The larger the distance from the grain boundary, the lower the MD value was.

4.3.6 The effect of loading history on misorientation value

Two interrupted tensile tests were performed at ~11% and 11.7% plastic strain for the TCFA and TIMETAL-21S alloys, respectively. The displacement was paused eight times during the test for the TCFA sample and five times for the TIMETAL-21S sample in plastic region. The $MD_{G(Min)}$ of the interrupted and monotonic tests are provided in Figure 4.16. The triangular and square points represent the $MD_{G(Min)}$ values for the interrupted and monotonic tests, respectively. The values of MD_{Min} for both interrupted tests were higher than the fit lines that were obtained by the linear regression analysis for the monotonic tests. These results indicate that the crystallographic orientation change becomes more pronounced for the interrupted tensile tests than the monotonic tests.

4.3.7 Digital Image Correlation

The correlation between two misorientation maps and the plastic strain map obtained from a DIC-SEM experiment was qualitatively investigated in this section. A TCFA sample was tensile tested inside a SEM. EBSD was performed on a selected area from the center of the sample gage section, both before and after the test. The posttest EBSD step size was 2 μm . Then, the sample was coated with gold nanoparticles (AuNP), following the procedure described in (Kammers and Daly, 2013b). The size of used AuNP was ~60 nm. Figure 4.17 exhibits the AuNP coating on the surface of the coated sample at high-magnification. The size of the studied area was ~ 500-600 μm^2 . The sample was loaded to ~11% plastic strain. During the test, the displacement was paused nine times to acquire SE SEM photomicrographs for calculating the strain at each pause on selected areas. At each pause, 30 SEM photomicrographs were acquired to cover the selected area with a 100 μm field of view.

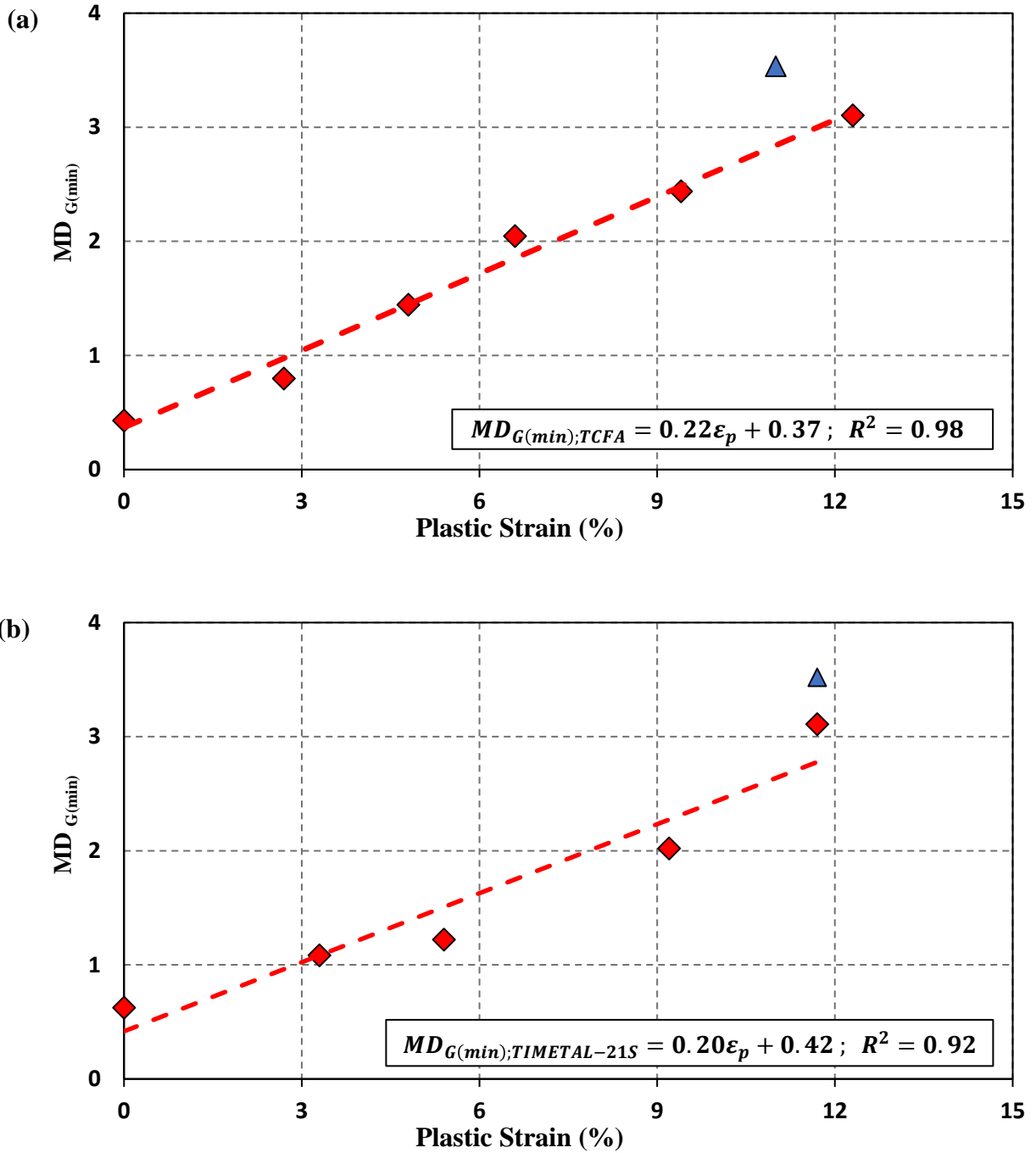


Figure 4.16 The $MD_{G(Min)}$ versus global plastic strain for monotonic tensile tests for (a) TCFA and (b) TIMETAL-21S. The linear regression indicates a linear relationship between global plastic strain and $MD_{G(Min)}$ with a relatively high R^2 value. The triangular points represent the $MD_{G(Min)}$ values of interrupted tensile tests.

In this study, the special distance was 50 nm and 2 μm for the DIC-SEM experiment and EBSD scan, respectively. Figure 4.18 presents the stress-displacement curve. The strain was calculated by measuring the distance between small Vicker's indents. The indents were made on the surface of the sample before the test. Figure 4.19 (a) and (b) present the SE SEM photomicrographs from the studied area before and after coating, respectively, prior to the deformation. Figure 4.19 (c) presents the same area after the deformation with the coating. The sample was polished slightly to remove the AuNP coating and then the posttest EBSD was performed (see Figure 4.19 [d]). Figure 4.20 shows EBSD IPF maps of the selected area of the sample before and after the tensile test. The black points in the posttest EBSD IPF map indicated the points where the confidence index was less than 0.05. The low confidence index was due to the remaining coating and/or the severe local plastic strain.

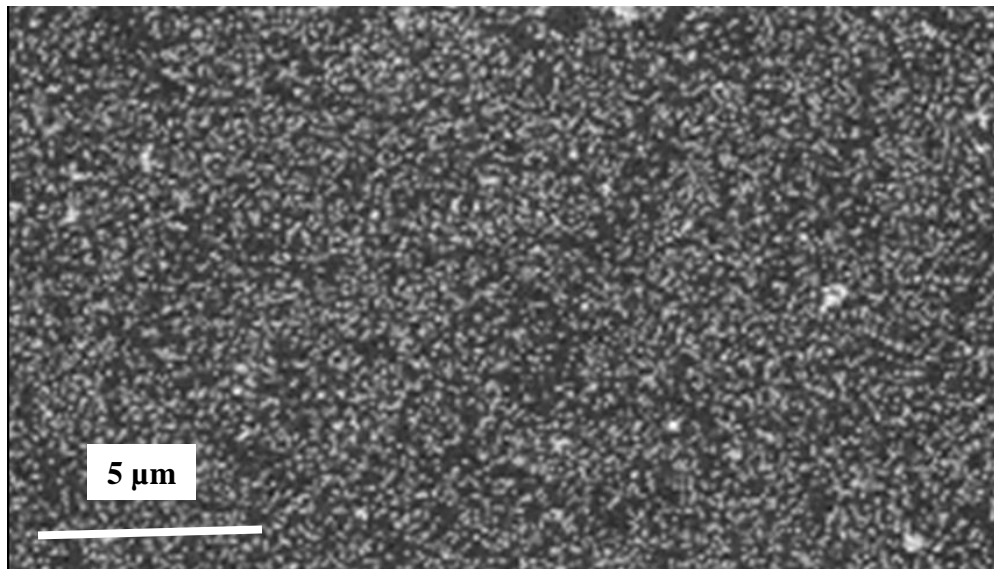


Figure 4.17 The surface of the sample that was coated with gold nanoparticles (AuNP).

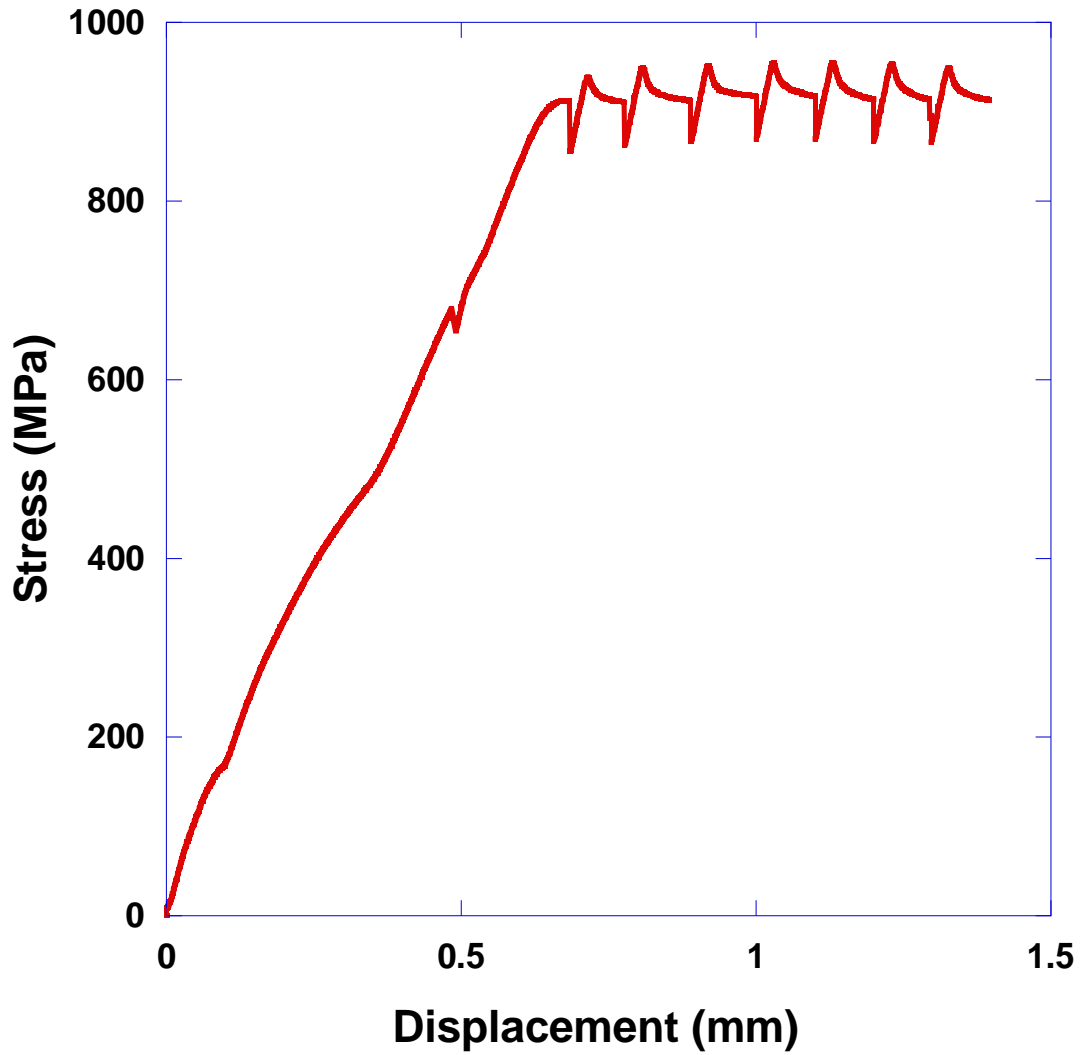


Figure 4.18 The stress versus displacement curve for the TCFA sample that was coated with AuNP. The test was paused nine times to acquire SE SEM photomicrographs for calculating the strain through DIC characterization. Each drop in stress indicates the position of each pause.

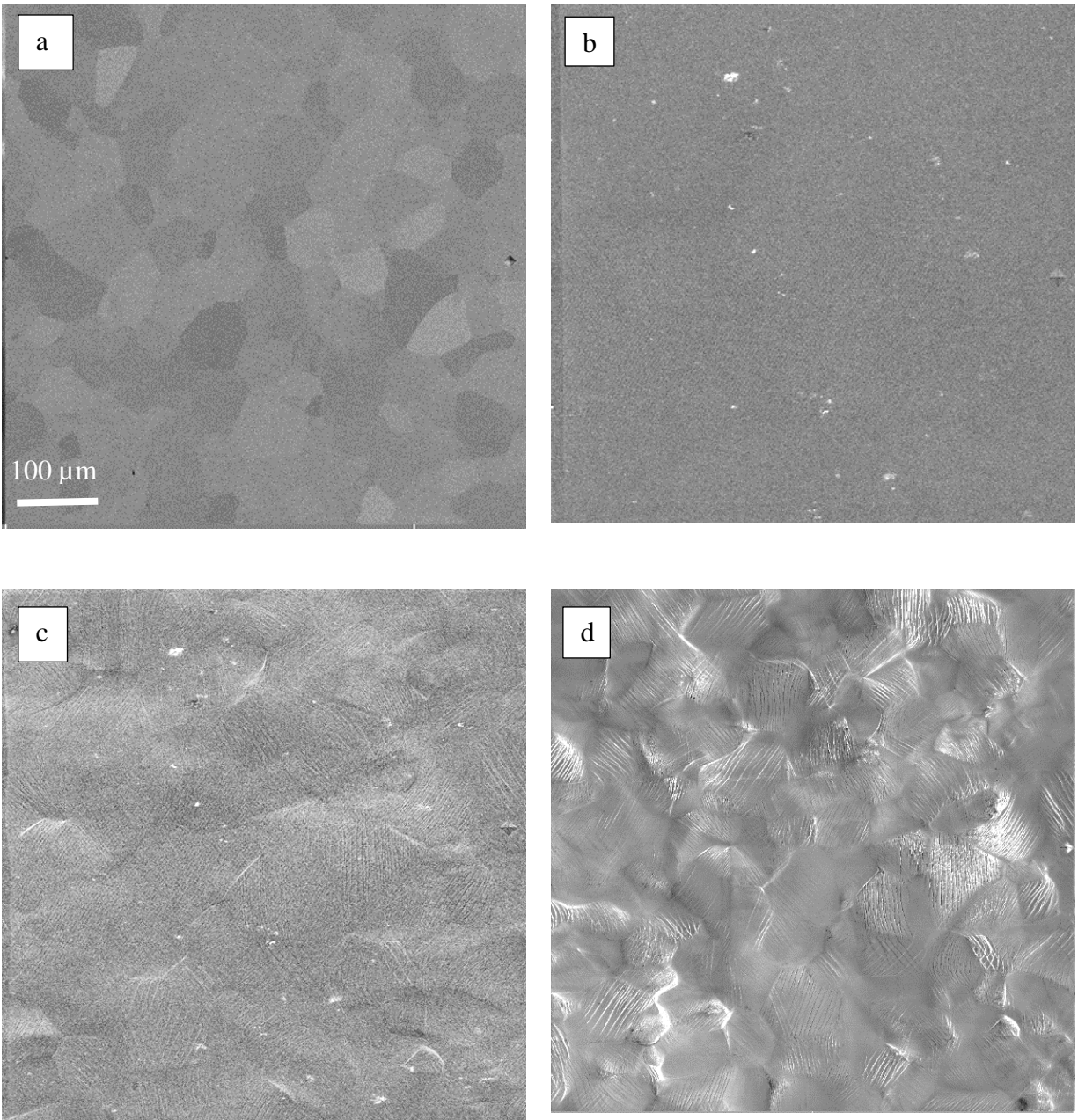


Figure 4.19 SE SEM photomicrographs of the selected area of the TCFA sample, (a) before the test and before the coating was applied to the surface, (b) before the test and after the coating was applied to the surface, (c) after the test with coating, and (d) after the test, after slight polishing (to remove the coating for performing posttest EBSD analysis).

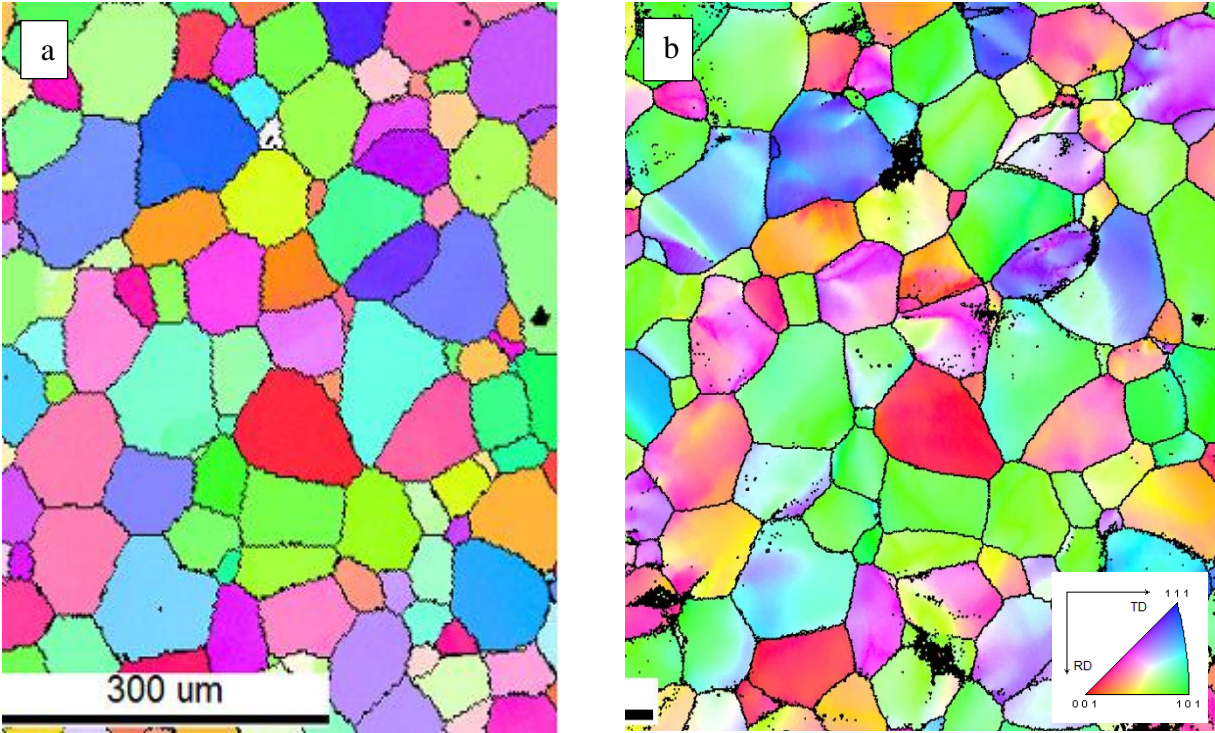


Figure 4.20 EBSD IPF maps from the selected area of the TCFA sample, (a) before the test, before coating and (b) after the test, the coating was removed by slight polishing. Black points indicate where the confidence index was less than 0.05. A substantial orientation change was observed in some of the grains.

4.3.7.1 DIC strain field map

The Vic2D (2009) software was used to calculate the strain components from the SE SEM photomicrographs. Figure 4.21 presents the equivalent strain field at 10.8% strain. This map was generated by combining 30 subareas. The equivalent strain was calculated using the following equation:

$$\varepsilon_{eq} = \sqrt{\frac{2}{3}(e_{xx}^2 + e_{yy}^2 + 2e_{xy}^2)} \tag{4.15}$$

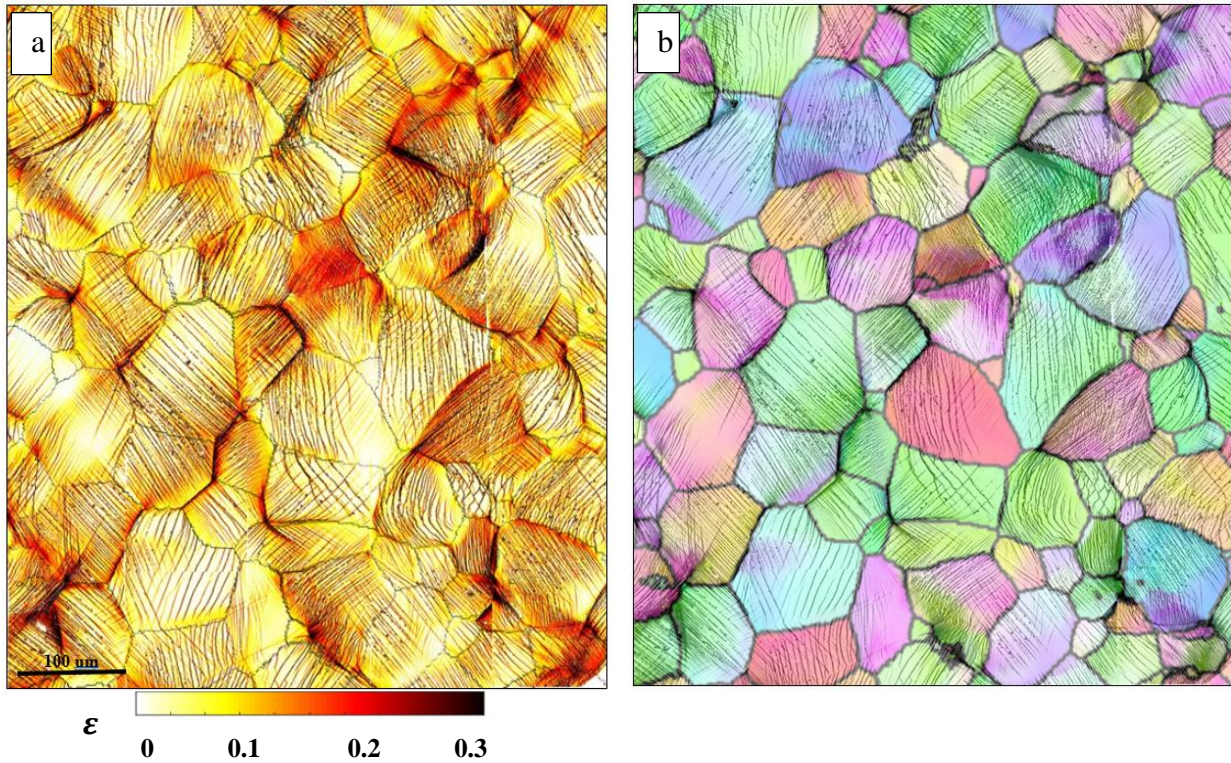


Figure 4.21 (a) The equivalent plastic strain map after 10.8% strain. This map was generated by combining 30 subareas. The areas, where the equivalent strain was more than three times the global strain, are exhibited in black. A local strain concentration was observed in most of the grains. (b) The posttest EBSD IPF map [Figure 4.20(b)] was overlaid on the equivalent plastic strain map. The IPF color code is similar to the color code in Figure 4.20.

4.4 Discussion

4.4.1 Evolution of orientation change

During plastic deformation, the local strain gradient causes formation of dislocation networks to accommodate the geometric continuity (Nye, 1953). These type of dislocation networks were named geometrically necessary dislocations [GNDs] (Ashby, 1970). Another type of dislocations is statistically stored dislocations (SSDs), which evolve during plastic deformation. Figure 4.22 provides a schematic of SSDs and GNDs. In Figure 4.22, (a) and (d) illustrate square lattices before deformation. When the material is subjected to shear loading, SSDs may be generated or the atoms may simply slide with respect to each other to accommodate the deformation [see Figure 4.22 (b) and (c)]. Figure 4.22 (e) presents the GNDs that were generated to accumulate the strain gradient between the top and bottom surfaces after applying a bending moment. The net Burgers vector was zero in the presence of SSDs and nonzero in the presence of GNDs. Thus, plastic deformation

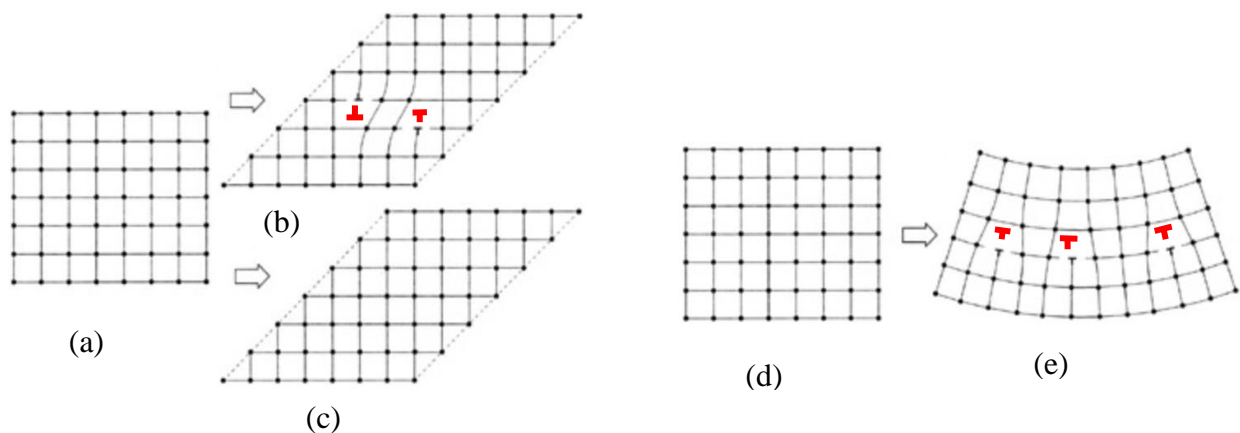


Figure 4.22 (a) Square lattices before deformation and (b) lattices after shear deformation where SSDs formed and where (c) no dislocations formed. (d) Square lattices before deformation and after bending deformation, where GNDs formed. ⁶

⁶ <https://www.globalspec.com/reference/39139/203279/chapter-10-size-effect-at-continuum-limit-on-approach-to-atomic-lattice-scale>

may occur in a material, while no significant orientation change occurs due to the formation of SSDs, e.g., under a controlled loading condition, a single crystal may be deformed permanently, while no substantial orientation change occurs. Although SSDs may form in some part of the grains without a significant change in the lattice orientation, the information gained from GNDs is still helpful to gain a better understanding of the relationship between the microstructure change and plastic deformation in the polycrystalline materials. Furthermore, studying the crystallographic orientation change may provide more detailed information about the nature of the heterogeneous plastic deformation at the microscale.

Strain gradients occur within individual grains in an anisotropic polycrystalline material subjected to loading. Strain gradients lead to GND formation within individual grains during the deformation, which results in local lattice orientation changes. The density of GNDs increases as the level of the plastic strain increases. Therefore, the orientation changes increase with an increasing level of plastic strain.

In the present work, both the TCFA and TIMETAL-21S alloys exhibited a relatively weak texture. For each EBSD unit triangle represented in Figure 4.5(a) and Figure 4.6(a), the individual clouds represent the orientation spread within one grain at 0% plastic strain (undeformed state). For example, three clouds, which represent the orientation spread of three TCFA grains at 0% plastic strain are highlighted by the red circle in Figure 4.5(a). The magnitude of the orientation spread at 0% plastic strain is a function of both the error in the EBSD measurement and the orientation variation within the grains in the as-received sheets. The orientation spread became larger as the level of plastic strain increased (see Figure 4.5 and Figure 4.6), which is an illustration of the increasing strain gradient with increased plastic deformation. During the loading, each individual grain experiences a unique strain distribution as a result of the unique networks of the

surrounding grains (unique geometries and unique grain orientations) to satisfy the deformation compatibility condition.

4.4.2 Misorientation and plastic strain

To estimate the remaining life of a part or the crack growth rate, it is essential to know the level of plastic strain. However, direct measurement of the plastic strain for operating parts is a challenging task. To overcome this challenge, some researchers have tried to estimate the level of the plastic deformation by correlating the plastic strain to the misorientation in the polycrystalline materials.

Equations (4.12) and (4.13a) suggest that linear regression satisfactorily describes the correlation between the $MD_{G(\min)}$ and the plastic strain for TCFA and TIMETAL-21S to ~12% and 9% plastic strain, respectively. This implies that the dispersion of the crystal orientations increases smoothly with an increasing level of plastic strain, i.e., the material heterogeneity response becomes more significant at higher plastic strain levels. This was consistent with previous work, where similar linear correlations were reported for a stainless steel and a nickel alloy (Kamaya et al., 2005, 2006).

As shown in Figure 4.7 (b), the $MD_{G(\min)}$ versus the plastic strain exhibited an upward curvature for TIMETAL-21S between 9% and 12% plastic strain. This nonlinearly suggests that the rate of the misorientation change accelerated with the deformation for TIMETAL-21S. This observation might be due the lower ε_f exhibited for TIMETAL-21S compared with TCFA. The ε_f was ~20% and ~ 12% for the TCFA and TIMETAL-21S⁷, respectively (Ogawa et al., 2007). When TIMETAL-21S subjected to ~12% plastic strain, the strain is close to its ε_f . Hence, the strain might

⁷ The minimum ε_f of TIMETAL-21S was extracted from the datasheet provided by TIMET company, <http://www.timet.com/assets/local/documents/datasheets/metastablebetaalloys/21S.pdf>

not be uniform at 12% global plastic strain and strain concentration might become more pronounced for the TIMETAL-21S. Consequently, the difference between the global plastic strain, which was measured according to the difference between the initial and final length of the sample, and the local plastic strain might be more substantial. To verify this hypothesis, the strain was measured and compared for three following cases:

- I. The plastic strain was measured according to the plastic region in the stress-displacement curves, which is shown in Figure 4.23 as “Stress-displacement curves”.
- II. The plastic strain was measured by a caliber, according to the total length of the specimen before and after the test, which is shown in Figure 4.23 as “Sample measurement”. A schematic of pretest specimen was provided in Figure 4.23, previously.
- III. The plastic strain was measured by using the pretest and posttest SE SEM photomicrographs, which is shown in Figure 4.23 as “SEM measurement”.

The measured plastic strains were similar for the cases I and II. However, the local plastic strain (measured by the SE SEM photomicrographs) was ~6% higher at ~12% global plastic strain (measured by case II). As shown in Figure 4.23, the R^2 exhibited the highest value where the SE SEM photomicrographs were used to measure the plastic strain. This implies that a linear regression could satisfactorily correlate the MD to the local plastic strain, even at relatively high plastic strain.

The substantial difference between the global and local plastic strain (the difference between cases II and case III) implies that the strain localization or even necking might have occurred on the sample. To investigate whether the necking occurred on the sample, two cases were considered:

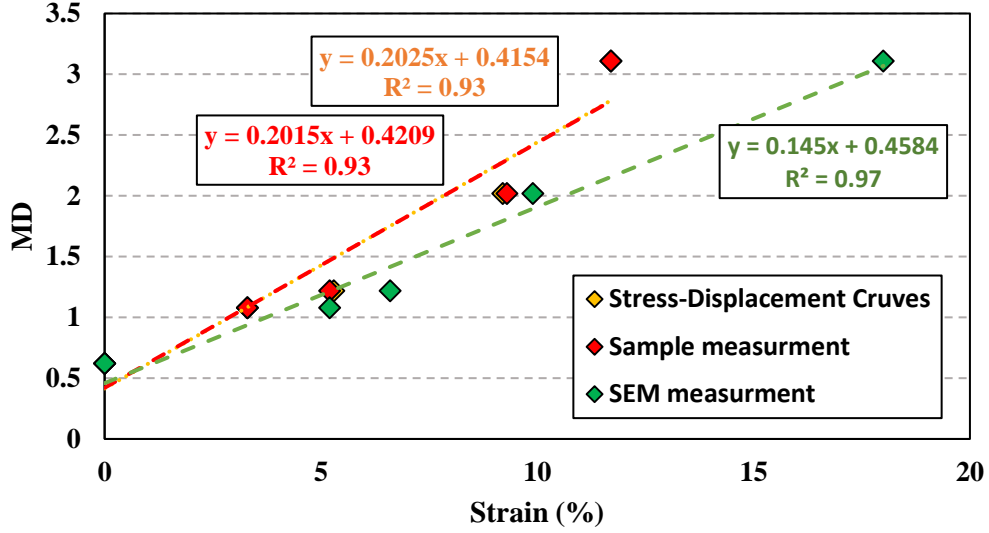


Figure 4.23 The MD versus plastic strain. The plastic strain was measured according to three cases, (I) according to the plastic region in the stress-displacement curves, which is shown as “Stress-displacement curves”, (II) by a caliber, according to the total length of the specimen before and after the test, which is shown as “Sample measurement”, and (III) by using the pretest and posttest SE SEM photomicrographs, which is shown as “SEM measurement”. The local plastic strain was measured by using the pretest and posttest SE SEM photomicrographs of the areas (case III), where the EBSD scans were performed. The local plastic strain was ~6% higher than the global plastic strain (case II), where the global plastic strain was ~12%.

- I. Assuming that necking did not occur. The true plastic strain was calculated by following equation for all the points:

$$\varepsilon_{true} = \ln(1 + \varepsilon_{eng.}) \quad (4.16)$$

- II. Assuming that necking occurred at ~18% local plastic strain. Thus, the true plastic strain was measured at 18% local plastic strain using the following equation:

$$\varepsilon_{true-after\ necking} = \ln\left(\frac{A_0}{A}\right) \quad (4.17)$$

As shown in Figure 4.24, the R^2 decreased for the case where necking was assumed to have occurred. This implies that necking might not occur on the sample. However, the applied strain might be close to the necking strain. Figure 4.25 exhibits the change in the width of the sample that was tensile loaded to ~18% local plastic strain (~12% global plastic strain). This suggested that necking did not occur in the sample.

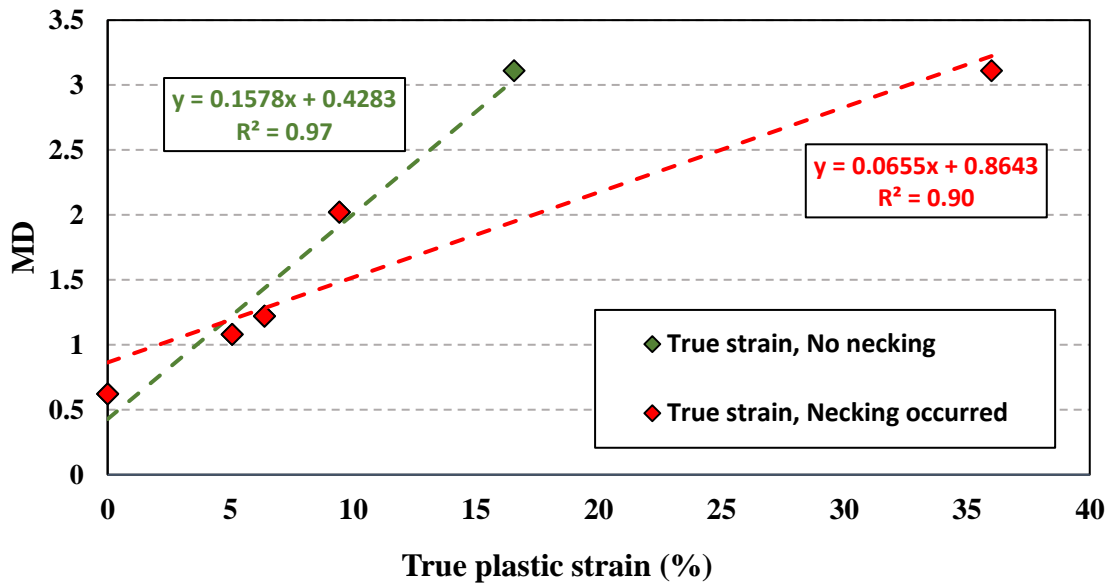


Figure 4.24 The Md versus true plastic strain using the plastic strain values measured by the SE SEM photomicrographs, for two cases: (I) assuming that necking did not occur. (The equation 4.16 was used to calculate the true plastic strain for all the points.), and (II) assuming that necking occurred at the highest level of plastic strain (the value of true strain for that highest plastic strain was calculated by equation 4.17, which resulted in a lower R^2 value).

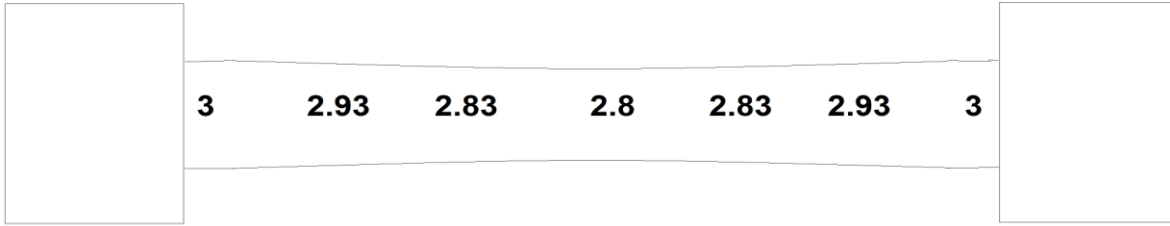


Figure 4.25 A schematic of the change in the width (in mm) of the sample that was subjected to ~12% global plastic strain. The local plastic strain at the center of the gage length was ~18%. The initial thickness of the sample was ~0.6 mm, and it was ~0.45 mm throughout the gage length after the loading.

4.4.3 On the orientation

It is essential to experimentally study the influence of crystallographic orientation on the mechanical properties of single crystal and polycrystalline materials in order to determine parameters to be input into simulations used for determining materials deformation (Badji et al., 2013; Bastos et al., 2006; Humphreys, 2001; Nicaise et al., 2011; Sémoroz et al., 2001; Zaaferani et al., 2006; Bache and Evans, 2001). As described in section 4.3.4, the misorientation level has been quantified as a function of plastic strain and the crystallographic orientation for three studied groups, i.e. orientations close to the {100}, {101}, and {111} with respect to tensile direction. As shown in Figure 4.11, the $MD_{(min)}$ values were similar in the undeformed state (0% plastic strain) for all the groups. The variation between each group gradually became more pronounced with increasing plastic strain. This implies that the heterogeneous response due to the crystallographic orientation became more substantial at higher strains. The highest $MD_{(min)}$ value belonged to the {100} group, while the {101} group exhibited the lowest $MD_{(min)}$ value for both alloys. Thus, the {100} and {101} groups exhibited the greatest and lowest tendency for orientation change, respectively. These results were consistent with another study that was conducted on a bcc single

crystal Fe, where tensile load was applied to samples of different orientations. Dislocation slip was the primary deformation mechanism in both works (Franciosi et al., 2015; Khademi et al., 2016).

As shown in Figure 4.26 (a) and (b), the [100] and [111] oriented single crystal Fe samples exhibited a notable rotation tendency toward the [111] and [011], respectively, when subjected to a tensile load (Franciosi et al., 2015). The [011] oriented sample (with respect to the tensile direction) experienced a relatively small orientation change compared with the [100] and [111] oriented

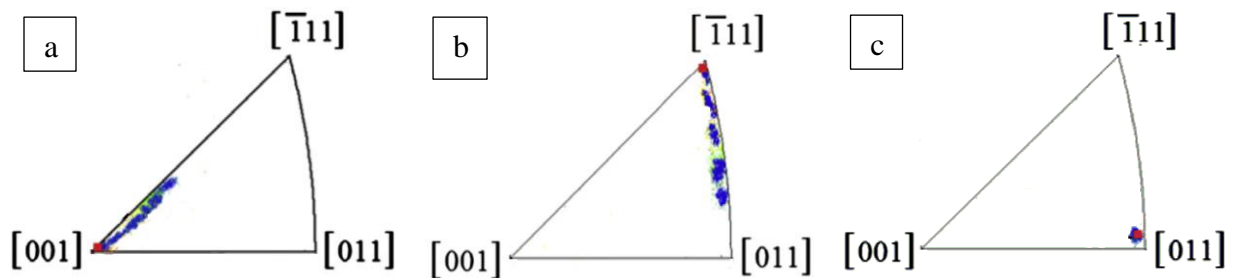


Figure 4.26 The orientation dispersion after tensile loading for a bcc single crystal Fe, where the initial orientation was close to (a) [100], (b) [111], and (c) [011], with respect to the tensile direction. The red points indicate the undeformed orientation state. The [001] exhibited an orientation tendency toward [111]. The [011] did not spread significantly, while the [111] rotated toward [011] (Franciosi et al., 2015).

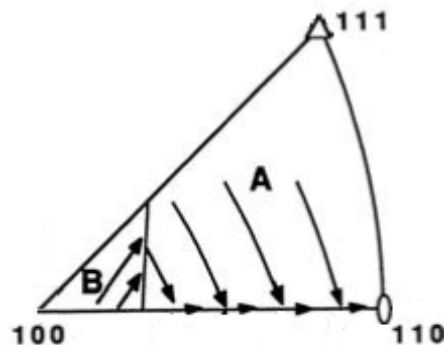


Figure 4.27 The orientation change tendency for a bcc structure tensile loaded in regions A and B is toward the [111] and [110], respectively. The [110] is considered as the stable orientation for the bcc structures (Hosford, 2009).

samples (Franciosi et al., 2015). Hence, the $\{110\}$ orientation (with respect to the tensile direction) is considered as the more stable orientation and this agrees with the rotation tendency trend for bcc materials, see Figure 4.27 (Hosford, 2009).

The $[100]$ orientation exhibited a relatively higher level of orientation dispersion compared with the $[110]$ in this work and the study of Franciosi et al. (2015) [see Figure 4.11 and Figure 4.26 (a) and (c)]. A higher number of possible slip systems are involved with $[100]$ compared with the $[110]$. Twenty slip systems containing non-zero Schmid factors could be activated along with four slip directions in the $[100]$, where the Schmid factor of the twelve slip systems were greater than 0.4 (see Table 4.4). For the $[111]$ orientation, with respect to tensile direction, fifteen slip systems with non-zero Schmid factors could be activated along with three slip directions, as provided in Table 4.4. However, for the $[110]$, ten slip systems with non-zero Schmid factors could be activated along with two slip directions. For this oriented sample, four $\{100\}\langle 111\rangle$ slip systems with a Schmid factor greater than 0.4 are symmetrical with respect to the tensile directions. Similarly, the two slip systems with a Schmid factor greater than 0.4 in the $\{112\}\langle 111\rangle$ are symmetrical with respect to the tensile direction. The equal and simultaneous contribution of symmetrical slip systems leads to a relatively small orientation change in a single crystal Fe (Franciosi et al., 2015). For illustration, consider the slip activity in $a_1a_2b_3b_4$ plane along with a_1b_3 direction and $b_1b_2a_3a_4$ plane along with b_1a_3 direction in Figure 4.28. The two systems are symmetrical with respect to loading direction (black dashed-line, y axis).

Although, the orientation dispersion was relatively small for the orientation close to $[110]$ for the bcc single crystal Fe, as shown in Figure 4.27 (c), the orientation dispersed more notably in the $\{110\}$ group in the current study (see Figure 4.11). This is expected to be due to the different boundary conditions and constraints between the single crystal and the polycrystalline materials.

In a single crystal, the stress tensor remains relatively constant throughout the sample when the sample is subject to a tensile loading. In the polycrystalline materials, even though a unidirectional load is applied to the sample, the local stress tensor is not uniaxial and constant throughout each grain, particularly at the grain boundaries. This is a result of the neighboring grains in the polycrystalline material in contrast to the single crystal, which does not have any neighboring grains and the geometry change.

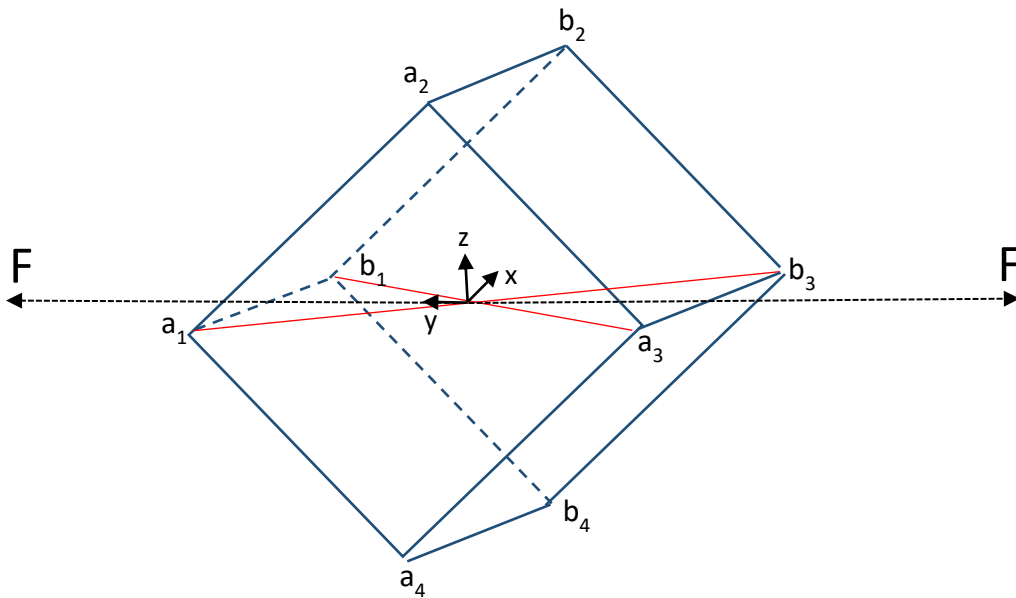


Figure 4.28 Slip can only occur in a_1b_3 and b_1a_3 directions in the $\{110\}\langle 111 \rangle$ slip system with respect to tensile loading, y axis. The other two slip directions are perpendicular to the y axis (a_2b_4 and b_2a_4 directions). For each possible slip plane, there is a symmetrical slip plane with respect to the loading direction, e.g., $a_1a_2b_3b_4$ and $b_1b_2a_3a_4$ planes are symmetrical with respect to y axis. Hence, the orientation change will be relatively small in the single crystal because the symmetrical systems activity equally contributes to accommodate plastic deformation.

Table 4-2 The number of possible slip directions (S.D) and the Schmid factors of the {110}<111> and {112}<111> slip systems (presented by S.S1 and S.S2, respectively) for the {100}, {111}, {110} orientation with respect to the tensile direction for a bcc structure

	S.D	S.S	Schmid factor												
{100}	4	S.S1	0.41	0.41	0.41	0.41	0.41	0.41	0.41	0.41	0.41	0	0	0	0
		S.S2	0.47	0.47	0.47	0.47	0.24	0.24	0.24	0.24	0.24	0.24	0.24	0.24	0.24
{111}	3	S.S1	0.27	0.27	0.27	0.27	0.27	0.27	0	0	0	0	0	0	0
		S.S2	0.31	0.31	0.31	0.16	0.16	0.16	0.16	0.16	0.16	0	0	0	0
{110}	2	S.S1	0.41	0.41	0.41	0.41	0	0	0	0	0	0	0	0	0
		S.S2	0.47	0.47	0.24	0.24	0.24	0.24	0	0	0	0	0	0	0

This implies that the RSS was not uniform throughout the grains for the polycrystalline β Ti alloys studied in this work. Consequently, the Schmid factor varied throughout the grains, which was unlike that for the single crystal, where the Schmid factor was relatively constant throughout the gage section. This can help explain the higher orientation dispersion level that occurred in the {110} oriented (with respect to tensile direction) grains in the polycrystalline materials.

In summary, as provided in Table 4.4, the {100}, {111}, and {110} orientations, with respect to tensile direction, have 4, 3, and 2 slip directions, and 20, 15, and 10 possible slip systems, respectively. In addition, the stress tensor varied within the grains and particularly at the grain boundaries. Consequently, the probability of activation a higher number of different slip systems was the highest for the {100} group and the lowest for the {110} group.

4.4.4 Grain size

The grain size has been known to have a significant influence on the mechanical properties of the polycrystalline materials. The empirical Hall-Petch relationship has been used to estimate the YS of a wide range of polycrystalline materials based on average grain size (Hall, 1951). The Hall-Petch strengthening (or grain boundary strengthening) is attributed to the dislocation mean free

path, where the grain boundaries impede the dislocations motion. The lattice is more distorted at the grain boundary, which hinders the dislocation motion across the grain boundaries. This results in grains with different sizes experiencing different levels of deformation, which leads to strain heterogeneity in the polycrystalline materials (Berbenni et al., 2007; Lavergne et al., 2013; Nicaise et al., 2011). Berbenni et al. reported that the YS depends not only on the average grain size but also on the of grain size distribution, especially when the average grain size is in order of micrometers (Berbenni et al., 2007). Based on numerical analysis, they stated that the higher dispersion in the grain size resulted in a decreased YS due to an increase in the plastic heterogeneity, e.g. when $\frac{\Delta D}{D} = 1$ (ΔD : the range of grain size, D : the average grain size) plastic deformation occurred in all the grains, whereas, when $\frac{\Delta D}{D} = 5$, a portion of the grains remained elastic. In this work, the influence of the grains size on the misorientation deviation heterogeneity was investigated at the grain scale.

As shown in Figure 4.13, the $MD_{(\min)}$ was a non-zero constant value regardless of the grain sizes in the undeformed state (0% plastic strain), which might be due to the error in EBSD measurement and the misorientation on the as-received sheets . The $MD_{(\min)}$ value was greater for the larger grains compared with the smaller grains at each level of plastic strain. This was consistent with previous work, where larger grains exhibited higher misorientation dispersion for a steel alloy (Allain-Bonasso et al., 2012). This might be explained by the fact that the equivalent grain size was between 0.5 and 2 times D_{avg} for each alloy, see Figure 4.12. Hence, the larger grains are surrounded by a larger number of neighboring grains. To satisfy the displacement compatibility condition, each part of the boundary of a large grain should locally accommodate its deformation with neighboring grains in order to retain continuity during deformation. In addition, the grain

boundaries are considered as common sources of dislocations (Espinosa et al., 2005; Fu et al., 2001; Hirth, 1972). This implies that more GNDs are generated in a larger grain compared with smaller grains (due to the fact that they have larger circumference), which leads to a higher degree of orientation change.

The $MD_{(\min)}$ variation between the subpopulation of the small and large grains became more pronounced with an increase in plastic strain level. The larger grains experience more local stress state variation, which led to activation of multiple slip systems with different local rotation axes at different part of grains. With an increase in plastic strain, the slip activities become more pronounced, which led to more local lattice rotations. Hence, each local slip system has its own rotation axis, the larger grain exhibited greater level of orientation change due to a larger number of local rotation axes than the smaller grains.

An empirical equation was suggested to estimate the local misorientation as a function of the grain equivalent diameter and the global plastic stain. From Figure 4.13, it can be inferred that the empirical equation should have a constant term to capture the level of the misorientation at 0% plastic strain (term c in the equation 4.18). The second term should be proportional to the global plastic strain as the average misorientation of each group increased with the global plastic strain, regardless of the grain size (term $b\varepsilon_p$ in equation 4.18). At each level of the plastic strain, as shown in Figure 4.13, the misorientation is proportional to the grain diameter. Thus, the third term should be a function of both strain and the grain size, i.e. the third term should be in the form of the $a\varepsilon_p \frac{D}{D_{Avg}}$. Combining these three terms leads to the following equation, which estimates the misorientation at the grain scale as a function of the global plastic strain and grain equivalent diameter:

$$MD_{L(min),grain} = a\varepsilon_p \frac{D}{D_{Avg}} + b\varepsilon_p + c \quad (4.18)$$

Where the $MD_{L(min),grain}$ is the estimated misorientation of an arbitrary grain, D is the equivalent diameter of that grain, D_{Avg} is the average grain diameter of the material, ε_p is the global plastic strain in percent. The least square estimator was acquired on the experimental data to determine the constants a , b , and c , which are provided in Table 4.2 for each alloy. In the following description, the nature and influence of each constant is explained:

- **Constant (a):** The first term indicates the influence of the relative grain size at a given plastic strain, where the other two terms are constant. In other words, this term determines the local variation of the misorientation between the individual grain at a given plastic strain. Hence, this term indicates the misorientation heterogeneity at the microscale.
- **Constant (b):** This term suggests that all the grains experience a relatively uniform level of misorientation deviation, which depends on the global plastic strain, regardless of the grain size.
- **Constant (c):** If the orientation of all the points within each grain are the same, the constant c becomes zero. However, c was determined to be about 0.4 for both alloys.

The $MD_{(min),Theory}$ (estimated by equation (4.15) versus the $MD_{(min),Experiment}$ (obtained by experimental data) is plotted in Figure 4.29 for the grouped data (~6000 grains). The ideal correlation between the theoretical and the experimental $MD_{(min)}$ is shown in the black-dashed line. As can be seen in Figure 4.12, the slope of the linear regression was nearly identical to the ideal slope for TCFA. The R^2 was 10% less for TIEMTAL-21S, which was explained previously in section 4.3.2. It is noted that the other parameters, such as crystallographic grain orientation and neighboring grains were not considered in equation 4.15. This suggests that the grain size

plays a substantial role in the local misorientation distribution compared to other factors at the microscale for these two alloys.

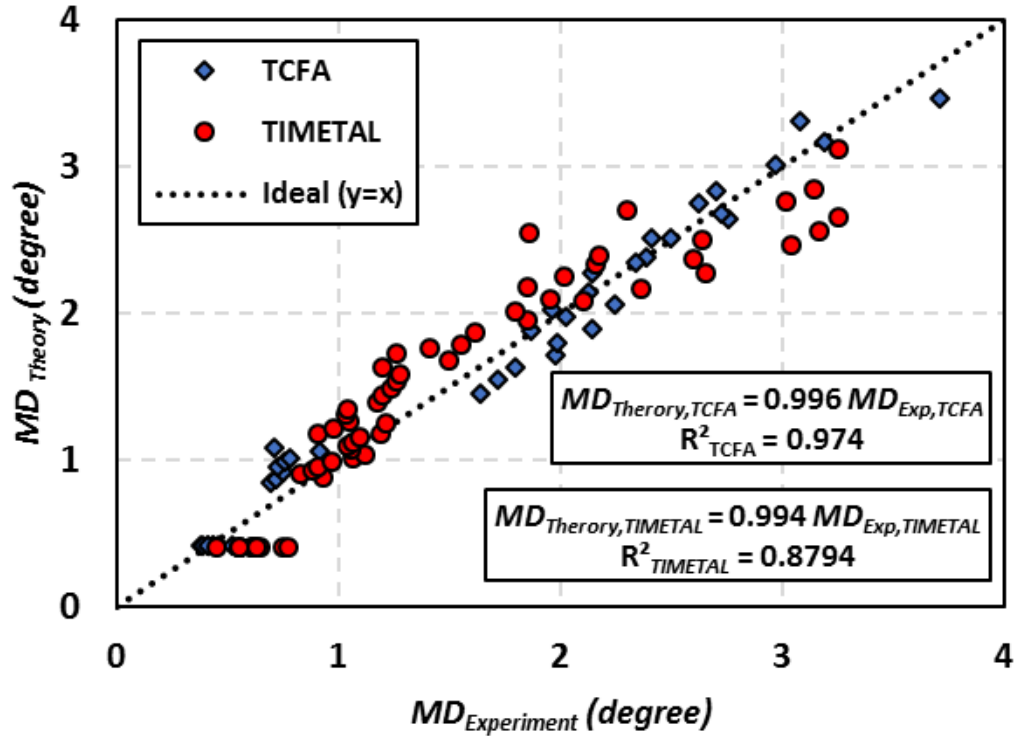


Figure 4.29 Theoretical MD values (obtained using equation [4.15]) versus the experimental MD values for TCFA (in blue) and TIMETAL-21S (in red). Almost 3000 grains were analyzed for each alloy.

Table 4-3 The constant values determined from equation (4.15) for each alloy. The least square estimator was acquired on the experimental data to obtain the constants and R^2 .

Alloy	a	b	c	R^2
TCFA	0.065	0.12	0.42	0.97
TIMETAL-21S	0.056	0.12	0.41	0.88

4.4.5 Distance from grain boundary

Many studies have been targeted to gain a better understanding of the deformation behavior of the polycrystalline materials at the grain boundaries (Bieler et al., 2009; Cahn et al., 2006; Swygenhoven, 2002; Telang et al., 2004; Wang et al., 2010; Zaefferer et al., 2003). The orientation gradient is expected to be greater at the grain boundaries than inside the grains due to higher GND densities. For quantifying the level of misorientation, the KAM approach has been frequently used (Calcagnotto et al., 2010; Mohtadi-Bonab et al., 2015; Mishra et al., 2009; Rollett et al., 2012). However, as mentioned previously, the KAM approach is sensitive to step size (Subedi et al., 2015). In this work, the misorientation deviation has been used to quantify the orientation dispersion at the grain boundaries. As shown in Figure 4.14, the MD_{Min} values of most of the grain boundaries were higher than the average MD_{Min} values as expected. At some grain boundaries, the local MD_{Min} values were even more than 3 times the average MD_{Min} values. This implies that the misorientation was more than 10° between the RO and some of the local areas at the grain boundaries at ~12% plastic strain for the TCFA. The MD_{Min} was plotted as a function of distance from the grain boundaries in Figure 4.15. The average MD_{Min} values of two outer layers of data points were higher than the average MD_{Min} . Two points should be noted here for interpreting the MD_{Min} values at the grain boundary vicinity. First, the MD_{Min} value vs distance from the grain boundary curve exhibited a relatively linear trend, while the KAM usually exhibited a relatively high misorientation gradient close to the grain boundaries and a relatively small values within the grains (Subedi et al., 2015). This contrast is due to the fact that in the MD_{Min} approach, the misorientation value for each point is measured by comparing with a unique reference orientation for each grain, while in the KAM approach, the misorientation of each point is determined by averaging the misorientation between selected point and its neighboring points. Second, both the

MD_{Min} and the KAM approaches were built based on the deformed state data, i.e., none of them represents the undeformed state of the materials.

4.4.6 Interrupted vs Monotonic tensile test

The interrupted test MD_{Min} values showed ~30% increase compared with the monotonic tests at ~11% plastic strain (see Figure 4.16). The stress-displacement curves of interrupted tensile tests indicated that stress relaxation (in order of ~ 50 MPa) occurred during each pause (Figure 4.30). This suggests that the atoms and defects rearranged in order to reduce the internal strain energy after each pause. After reloading, the upper yield point was ~ 40 MPa and ~20 MPa greater than the lower yield point for the TCFA and TIMETAL-21S, respectively [see Figure 4.30 (b) and (d)]. This behavior suggests that some of the interstitial atoms diffused toward the stationary dislocation cores after each pause to release the local stress fields and formed new Cottrell atmospheres. Therefore, a number of dislocations were pinned by the interstitial atoms at this step. After reloading, the pinned dislocations acquired extra force to be activated, compared to the force required to keep moving the dislocations before the pause (this could be inferred from the occurrence of upper yield point during reloading).

The rearrangement of the dislocations (due to the relaxation), pinned dislocations (due to the Cottrell atmospheres) might affect the local stress states at different region of the grains. Therefore, it was likely that new slip systems were activated locally at different regions of the grains after reloading, especially at the boundaries. This implies that the orientation dispersion became more pronounced within each grain, which resulted a higher MD_{Min} value of the interrupted test compared to the monotonic test. This hypothesis needs to be verified throughout a simulation study or an in-situ TEM tensile test.

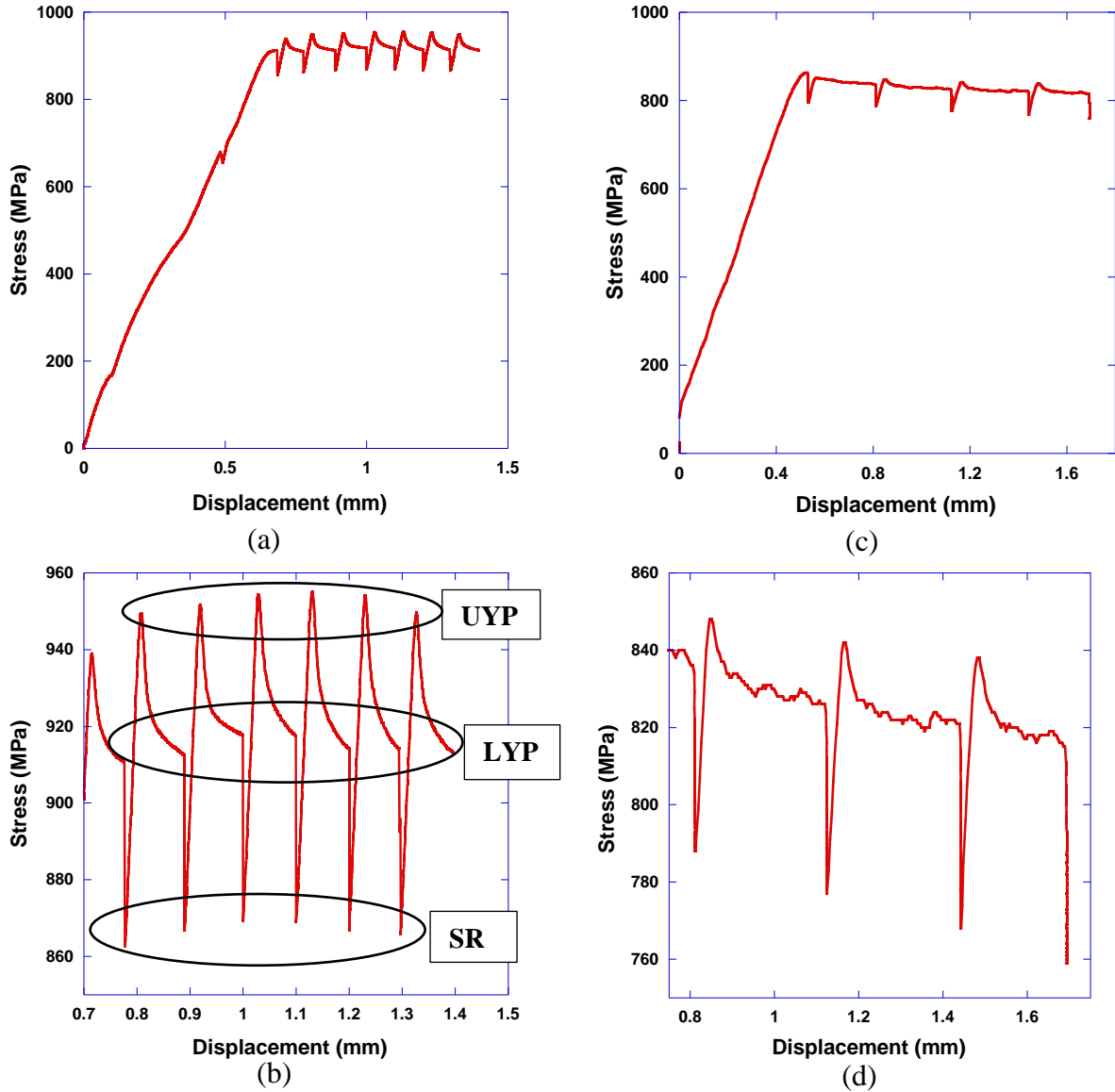


Figure 4.30 (a) Stress-displacement curve of TCFA interrupted test and (b) the upper yield point (UYP), lower yield point (LYP), and stress relaxation (SR) for TCFA sample. (c) Stress-displacement curve of TIMETAL-21S interrupted test and (d) the UYP and LYP and SR for TIMETAL-21S sample

4.4.7 DIC

The heterogenous strain distribution at the microscale was only possible when the area of interest was properly prepared before the loading. Otherwise, it was not feasible to measure the local strain distribution. A correlation between plastic strain and a measurable microstructural parameter is beneficial for failure analysis of a component. In this work, the EBSD misorientation

maps were qualitatively compared with the strain field map obtained from a DIC-SEM tensile experiment.

As observed in Figure 4.21, a strain concentration occurred close to most of the grain boundaries. In some grain boundaries, the local strain was more than three times the global strain (see the black regions in Figure 4.21). In Figure 4.31, the $MD_{Avg,After}$ and $MD_{Avg,Before}$ maps are qualitatively compared with the strain field map obtained from the DIC-SEM experiment. The $MD_{Avg,Before}$ map presents the misorientation distribution, where the reference orientation was obtained by averaging the orientation of all the points within the grain before the tensile loading, and similarly, the $MD_{Avg,After}$ map presents the misorientation distribution, where the reference orientation was obtained by averaging the orientation of all the points within the grain after the tensile loading. Most of the grains (green stars) showed a better correlation between the DIC-SEM map and the $MD_{Avg,Before}$ map. The grains, highlighted with black circles, exhibited a better correlation between the DIC-SEM map the $MD_{Avg,After}$ map. A number of the grains (blue rhombuses) exhibited a relatively similar misorientation distribution in both maps. However, a poor correlation between strain map and MD misorientation maps was observed in a fraction of the grains (black triangles).

The DIC-SEM field strain map and the 3rd nearest neighbor KAM map are presented in Figure 4.32. The green spots are the areas, where the CI was less than 0.1. The KAM_{Avg} was 1.4°. There was a good agreement between the KAM map and the DIC-SEM map hot spots, specifically at the grain boundaries. The KAM values were relatively high at the grain boundaries, which was consistent

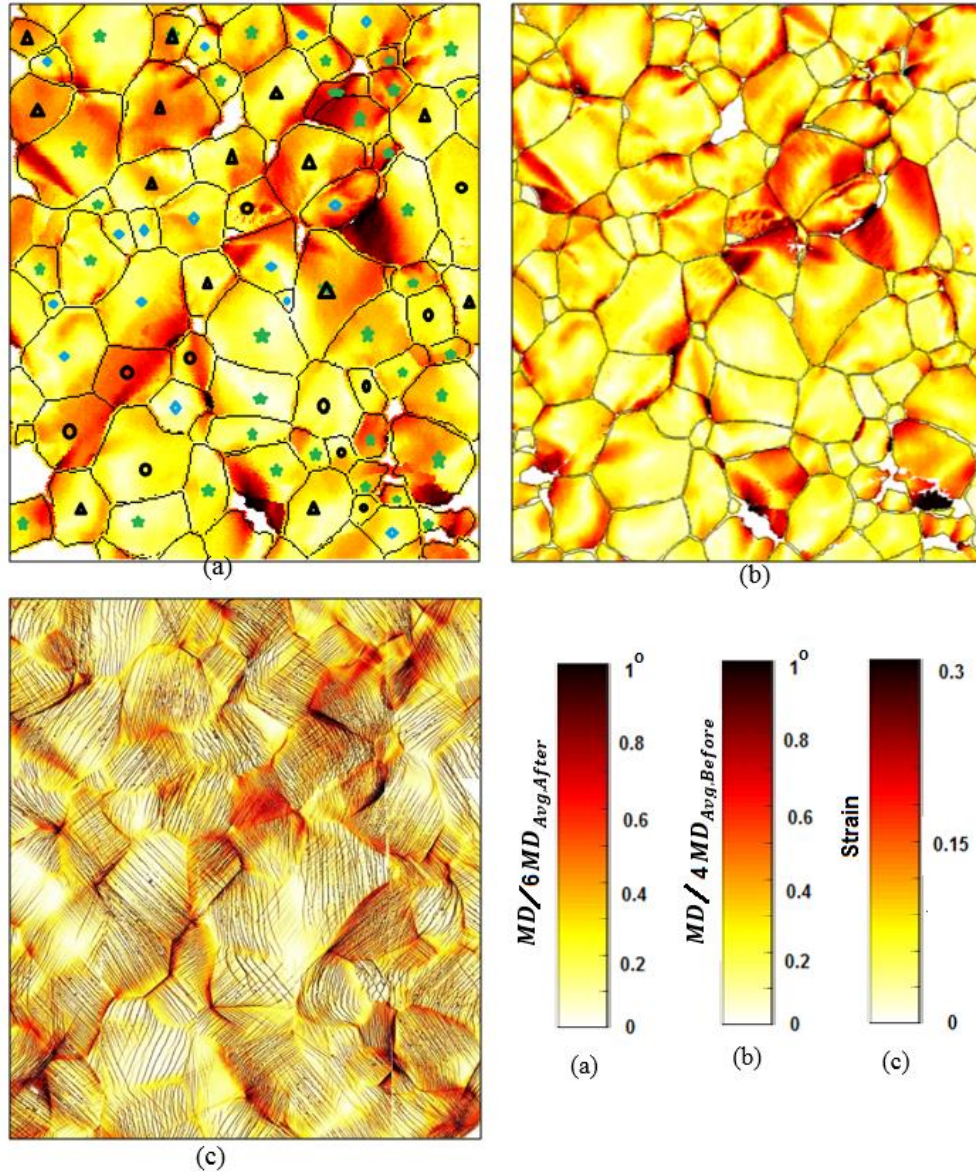


Figure 4.31 The misorientation distribution maps for the (a) $MD_{Avg,Before}$, (b) the $MD_{Avg,After}$, and (c) the strain field map at 0.11 strain. Some grains (green stars) showed better correlation in the $MD_{Avg,Before}$ map (the RO was the average orientation before the deformation), while some other grains (black circles) exhibited better correlation in $MD_{Avg,After}$ map (the RO was the average orientation after the deformation was considered), (comparing with strain field map). The grains, with blue rhombuses inside, exhibited similar misorientation distribution in both maps. However, poor correlation was observed in other grains (black triangles).

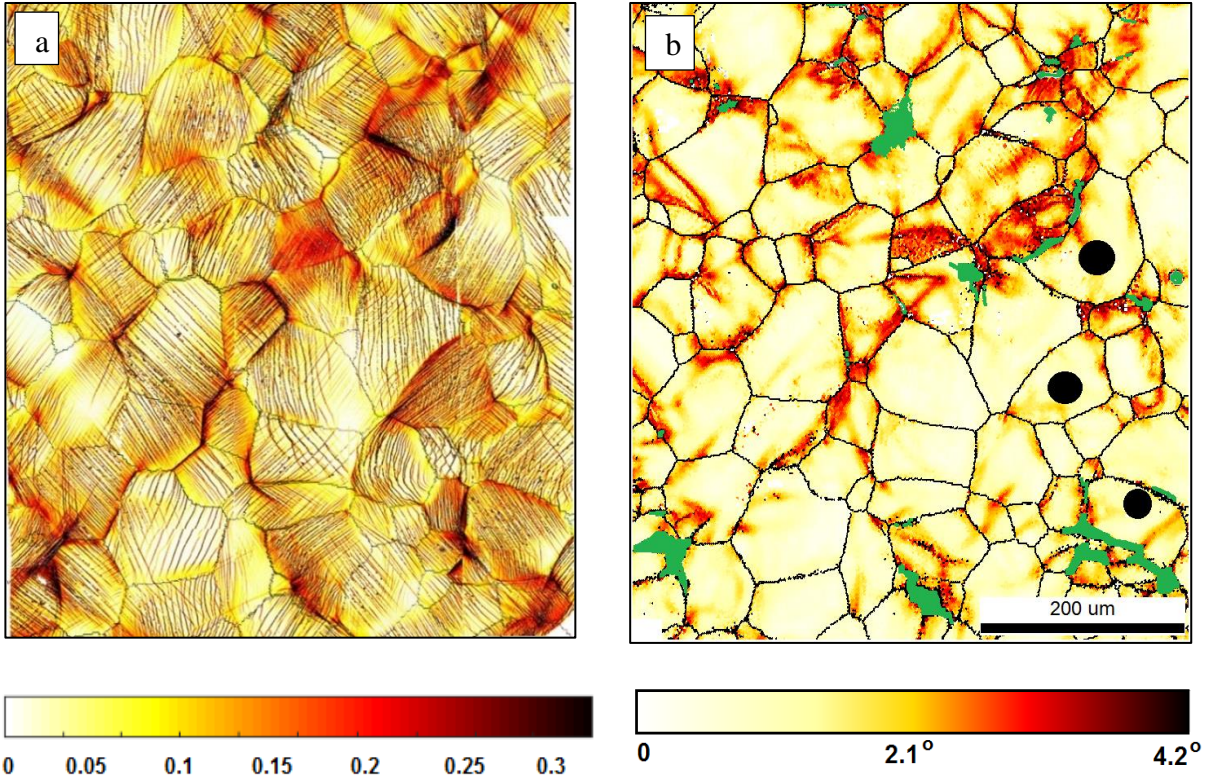


Figure 4.32 (a) The DIC-SEM strain field map at 0.11 strain and (b) the 3rd nearest KAM map from similar area at 0.11 strain. The $KAM_{Avg.}$ was 1.4° . The corresponding hot spots at the grain boundaries in the DIC-SEM strain map exhibited higher values in the KAM map for most of the grains. There was not good correlation between hot spots in two maps for the grains that are highlighted with black circles. The areas, where the CI was less than 0.1, were colored in green.

with the previous work, where the KAM was higher at the grain boundaries compared with the KAM within the grains (Mishra et al., 2009; Rollett et al., 2012; Subedi et al., 2015).

As shown in Figure 4.27, there was a good agreement between the hot spots of the KAM map and the DIC-SEM strain map for a large fraction of the studied grains. However, the DIC-SEM strain map exhibited higher value at some grain boundaries, where the corresponding KAM values did not exhibit any hot spots (see the grains, which are highlighted in black circles in Figure 4.32).

Although the MD approach was independent of the RO metric and step size, which made it a useful tool to estimate the global plastic strain at the macroscale (here in order of mm), the MD did not provide promising results in capturing the localized strain at the sub-grain scale. In the MD approach, the microstructure changes within the grain (here the misorientation) are quantified with respect to one reference point (here the RO). Consequently, the MD values are relatively small close to the RO, e.g., see the MD values in Figure 4.2 (b) where all the points close to the RO (red star) exhibited a low value. Furthermore, the high MD values at one region do not necessarily imply that the rate of microstructure change (i.e. misorientation) is high in that region. The relatively high and low MD values occurred at the regions highlighted by the red and blue ovals, respectively, in Figure 4.2(b). The variation between the RO (here is shown with a red star) and each individual point in the red oval is high and, similarly, the variation between the RO and each individual point in the blue oval is low. The local variation between each individual point and its neighbor points in the blue oval might be higher or lower than the local variation between each individual point and its neighboring points in the red oval. The DIC strain is calculated by measuring the local relative position change between each point and its neighboring points during the loading (Kammers and Daly, 2013a). Similar to the DIC-SEM approach, in the KAM method, the assigned value (here the orientation change) of each point is measured by averaging the misorientation between each point and its neighboring points. Hence, the local distribution trend of the KAM approach is in better agreement with the DIC-SEM approach than the MD approach. Hence, although the average KAM for a microstructure patch is sensitive to step size (the main reason that it is not a very useful approach to estimate the global plastic strain), the KAM map exhibited a better correlation with the DIC-SEM map at the sub-grain scale (see Figure 4.32). While interpreting the KAM maps, one should consider the followings:

- The KAM approach is sensitive to the step size. For example, consider the 1st nearest KAM distribution in the vicinity of a grain boundary in a polycrystalline microstructure patch in two scenarios. If the spatial distance during data acquisition is very small, for example, on the order of few nanometers, the orientation change between neighboring points is very small, which results in a very small KAM values, even though the material is subjected to a relatively high plastic strain. This concern becomes more evident by considering the error of the data acquisition system, i.e. if the local change in orientation is less than the accuracy of the measurement system, the results are not repeatable. Hence, the KAM distribution depends on the spatial distance of the data acquisition.
- The hot spots in the KAM map [see Figure 4.32 (b)] represented the areas where strain concentration occurred (compare Figure 4.32 (b) with Figure 4.27 (a) hot spots). Although the stress concentration was observed in some grain boundaries, the corresponding areas in the KAM map did not exhibit hot spots [compare the grains, which are highlighted in black circles in Figure 4.32(b), with the corresponding grains in Figure 4.32(a)]. In these regions, at least two slip systems were activated simultaneously to accommodate the local plastic strains, while their net Burgers vectors were relatively small. This inconsistency occurred in less than 10% of the studied grain population.

4.5 Summary and Conclusion

It is essential to know the level of the plastic strain to estimate the remaining life of a metallic component. However, it is a challenging task to measure the plastic strain for a part under its operating condition. In this chapter, the level of plastic strain has been estimated by quantifying the misorientation of the deformed microstructure, i.e., no information from undeformed state was used, for two bcc Ti alloys. The statistically analyzed data showed that the {100} and {110} groups (with respect to tensile direction) exhibited the largest and smallest tendency for the orientation change. This might be due to the fact that the grains near {100} and {110} orientations have the highest and lowest number of possible slip systems and slip directions, respectively. The subpopulation of large grains exhibited a greater misorientation level than the small grains, where the difference became more pronounced with increased strain. This implies that the level of misorientation heterogeneity became more substantial at higher level of plastic strain. This could be explained by the fact that the large grains are surrounded by a greater number of the grains. This leads to a variation in the local stress states throughout the grain, which results in different local slip activities. An empirical equation was proposed to estimate the misorientation level at the grain scale as a function of global plastic strain and the local grain diameter at the microscale. It was found that the misorientation level was higher for the interrupted tests than for the monotonic test. The rearrangement of dislocations (due to the relaxation), pinned dislocations (due to the Cottrell atmospheres), and permanent change in the orientation and geometry at submicron scale may affect the local stress states at different regions of the grains. These factors may result in activation of new slip systems with different rotational axis, which lead to a higher misorientation dispersion for the interrupted tests. A qualitative comparison between the DIC-SEM strain field map and the misorientation maps revealed that there is a better correlation between the hot spots

in the KAM map and the DIC-SEM strain field map compared with the correlation between the hot spots in the MD maps and the DIC-SEM strain field map. Although stress concentrations may occur in some areas and this may not be pointed out in the corresponding areas in the KAM map. In these regions, at least two slip systems should be activated simultaneously to accommodate the local plastic strains, while their net Burgers vectors could be relatively small. In the current study, this inconsistency occurred in less than 10% of the studied grains.

CHAPTER 5

5 DEFORMATION BEHAVIOR OF BCC TI ALLOYS

In this chapter, the deformation behavior of TCFA and TIMETAL-21S was investigated at RT, 200 °C and 300 °C. In addition, the effect of oxygen content on the deformation behavior of TNTZ-xO (where x was 0.1, 0.3 and 0.7 wt.%) was studied. The slip trace analysis used for this work is explained. The microstructure and texture of each of the alloys is also provided. The results revealed that slip was the dominant plastic deformation mode for TCFA, TIMETAL-21S, and TNTZ-0.3O and TNTZ-0.7O, while mechanical twinning was the dominant deformation mode for TNTZ-0.1O. Some content of this chapters was published in: (Dastidar et al., 2015; Khademi et al., 2016; Liu et al., 2017b). Therefore, some content in Chapter 5 is similar to these published papers.

5.1 Slip trace analysis procedure

A slip trace analysis was used to identify the active slip deformation systems. The slip trace analysis focused only on the bcc microstructure as the β phase was dominant for all the studied alloys. The EBSD data provided the crystallographic orientation of each grain with reference to the sample coordinate system, in the form of three Euler angles ($\varphi_1, \Phi, \varphi_2$). The orientation matrix (g) between the crystal coordinate system and the sample coordinate system was calculated by

$$g = \begin{bmatrix} \cos(\varphi_2) & \sin(\varphi_2) & 0 \\ -\sin(\varphi_2) & \cos(\varphi_2) & 0 \\ 0 & 0 & 1 \end{bmatrix} \begin{bmatrix} 1 & 1 & 0 \\ 0 & \cos(\Phi) & \sin(\Phi) \\ 0 & -\sin(\Phi) & \cos(\Phi) \end{bmatrix} \begin{bmatrix} \cos(\varphi_1) & \sin(\varphi_1) & 0 \\ -\sin(\varphi_1) & \cos(\varphi_1) & 0 \\ 0 & 0 & 1 \end{bmatrix} \quad (5.1)$$

For a given observed slip trace, the slip plane and the slip direction can be expressed as (h k l) [u v w] in the crystal coordinate system using Miller indices. The transformation of the slip plane and the slip direction from the crystal coordinate system to the sample coordinate system can be achieved using the rotation matrix (transpose of the orientation matrix) in equations (5.2) and (5.3).

$$n = g^T \cdot \begin{bmatrix} h \\ k \\ l \end{bmatrix} \quad (5.2)$$

$$b = g^T \cdot \begin{bmatrix} u \\ v \\ w \end{bmatrix} \quad (5.3)$$

where n and b are the corresponding slip plane normal and slip direction, respectively, of a given slip system in the sample coordinate system. The superscript “T” stands for the transpose of the matrix. The slip plane trace was then calculated by the cross product of the slip plane normal (n), expressed in the sample coordinate, and the sample normal direction ([001]). A MATLAB code was used to calculate all the possible plane traces of the deformation systems for a given grain orientation. Identification of the experimentally-observed deformation systems in a given grain was accomplished by comparing the calculated plane traces with the slip plane traces observed in the SE SEM photomicrographs.

The global Schmid factor (m) of each slip system in an individual grain is estimated by resolving an assumed uniaxial stress σ in the slip direction (Burgers vector direction b) on the slip plane (with normal n) (all expressed in the crystal coordinate system) by

$$m = n \cdot \sigma \cdot b^T \quad (5.4)$$

For illustration, the slip trace analysis procedure is explained here with an example. Average Euler angles (ϕ_1 , Φ , ϕ_2) were measured by EBSD. All possible slip systems were calculated for each grain utilizing a MATLAB code. The uniaxial tensile global stress state was applied by determining the Schmid factor and slip system (out of the all possible slip systems for a bcc material). Three families, with a total of 48 slip systems, were considered in this analysis. Family (1), Family (2), and Family (3) represent $\{110\}\langle 111\rangle$, $\{112\}\langle 111\rangle$, and $\{123\}\langle 111\rangle$, respectively. In bcc materials, slip occurs in the close packed direction, $\langle 111\rangle$, regardless of the slip plane.

The slip trace analysis procedure used in this work is now explained and an example is provided for illustration. The black solid line shows the active slip trace from the SEM micrograph for the grain highlighted in Figure 5.1(a). Figure 5.1 (b) displays an EBSD IPF map and Figure 5.1(c) portrays all the possible slip systems represented for the grain highlighted in Figure 5.1 (a), which had a Euler angles of [154.6, 12.2, 201.6]. The black dashed lines show a tolerance angle of 4 degrees for the slip trace in Figure 5.1 (c). The active slip system was chosen among all the calculated possible slip systems that are located between the two dashed black lines. For this grain, system 29 and 32 are located between the two tolerance (black dashed) lines. Their Schmid factors are 0.43 and 0.48, respectively. The system that had the maximum Schmid factor, system 32, $(13\bar{2})[\bar{1}11]$, was considered to be the active slip system for this grain.

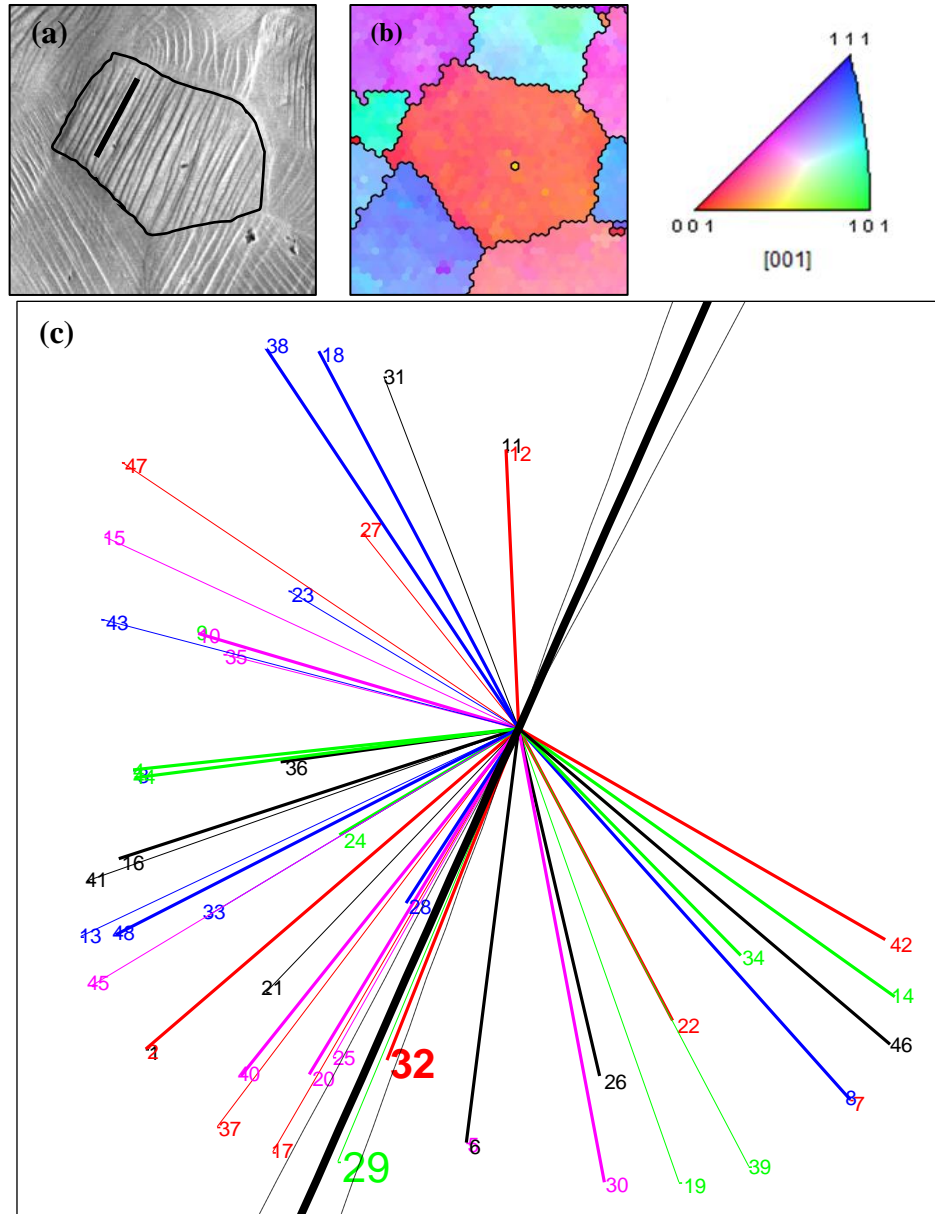


Figure 5.1 Example of the slip trace analysis provided for a RT test of a TCFA tensile deformed to ~8% strain. (a) The slip trace was indicated by the solid line on the SE SEM micrograph in the highlighted grain. (b) Corresponding EBSD IPF map. (c) All possible trace lines, which were calculated by a MATLAB code, are shown. A black solid line was drawn parallel to the observed slip trace in (a). The 2 black dashed lines were drawn with a tolerance angle of 4 degrees from the black solid line. The system 32 with Schmid factor of 0.48 was chosen as the active slip system because it exhibited the highest Schmid factor and was located between the two dashed lines (Khademi et al., 2016).

5.2 Deformation behavior of TCFA

5.2.1 Microstructure and texture

The average grain diameter was approximately 50 μm . Figure 5.2 presents the SE SEM photomicrographs of the microstructure of the as-received TCFA. Figure 5.3 exhibits the grain size distribution of the as-received TCFA microstructure.

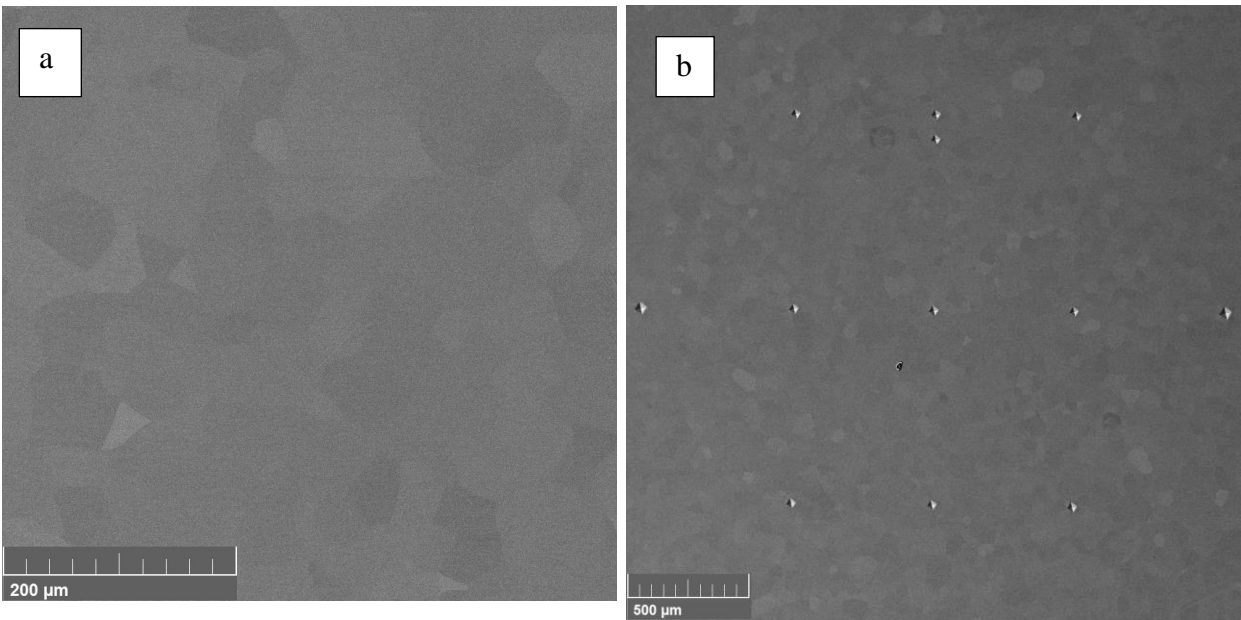


Figure 5.2 SE SEM photomicrographs of the microstructure of an as-received TCFA: (a) high magnification and (b) low magnification.

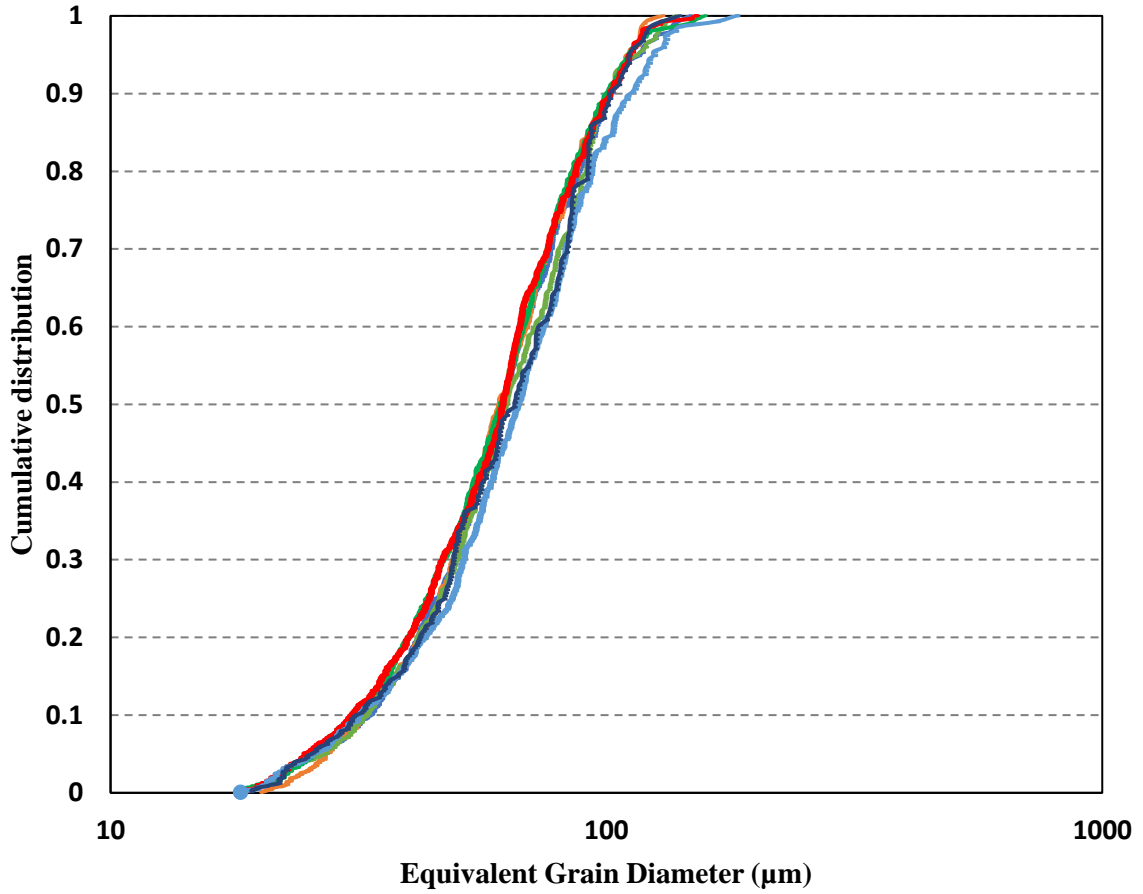


Figure 5.3 The cumulative distribution of the equivalent grain diameter for seven different microstructure patches for the as-received TCFA.

A representative EBSD IPF map and texture plots in the form of $\{100\}$ and $\{110\}$ pole figure in the normal direction are illustrated in Figure 5.4. The pole figures suggest that the alloy was not strongly textured

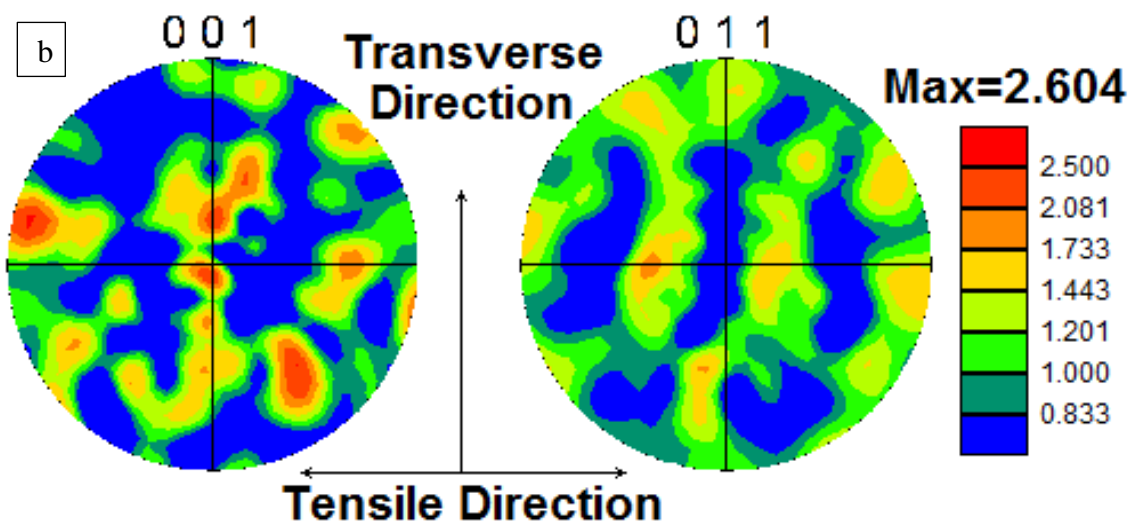
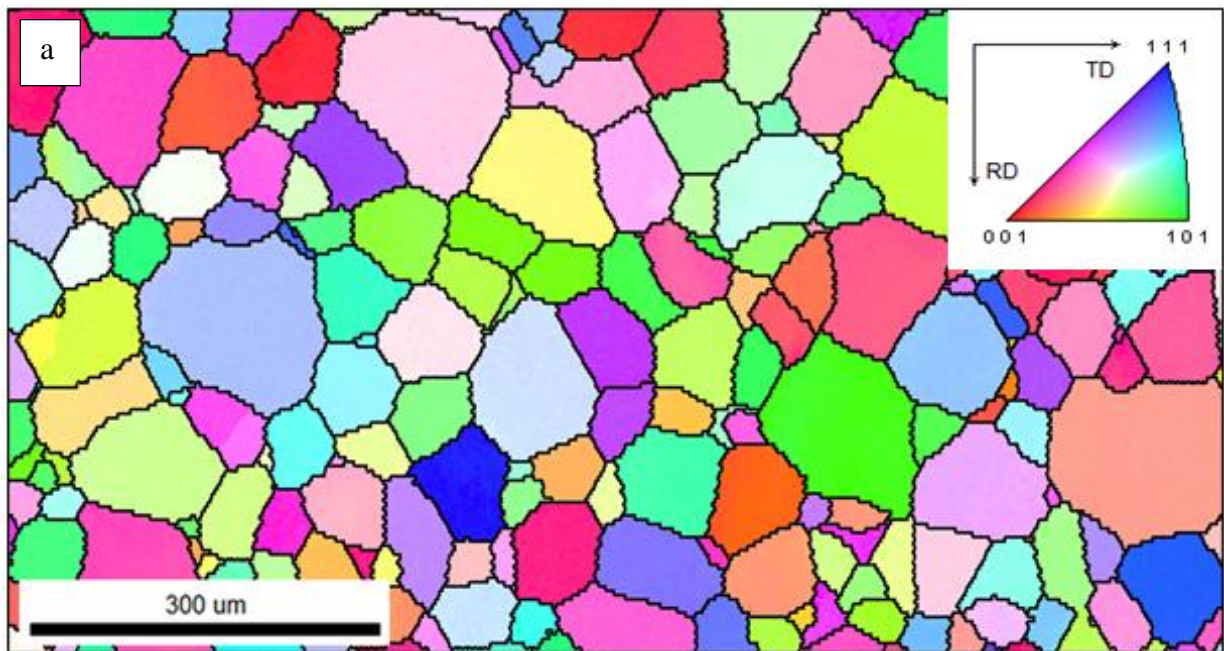


Figure 5.4 EBSD data of an undeformed TCFA tensile-tested specimen: (a) EBSD IPF map in the tensile direction and (b) The representative texture of the TCFA microstructure in the form of $\{100\}$ and $\{110\}$ pole figures in the normal direction. The pole figures suggest that the alloy was not strongly textured.

5.2.2 In situ tensile test of TCFA

In situ tensile tests were performed at RT, 200 °C, 300 °C, 400 °C, 450 °C, and 475 °C. It was observed that a phase transformation occurred at a temperature higher than 300 °C. Therefore, in this section, the results of the tensile tests at RT, 200 °C, and 300 °C are discussed. Two tensile test experiments were conducted at RT, while one tensile test was performed for each of the following temperatures: 200 °C, and 300 °C. The EBSD data were acquired from a selected area in the middle of the gage section. Patterns were collected using a 20 kV electron beam and a working distance of ~20mm. The EBSD scans were performed on two areas, approximately 800 μm by 2000 μm , for each sample, using a step size of 4 μm . The engineering stress versus displacement curves for the RT, 200 °C, and 300 °C tensile tests are illustrated in Figure 5.5. None of the specimens were taken to failure. The UTS was ~950 MPa at RT. As expected, the UTS decreased from 820 MPa to 720 MPa with increasing test temperature from 200 °C to 300 °C, respectively (see Figure 5.5). The plastic region exhibited a plateau for the RT and 200 °C tests. This suggests that material was elastic, perfectly plastic. For the 300 °C experiment, the stress decreased after reaching 720 MPa due to necking. In the following sections, the sequential SE SEM photomicrographs of the selected areas and the slip trace analysis results are provided for each test temperature.

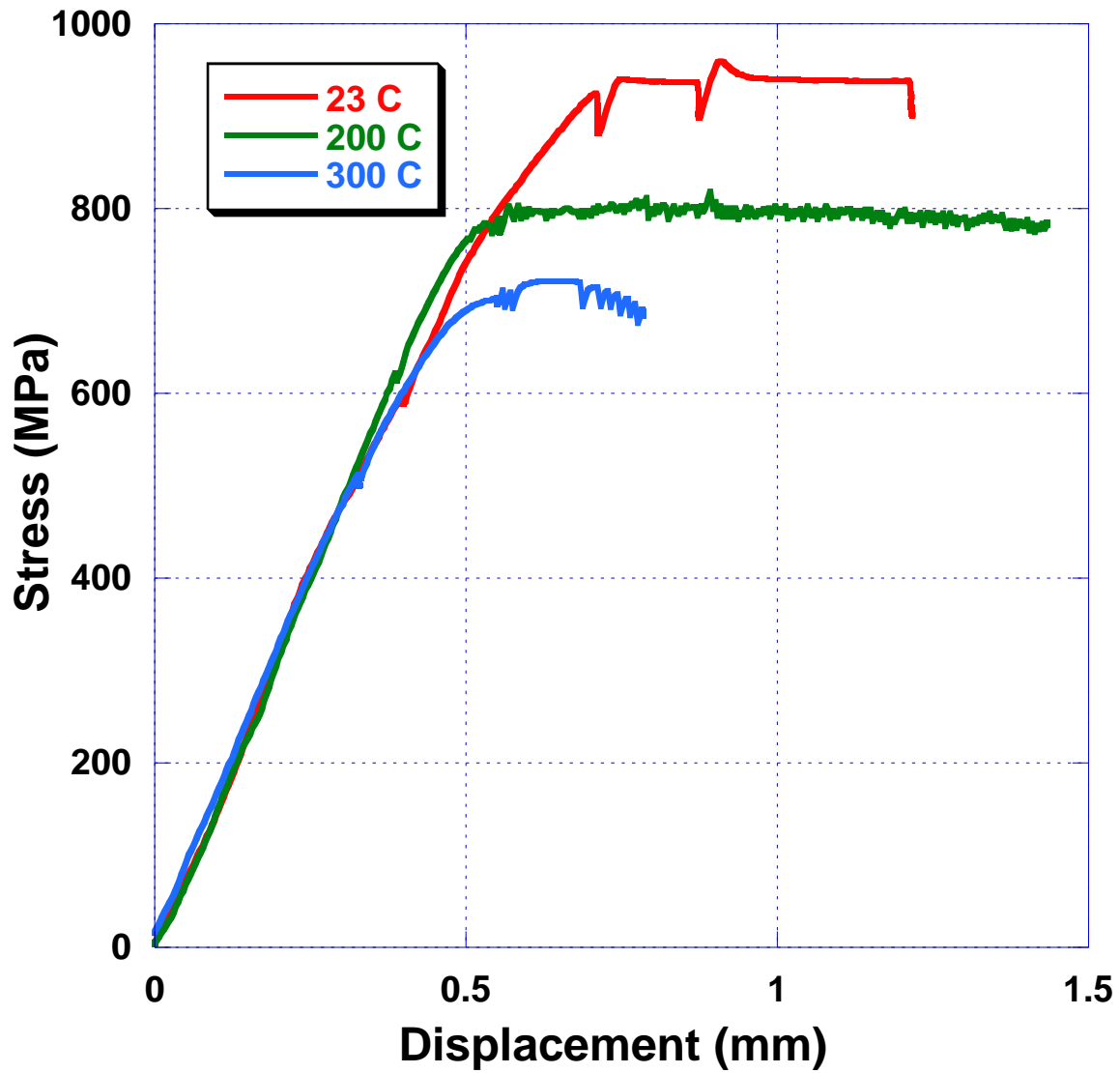


Figure 5.5 Engineering stress vs. displacement for TCFA samples tensile tested at RT, 200 °C, and 300 °C. The stress drops indicate that stress relaxation occurred when the tests were interrupted for SEM imaging. None of the tests were taken to failure.

5.2.3 RT tensile test of TCFA

Figure 5.6 exhibits a SE SEM photomicrograph of the gage section after 8.4% plastic strain. Uniform plastic strain was observed throughout the gage section. The UTS was ~940 MPa. A scratch mark, scribed at the center of the sample using a razor blade before the test, was used as a fiducial marker. The tensile axis was horizontal. The sequential SE SEM photomicrographs acquired during the test are presented in Figure 5.7 in combination with the corresponding EBSD IPF map from the same area.

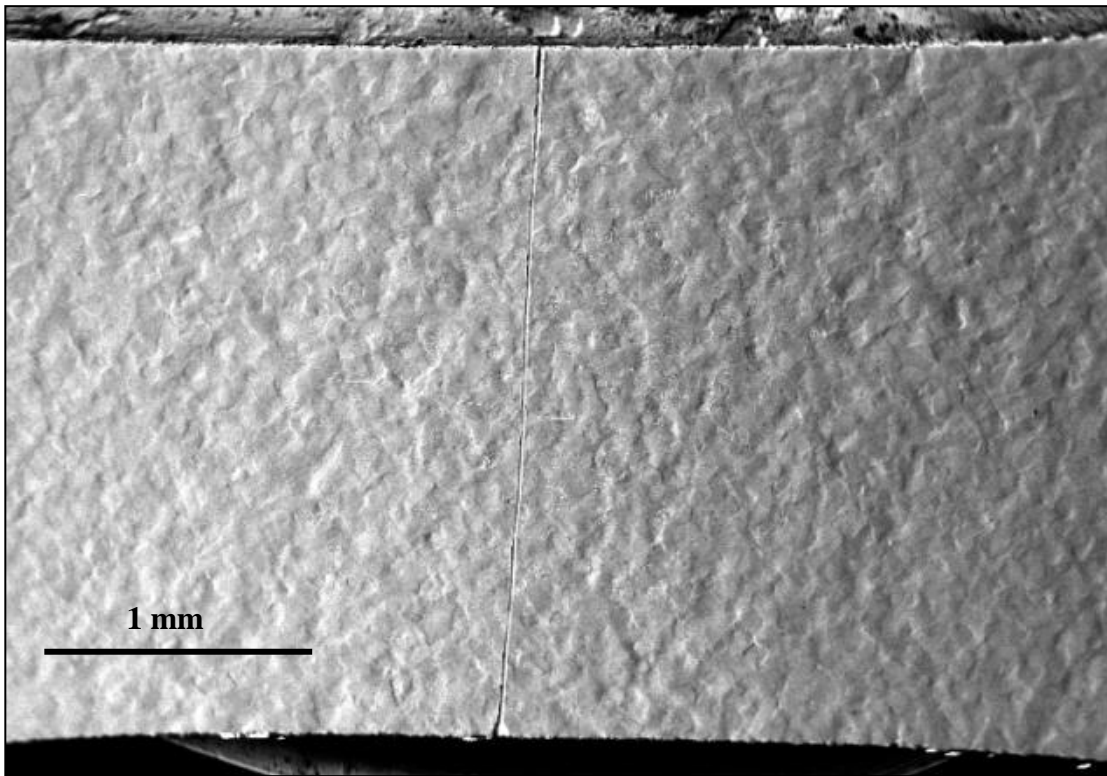


Figure 5.6 Low-magnification SE SEM photomicrograph of a RT deformed TCFA sample tested to 940 MPa and 8.4% strain. Uniform plastic strain was observed throughout the gage section. The center line, scribed on the sample using a razor blade before the test, was used as a fiducial marker. The tensile axis was horizontal.

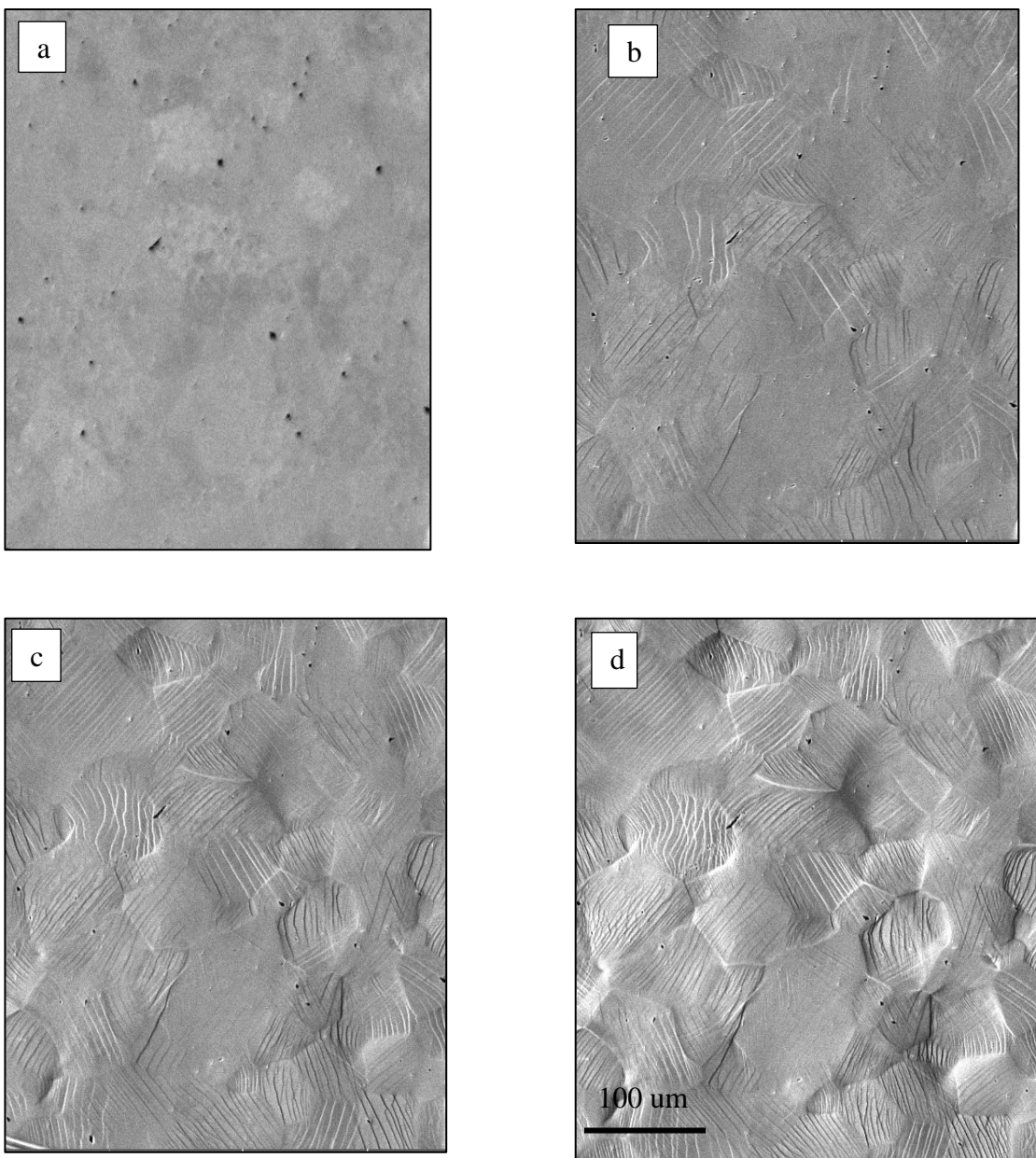
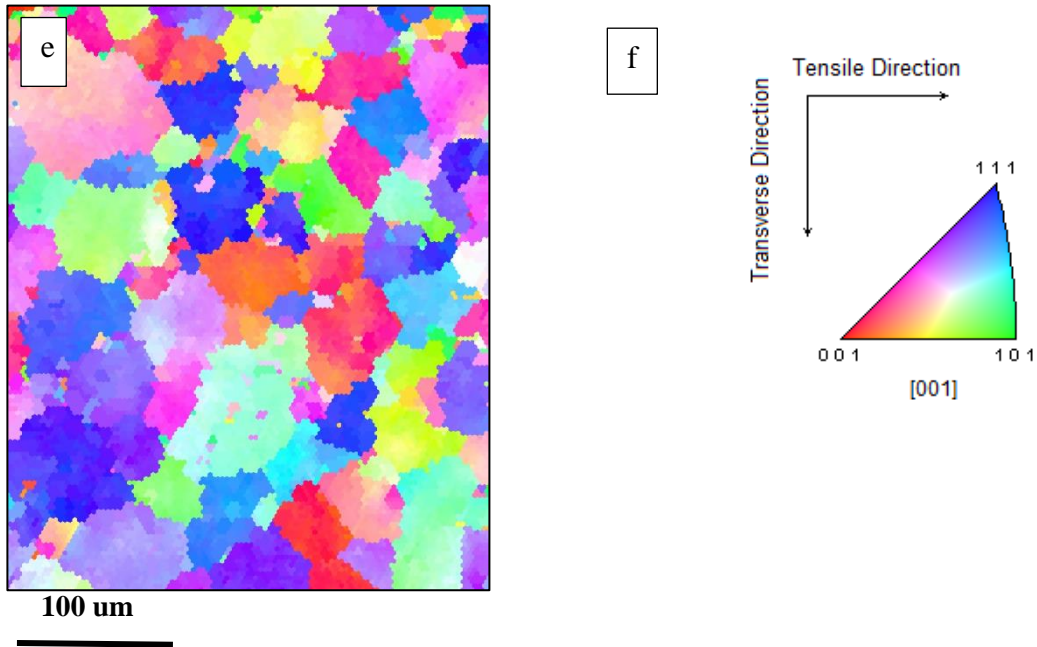


Figure 5.7 Sequential SE SEM photomicrographs acquired during the RT TCFA test: (a) 1.3% strain, (b) 3.4% strain, (c) 4.4% strain, (d) 8.4% strain, (e) posttest EBSD IPF map, and (f) EBSD color code and scale bar. Each of these images represents the same microstructural patch. The tensile axis was horizontal.

Figure 5.7 (cont'd)



The distribution of the different slip modes identified at ~8.4% strain versus the corresponding in Figure 5.8 Schmid factor range. The slip trace analysis was performed on 530 grains. The majority of the deformation systems belonged to Family (3) and the lowest contribution belonged to Family (1). The activation of most of the slip systems occurred over a global Schmid factor range of 0.35 to 0.5. The percentage contribution and normal distribution of the different slip modes will be discussed later in this chapter.

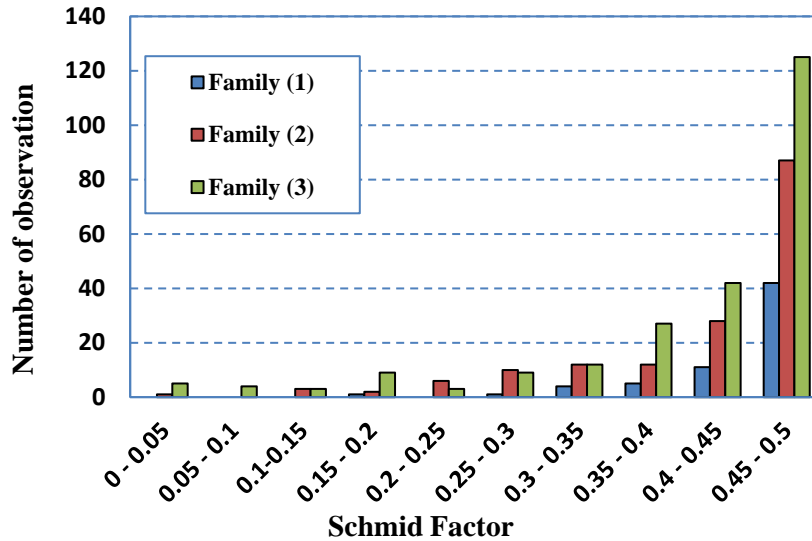


Figure 5.8 A histogram of the Schmid factor distribution of the slip systems for TCFA samples tested at RT to 8.4% strain.

5.2.4 200 °C tensile test of TCFA

Figure 5.9 exhibits a SE SEM micrograph of the gage section and the location of the heater at low-magnification after the test. Local plastic strain was observed in the heated area of the gage section. No evidence of plastic strain was observed outside of the heated region. The UTS was 820 MPa, which was 120 MPa lower than for the RT test. The tensile axis was horizontal. Figure 5.10 shows an EBSD IPF map and sequential SE SEM photomicrographs acquired during the test from a selected area at the middle of the gage section of the 200 °C tensile tested specimen. Some slip trace lines were observed at a stress level of 790 MPa, which was less than the global yield stress, ~820 MPa (see Figure 5.10 [c]), which indicated that microyielding occurred before global macroyielding. The slip trace analysis was performed on 232 grains after ~8% strain. Almost all the grains exhibited slip traces. Figure 5.11 shows the distribution of the different slip modes identified at ~8% strain versus the corresponding Schmid factor range. The majority of the

deformation systems belonged to Family (3) and the lowest contribution belonged to Family (1). This result was similar to that observed for the RT deformed specimen, see Figure 5.8. The activation of most of the slip systems occurred over a global Schmid factor range of 0.35 to 0.5. The percentage and normalized contribution of the different slip modes will be discussed later in this chapter.

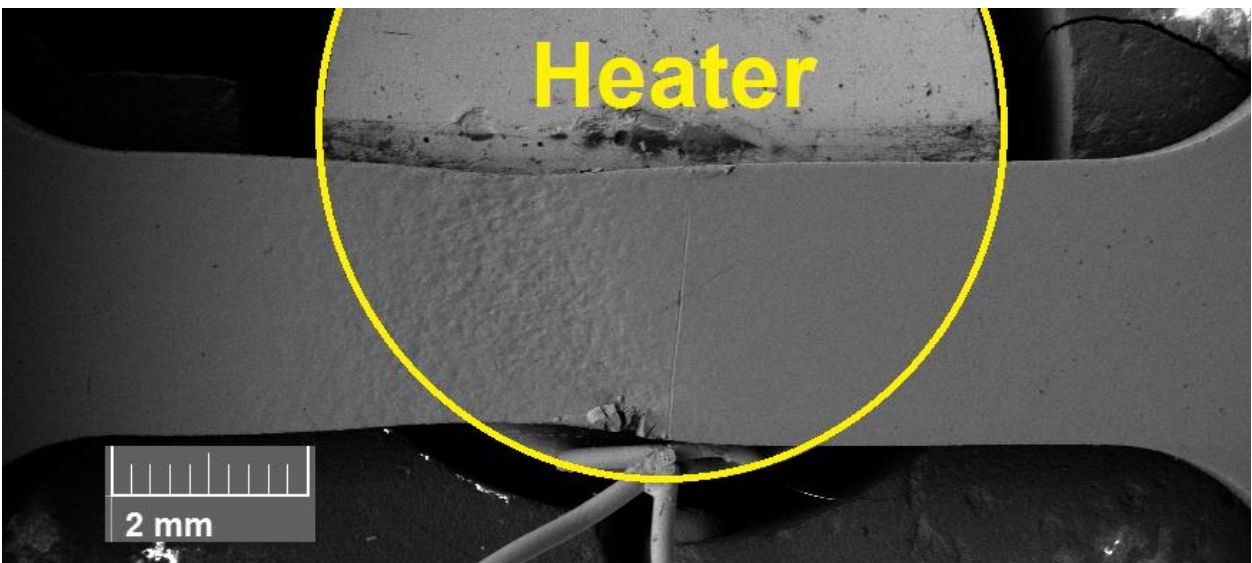


Figure 5.9 Low-magnification SE SEM micrograph of the 200 °C tensile deformed TCFA sample, which was taken ~8% strain. The heater location is specified by the yellow circle. Local plastic strain occurred in the heated area of the gage section. The center line, scribed on the sample before the test, was used as a fiducial marker. The tensile axis was horizontal.

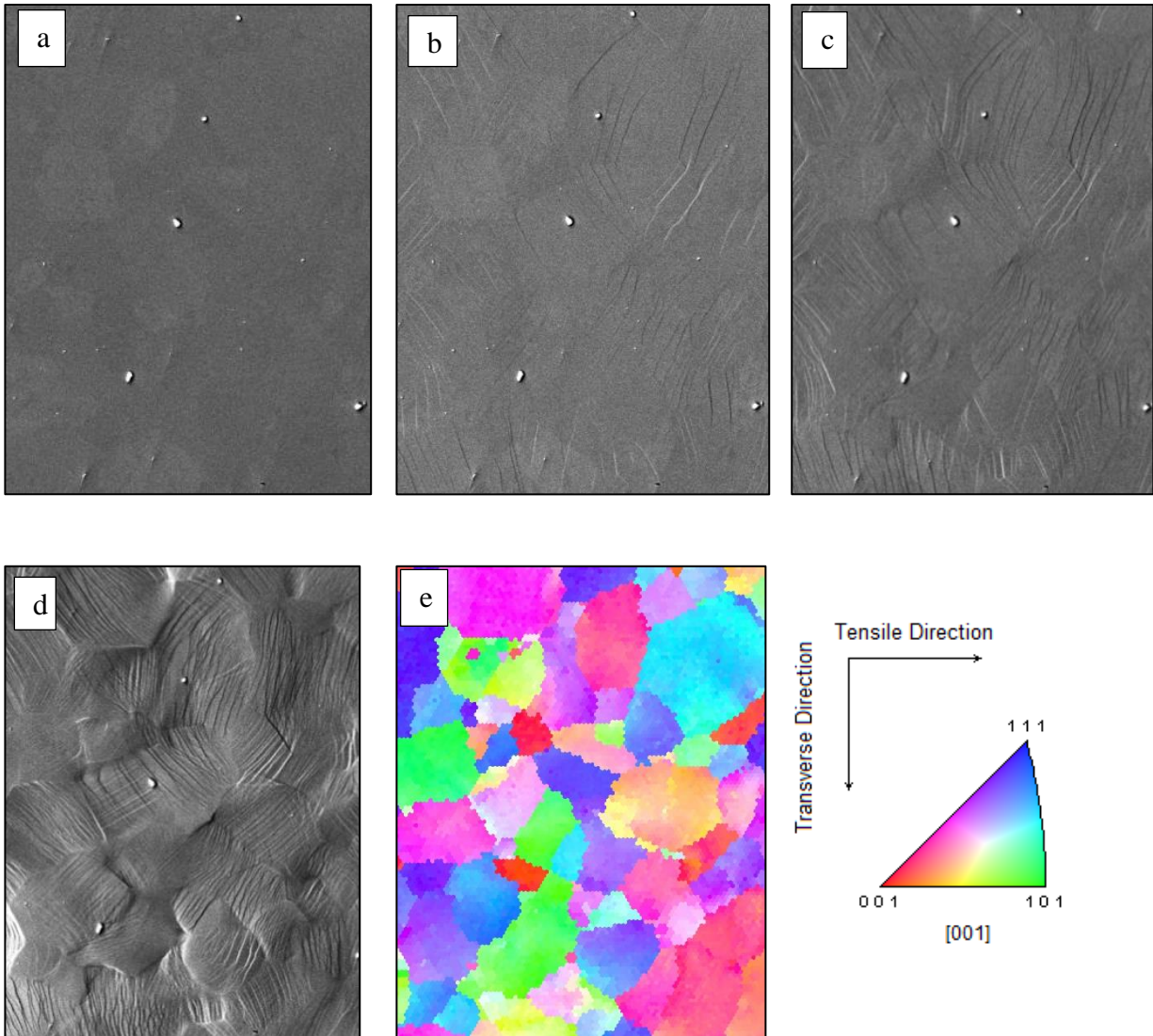


Figure 5.10 Sequential SE SEM photomicrographs acquired during the 200 °C TCFA test at (a) 0% strain, (b) 1.2% strain, (c) 2% strain, (d) 8% strain, and (e) posttest EBSD IPF map. Each of these images represents the same microstructural patch. The tensile axis was horizontal.

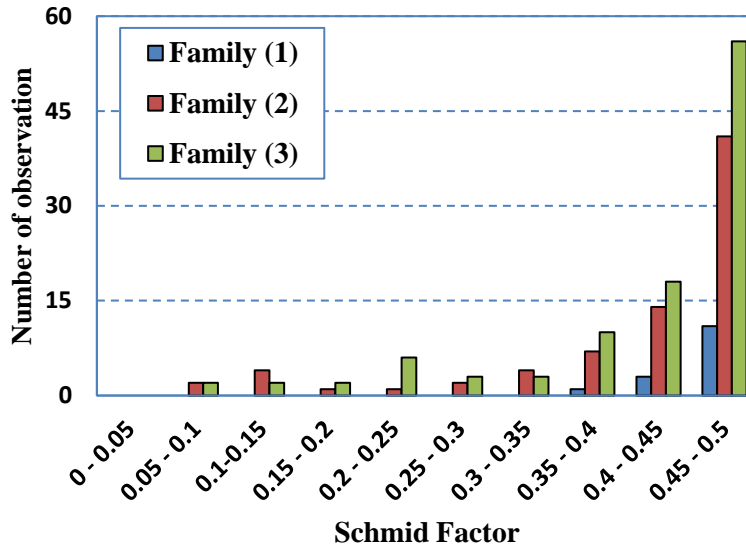


Figure 5.11 A histogram of the Schmid factor distribution of the observed slip systems for the TCFA sample tensile tested at 200 °C to ~8% strain.

5.2.5 300 °C tensile test of TCFA

Figure 5.12 presents a SE SEM photomicrograph of the gage section as well as the location of the heater at low-magnification after the 300 °C tensile test. A second thermocouple was spot-welded outside of the heated area (close to grip) to measure the temperature gradient. The maximum temperature difference between the two thermocouples was ~ 80 °C. The distance between the thermocouples was ~3 mm. The center line, scribed on the sample before the test, was used as a fiducial marker. The tensile axis was horizontal. No evidence of plastic strain was observed outside of the heated region. Figure 5.13 exhibits an EBSD IPF map from a selected area and sequential SE SEM photomicrographs at different level of plastic strain at the middle of the gage section of the 300 °C tensile tested specimen. The UTS was 720 MPa at 300 °C, which was 100 MPa and 220 MPa less than the 200 °C and RT tests, respectively. No slip traces were observed at 515 MPa. However, slip traces were observed at a stress level of 700 MPa.

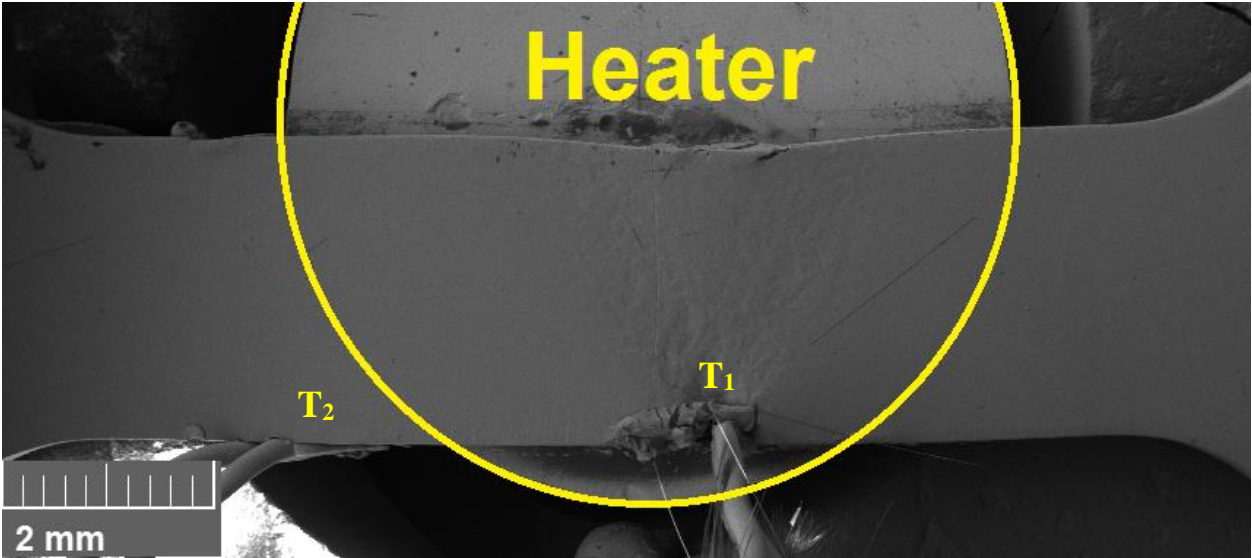


Figure 5.12 Low-magnification SE SEM micrograph of the 300 °C tensile deformed TCFA sample after achieving 2.2% strain. The heater location was specified by the yellow circle. Local plastic strain occurred at the center of the heated area of the gage section. The center line, scribed on the sample before the test, was used as a fiducial marker. The tensile axis was horizontal. The temperature of second thermocouple (T_2), which was spot-welded outside of the heater, was ~ 220 °C during the test, while the temperature of the test thermocouple (T_1) was 300 °C. This indicated the nature of the temperature gradient in the sample.

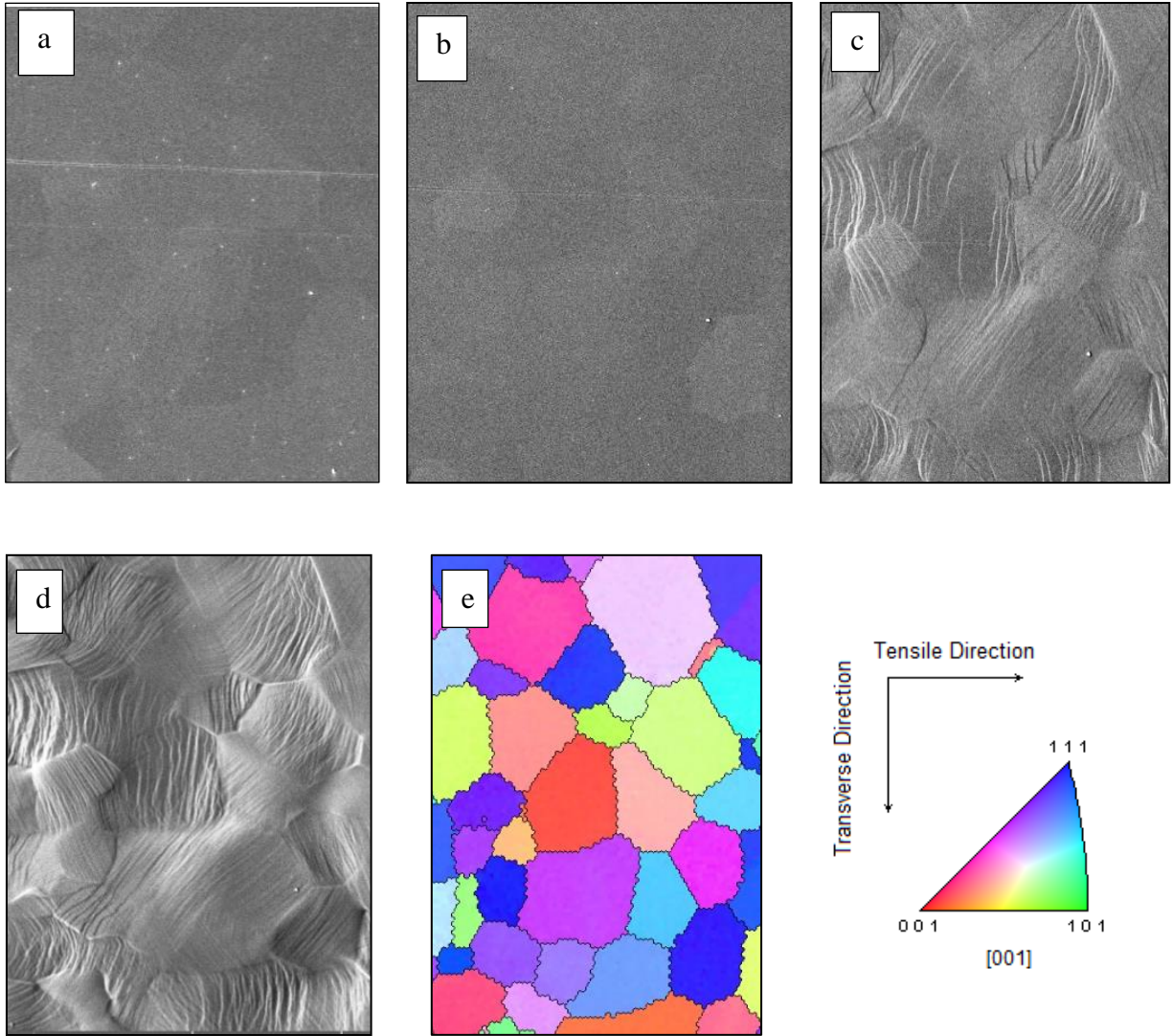


Figure 5.13 Sequential SE SEM photomicrographs acquired during the 300 °C TCFA test: (a) 0% strain, (b) 1% strain, (c) 2.2% strain, (d) 12% strain, and (e) Pretest EBSD IPF map. Each of these images represents the same microstructural patch. The tensile axis was horizontal.

The slip trace analysis was performed on 104 grains. Figure 5.14 shows the distribution of the different slip modes identified at ~2.2% strain versus the corresponding Schmid factor range. The majority of the deformation systems belonged to Family (3) and the lowest contribution belonged to Family (1), which was similar to that observed for the RT and 200 °C specimens, (see Figure 5.8 and Figure 5.11, respectively). The activation of most of the slip systems occurred over a global Schmid factor range of 0.35 to 0.5. The percentage and normal contribution of the different slip modes will be discussed later in this chapter.

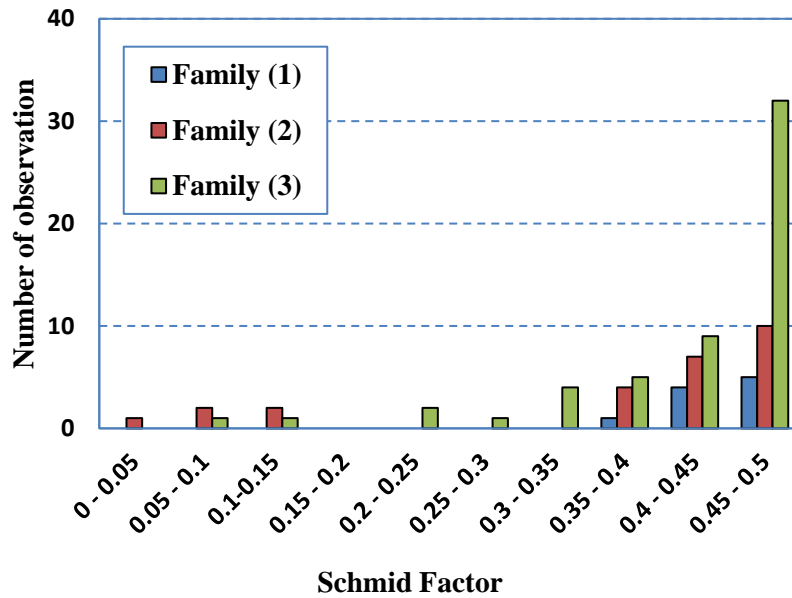


Figure 5.14 A histogram of the Schmid factor distribution of the slip systems for the TCFA sample tested at 300 °C at ~2.2% strain.

5.3 Deformation behavior of TIMETAL-21S

5.3.1 Microstructure and texture of TIMETAL-21S

The average grain diameter of TIMETAL-21S was approximately 15 μm . Figure 5.15 presents SE SEM photomicrographs of the microstructure of the as-received TIMETAL-21S. Figure 5.16 depicts the grain size distribution of the TIMETAL-21S samples before tensile testing. A representative EBSD IPF map and texture plots, in the form of $\{100\}$ and $\{110\}$ pole figures in the normal direction, are illustrated in Figure 5.17. The pole figures show a relatively moderate fiber texture where the $\{100\}$ plane normals were aligned almost parallel to the tensile direction, and a relatively strong texture resulted, where $\{100\}$ peaks were aligned parallel to the transverse direction. Each grain exhibited very little misorientation before the test (see Figure 5.17 [a]).

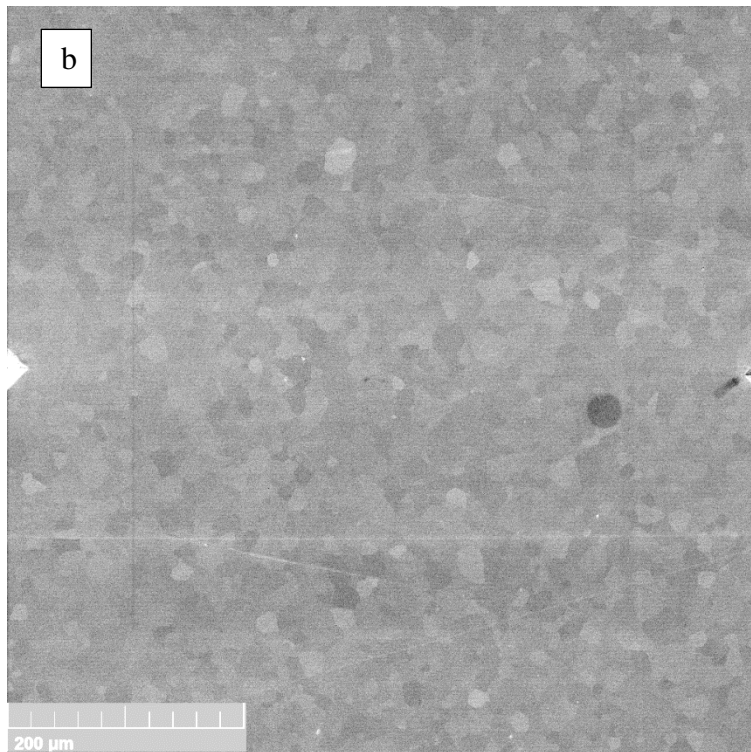
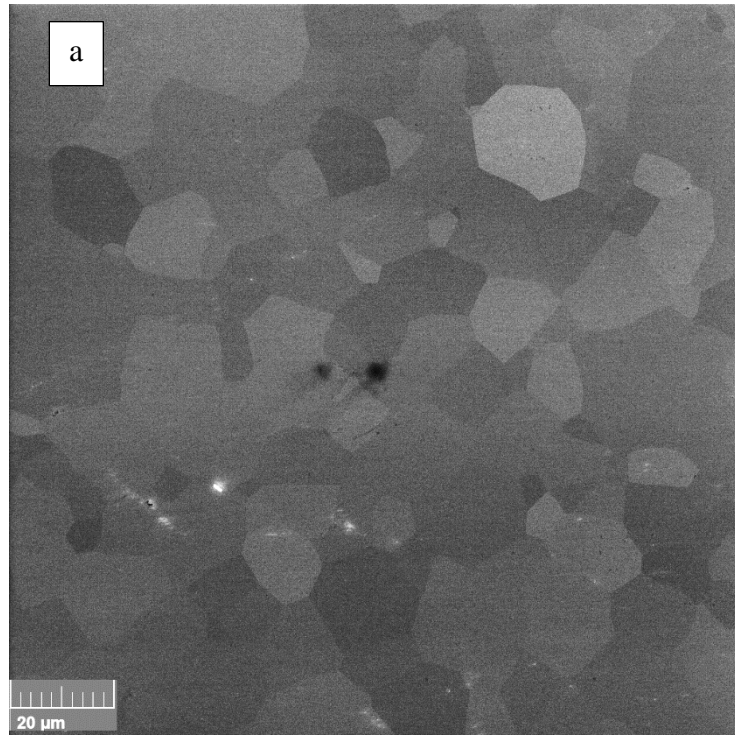


Figure 5.15 SE SEM photomicrographs from the microstructure of the as-received TIMETAL-21S (a) high magnification and (b) low magnification.

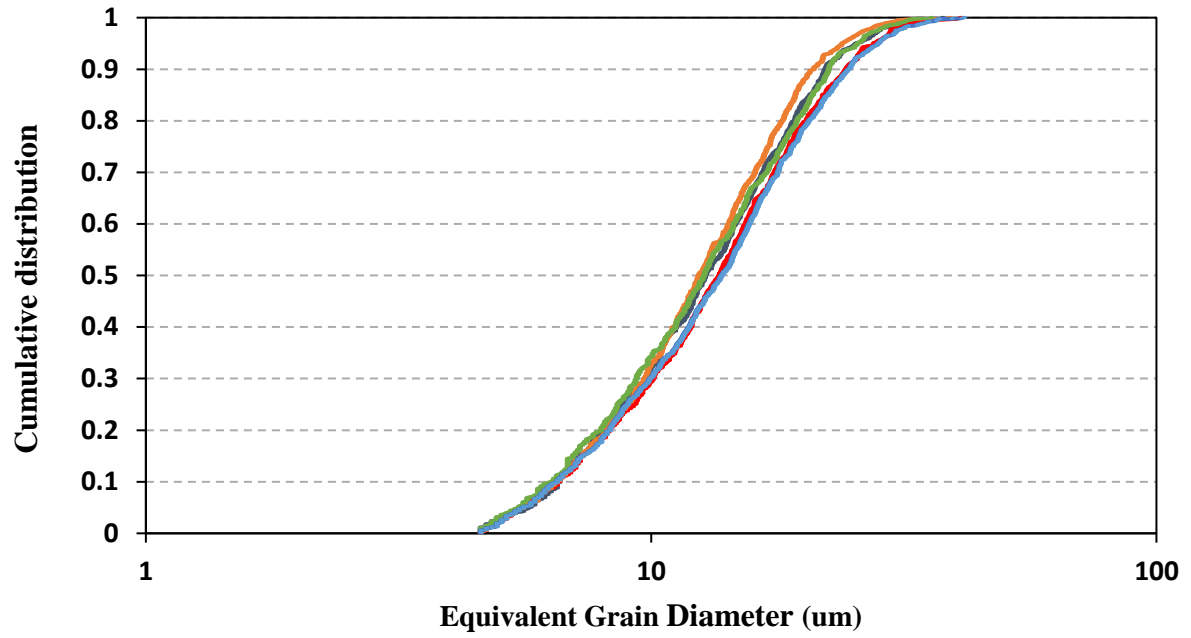


Figure 5.16 The cumulative grain size distribution for TIMETAL-21S of separated microstructural patches

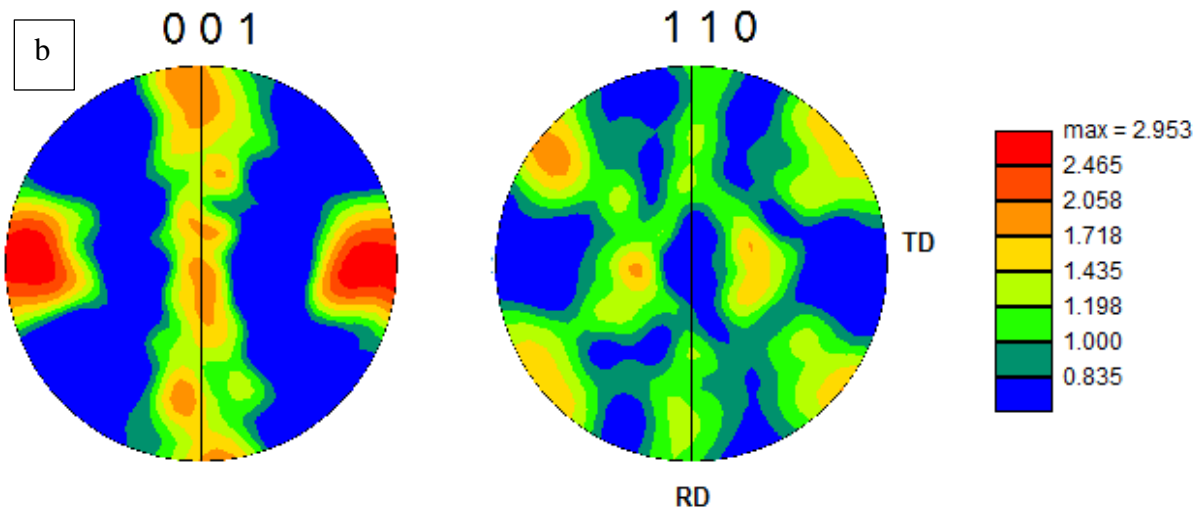
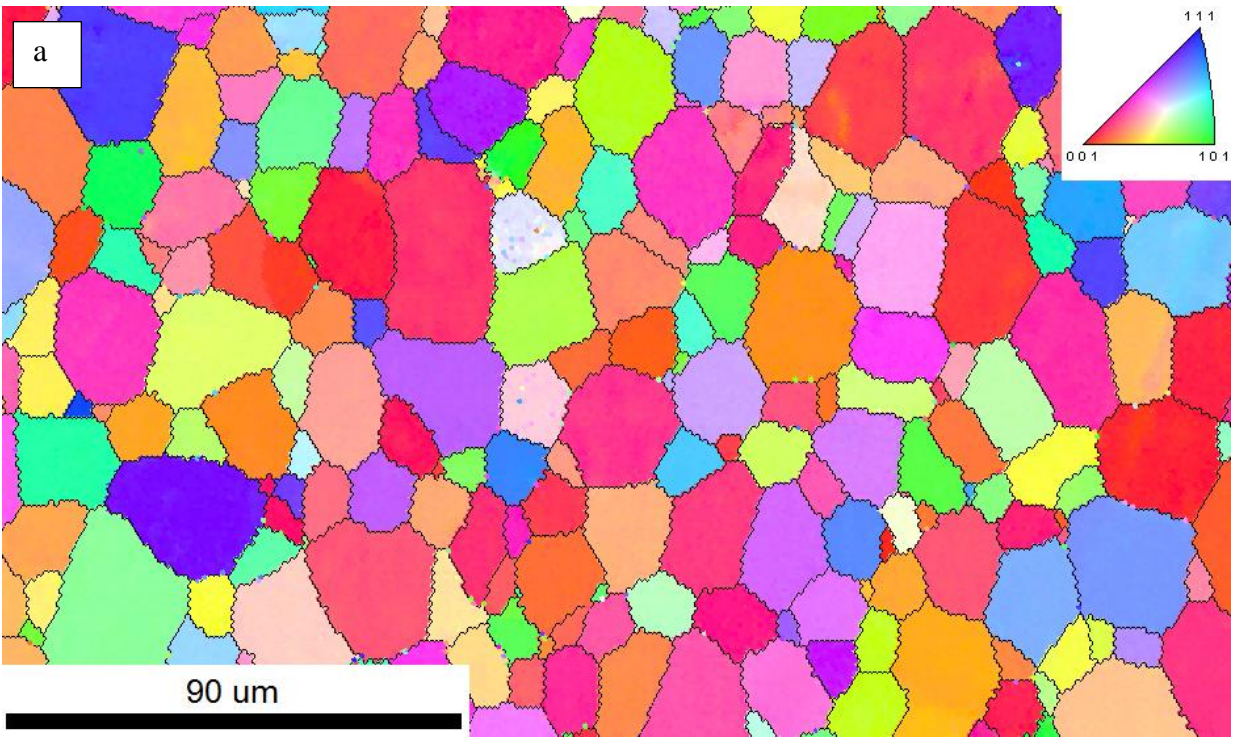


Figure 5.17 EBSD data of the undeformed TIMETAL-21S: (a) EBSD IPF map in the tensile direction and (b) The representative texture of TIMETAL-21S microstructure in the form of $\{100\}$ and $\{110\}$ pole figures in the normal direction.

5.3.2 In situ tensile test of TIMETAL-21S

In situ tensile tests were performed at RT, 230 °C, and 300 °C, as described in section 3. One tensile test was conducted at each temperature. The EBSD data were acquired from a selected area at the middle of the gage section at RT. Patterns were collected using a 15kV electron beam and a working distance of ~20mm. The EBSD scans were performed on two areas of approximately 400 μm by 600 μm for each sample, using a step size of 1 μm. The engineering stress versus displacement curves for the RT, 230 °C, and 300 °C tensile tests are illustrated in Figure 5.18. None of the specimens were taken to failure. The UTS was ~ 845 MPa at RT. The UTS was 665 MPa for the test performed at 230 °C. The UTS was 660 MPa at 300 °C. Stress relaxation occurred when the tests were paused for acquiring the SEM photomicrographs. In the following sections, sequential SE SEM photomicrographs of selected areas and slip trace analysis results are provided for each test.

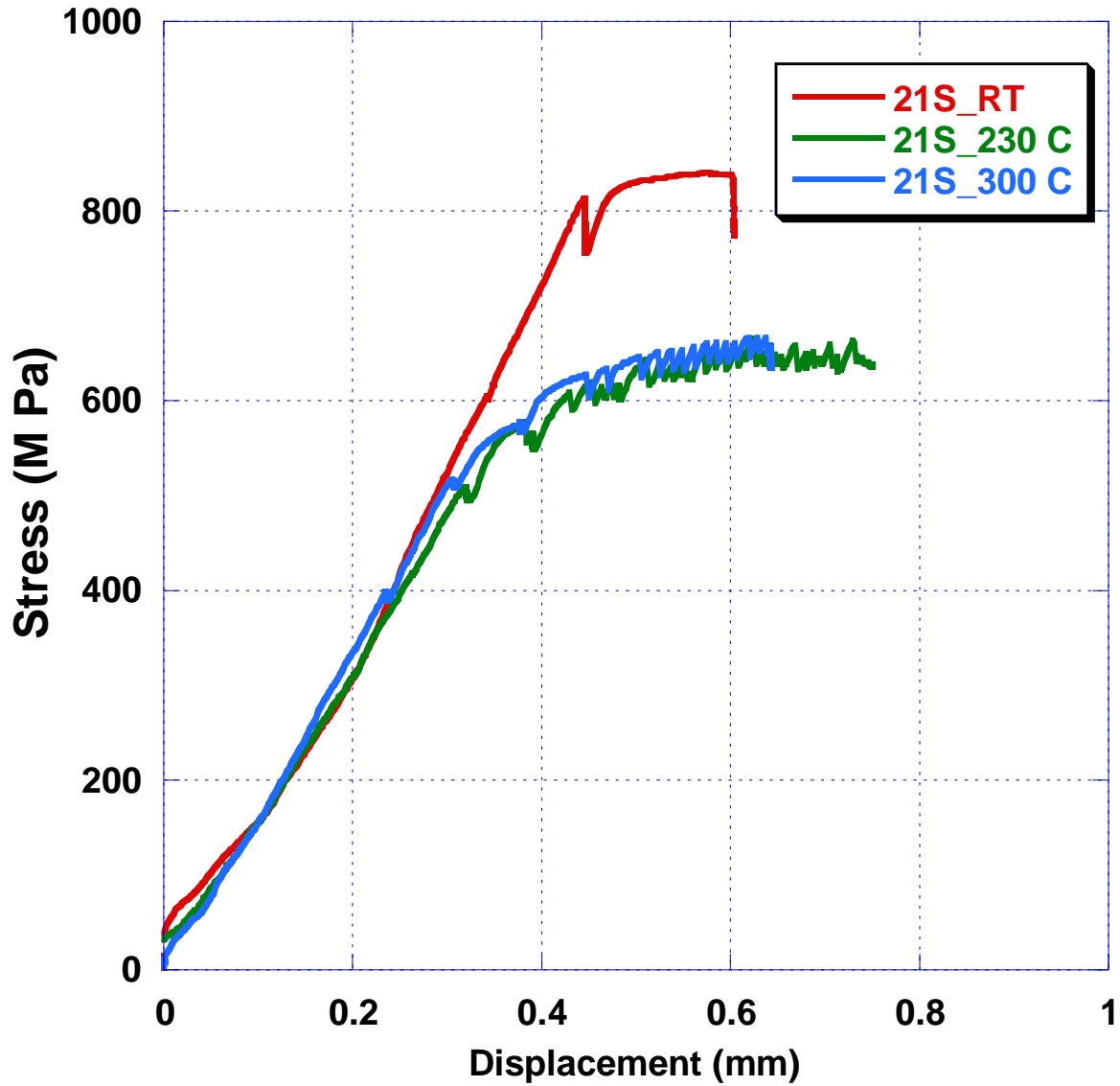


Figure 5.18 Engineering stress vs. displacement for TIMETAL-21S samples tensile tested at RT, 230 °C, and 300 °C. The stress drops indicate that stress relaxation occurred when the tests were interrupted for SEM imaging. None of the tests were taken to failure.

5.3.3 RT tensile test of TIMETAL-21S

Figure 5.19 exhibits a SE SEM micrograph of the gage section at 6.5% plastic strain. The tensile axis was horizontal. Uniform plastic strain was observed throughout the center of gage section. The Vickers hardness indents were used as fiducial markers to measure the local strain. The sequential SE SEM photomicrographs acquired during the test are presented in Figure 5.20, along with the corresponding EBSD IPF map from the same area. Some slip traces were observed at a stress level of 820 MPa, which was below the global yield stress, ~ 845 MPa (see Figure 5.20 (c), indicating that microyielding occurred before global yielding.

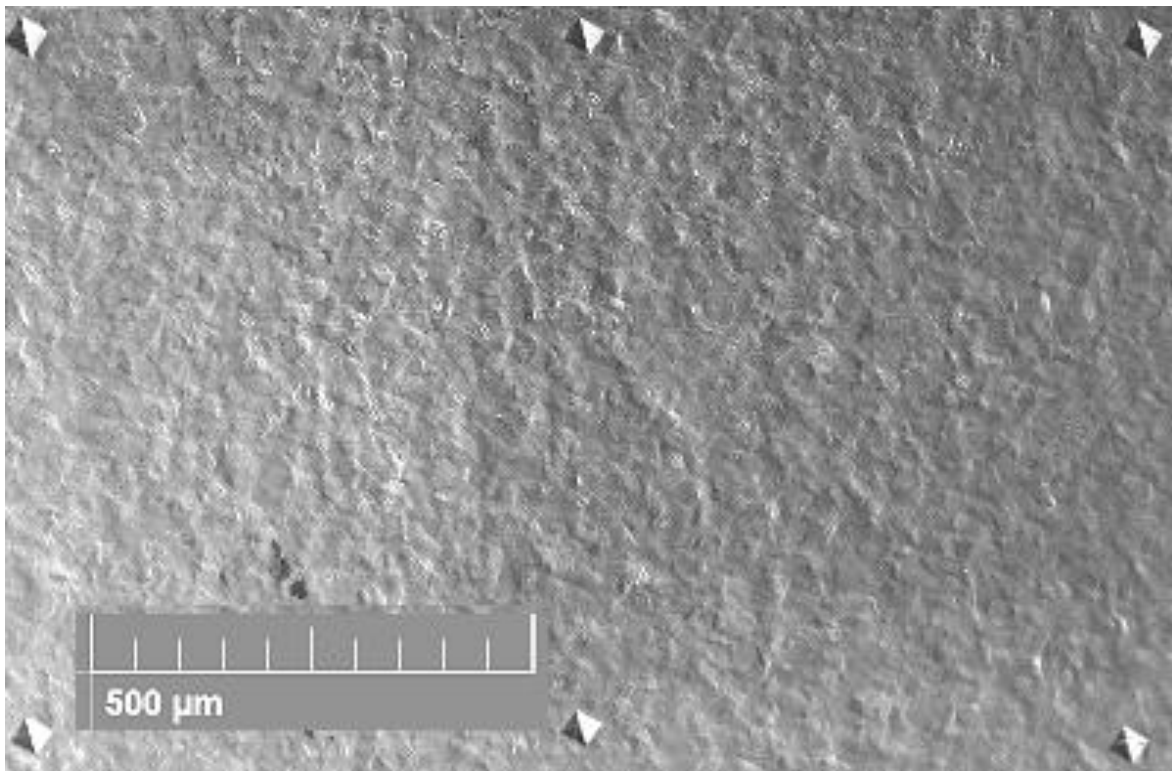


Figure 5.19 Low-magnification SE SEM micrograph of a RT deformed TIMETAL-21S sample. Uniform plastic strain was observed throughout the gage section. The small Vickers hardness indents, made before the test, were used as fiducial markers to help measure the strain. The tensile axis was horizontal.

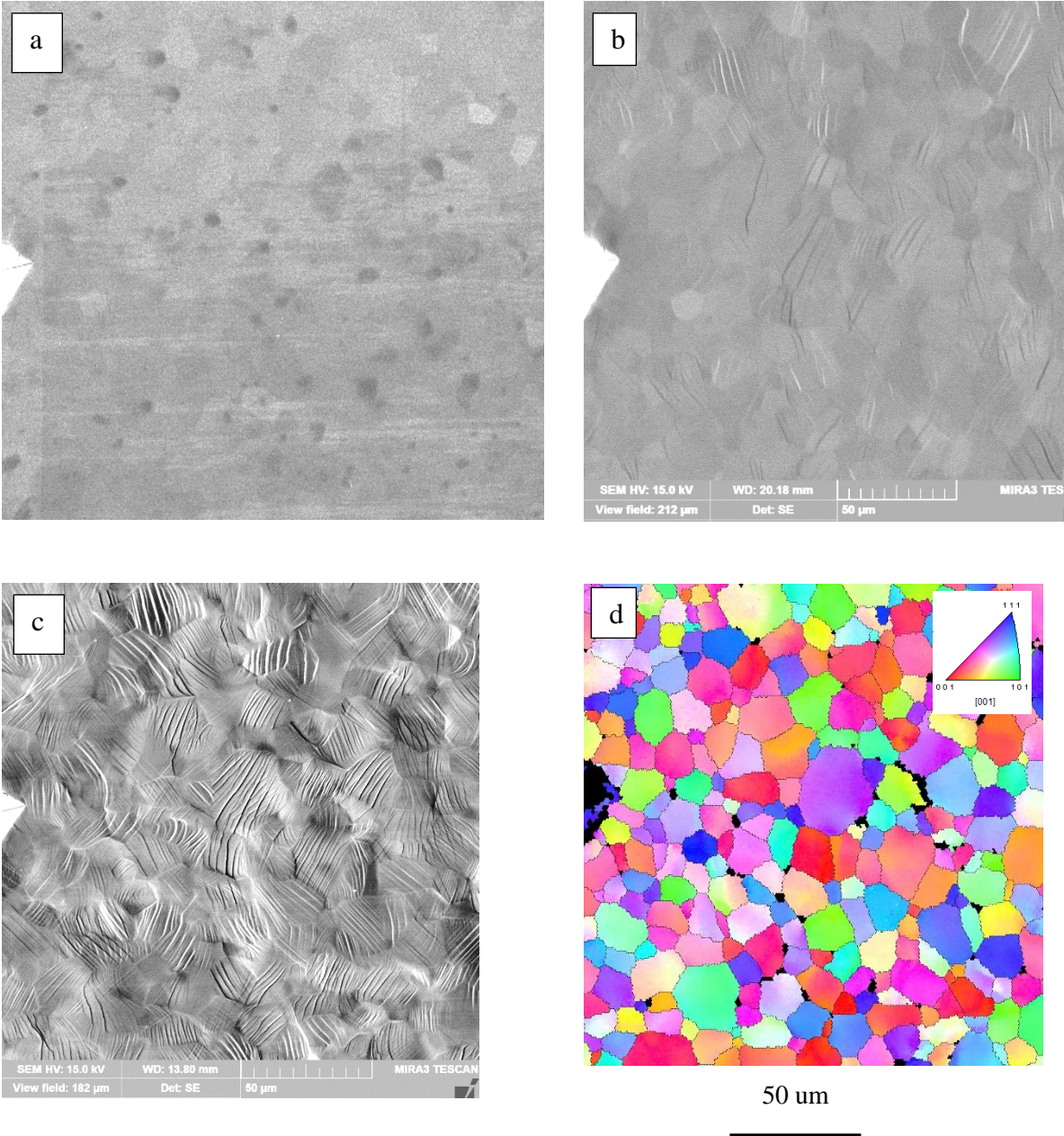


Figure 5.20. Sequential SE SEM photomicrographs of a TIMETAL-21S sample tested at RT: (a) 0%, (b) at 1.2% strain, (c) at 6.5% strain, and (d) posttest EBSD IPF map. Each of these images represents the same microstructural patch. The tensile axis was horizontal.

Figure 5.21 shows the distribution of the different slip modes, identified at ~6.5% strain versus the corresponding Schmid factor range. The slip trace analysis was performed on 213 grains. Most of the deformation systems belonged to Family (3) and the lowest contribution belonged to Family (1). The activation of most of the slip systems occurred over a global Schmid factor range of 0.4 to 0.5. The percentage contribution and normal distribution of the different slip modes will be discussed later in this chapter.

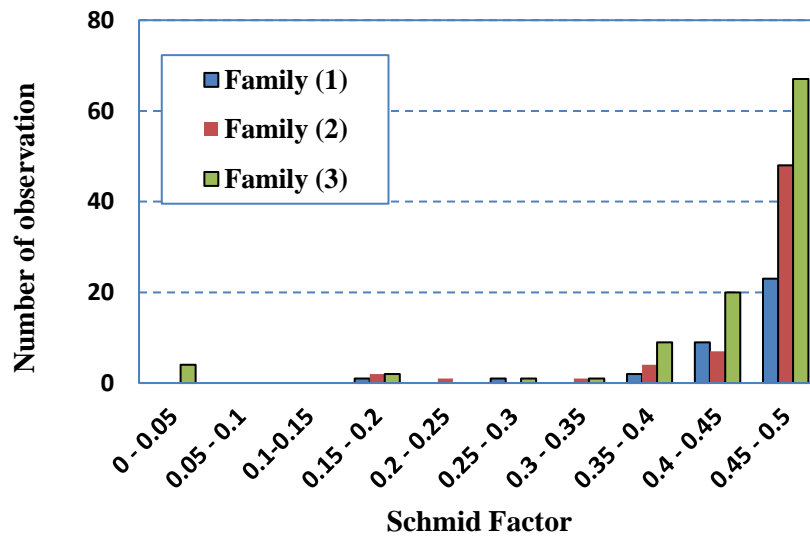


Figure 5.21 A histogram of the Schmid factor distribution of the slip systems for the TIMETAL-21S sample tensile tested at RT to ~6.5% strain.

5.3.4 230 °C tensile test of TIMETAL-21S

Figure 5.22 exhibits a SE SEM micrograph of the gage section of the TIMETAL-21S specimen after ~18% local plastic strain. The tensile axis was horizontal. Local plastic strain was observed in the heated area of the gage section. The UTS was 665 MPa. The sequential SE SEM photomicrographs acquired during the test are presented in Figure 5.23, along with the corresponding EBSD IPF map for the same microstructure patch. Some slip trace lines were observed at a stress level of 505 MPa, which was below the global yield stress (see Figure 5.23 (c)), indicating that microyielding occurred before global yielding. The Vickers hardness indents were used as fiducial markers to measure the strain.

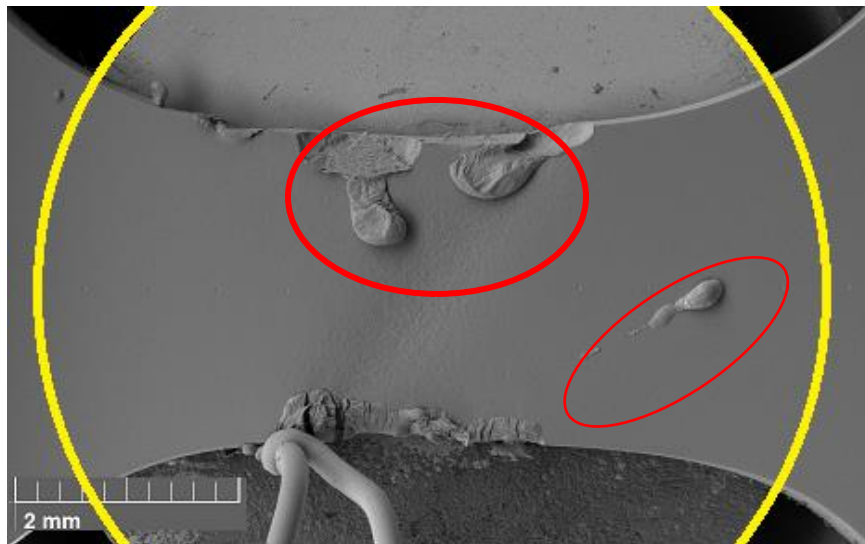


Figure 5.22 Low-magnification SE SEM micrograph of a 230 °C deformed TIMETAL-21S sample. Localized plastic strain was observed in the heated area of the gage section. The Vickers hardness indents, made before the test, were used as fiducial markers to measure the local strain. The tensile axis was horizontal. The features that are shown inside the red ovals are spot-welding artifacts that occurred before the test.

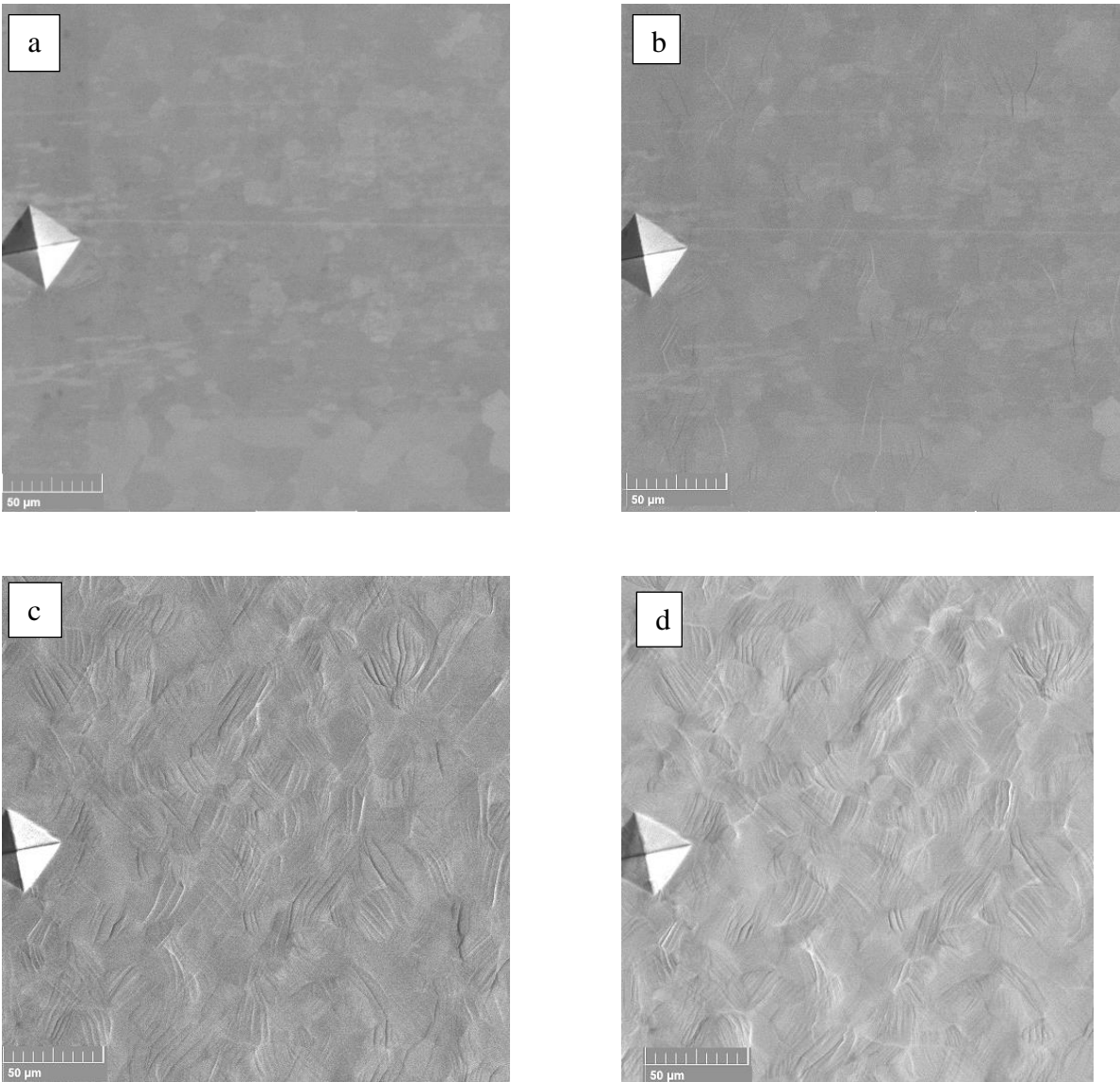
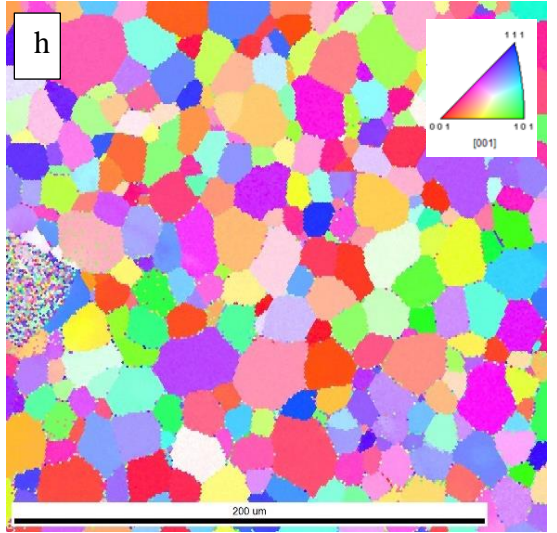
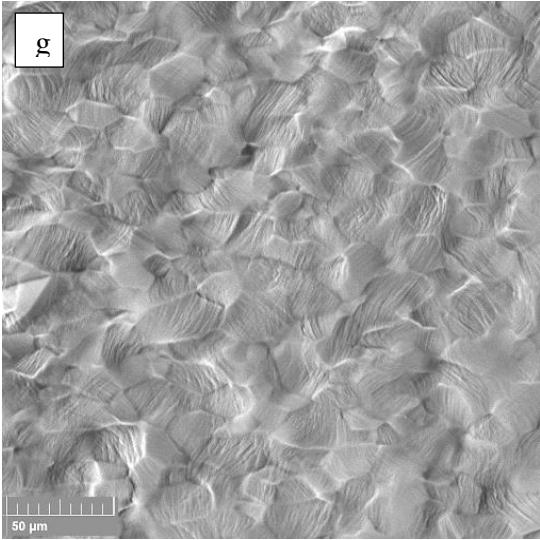
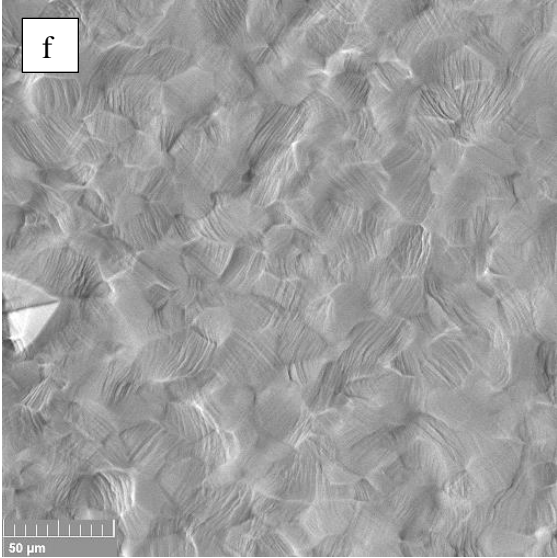
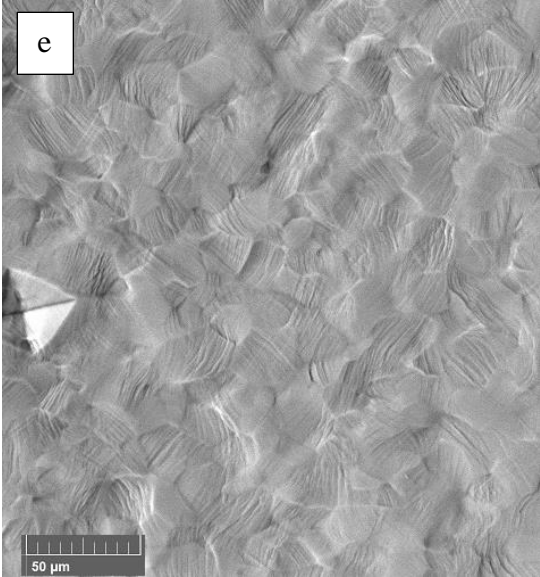


Figure 5.23 Sequential SE SEM photomicrographs of the TIMETAL-21S sample tested at 230 °C acquired during the test at (a) 0% strain, (b) at 0.9% strain, (c) at 2% strain, (d) at 5.5% strain, (e) at 8.2% strain, (f) at 10.8% strain, (g) at 18.4% strain, and (h) pretest EBSD IPF map. Each of these images represents the same microstructural patch. The tensile axis was horizontal.

Figure 5.23 (Cont'd)



100 μm

5.3.5 300 °C tensile test of TIMETAL-21S

Figure 5.24 exhibits a low-magnification SE SEM micrograph of the gage section of the TIMETAL-21S specimen tested at 300 °C after 11% plastic strain. The tensile axis was horizontal. The Vickers hardness indents were used as a fiducial marker to measure the local strain. Local plastic strain was observed in the heated area of the gage section. The UTS was 660 MPa. The sequential SE SEM photomicrographs acquired during the test are presented in Figure 5.25 as well as the corresponding EBSD IPF map for the same microstructure patch. Some slip trace lines were observed at a stress level of 520 MPa, which was below the global yield stress (see Figure 5.25 [c]), indicating that microyielding occurred before global yielding.

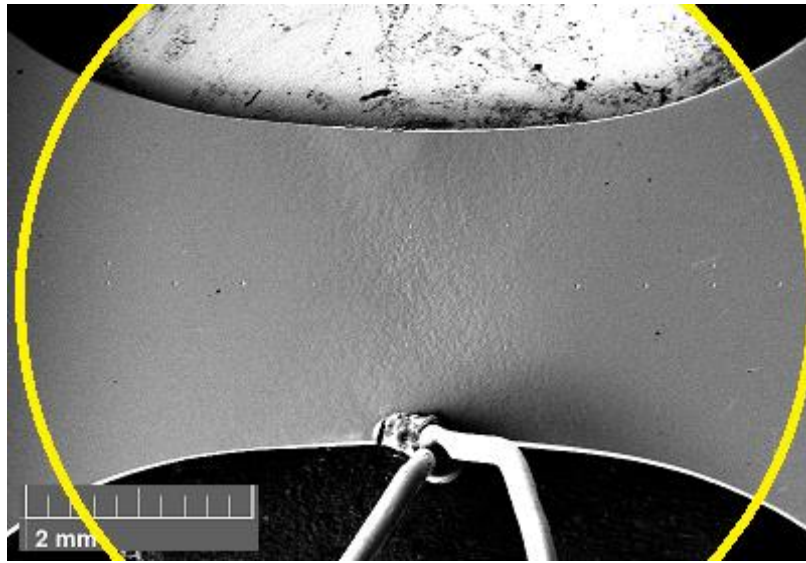


Figure 5.24 Low-magnification SE SEM micrograph of a 300 °C deformed TIMETAL-21S sample after 11% strain. Local plastic strain was observed at the center of the heated area of the gage section. The Vickers hardness indents, made before the test, were used as fiducial markers to measure the local strain. The tensile axis was horizontal.

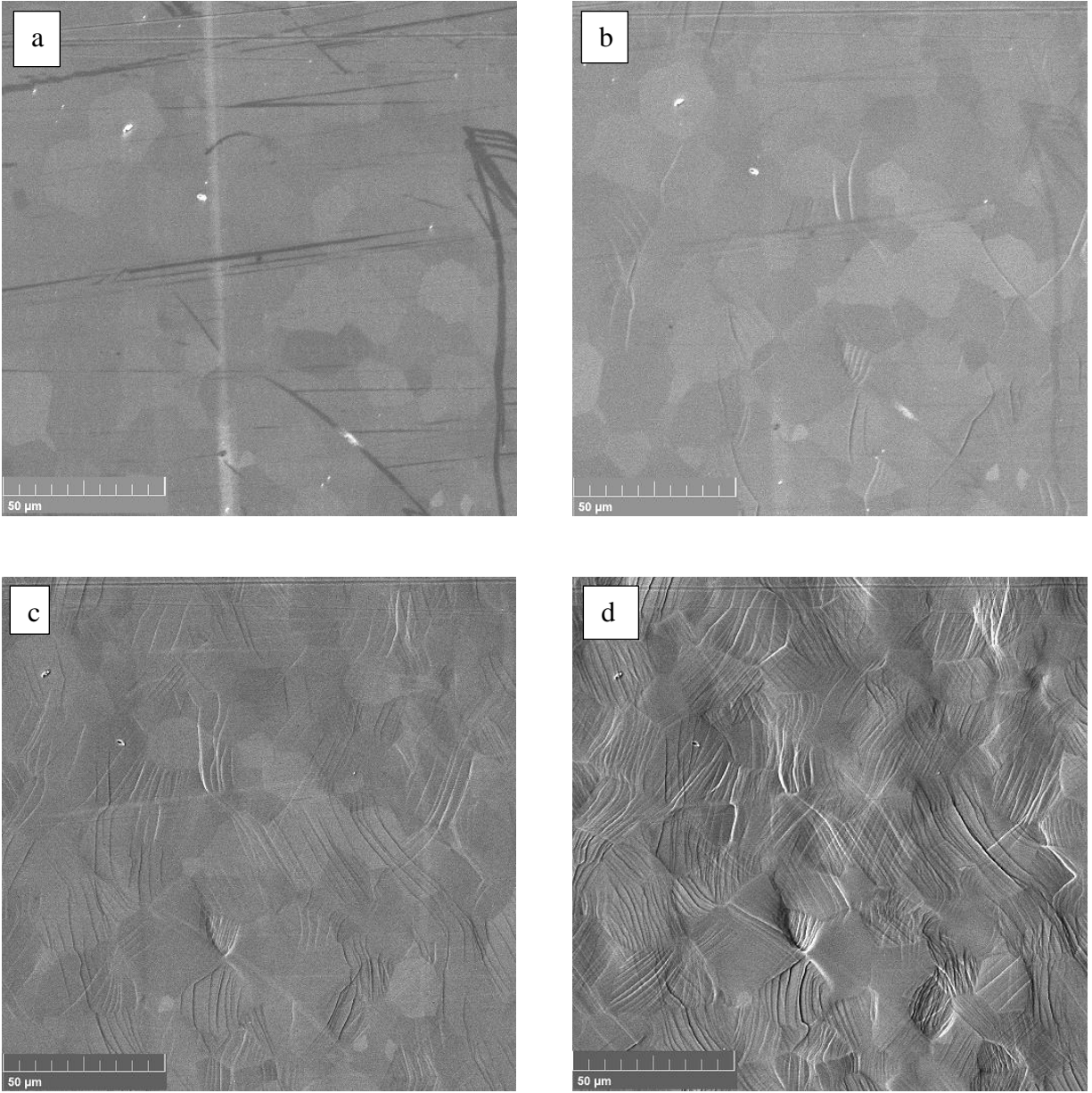


Figure 5.25 (a) before test EBSD IPF map. Sequential SE SEM photomicrographs of TIMETAL-21S sample tested at 300 °C: (a) 0%, (b) at 0.8% strain, (c) at 1.6% strain, and (d) at 11% strain. Each of these images represents the same microstructural patch. The tensile axis was horizontal.

Figure 5.26 shows the distribution of the different slip modes identified at ~11% strain versus the corresponding Schmid factor range. The slip trace analysis was performed on 275 grains. Most of the deformation systems belonged to Family (3) and the lowest contribution belonged to Family (1). The activation of most of the slip systems occurred over a global Schmid factor range of .4 to 0.5. The percentage contribution and normal distribution of the different slip modes will be discussed later.

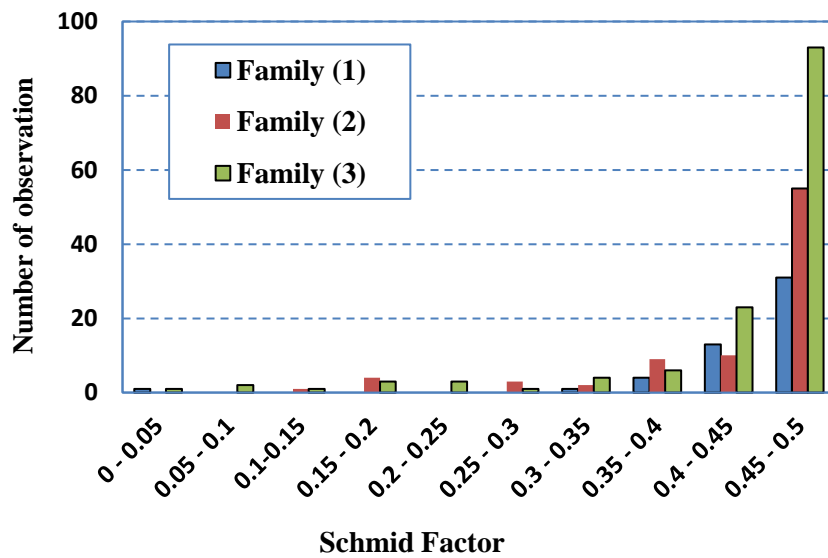


Figure 5.26 The histogram of Schmid factor distribution of slip systems for the TIMETAL-21S sample tested at 300 °C, after ~11% strain.

5.4 Deformation behavior of TNTZ-xO

The Ti-29Nb-13Ta-4.6Zr alloy is a bcc Ti alloy, designed and fabricated for biomedical applications (Niinomi, 1998). It was reported that the mechanical properties of TNTZ can be enhanced by adding a small fraction of oxygen (Geng et al., 2011). Table 5.1 provides the composition for each of the TNTZ alloys. In the following section, the deformation mechanisms of these alloys will be discussed. Two in situ tensile tests were performed inside a SEM at RT for TNTZ-0.1O, while one RT test was performed for both TNTZ-0.3O and TNTZ-0.7O. The EBSD data was acquired from a selected area at the middle of gage section. The EBSD IPF map was collected using a 20 kV electron beam, a working distance of ~20mm, and using a step size of 4 μm . The engineering stress versus displacement curves for the tensile tests are illustrated in Figure 5.27. None of the specimens were taken to failure. The UTS values were 520 MPa, 800 MPa, 980 MPa for the 0.1O (wt.%), 0.3O (wt.%), and 0.7O (wt.%) samples, respectively. Stress relaxation occurred when the tests were paused for acquiring the SEM photomicrographs. In the following sections, sequential SE SEM photomicrographs of selected areas and the analysis (i.e., slip trace analysis and twinning) results are provided for each composition.

Table 5-1 The analyzed chemical compositions of TNTZ-0.1O, TNTZ-0.3O, and TNTZ-0.7O (Geng et al., 2011)

Alloys	Ti	Nb	Ta	Zr	O	N
TNTZ-0.1O	bal.	29.3	13.2	4.67	0.091	0.0068
TNTZ-0.3O	bal.	27.7	13.5	4.65	0.28	0.006
TNTZ-0.7O	bal.	28.8	12.2	3.72	0.724	0.0143

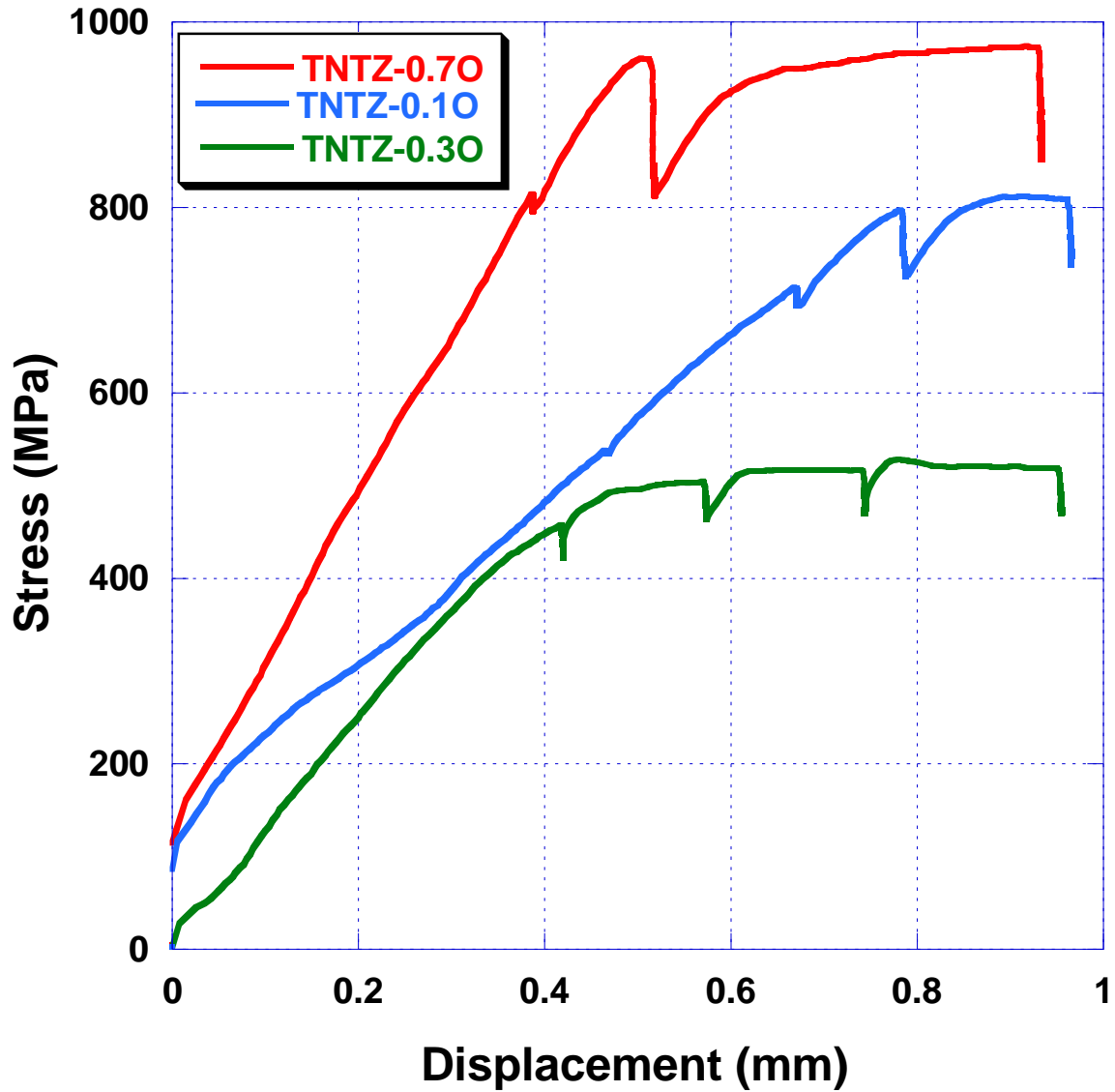


Figure 5.27 Engineering stress vs. displacement curve for each of the TNTZ-xO samples tensile tested at RT. The stress drops indicate that stress relaxation occurred when the tests were paused for acquiring the SE SEM photomicrographs. None of the tests were taken to failure. The slope variation was due to slipping of the sample during loading in the grips.

5.4.1 RT tensile test of TNTZ-0.1O

The sequential SE SEM photomicrographs and pretest and posttest EBSD IPF maps are provided in Figure 5.28 for a TNTZ-0.1O sample that was tensile tested at RT. The tensile axis was horizontal. The UTS was 520 MPa. As shown in Figure 5.28 (a), evidence of local plastic strain was observed at a stress level of 450 MPa (1.7% strain), indicating microyielding occurred before macroyielding. Lentoid structures were observed in some grains. Figure 5.29 shows an EBSD IPF map from the gage section of the TNTZ-0.1O tensile tested sample after the deformation. The misorientation angle between the lentoid structure and the matrix was approximately 50.5 degree along the $\langle 110 \rangle$ β direction. The lentoid structures observed are thus identified as $\{332\} \langle 113 \rangle$ mechanical twins [Liu et al. 2017]. For the 667 grains analyzed, mechanical twins were observed in 166 (17%) grains after 8.4% strain. Slip lines were observed in some other grains (see Figure 5.30). For the 44 gains analyzes, slip traces were observed in 9 (20%) of grains. The results of slip trace analysis are provided in Table 5.2.

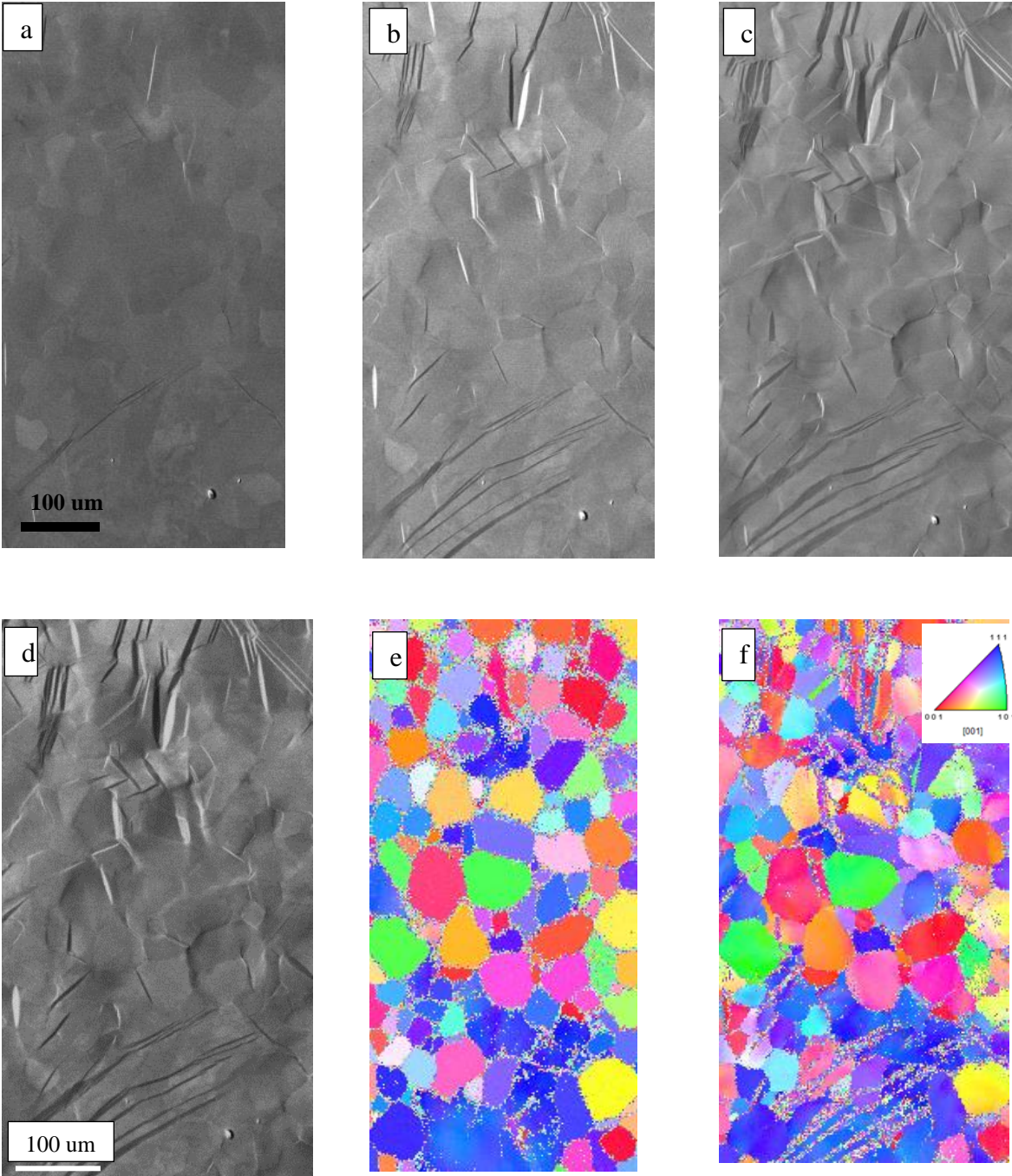


Figure 5.28 Sequential SE SEM photomicrographs acquired during the RT TNTZ-0.1-O test at (a) 1.7% strain, (b) 3.1% strain, (c) 5.2% strain, and (d) 8.4% strain. Each of these images represents the same microstructural patch. (e) Pretest EBSD IPF map, and (f) Posttest EBSD IPF map. The tensile axis was horizontal.

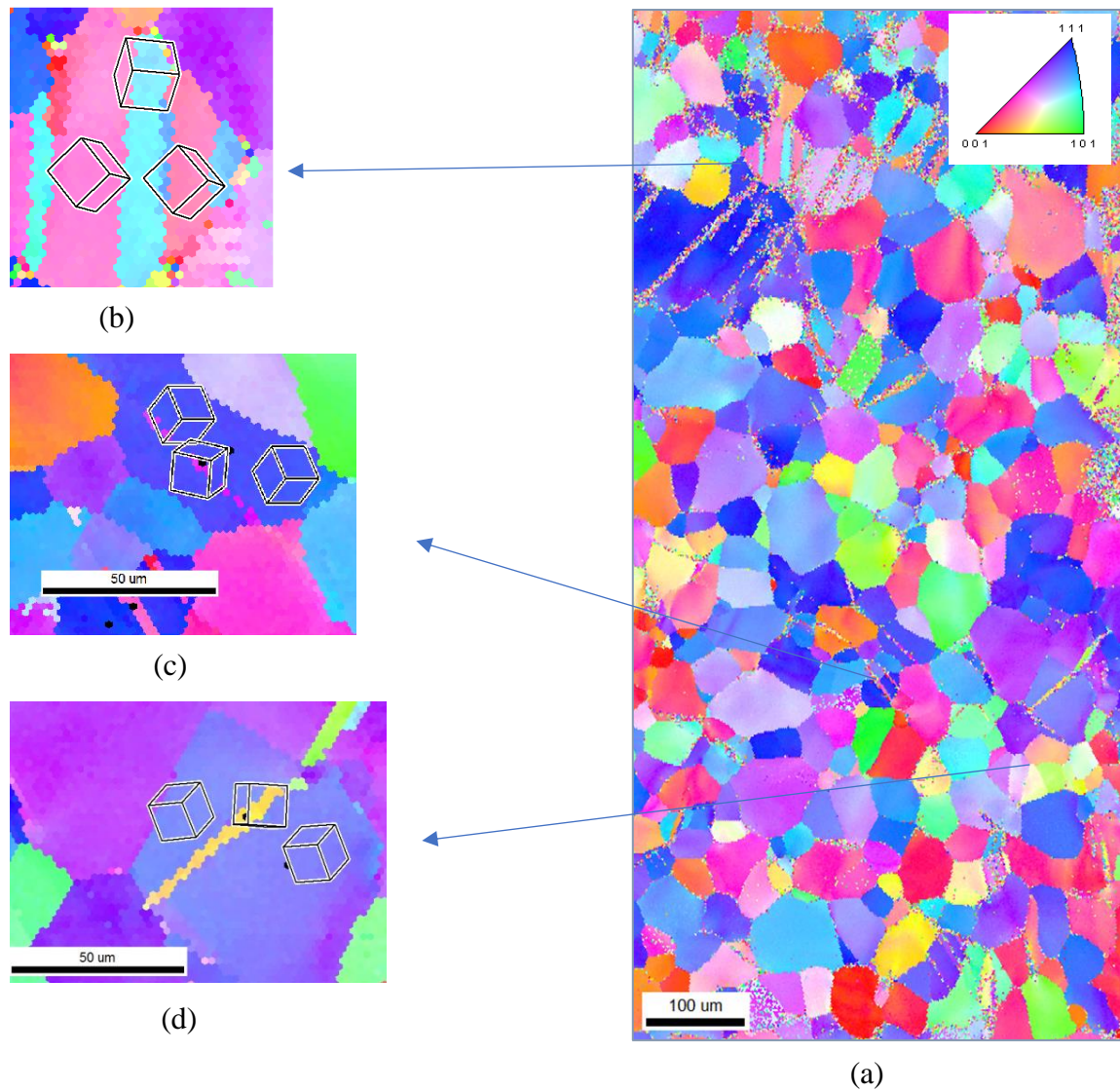


Figure 5.29 (a) EBSD IPF map from the gage section of the TNTZ-0.10 tensile tested sample after 8.4% strain. (b), (c), and (d) mechanical twins were observed in some grains. The misorientation angle between the $\{332\}\langle 113\rangle$ and the matrix was approximately 50.5 degrees along the $\langle 110\rangle_{\beta}$ direction.

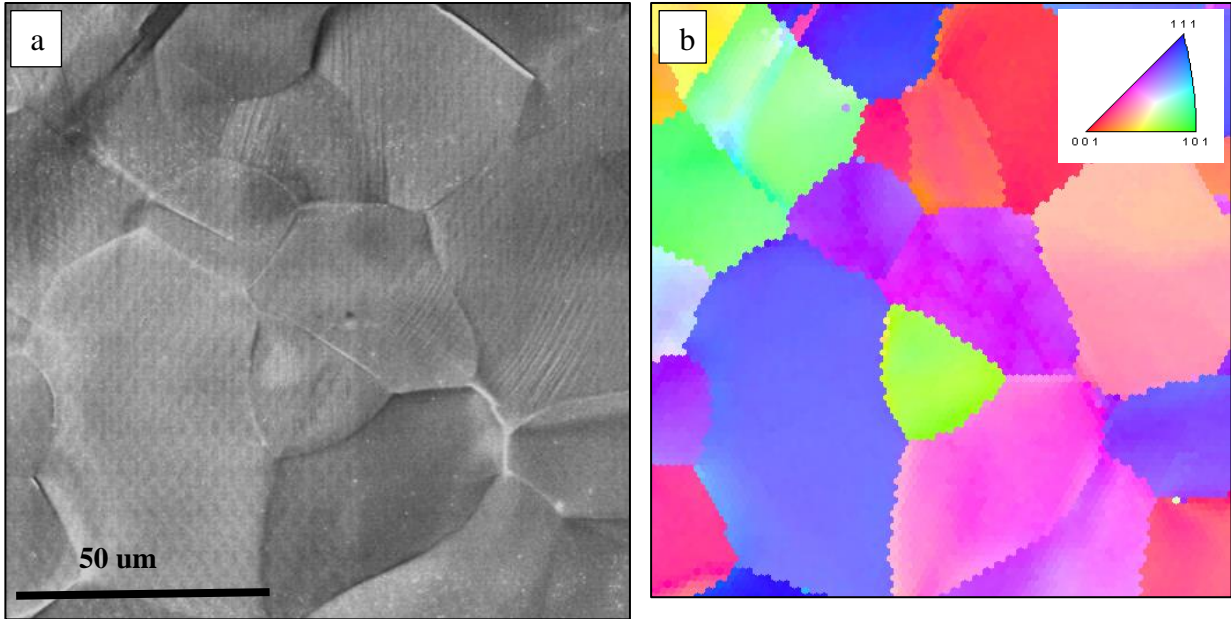


Figure 5.30 (a) high-magnification SE SEM micrograph of a TNTZ-0.1O sample tensile tested at 5.8% strain at RT. Fine slip traces are evident in some grains. (b) Posttest EBSD IPF map.

Table 5-2 Schmid factor for the RT deformed TNTZ-0.1O sample. The strain was 5.8%.

Family (1)	Family (2)	Family (3)
0.2622	0.4642	0.3306
-0.4733	0.4946	-0.307
0.3598		0.4164
		0.4795

5.4.2 RT tensile test of TNTZ-0.3O

Figure 5.31 exhibits sequential SE SEM photomicrographs of the gage section after 4.6% strain. The tensile axis was horizontal. Some boundary cracks were observed throughout the gage section. The UTS was 800 MPa. Figure 5.32 shows the pretest EBSD IPF map and corresponding sequential SE SEM photomicrographs for the same microstructure patch acquired during the RT TNTZ-0.3O test: (a) 0.9% strain, (b) 1.8% strain, (c) 2.9% strain, (d) 4.6% strain. As shown in Figure 5.32 (b), evidence of local plastic strain was observed at a stress level of 700 MPa. Furthermore, grain boundary cracks were observed in some grains at a plastic strain as low as 1.8%. As shown in Figure 5.33, few slip traces were evident in the grains next to cracks. The grain boundary cracks usually formed perpendicular to the tensile axis.



Figure 5.31 Low-magnification SE SEM micrograph of a RT deformed TNTZ-0.3O sample. Some boundary cracks were observed throughout the gage section. The tensile axis was horizontal.

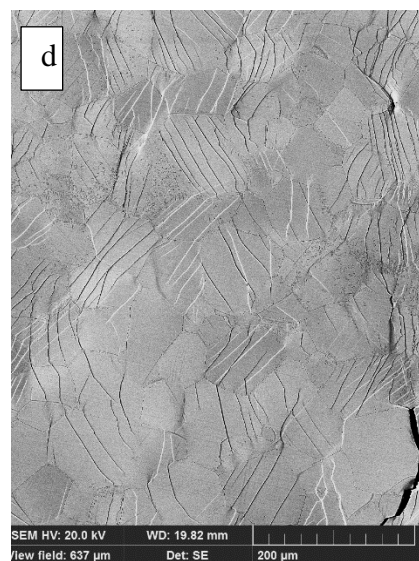
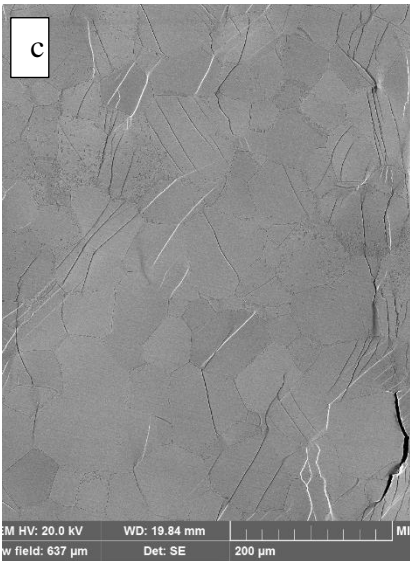
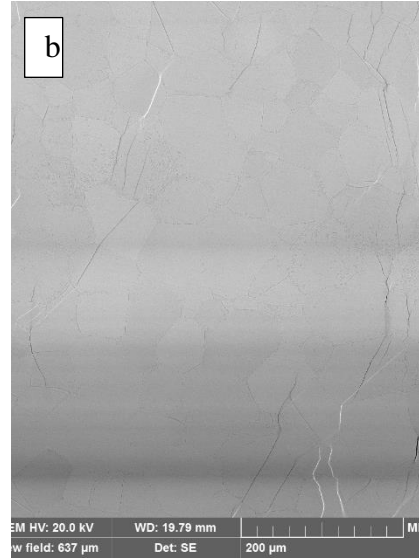
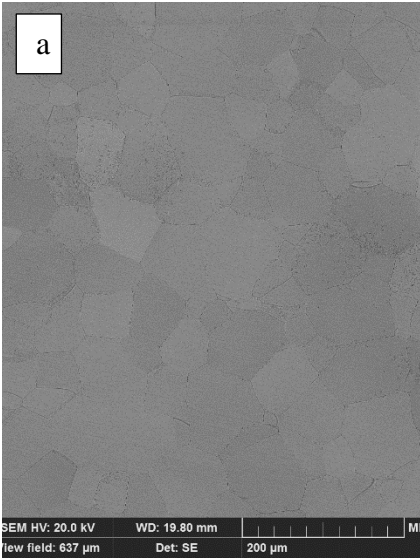


Figure 5.32 Sequential SE SEM photomicrographs acquired during the RT TNTZ-0.3O test: (a) 0.9% strain, (b) 1.8% strain, (c) 2.9% strain, (d) 4.6% strain, and (e) Pretest EBSD IPF map. Each of these images represents the same microstructural patch. The tensile axis was horizontal.

Figure 5.32 (cont'd)

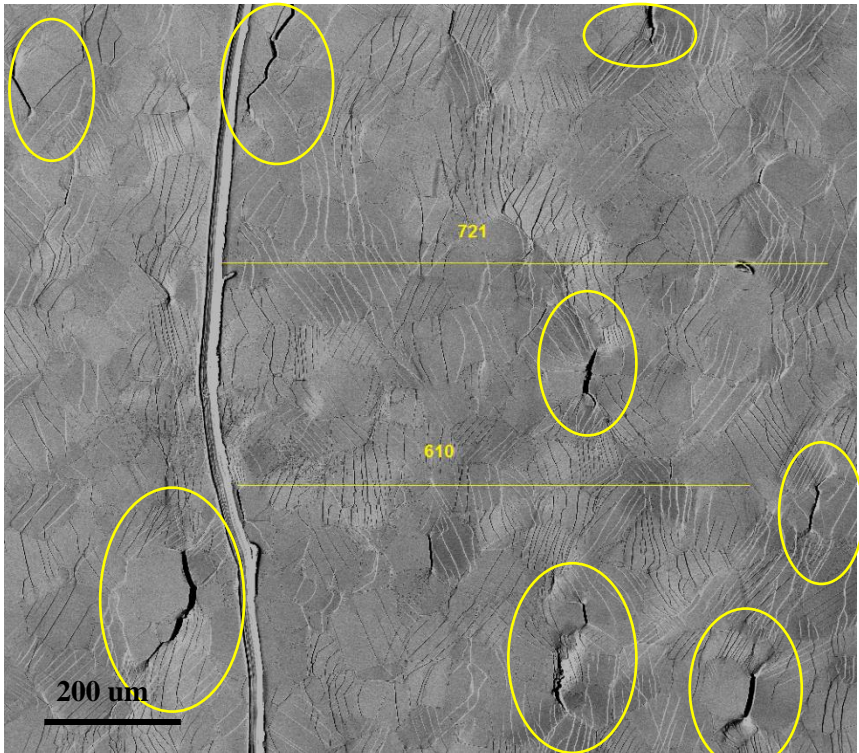
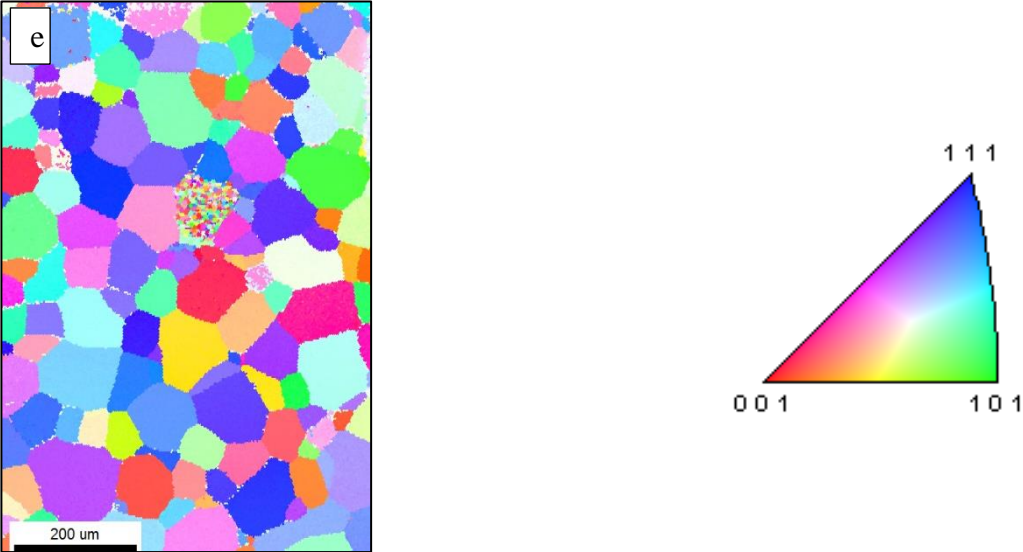


Figure 5.33 SE SEM photomicrographs indicating that the grain boundary cracks formed after 4.6% strain for the TNTZ-0.3O sample deformed at RT. Few slip trace lines were observed in the grains next to cracks. The cracks usually formed perpendicular to the tensile axis.

Figure 5.34 shows the distribution of the different slip modes (identified after 2.9% strain) versus the corresponding Schmid factor range. The slip trace analysis was performed on 215 grains (of which 177 grains exhibited at least one active slip system). The majority of the deformation systems belonged to Family (3) and the lowest contribution belonged to Family (1). The percentage contribution and normal distribution of the different slip modes will be discussed later in this chapter.

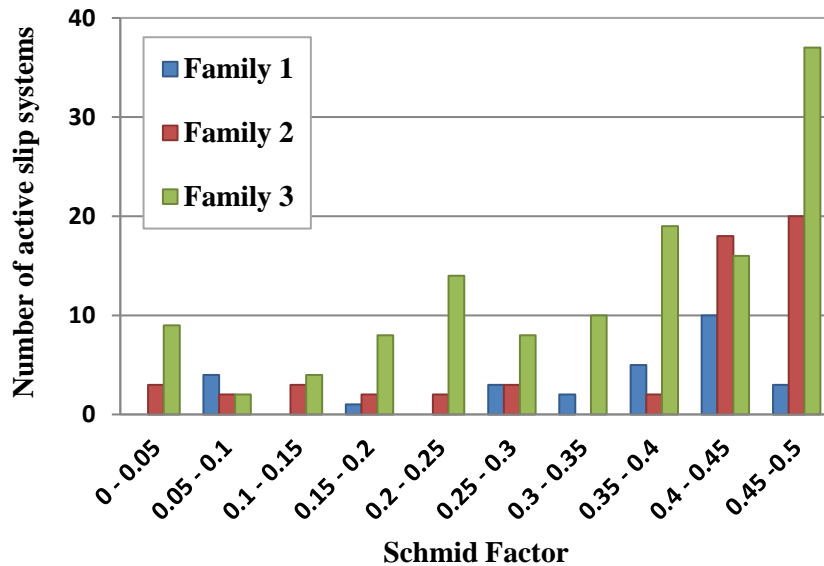


Figure 5.34 The histogram of Schmid factor distribution of slip systems for the TNTZ-0.3O at RT, tension experiment after ~2.9% strain.

5.4.3 RT tensile test of TNTZ-0.7O (Sample20-lhs)

Figure 5.35 exhibits a SE SEM micrograph of the gage section at low-magnification after 0.96 mm displacement. The tensile axis was horizontal. Some grain boundary cracks were observed throughout the gage section. The UTS was 975 MPa. Figure 5.36 shows the pre and posttest EBSD IPF map and corresponding sequential SE SEM photomicrographs for the same microstructure patch acquired during the RT TNTZ-0.7O test.

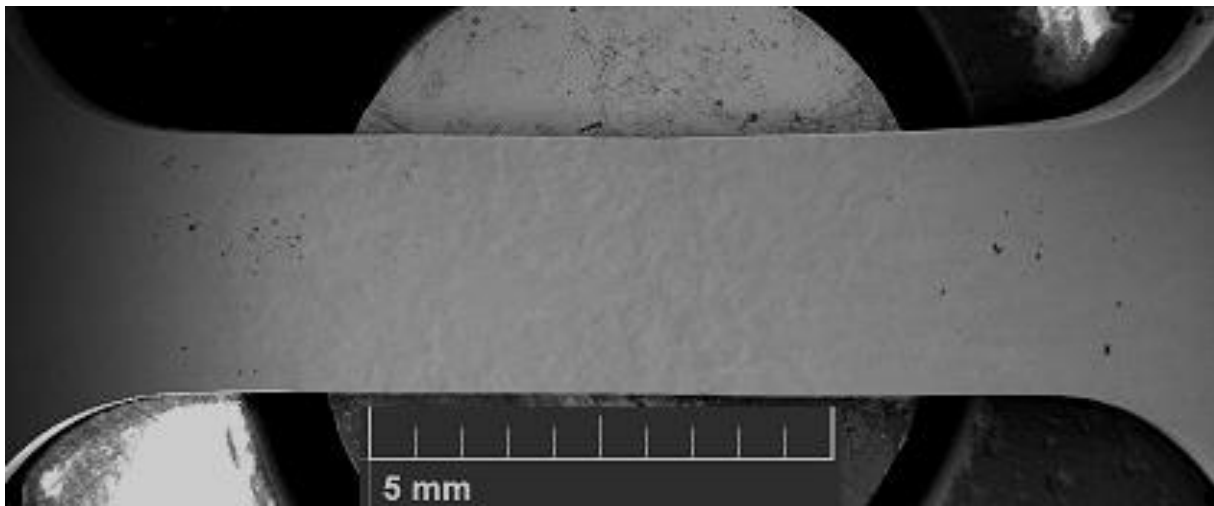


Figure 5.35 Low-magnification SE SEM micrograph of a RT deformed TNTZ-0.7O sample. Uniform plastic strain was observed throughout the gage section. The tensile axis was horizontal.

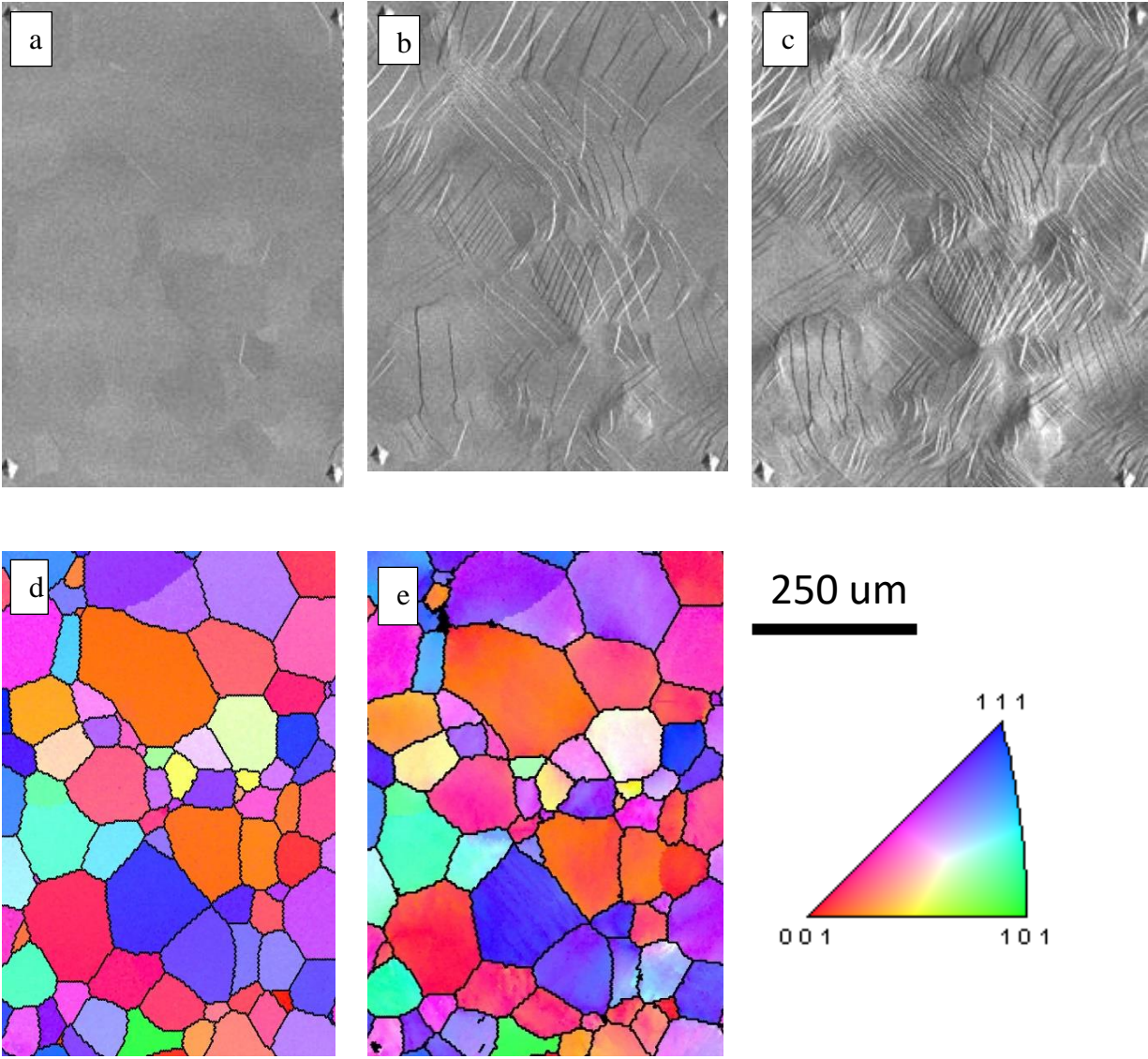


Figure 5.36 The sequential SE SEM photomicrographs acquired during the RT TNTZ-0.7O test (a) elastic region, (b) 1.4%, (c) 6.1% strain, and (d) Pretest EBSD IPF map, (e) posttest EBSD IPF map. Each of these images represents the same microstructural patch. The tensile axis was horizontal.

Figure 5.37 shows the distribution of the different slip modes identified at 6.1% strain versus the corresponding Schmid factor range. The slip trace analysis was performed on 84 grains. The majority of the deformation systems belonged to Family (3) and the lowest contribution belonged to Family (1). The percentage contribution and normal distribution of the different slip modes will be discussed later in this chapter.

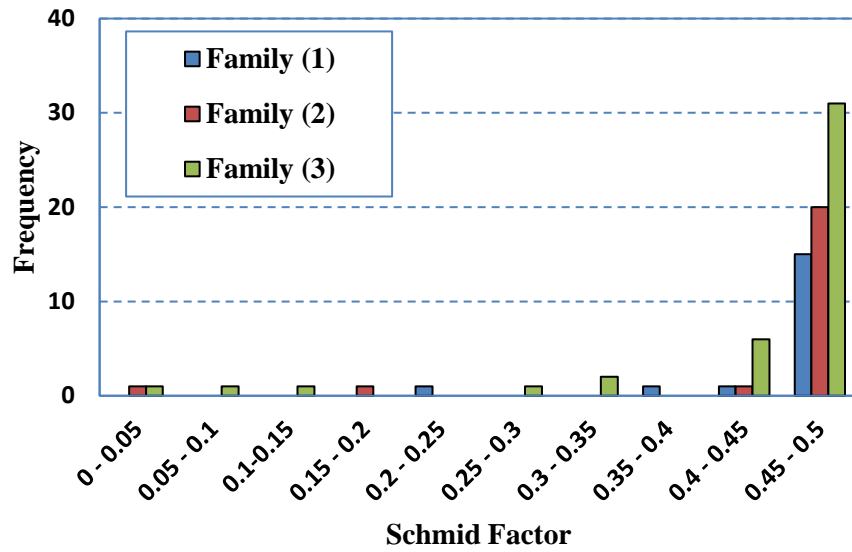


Figure 5.37 A histogram of Schmid factor distribution of slip systems for the TNTZ-0.70 sample tested to 6.1% strain at RT

5.5 Discussion

5.5.1 Microstructure

The TCFA and TIMETAL-21S samples were cut from solution treated sheets, which exhibited equiaxed β grains after cooling to RT. The TCFA samples exhibited grains with diameters ranging from $\sim 10 \mu\text{m}$ to $180 \mu\text{m}$ (see Figure 5.3). The average grain size was $\sim 50 \mu\text{m}$. The orientation gradient was relatively low within the grains for the as-received TCFA alloy. The TIMETAL-21S exhibited grains with diameters ranging from a few microns to $40 \mu\text{m}$ (see Figure 5.16). The average grain size was $\sim 15 \mu\text{m}$. The as-received TIMETAL-21S alloy showed low orientation variation within each grain. As shown in Figure 5.4 and Figure 5.17, both TCFA and TIMETAL-21S exhibited relatively weak textures (2.6 and 3 times random, respectively). Similar to the other two studied alloys, TNTZ-xO exhibited a relatively weak texture. Table 5.3 lists the distribution of the alloying elements for of the each studied alloys.

5.5.2 Mechanical proprieties

In-situ tensile SEM tests have been performed on the solution treated TIMETAL-21S and TCFA at RT, $200 \text{ }^\circ\text{C}$ and $300 \text{ }^\circ\text{C}$. TIMETAL-21S is a commercial β Ti alloy, which has been developed by TIMET company in 1988 for high temperature applications (Cotton et al., 2015). The TCFA alloy is a relatively new low-cost β Ti alloy that has been developed in Japan for structural and

Table 5-3 Summary of the distribution of the alloying elements

Material	Alloying element (wt.%)
TCFA	Ti (balance), Cr (13%), Fe (1%), Al (3%)
TIMETAL-21S	Ti (balance), Mo(15%), Nb(3%), Si (0.2%)
TNTZ-0.1O	Ti (balance), Nb(29%), Ta(13%), Zr(4.6%), O (0.1%)
TNTZ-0.3O	Ti (balance), Nb(29%), Ta(13%), Zr(4.6%), O (0.3%)
TNTZ-0.7O	Ti (balance), Nb(29%), Ta(13%), Zr(4.6%), O (0.7%)

biomedical uses (Ogawa et al., 2007). Both alloys exhibited a higher YS than the CP Ti due to solid solution strengthening. Both alloys exhibited little work-hardening at RT (see Figure 5.5 and Figure 5.18). Figure 5.40 compares the approximate YS values of the studied alloys as a function of test temperature. Although, the average grain size of the TCFA was ~3 times more than the TIMETAL-21S, the TCFA exhibited higher YS at all test temperatures. The higher YS of TCFA is attributed to its composition.

An increase in temperature usually results in a higher mean distance between the atoms, which leads to a reduction in the YS and UTS. A reduction in the UTS with an increase in temperature has been observed in many Ti alloys (Welsch et al., 1993). As expected, the TCFA YS decreased with an increase in the test temperature from RT to 300 °C (see the blue bars in the Figure 5.38). Similarly, the TIMETAL-21S YS decreased with an increase in the test temperature from RT to 230 °C. However, the TIMETAL-21S YS did not exhibit a significant decrease when the test temperature increased from 230 °C to 300 °C (see the orange bars in Figure 5.38). It should be noted the tensile test performed on TIMETAL-21S at 300 °C lasted 2 hr, as the test was paused several times during the test for acquiring the SE SEM photomicrographs. Thus, this abnormal behavior might be due to a phase transformation in the solution treated TIMETAL-21S at 300 °C [β phase to ω phase] (Mantri et al., 2015).

The TNTZ is a non-toxic and allergy-free β Ti alloy, which has been designed and developed for biomedical applications (Niinomi, 1998). The TNTZ exhibited a relatively low elastic modulus (less than 100 GPa) and good workability. However, its YS is not high enough to satisfy the requirement for the long service life in many implants (Geng et al., 2011). For enhancing the TNTZ YS and UTS, O has been added as a low-cost interstitial element. The UTS increased with

increasing O content (see Figure 5.39). Two mechanisms are expected to be responsible for the increase in the TNTZ UTS with an increasing in O content:

- (I) The interstitial O atoms may occupy the octahedral or tetrahedral interstitial sites in the crystal lattice of the β Ti alloys and thereby distort the lattice, which results in local stress fields that hinder the dislocation motion (Tahara et al., 2011). Higher O content results in a higher fraction of occupied sites and thus, more potential barriers for dislocation motion.
- (II) The solute O atoms may interact with screw and edge dislocations and impede the dislocation motion (Miura et al., 2001).

The measured YS values of the TNTZ-xO in this study were in a good agreement with the YS values reported in another laboratory (Geng et al., 2011). In this study, the measured UTS of the TNTZ-0.15 and TNTZ0.3 were ~500 MPa and ~800 MPa, respectively, which were similar to the values reported by Geng et al. (Geng et al., 2011). However, the measured TNTZ-0.7O UTS in this work was ~975 MPa, which was ~10% less than that reported by Geng et al. (Geng et al., 2011). This difference might be due to the fact that the specimens were cut from different ingots. Thus, the composition of the ingots in the current and previous work might not be exactly the same, especially with respect to the amount of the O content. As observed, only a small variation in the O content leads to a significant UTS change, which can explain the difference between the measured UTS values in two studies.

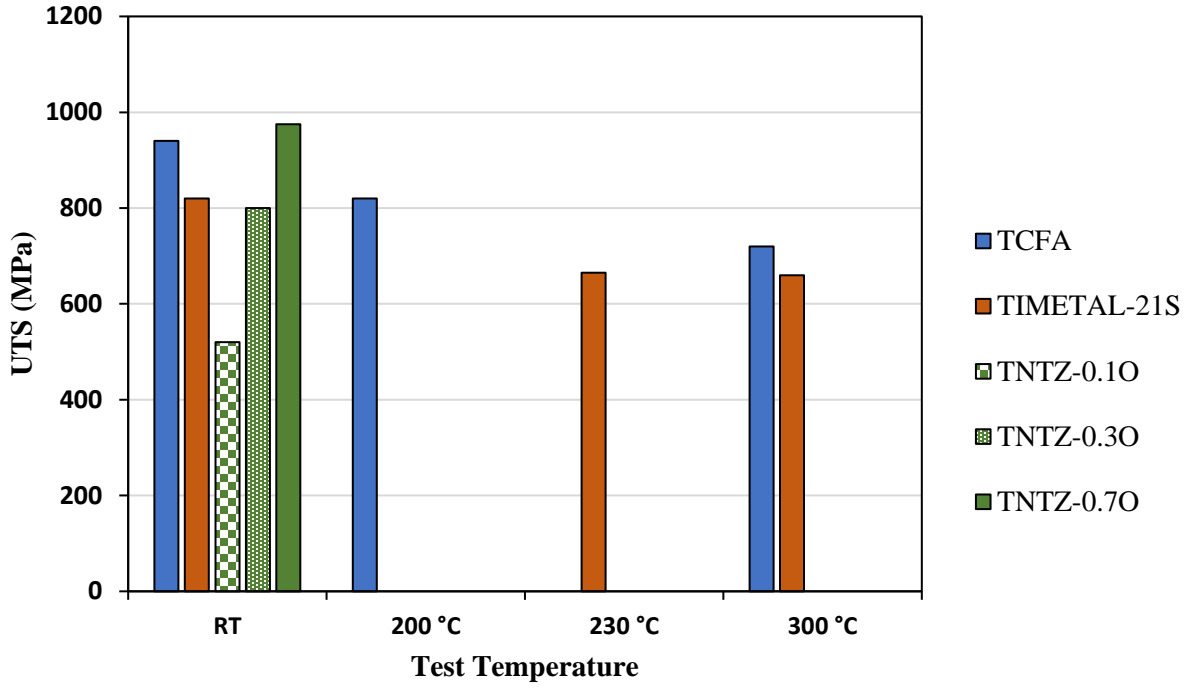


Figure 5.38 Approximate UTS values of the studied alloys as a function of test temperature

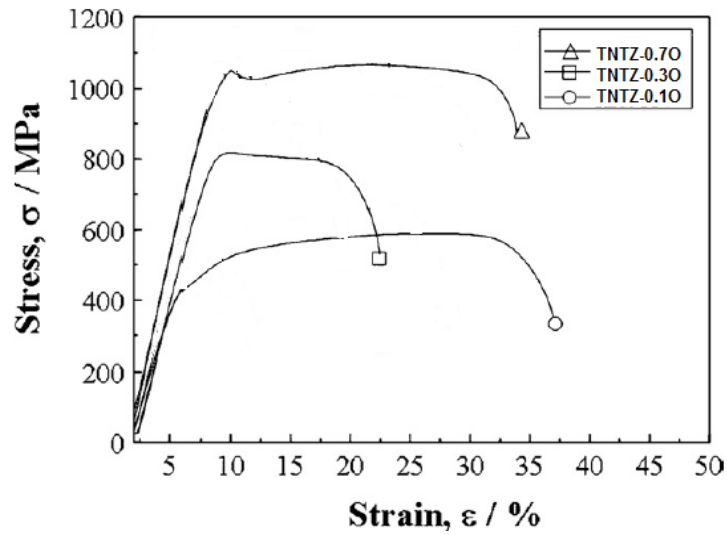


Figure 5.39 Tensile stress–strain curves of TNTZ–0.1O, TNTZ–0.3O, and TNTZ–0.7O (Geng et al., 2011)

5.5.3 Deformation mechanism

The plastic deformation of β Ti alloys is normally attributed to the activation of slip systems, while mechanical twinning and martensite transformation have been observed in some β Ti alloys (Lütjering and Williams, 2003). Unlike the fcc and hcp structures, there is no close packed plane for bcc crystals. In bcc materials, slip occurs in the close packed direction of the $\langle 111 \rangle$. The bcc materials exhibit a greater number of slip systems than fcc and hcp materials. 48 slip systems are distinguished in the bcc structure, while the fcc and hcp crystals have 12 and 24 slip systems, respectively. The high number of slip systems makes slip trace analysis of the bcc materials more complicated than the fcc and hcp materials. This complexity becomes more apparent considering that there are 42 different possible slip planes (6 belonging to the $\{110\}$, 12 belonging to the $\{112\}$, and 24 belonging to the $\{123\}$ systems, all with a Burgers vector of $\langle 111 \rangle$) in a 180° range of angles. Thus, there is 4.3° between each plane trace on average. Furthermore, there are some sources of uncertainty in determining the active slip systems using the 2D EBSD and SE SEM photomicrographs from the deformed surface such as:

- Misalignment of the sample during acquisition of the SE SEM photomicrographs and also during EBSD scan
- Error in measuring the slip trace angle from SE SEM photomicrographs (some slip traces may not be perfectly straight)
- Uncertainty in determining the Euler angles by the EBSD system

Due to the above-mentioned sources of uncertainty, a threshold angle of $\pm 4^\circ$ was considered to determine the active slip system based on the highest Schmid factor, as explained in 5.1.

5.5.3.1 TCFA and TIMETAL-21S

Slip was the dominant deformation mechanism for TCFA and TIMETAL-21S at temperatures between RT and 300 °C. As presented in the histograms of the observed slip traces versus Schmid factor, most of the observed slip systems occurred at relatively high Schmid factors (ranging from 0.4 to 0.5) (see Figure 5.8, Figure 5.14, Figure 5.21, Figure 5.26, Figure 5.34, and Figure 5.37). This was consistent with a previous slip trace study performed on ferritic (bcc structure) grains in a duplex stainless steel subjected to fatigue (Bartali et al., 2009; El Bartali et al., 2008). To calculate the Schmid factor, the global stress state (uniaxial tensile load) was applied, so that, the local stress variations were not considered. This assumption expects that the activation of the deformation modes was mainly influenced by the global stress state. However, some traces exhibited a relatively low Schmid factor (i.e., less than 0.2). Furthermore, approximately 5% of the visible slip traces did not match any of the slip systems within the $\pm 4^\circ$ threshold. Those observations might be an indirect indicator of the stress heterogeneity resulting from the neighboring-grain orientation and geometry or the activation of pencil glide (Gilormini et al., 1988; Taylor and Elam, 1926). Also, pencil glide states that slip occurs in the maximum resolved shear stress plane (MRSSP) in the $\langle 111 \rangle$ direction, even though the MRSSP may not even be one of the crystallographic planes.

The distribution of the active slip systems is presented for all the tests in Figure 5.40. The $\{123\}\langle 111 \rangle$ slip system (Family 3) was the most frequently observed system, while the $\{110\}\langle 111 \rangle$ slip system (Family 1) was the least frequently observed system. For a ‘sanity check’ of contribution by slip systems in this work, a total of 485 slip traces were analyzed and discussed with respect to the following three scenarios for a TCFA sample tensile loaded to 12% at RT as follows:

- I. Only the $\{110\}$ slip system was considered.

- II. only the {110} and {112} slip systems were considered.
- III. All three slip systems ({110}, {112}, and {123}) were considered.

For all, the threshold angle was constant ($\pm 4^\circ$). Only 99 slip traces, ~20% of the total observed slip traces, matched when the first scenario was considered. In other words, 80% of the observed traces were not in the vicinity of any of the {110} slip systems at a threshold angle of $\pm 4^\circ$. This confirms that most of the slip systems did not belong to the {110}<111> system. As shown in Figure 5.41(a), most of the matched traces exhibited a high Schmid factor (>0.4) in the first scenario. This implies that the activated {110} slip systems obeyed the Schmid law. In the second scenario, where the {110} and {112} slip systems were taken into account, 333 traces (~70% of the total observed traces) were associated to one of the {110} and {112} slip systems [$\sim 17\%$ belonged to the {110} and $\sim 52\%$ to the {112}], see Figure 5.41(b)]. Similar to the first scenario, the matched slip systems exhibited a relatively high Schmid factor (>0.4) in the second scenario. However, ~30% of the observed slip traces did not match the {110} nor the {112} slip systems. The unmatched traces might have been activated by the {123} slip system or by pencil glide. For the third scenario, where all three systems were considered, ~95% of the traces matched with a relatively high Schmid factor (>0.4). This implies that 5% of the active systems should be activated by pencil slip [see Figure 5.41(c)]. Approximately, 50% of the observed traces were associated with the {123} system, while ~13% and 33% matched with the {110}<111> and {112}<111> in the third scenario, respectively.

The contribution of the {110} <111> slip system was slightly higher in the scenario I compared with scenarios II and III. Although, the contribution of the {110}<111> slip system was less than 20% in all of the studied scenarios, the results of the scenario II suggests that most of the slip activities occurred in the {112}<111> systems (~50%), while the scenario III suggests that the

contribution of the $\{123\}\langle 111\rangle$ was the highest (~50%) and the $\{112\}\langle 111\rangle$ was ~30%. This implies that for ~20% of the observed traces, at least one possible slip system of each of the $\{112\}$ and $\{123\}$ slip systems existed with a threshold of $\pm 4^\circ$ and the Schmid factor of the $\{123\}\langle 111\rangle$ slip system was higher than the corresponding Schmid factor of the $\{112\}\langle 111\rangle$ slip system.

Although dislocation activity has been observed in all three slip systems ($\{110\}$, $\{112\}$, and $\{123\}$) in tensile tests inside a TEM on a β Ti alloy (Castany et al., 2012), in other studies only the $\{110\}\langle 111\rangle$, $\{112\}\langle 111\rangle$, or/and the pencil glide were active slip systems (Franciosi et al., 2015; Gilormini et al., 1988; Hsiung, 2010; Taylor and Elam, 1926; Weinberger et al., 2013). The result of this work (third scenario) suggested that the $\{123\}\langle 111\rangle$ had the most contribution to the slip activities of studies bcc Ti alloys.

This might be due to the composition of the studied alloys, conditions, and assumptions of the slip trace analysis of the current work. In this study, the CRRS was assumed to be equal for all three slip systems and the global uniaxial stress was conserved for all the grains. Furthermore, the texture was relatively weak for studied alloys. Consequently, the probability of the activation of each of the slip systems is proportional to the number of the associated planes to the corresponding slip systems. Figure 5.40 (b) presents the normalized slip activity according to the possible slip planes of each system, i.e. the observed slip belonged to the $\{123\}$ and $\{112\}$ systems divided by 4 and 2, respectively. The normalized activity of all the systems for the TCFA were ~30%, while the $\{112\}$ system was slightly greater than the other two. However, for the TIMETAL-21S, the activity of the $\{110\}$ system was ~40%, while the activity of the $\{112\}$ and $\{123\}$ systems were ~35% and ~25%, respectively. It should be noted that it is possible that the observed slip traces might be activated by pencil glide, so then it would be happenstance that they matched the

crystallographic slip traces. One would need to look at the slip traces at the atomistic scale to verify it.

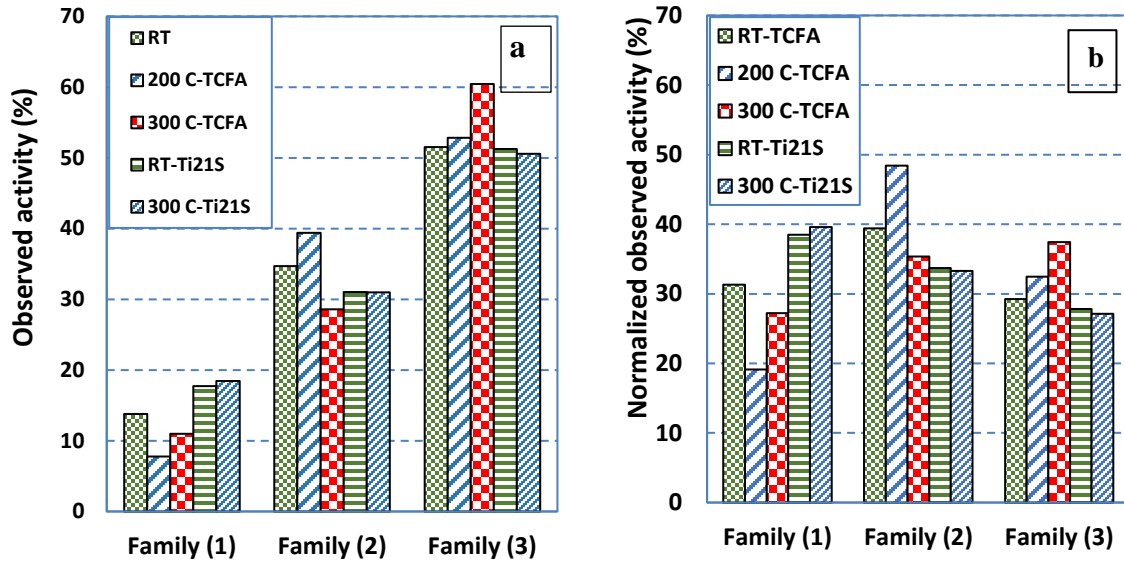


Figure 5.40 The observed activity of the different families of slip systems for each of the test temperatures. (a) The analyzed data show that Family (3) exhibited the highest activity at each temperature. (b) The total observed traces for each Family was divided by the total number of possible slip planes for the corresponding Family and this represented the normalized data. The normalized data illustrate that the contribution of Family (2) was slightly higher than that for the other two Families for TCFA. However, the contribution of Family (1) was the most and the contribution for Family (3) was the least for the TIMETAL-21S.

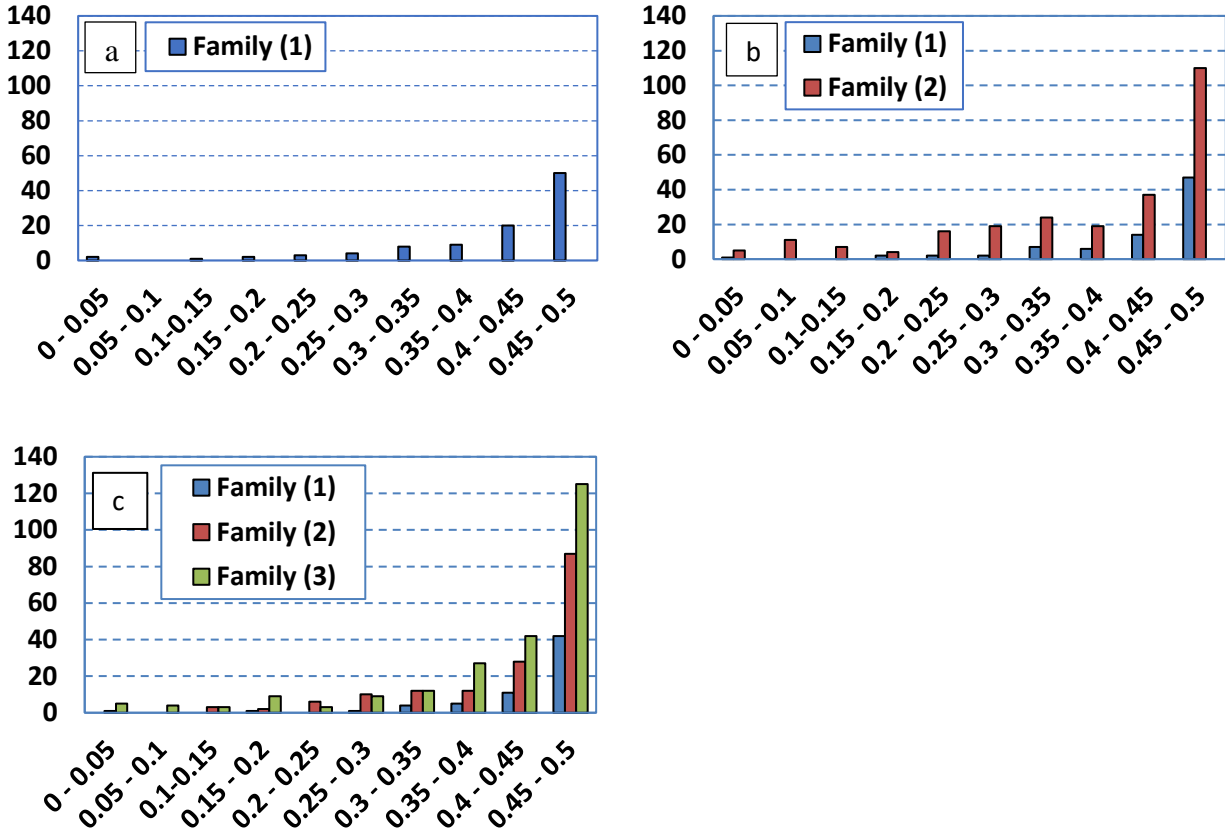


Figure 5.41 A histogram of the Schmid factor distribution of the slip systems for TCFA samples tested at RT to 8.4% strain for 485 observed traces. (a) only ~20% of the observed traces were matched when the $\{110\}\langle 111\rangle$ slip system was considered, (b) ~70% of the observed traces were matched when the $\{110\}\langle 111\rangle$ and the $\{112\}\langle 111\rangle$ slip systems were considered, and (c) ~95% of the observed traces were matched when all three slip systems were considered.

5.5.3.2 TNTZ-xO

Stress-induced martensitic (SIM) transformation, machinal twinning, and slip activities were observed in the TNTZ-0.1O after plastic deformation. The XRD and TEM investigations on the deformed sample revealed that the SIM transformation (the β phase to the orthorhombic (α'') phase) occurred during plastic deformation in the TNTZ-0.1O (Liu et al., 2017b). The SIM transformation has been frequently observed in other β Ti alloys during mechanical loading (Talling et al., 2009; Xing and Sun, 2008; Yang et al., 2008, 2010). During straining, the lattice of the β unit cell became slightly larger in one direction and smaller in other two directions. The lattice parameter changes caused the β phase to be transformed to the α'' phase. Furthermore, it has been reported that the low O content in Ti alloys enhances twinning (Zaefferer 2003). For example, the Ti with 1000 ppm (0.1 wt.%) O exhibits more twinning activity than the Ti with 2000 ppm (0.2 wt.%) O (Zaefferer 2003). Similarly, $\{332\} \langle 113 \rangle$ mechanical twinning formed during loading in the TNTZ-0.1O, as shown in Figure 5.29. This is consistent with a previous study by Bertrand et al., where they reported that $\{332\} \langle 113 \rangle$ mechanical twinning systems forms in some bcc alloys, when the SIM transformation occurs (Bertrand et al., 2011). In addition to twinning and SIM α'' transformation, very fine slip traces were also observed in the SE SEM photomicrographs of the current work (see Figure 5.30). It is believed that such slip was activated after the twinning and SIM transformation (Liu et al., 2017b). As shown in Figure 5.39, the TNTZ-0.1O exhibited strain hardening. At the initial stage of plastic deformation, the RSS was not high enough to activate any slip system. However, the stress was high enough to activate the SIM transformation and twinning. During the straining, the RSS was increased due to hardening. At some threshold stress level, the RSS became equal to the CRSS, which led to initiation of the slip activity.

Slip was the primary deformation mode for the TNTZ-0.3O and TNTZ-0.7O, i.e. neither martensitic transformation nor twinning was observed during straining. This indicated that the O suppressed the twinning and the SIM transformation. These results are consistent with other studies. For example, no twinning occurred during deformation at higher O contents in Ti-23Nb-0.7Ta-2Zr-xO (x was 0 and 1.2), where the martensite α'' phase was also suppressed by the addition of oxygen during quenching (Besse et al., 2011). Mechanical twinning and SIM transformation are more likely in Ti alloys with relatively unstable β phase and this leads to lower YS values and larger elongation-to-failure values. However, when the β phase is stable, slip is the dominant deformation mechanism and results in higher YS values (Hanada and Izumi, 1987; Liqiang et al., 2009). O is usually considered to be an α stabilizer due to the fact that the β transus temperature increases with increasing O content (Geng et al., 2011). In contrast, the presence of O suppressed the formation of the α'' and the ω phases, which suggests that O behaves as a β stabilizer in some β Ti alloys (Besse et al., 2011; Hickman, 1969; Qazi et al., 2005). In this work, the O addition enhanced the YS and also suppressed the SIM transformation and mechanical twinning during deformation, which indicated that O acted as a β stabilizer in the TNTZ-xO alloys.

This phenomenon can be explained as follows. Both mechanical twinning and SIM transformation are diffusionless processes. Twinning occurs due to simultaneous and homogenous motion of a groups of the atoms parallel to the twinning plane due to a uniform shearing of the atoms parallel to the twin boundary. During the SIM transformation, a group of atoms moves cooperatively and homogeneously that leads to a change in the crystal structure, unlike the twinning in which the crystal structure remains the same. On the other hand, the O atoms occupy the octahedral and tetrahedral interstitial sites in bcc Ti alloys, which introduces local stress-strain fields within the crystalline lattice (Tahara et al., 2011). The local stress-strain fields prevent

homogenous atomic rearrangements, which is required for both twinning and SIM transformation. Therefore, the addition of O serves as an obstacle and suppresses the mechanical twinning and SIM transformation in TNTZ-xO.

Although, the TNTZ-0.7O UTS was higher than the TNTZ-0.3O UTS, the elongation-to-failure of the TNTZ-0.7O exhibited an abnormal behavior, i.e. the TNTZ-0.7O ϵ_f was greater than the TNTZ-0.3O ϵ_f . In another β Ti alloy (Ti-35Nb-7Zr-5Ta), the YS increased from 937 MPa to 1081 MPa, when the O content increased from 0.46 wt.% to 0.68 wt.%. Similar to the TNTZ-xO, the ϵ_f increased with increased O content (Qazi et al., 2004). However, no explanation was provided for that observation.

As shown in Figure 5.42(a), many intergranular cracks observed at ~5% strain in a tensile tested TNTZ-0.3O sample, which was consistent with results of Geng et al., (2011) and Liu et al., (2017b). Some of those cracks were initiated at a low strain of ~2%, which was the early stage of plastic deformation (see Figure 5.43). The cracks propagated tortuously throughout other grain boundaries at ~3% strain. At ~5% strain, the cracks appeared to widen. No new slip traces occurred within the grains at the crack edges due to the fact that those areas were within the stress-free zone. On the other hand, no cracks were observed in the deformed TNTZ-0.7O. The propagation and accumulation of the cracks led to early fracture of the TNTZ-0.3O compared to the TNTZ-0.7O. Furthermore, the observed slip activity was higher and more homogenous in the TNTZ-0.7O compared with the TNTZ-0.3O. The SE SEM microphotographs of both alloys are provided at similar strain level in Figure 5.44. Few slip traces were observed in the TNTZ-0.3O at ~5% strain as illustrated in the red ovals in Figure 5.44(a), while substantial and relatively more homogenous slip occurred in TNTZ-0.7O at ~6% strain.

The frequency of observed slip traces was relatively low in some areas of TNTZ-0.3O. As highlighted in white ovals in Figure 5.42, most of the cracks initiated in the regions where less slip traces were observed. The heterogeneous slip activities might be due to the inhomogeneous O distribution in TNZT-0.3O. As discussed above, the CRSS was relatively high in TNTZ-0.1O, which resulted in activation of the SIM transformation and twinning in the early stages of plastic deformation. Similarly, the CRSS might be higher in the areas of the TTNZ-0.3O where the O content was lower. In the other regions, where the O content was higher, the CRSS may have been relatively lower, such that slip activity could accommodate the plastic deformation. Consequently, the lower slip activities resulted in crack initiation to accommodate the local deformation in those areas. Some of these cracks initiated at the grain boundaries of grains close to the hard orientation, i.e. the crack initiated in the vicinity of the $\{111\}$ oriented grains with respect to tensile direction, which are highlighted with back dashed-lines. In-situ tensile TEM experiments and/or numerical simulation on the TNTZ-0.3O and TNTZ-0.7O is essential to provide an accurate and detailed explanation of this abnormal behavior.

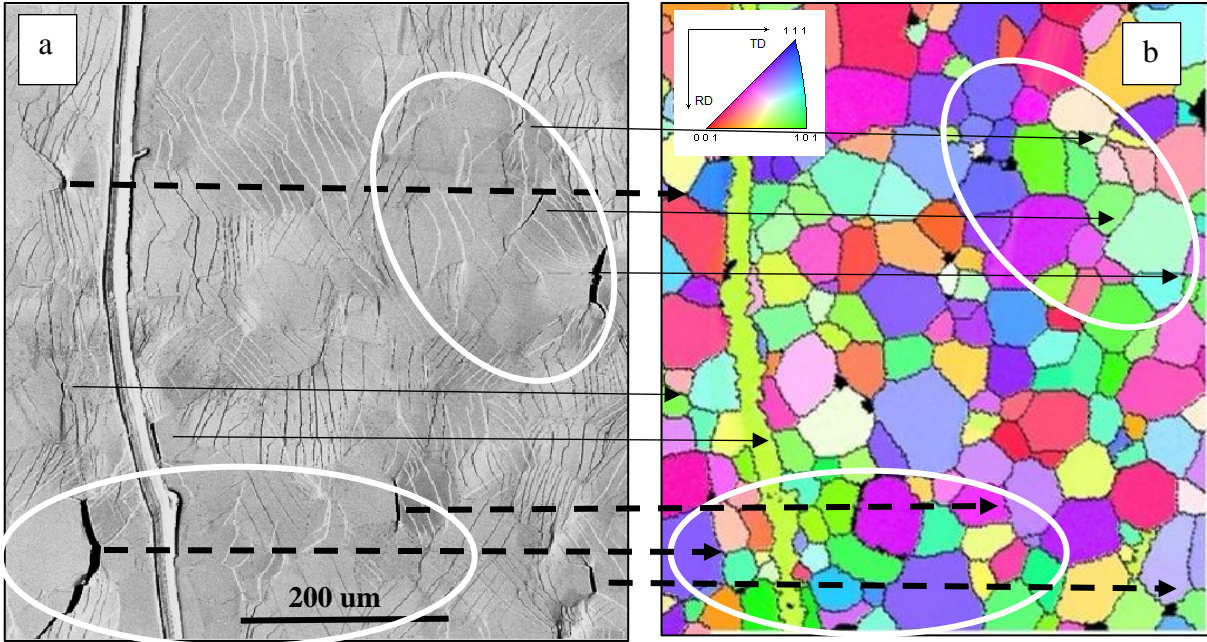


Figure 5.42 (a) SE SEM micrograph of a TNTZ-0.3O sample after ~5% strain. Some intergranular cracks observed, where some of them initiated in vicinity of a grain close to the hard orientation, the {111} with respect to tensile direction, as indicated with dashed-lines in (b) EBSD IPF maps. Two areas, where the observed slip activity was relatively low, are indicated by white ovals. The non-homogenous O distribution might be the reason for heterogenous slip activity. The scratch was scribed before the test as a fiducial marker.

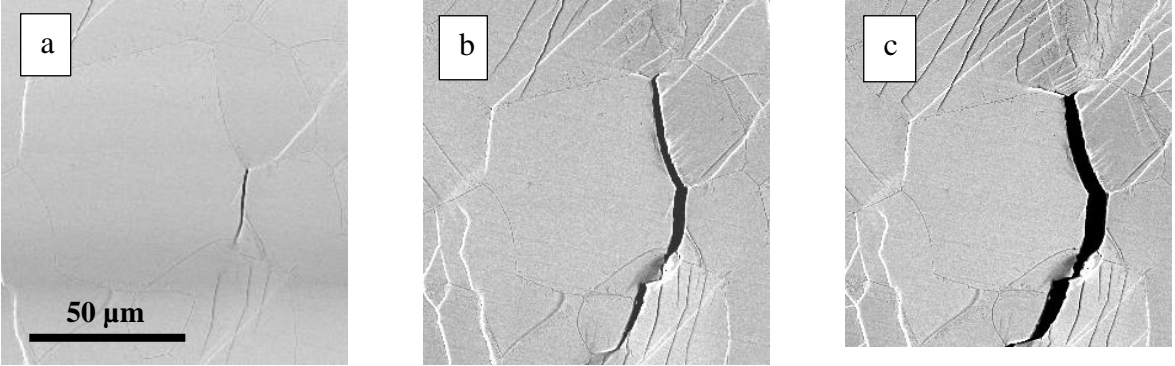


Figure 5.43 Some cracks initiated at relatively small strains in a tensile tested TNTZ-0.3O sample. One crack initiated at (a) ~2% strain and then (b) propagated both upward and downwards throughout other grain boundaries (3% strain), and (c) started to open at 5% strain

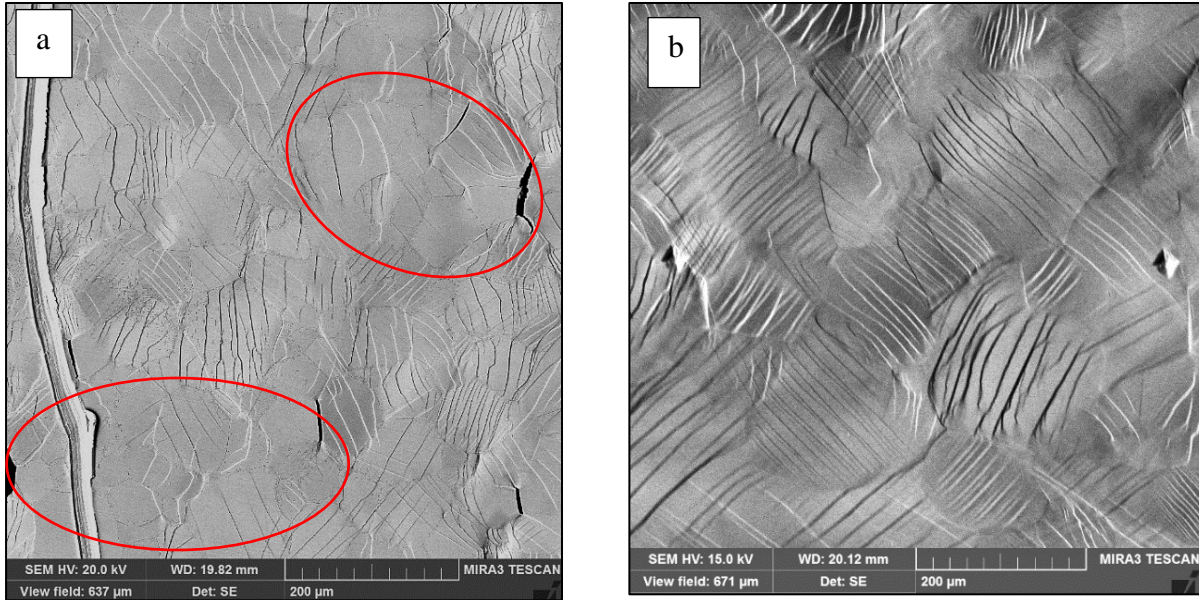


Figure 5.44 (a) TNTZ-0.30 after ~5% strain, the red ovals indicate that some grains exhibited few traces (the scratch was scribed before the test as marker for measuring the strain) and (b) TNTZ-0.70 at ~ 6% strain (the Vickers indents were made before the test for measuring the strain)

5.6 Summary and Conclusion

Identifying the distribution of the slip activity has been a challenging task in bcc materials compared with the fcc and hcp materials. This is mainly due to the lack of the close packed planes in the former. The bcc slip activity is mainly attributed to the $\{110\}\langle 111\rangle$ and $\{112\}\langle 111\rangle$ slip systems, while the $\{123\}\langle 111\rangle$ system has also been observed. However, it has been reported that some bcc materials do not obey the Schmid law, where the slip may occur in the plane with the MRSSP in the close packed direction ($\langle 111\rangle$), even without crystallographic planes (Pencil glide).

In this work, the slip activity of two bcc Ti alloys have been investigated based on the observed surface slip traces of the deformed specimens inside a SEM. The slip trace analysis results revealed that ~ 95% of the observed traces could be associated with one of three slip system for the TCFA and TIMETAL-21S using a threshold of $\pm 4^\circ$. Although, the Schmid factor was relatively high (>0.4) for most of the observed traces, in some of the grains the Schmid factor was less than 0.2. This might indicate that the stress states were locally heterogeneous.

The $\{123\}\langle 111\rangle$ systems exhibited the highest contribution, while the $\{110\}\langle 111\rangle$ showed the least contribution of the observed traces. However, the normalized slip activity suggested that the activity of all the systems were relatively equal for the TCFA, while the activity of the $\{110\}\langle 111\rangle$ was slightly greater than other two slip systems in the TIMETAL-21S. For a sanity check of this observation, slip traces analysis was performed on ~500 traces, where the $\{110\}\langle 111\rangle$ systems were considered as the only possible slip systems. In this scenario, only ~20% of traces matched. In the second scenario, both the $\{110\}\langle 111\rangle$ and $\{112\}\langle 111\rangle$ were considered, where more than 70% of traces were associated with one slip system. Hence, at least 30% of the active slip systems belonged to the $\{123\}\langle 111\rangle$ and/or MRSSP in those bcc Ti alloys. It should be noted that it is possible that the observed slip traces might be activated by pencil glide, so then it would be

happenstance that they matched crystallographic slip traces. One would need to look at the slip traces at the atomistic scale to verify it.

The effect of O content on the mechanical properties and deformation mode of the TNTZ-xO alloys was investigated in the second part of this chapter. The TNTZ-0.1O exhibited the largest elongation-to-failure compared with the other two TNTZ-xO alloys. This was explained to be a result of the activation and cooperation of three deformation mechanisms, i.e. SIM transformation (β phase to α'' phase), $\{332\}\langle 113\rangle$ mechanical twinning, and the slip activity. The higher content of the O suppressed both mechanical twinning and SIM transformation. Slip was the primary deformation mode for both TNTZ-0.3O and TNTZ-0.7O. The TNTZ-0.7 exhibited greater UTS and ε_f values. In-situ SEM tensile tests revealed the initiation of intergranular cracks at the early stage of the plastic deformation in the TNTZ-0.3O. The crack propagation and accumulation accelerated the fracture of the TNTZ-0.3O. On the other hand, no cracking occurred in the TNTZ-0.7. In addition, the SE SEM microphotographs indicated that the slip activity was more homogenous in the TNTZ-0.7O, which might be a consequence of a more homogenous distribution of the O atoms throughout the TNTZ-0.7O. In-situ tensile TEM study may provide a more accurate and detailed explanation for this abnormal behavior. The slip trace analysis suggested that the $\{123\}\langle 111\rangle$ had the greatest contribution to the plastic deformation for both TNTZ-0.3O and TNTZ-0.7O, similar to the TCFA and TIMETAL-21S.

CHAPTER 6

6 ENHANCING THE STRENGTH OF TCFA

In this Chapter, the influence of heat treatment and thermomechanical processes on the TCFA UTS have been investigated. A detailed characterization, beyond the scope of this dissertation work, will be performed by another MSU PhD graduate student, Ms. Joann Patricia under the supervision of professor Carl Boehlert. In the following section, the approximate temperature range of the phase transformation has been determined. Heat treatments have been performed to study the effect of the phase transformation on the hardness, which provided us a rough estimation of the UTS. Thermomechanical experiments have been conducted inside a SEM at the target temperatures (from ~ 400 °C to ~ 500 °C) and loads to study the effect of temperature and loading on the TCFA UTS. The results are discussed in section 6.6, which is followed by the summary for this Chapter.

6.1 Determining the temperature range of phase transformation

For determining the temperature range of the phase transformations for TCFA, Dynamic Mechanical Analysis (DMA) and Differential Scanning Calorimetry (DSC) were used. As provided in section 3.1.8, DMA was used to determine the phase transformation by measuring the phase lag between the applied stress and the corresponding strain. A rectangular specimen ($50 \times 7 \times 0.75$ mm³) was used for the DMA test. In the DMA test, the temperature was raised from RT to 500 °C at an approximate rate of 2 °C per minute. Figure 6.1 shows the Storage Modulus and $\text{Tan}(\delta)$ versus temperature, where δ is the phase angle between the loss modulus and the storage modulus (see section 3.1.8). The local maximum and minimum of $\text{Tan}(\delta)$ represent the temperature range of the phase transformation, which was between ~ 385 °C and ~ 450 °C. The

results of the DSC test indicated a change in the slope of the heat flux versus temperature at ~380 °C (see Figure 6.2). The local drop of the Storage Modulus (E') might be due to the test error, at ~350 °C and 400 °C. For example, a change in sample position or undesirable temperature variation might have occurred during the experiment.

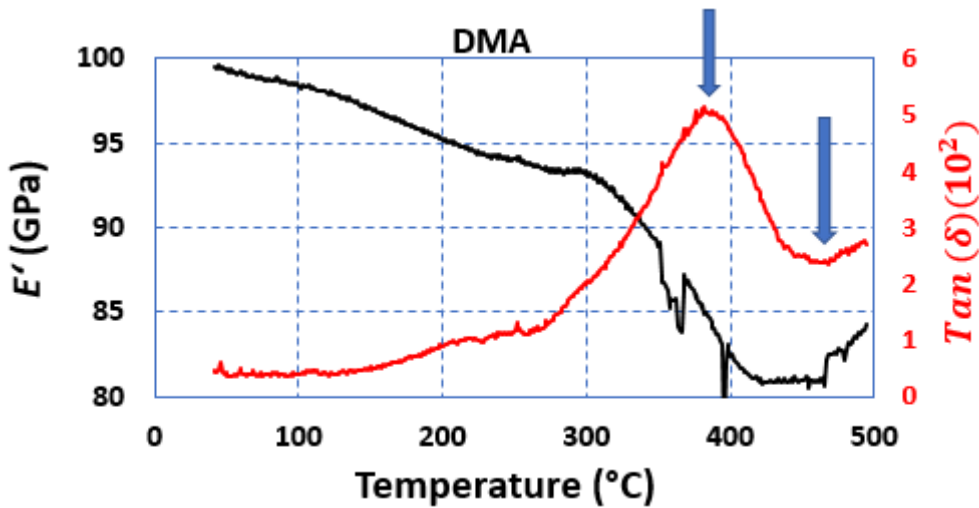


Figure 6.1 The storage Modulus (E') and $Tan(\delta)$ versus temperature for the TCFA alloy, obtained by a DMA test. The local maximum and minimum of $Tan(\delta)$ represents the temperature range of the phase transformation, which occurred between ~ 385 °C and ~450 °C

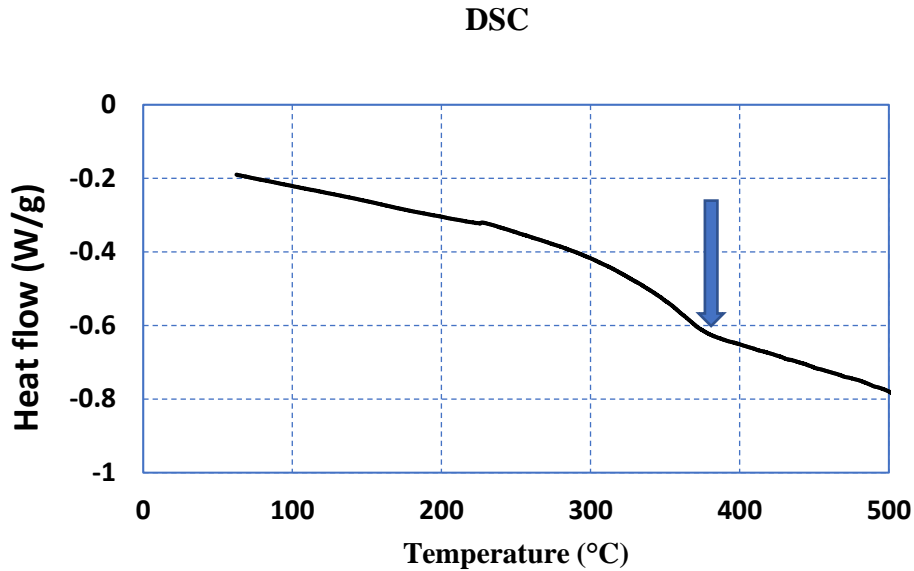


Figure 6.2 A slight change in slope of heat flux versus temperature is seen at $\sim 380^\circ\text{C}$ for the TCFA alloy, which indicates a phase transformation occurred.

6.2 Heat treatment

Heat treatment was performed on the as-received TCFA samples using an electrical vacuum tube furnace. For real-time temperature measurement, a test set up was designed and fabricated as shown in Figure 3.3. The samples were placed in a vacuum tube and manually heated until they reached the target temperature. This step took between 30 minutes to one hour. The sample was then soaked at the target temperature for 2 hours. Then, the sample was air-cooled to RT. By rough polishing (using 200 grit paper), ~ 0.1 mm of the surface was polished to remove the oxidation layer. Then following the procedure explained in 3.3, the samples were polished to a mirror surface. Vickers hardness tests were performed on the surface of the polished samples. The measured hardness is presented in Figure 6.3 as a function of the heat treatment temperature. Each data point represented the average of at least three measurements. The results indicated that the

hardness increased with an increase in temperature up to 500 °C. However, for the temperature range between 500 °C to 600 °C, the hardness decreased with increasing temperature. Figure 6.4 shows the SE SEM photomicrographs of the microstructure of TCFA after heat treatment for 2 hours. A second phase was visible in the SE SEM photomicrographs after the heat treatment at temperatures of 500 °C and above.

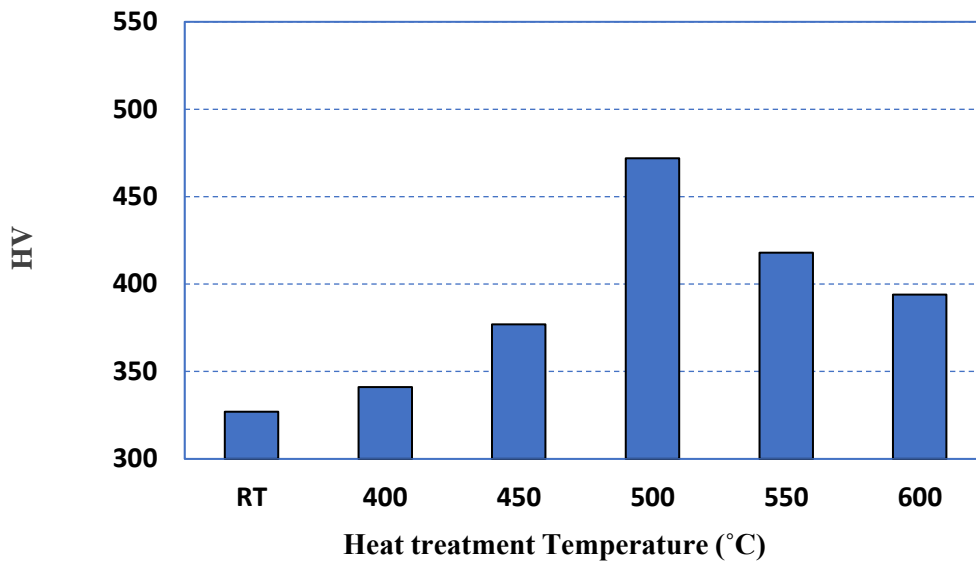


Figure 6.3 The effect of heat treatment on the Vickers hardness of TCFA. The samples were heated for 2 hours at the target temperature and then air-cooled.

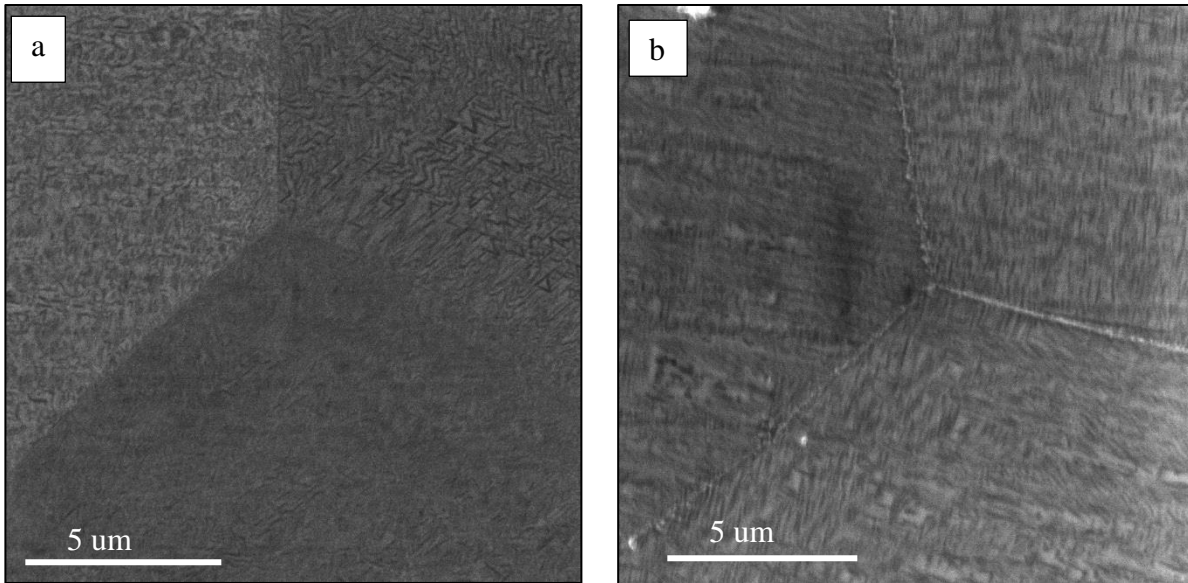


Figure 6.4 The microstructure of the TCFA after heat treatment for 2 hours at (a) 500 °C and (b) 550 °C. The microscale precipitates were observed in both samples, and are believed to be the α platelets. Also, the continuous layers at the grain boundaries in (b) might be α layers (Lütjering and Williams, 2003).

Figure 6.5 presents the hardness of the samples that were heat treated at temperatures between 350 °C to 450 °C for 24 hours. The hardness increased from ~320 Hv to 520 Hv. The maximum hardness (~500 Hv) was achieved after heat treatment at 410 °C and the minimum hardness (436 Hv) was achieved after the 300 °C heat treatment. For investigating the effect of aging time, the samples were heat treated for 6, 12, 24, and 48 hours at 410 °C. As shown in Figure 6.5 (blue curve), the hardness increased with an increase in heat treatment duration up to 24 hours. No significant change in hardness was observed with increased heat treatment after 24 hours.

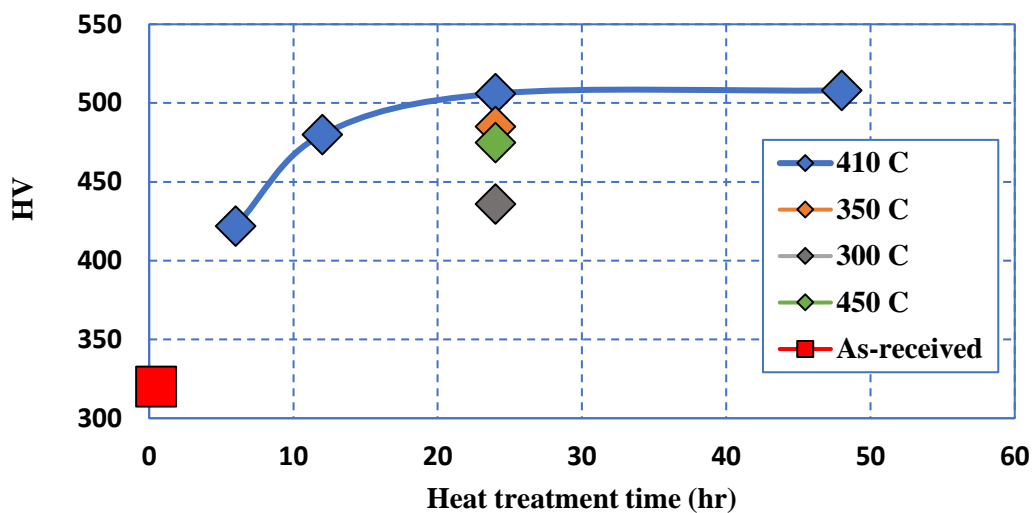


Figure 6.5 The effect of heat treatment temperature and duration on the Vickers hardness for temperatures between 300 °C and 450 °C, aged for 24 hr. The maximum hardness (506 Hv) was obtained after the heat treatment at 410 °C for 24 hours. The measured hardness as a function of aging time at 410 °C (blue curve). No significant change was observed in the hardness of the samples aged for 24 hours and 48 hours.

6.3 In-situ tensile test at 400 °C

In-situ tensile tests were performed inside a SEM at ~400 °C to investigate the effect of temperature and loading on the mechanical properties and deformation behavior of TCFA. SE SEM photomicrographs were acquired during the tests. Figure 6.6 presents the stress-displacement curve for a test that was performed at 400 °C and lasted for ~ 1.5 hours (due to pausing for acquiring SE SEM photomicrographs). The drop in the stress indicated the stress relaxation that occurred during each pause. Comparing the heated central zone and the outside of heated zone, more severe plastic deformation was observed outside of the heated region, which resulted in two necking areas at 850 MPa [see Figure 6.7a)]. This stress was significantly higher than the UTS of this alloy at 300 °C, which was 720 MPa. This suggested that the central heated region underwent a phase

transformation that strengthened the alloy such that the strength of the heated zone became higher than the strength of the region outside the heated zone. The high-resolution SE SEM photomicrographs of the necked area and the center of the gage length are shown in Figure 6.7(b) and (c), respectively. The hardness of these two regions was measured after the test. The Vickers hardness of the central heated zone was ~ 500 Hv, while the hardness outside of the heated region was ~ 340. It is noted that the as-received hardness was ~ 320 Hv. This significant difference suggested that a phase transformation occurred within the heated region.

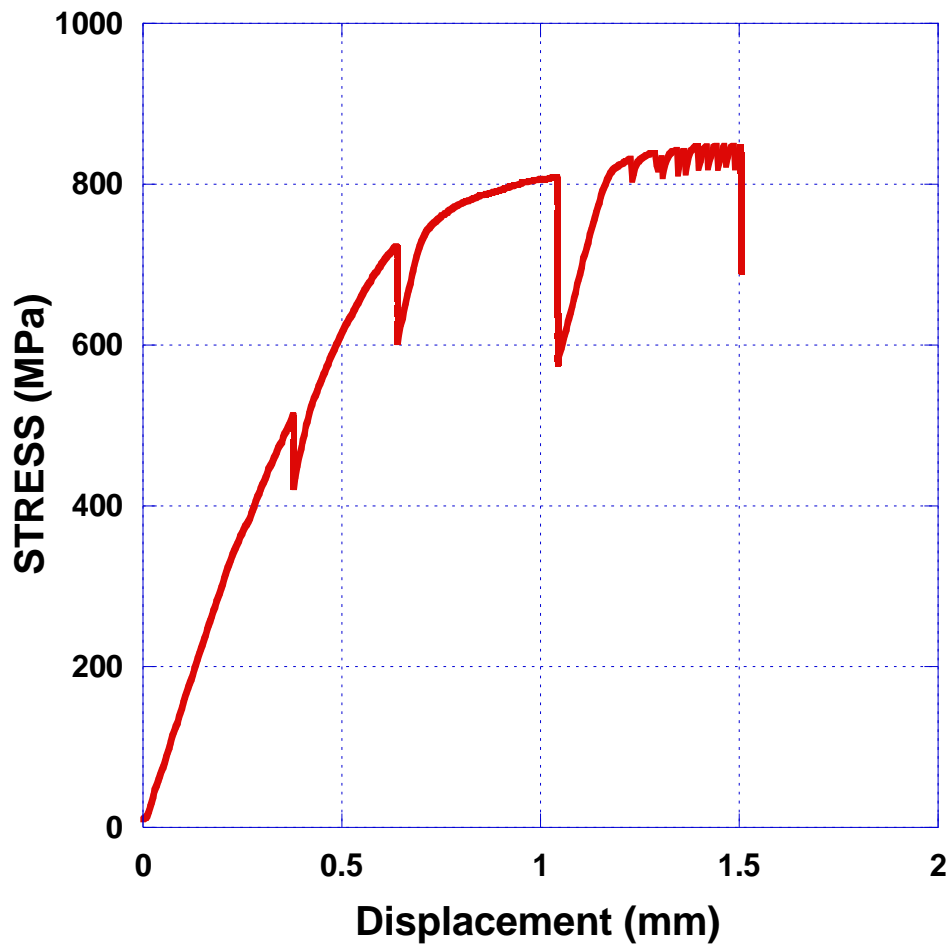


Figure 6.6 The stress-displacement curve for a TCFA sample tested at 410 °C. Stress relaxation occurred when the test was paused for acquiring SE SEM photomicrographs. The test lasted for ~1.5 hrs.

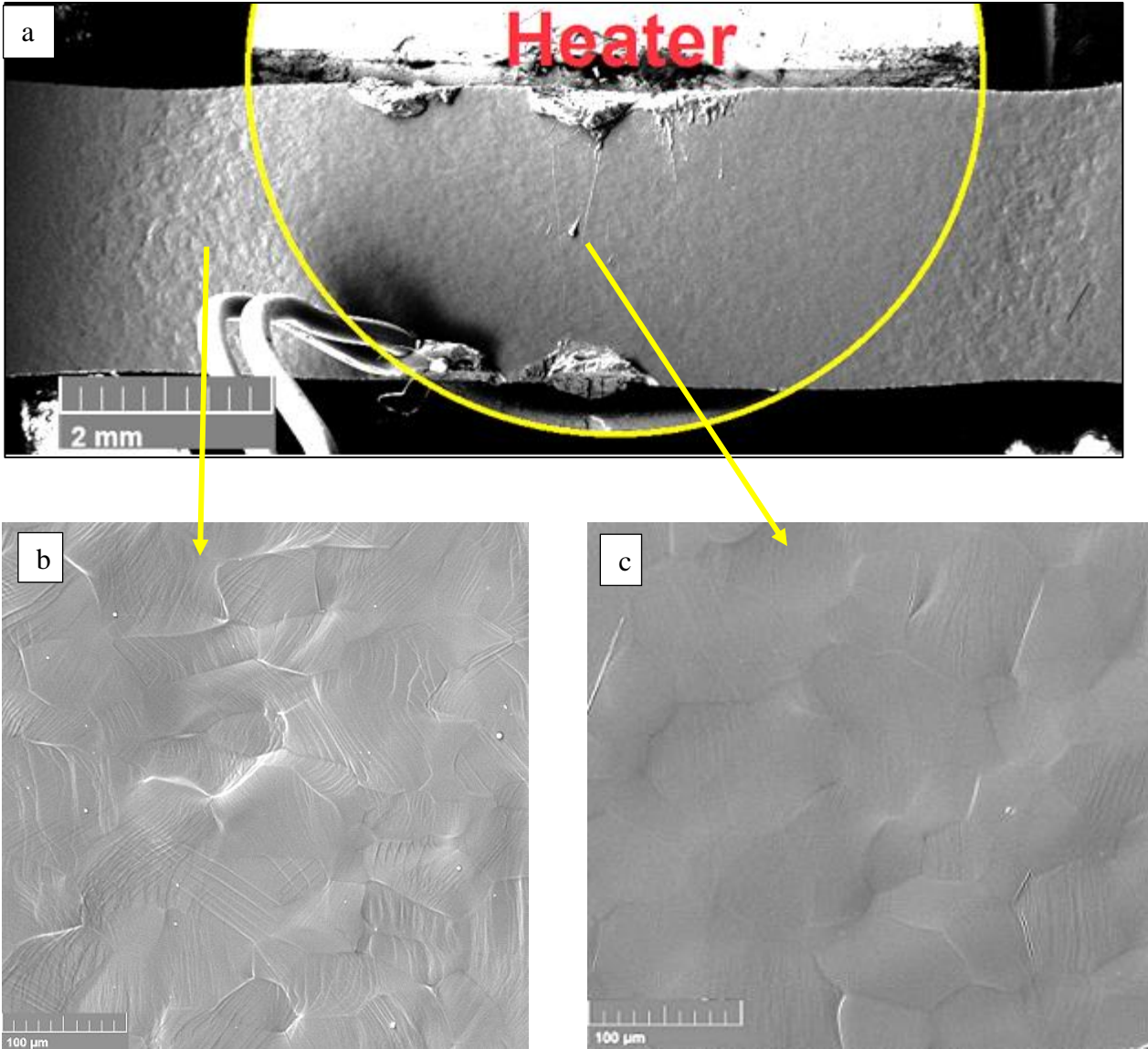


Figure 6.7 (a) Low-magnification SE SEM photomicrographs of the TCFA sample tested at 410 °C to 850 MPa. The test was interrupted for acquiring SE SEM photomicrographs. (b) Severe plastic deformation and many trace lines were observed outside the heated area, (c) The SE SEM photomicrographs of the heated area showed fewer trace lines. The hardness of the central region was ~500 Hv, while the hardness of outside of the heater (where the severe plastic deformation was observed) was ~340 Hv. The as-received hardness was ~ 320 Hv.

6.3.1 Interrupted tensile test at 410 °C

In order to measure the UTS of TCFA at 410 °C, the sample geometry was modified such that the stress of the area outside of the central heated area was significantly lower than the stress at the center of the sample. Figure 6.8 presents the modified sample design and the relative location of the heater. The new sample was heated to 410 °C inside the SEM chamber at a rate of ~5 degree °C per minute. Two thermocouples were spot welded to the sample to measure the temperature of the sample within the centrally-heated area and outside of this area, see Figure 6.9. The temperature difference between these two locations ranged between 60 °C to 100 °C during the test. SE SEM photomicrographs were acquired during the test after pausing, which resulted in stress relaxation. The magnitude of the stress relaxation was relatively high, especially after the last pause, where the stress relaxation was ~ 400 MPa. Each pause took approximately 30 minutes. The stress was ~1400 MPa when the sample fractured at the center of gage length. Figure 6.10 shows the stress-displacement curve of a 410 °C tensile test that was performed using the modified geometry. The sequential SE SEM photomicrographs of the selected area at the center of the sample are presented in Figure 6.11. Few slip lines were observed when the test was paused at 0.36 mm displacement, where the stress was 612 MPa. Evidence of global plastic deformation was observed when the test was paused at 0.5 mm displacement (740 MPa). As shown in Figure 6.11 (c), slip lines were evident in most of the grains.

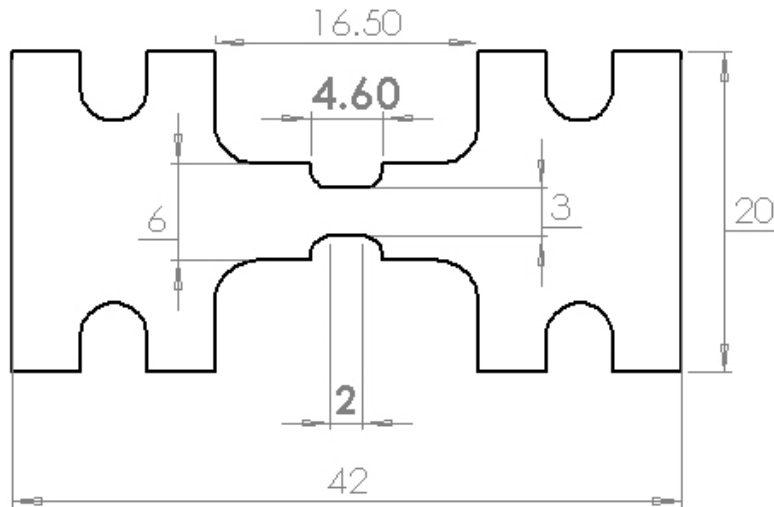


Figure 6.8 A schematic of the modified sample geometry used for the elevated temperature tensile tests on TCFA. The blue circle shows the relative location of the heater. All dimensions are provided in mm.

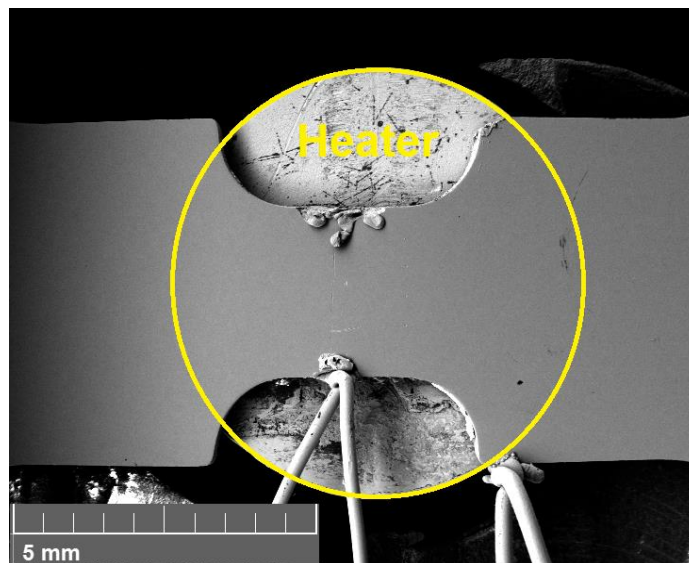


Figure 6.9 The relative location of the heater and the sample for a tensile test performed at 410 °C. Two thermocouples were spot welded to the sample to measure the temperature in the heated area and outside of the heater. The temperature difference between these two locations ranged between 60 °C to 100 °C during the test.

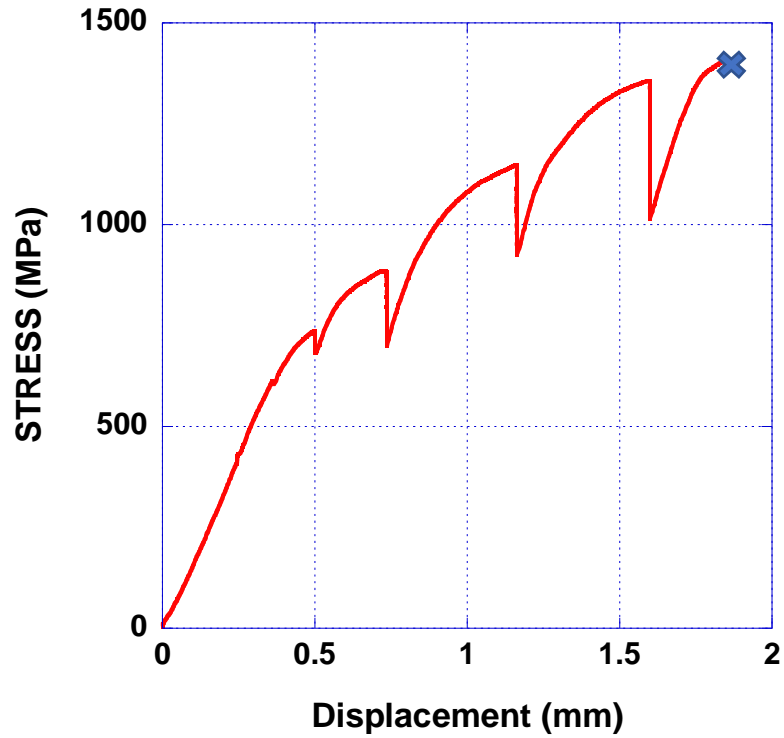


Figure 6.10 The stress-displacement curve for a TCFA sample that was tensile tested at 410 °C. Stress relaxation occurred as a result of pausing the test for acquiring SEM photomicrographs. The UTS was 1400 MPa. The '×' indicates when the fracture occurred

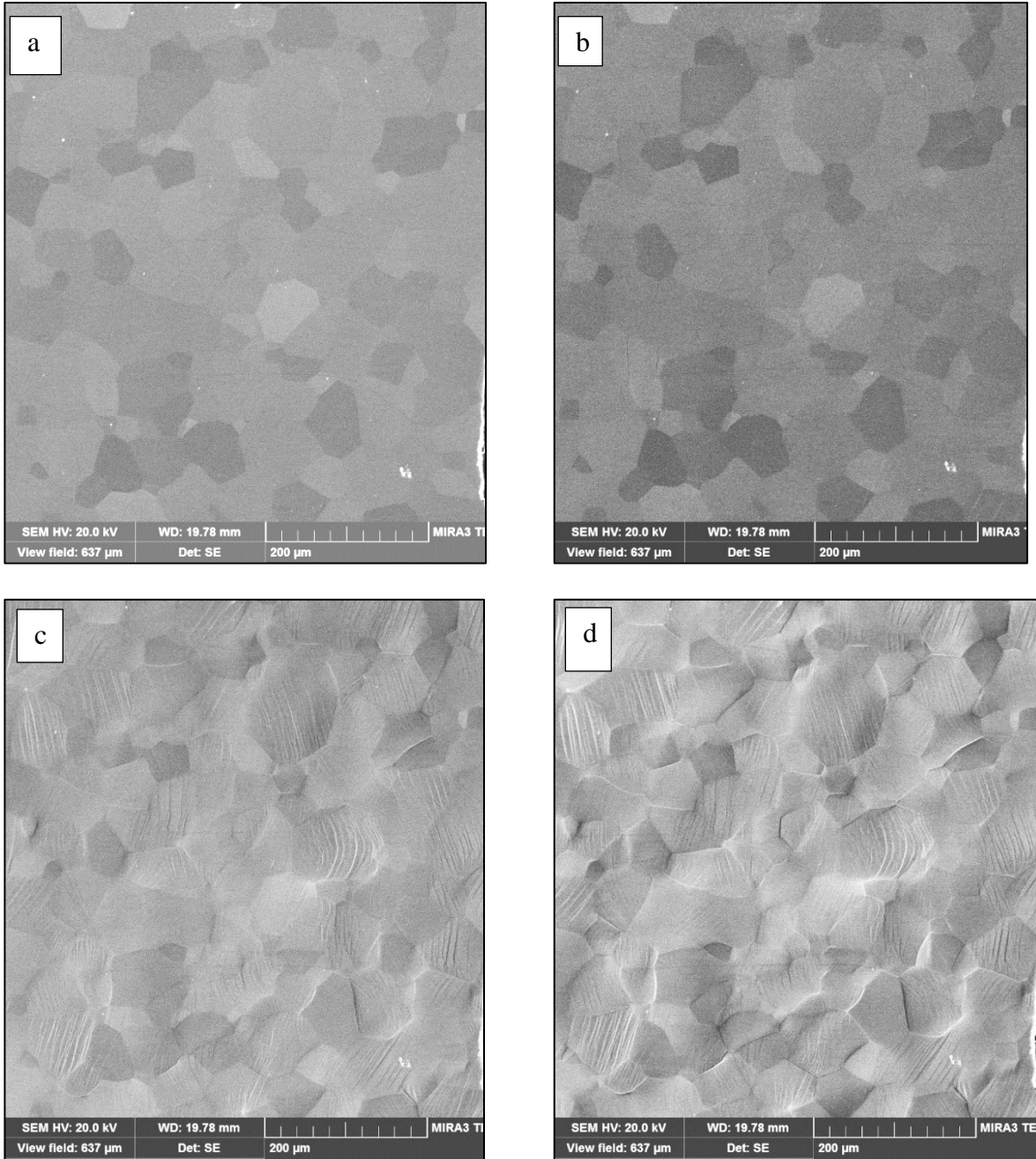
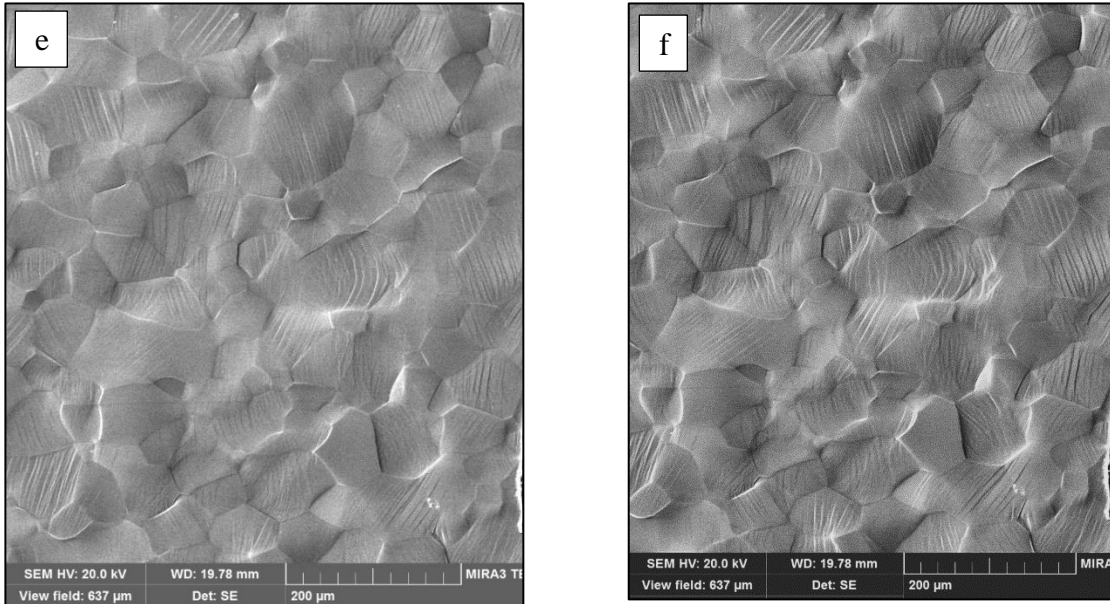


Figure 6.11 Sequential SE SEM photomicrographs acquired from a selected area at the center of a TCFA sample tested at 410 °C. (a) first pause at 0.25 mm, 202 MPa, (b) second pause at 0.36 mm, 612 MPa, (c) third pause at 0.5 mm, 740 MPa, (d) fourth pause at 0.74 mm, 886 MPa, (e) fifth pause at 1.16 mm, 1150 MPa, (f) sixth pause at 1.6 mm, 1359 MPa. The sample fractured at ~ 1400 MPa.

Figure 6.11(cont'd)



A low-magnification SE SEM micrograph of the fractured area, which was located at the center of the gage length is shown in Figure 6.12 shows. Many dimples were observed in the fractured area as presented in the high-magnification SE SEM micrograph in Figure 6.13. The stress was 1404 MPa when the fracture occurred.

6.3.2 Monotonic tensile test at 410 °C

Figure 6.15 shows the stress-displacement curve for a tensile test performed monotonically (i.e., without pausing the test) at 410 °C. The sample was heated to the test temperature at a rate of ~5 °C inside the SEM chamber. The slope of the stress curve changed significantly at ~ 700 MPa. The sample fractured close to the shoulder at 1100 MPa. Plastic deformation occurred in the gage section. However, more slip traces were observed close to the shoulder. Figure 6.16 shows a low-magnification SE SEM micrograph of the fractured sample, a high-magnification SE SEM

micrograph of the center of the gage length, and a high-magnification of the shoulder area after the test.

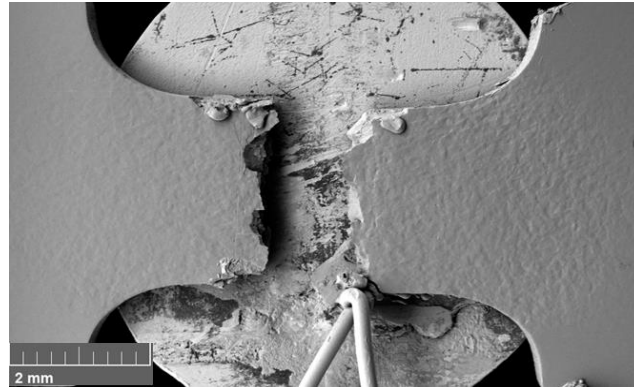


Figure 6.12 Low-magnification SE SEM photomicrograph of the fractured area of a TCFA sample, tensile tested at 410 °C. The stress was 1400 MPa when the fracture occurred.

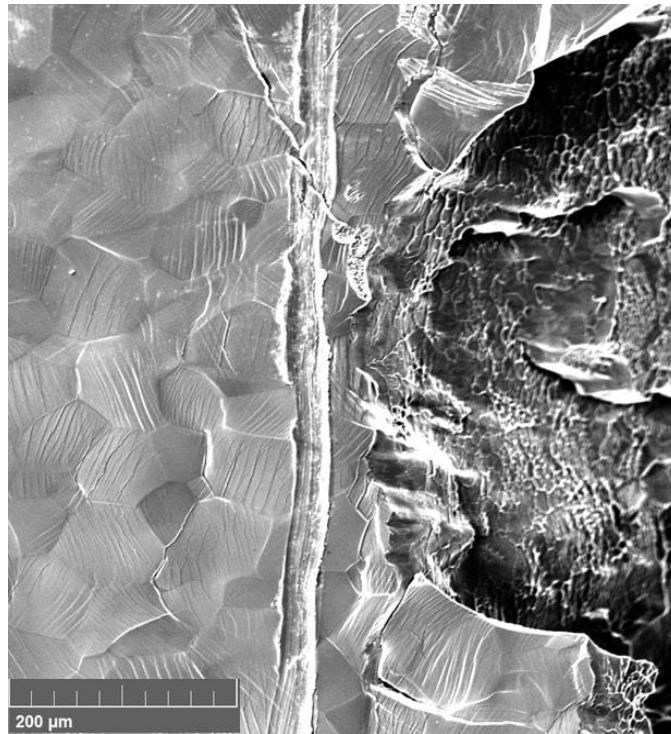


Figure 6.13 Dimples were observed in the high-magnification SE SEM photomicrograph of the fractured area for a TCFA sample that was tested in 410 °C (Figure 6.14). The central scratch was scribed before the test and used as a reference marker.

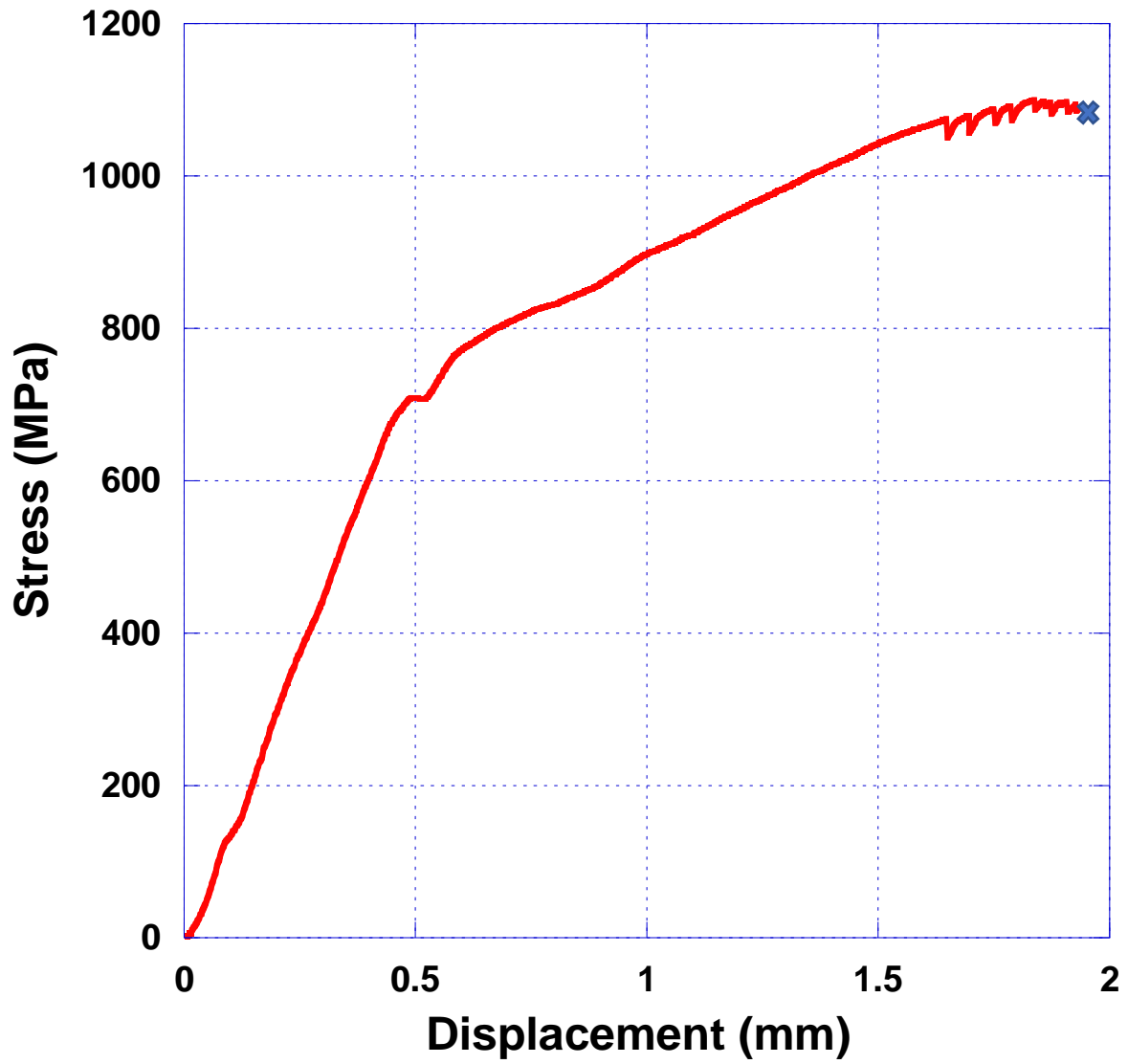


Figure 6.15 The stress-displacement curve for a 410 °C tensile experiment of TCFA. This test was performed monotonically. The 'x' indicates when the fracture occurred.

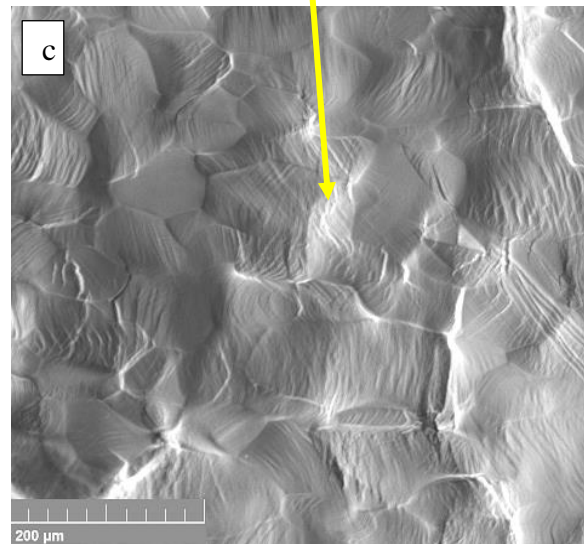
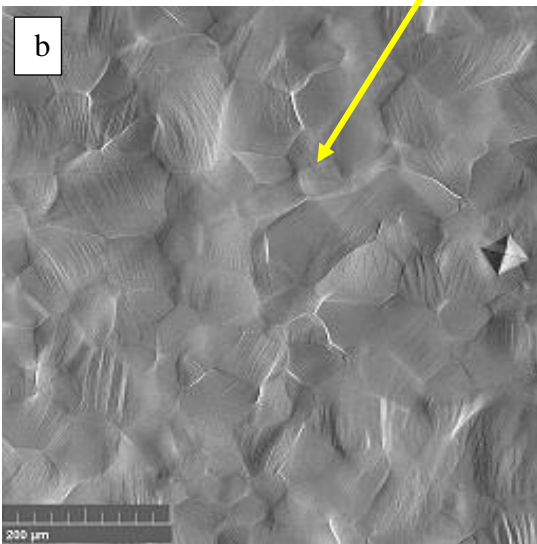
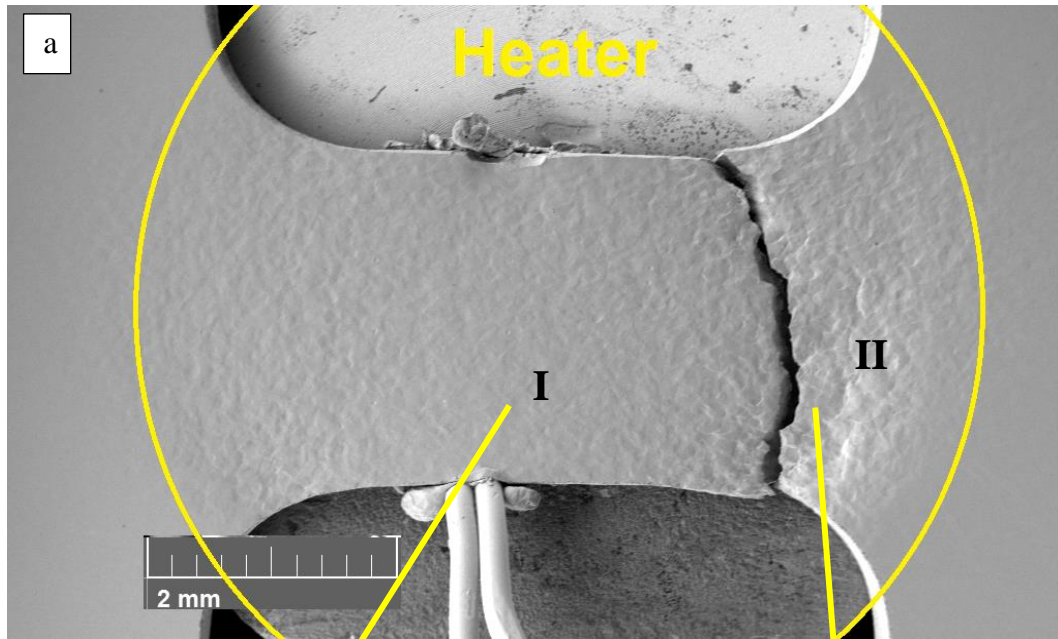


Figure 6.16 (a) The gage section of a TCFA sample that was tested at 410 °C, monotonically (i.e., without pausing). The sample fractured near the shoulder. (b) High-magnification SE SEM photomicrograph taken at the center of the gage section [area I in (a)]. (c) More slip traces were observed next to the fractured area at the shoulder [area II in (a)].

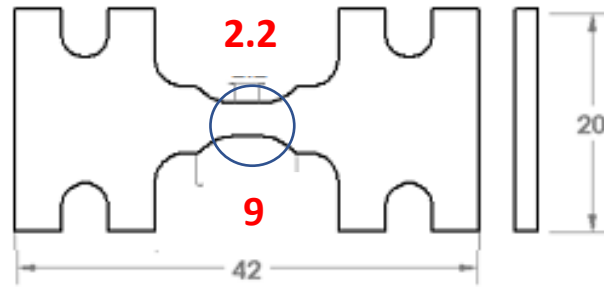


Figure 6.17 A schematic of the modified sample geometry used for the elevated temperature tests. The blue circle shows the relative location of the heater. All displacements are provided in mm.

The sample geometry was modified in order to avoid fracture at the shoulders. In particular, the fillet radius was increased. Figure 6.17 shows a schematic view of the modified sample geometry that was used for the rest of the elevated in-situ tensile tests. As a result of this modification, none of the modified samples broke at the shoulder.

6.3.3 The effect of preloading on UTS at 410 °C

For investigating the effect of preloading and heat treatment on TCFA, one sample was tensile loaded to 600 MPa at 410 °C, and the test was paused for 3 hrs (i.e., the displacement during this period was zero). The stress relaxation occurred during aging, and the stress dropped to ~500 MPa. Then, the sample was subjected to a tensile load until it fractured. The UTS was ~1130 MPa. Figure 6.18 presents the stress-displacement curve for the portion including the 500 MPa to 1130 MPa loading excursion. Figure 6.19 presents a low magnification SE SEM photomicrograph of the fractured sample. The fractured occurred at the center of the gage section. Many slip traces were observed in the gage section after the fracture (see Figure 6.20).

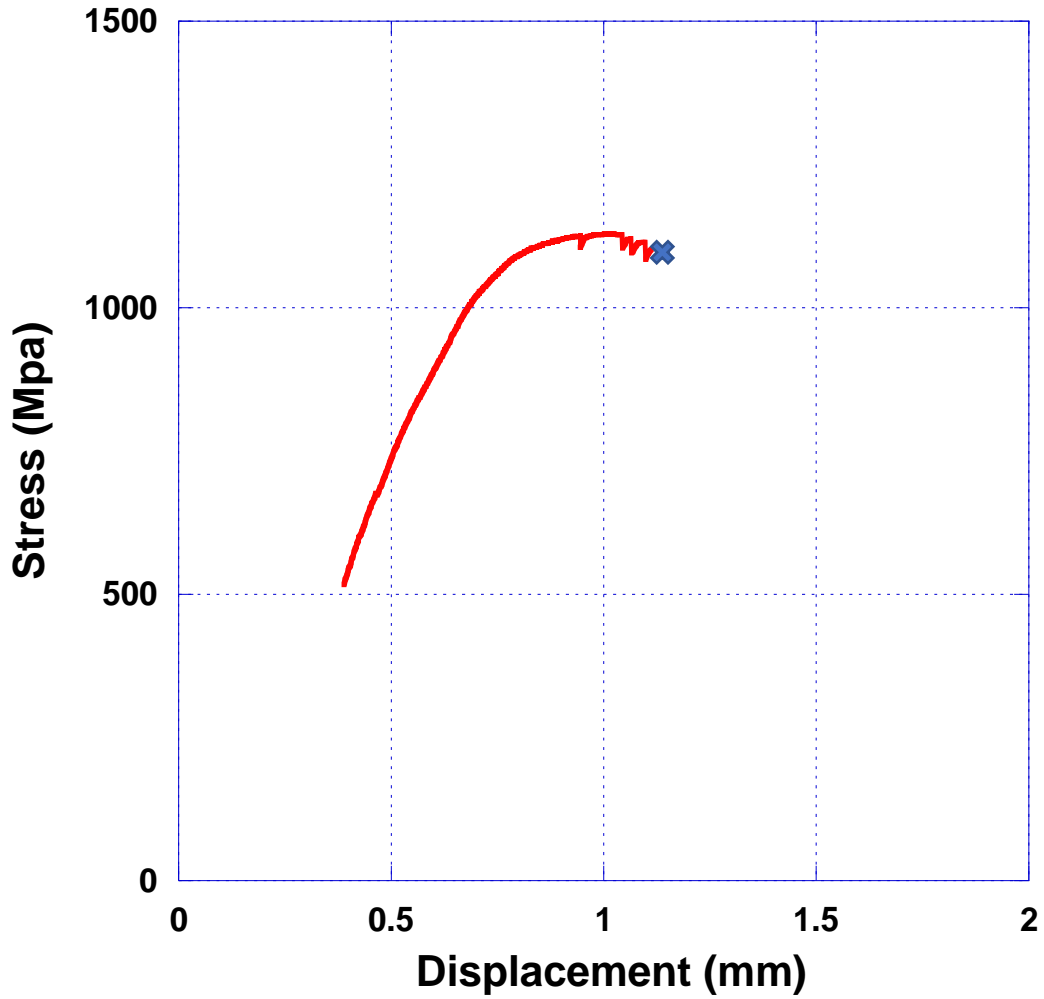


Figure 6.18 The effect of preloading on the UTS. A TCFA sample was heat treated at 410 °C for 3 hours, while the sample was subjected to a stress of 600 MPa. Then, due to stress relaxation, the stress dropped to ~520 MPa. After 3 hours, the sample was monotonically loaded until fracture (see the point X).

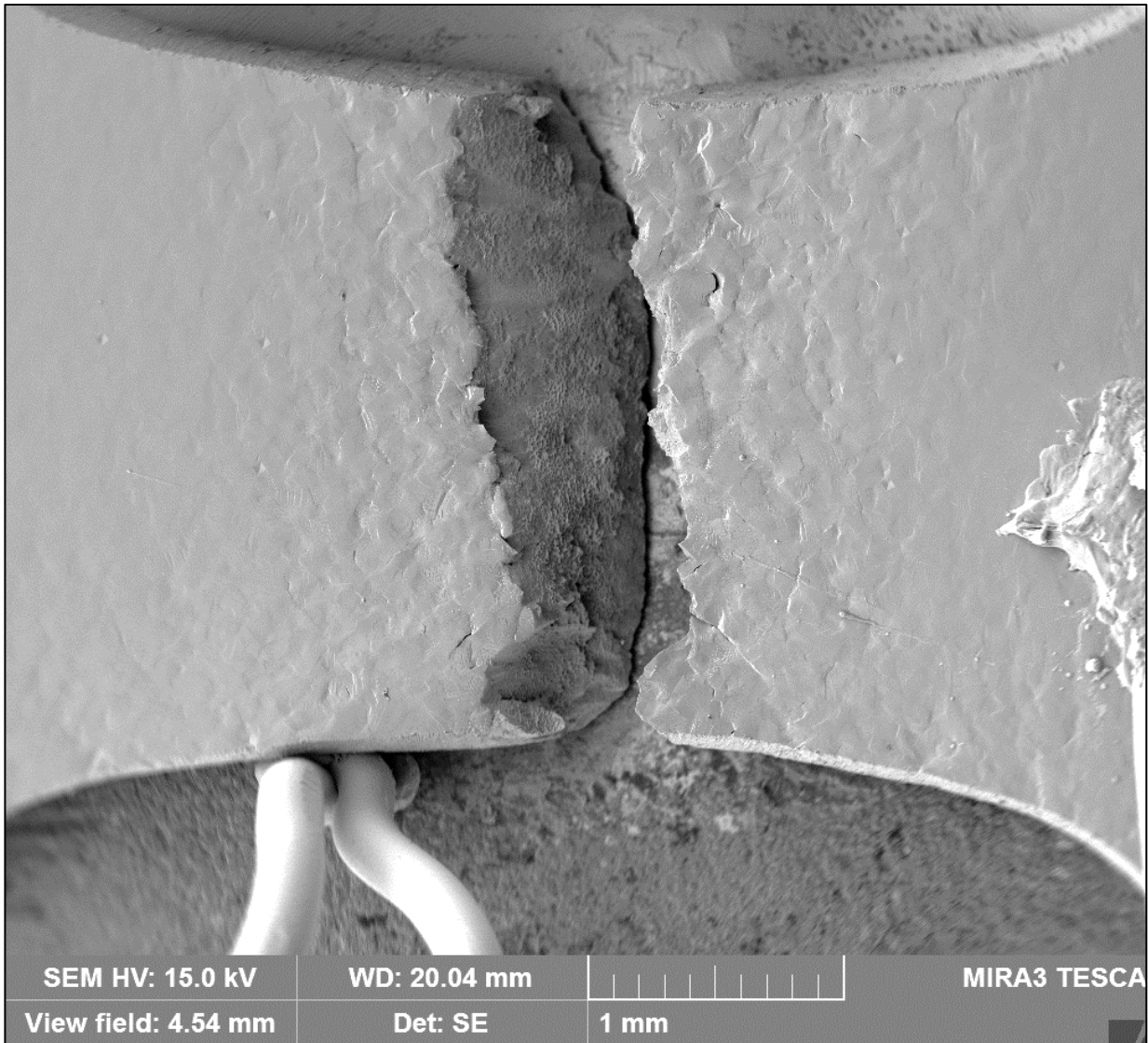


Figure 6.19 Prior to tensile loading, the sample was aged for 3 hrs at 410 °C while also being subjected to a stress of 600 MPa. The UTS was ~1130 MPa. The fracture occurred at the center of the sample in the heated area. Evidence of plastic deformation was observed close to the fracture surface.

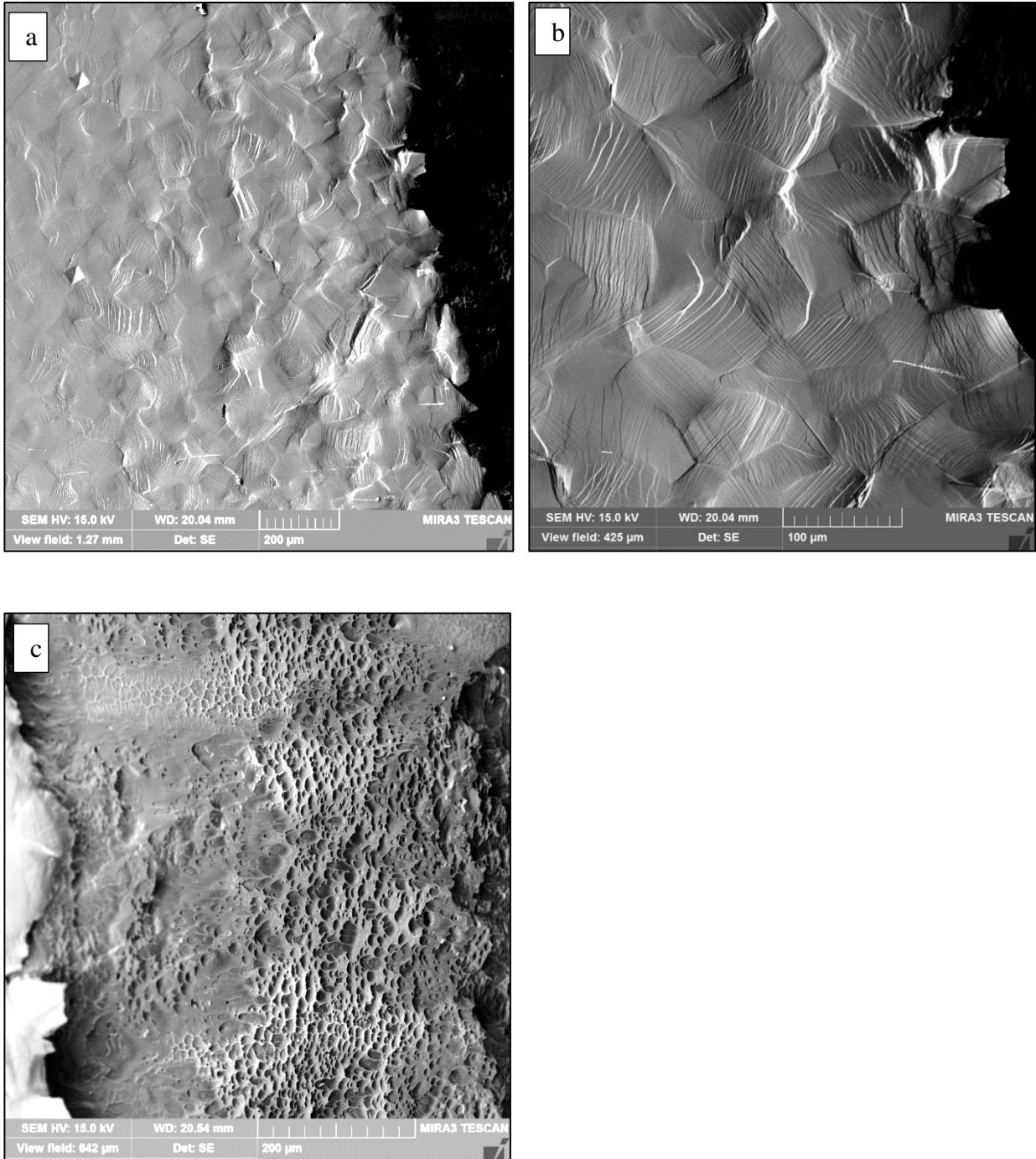


Figure 6.20 SE SEM photographs taken for the TCFA sample illustrated in Figure 6.19. (a) Low-magnification SE SEM photomicrograph of the fractured area, (b) high-magnification SE SEM photomicrograph of fractured area. Many slip traces observed close to the fracture surface, (c) Many dimples were observed in the fracture surfaces.

6.3.4 Interrupted tensile test at 410 °C

An in situ tensile test was performed inside the SEM at 410 °C. The test was paused 17 times during the test, which lasted ~5 hrs. Some slip traces were observed on the surface of the sample at a stress level of ~ 700 MPa. Figure 6.21 presents the stress-displacement curve. The UTS was 1435 MPa. Many slip traces and cracks were observed on the sample surface in the gage section (see Figure 6.22).

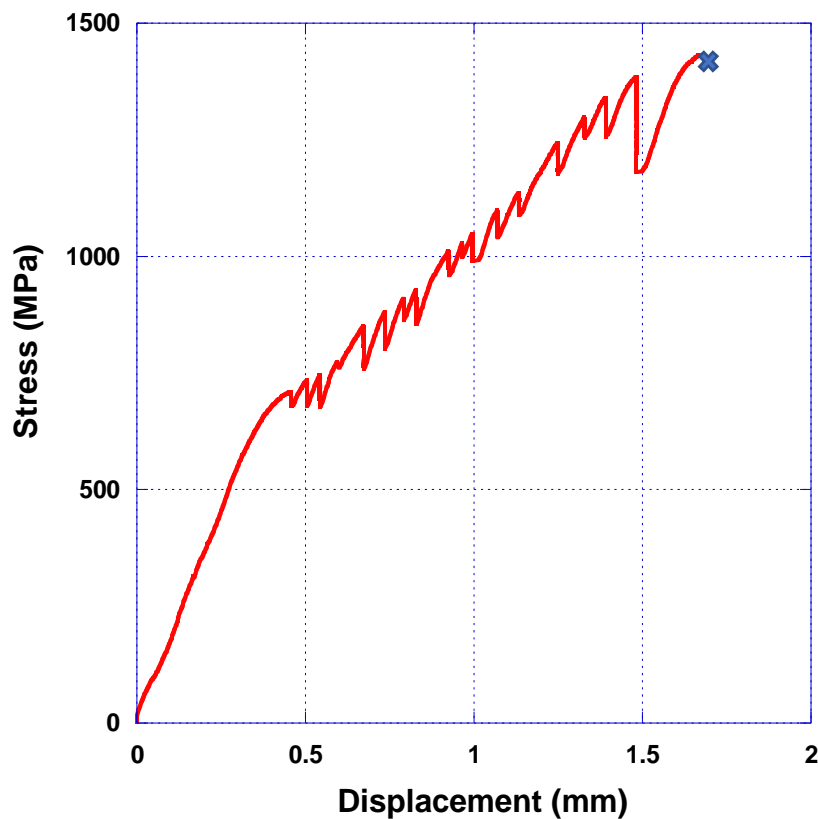


Figure 6.21 The stress-displacement curve for TCFA sample at 410 °C. The test was paused 17 times during the test, which lasted ~5 hrs. The UTS was 1435 MPa. “X” indicates where the sample fractured.

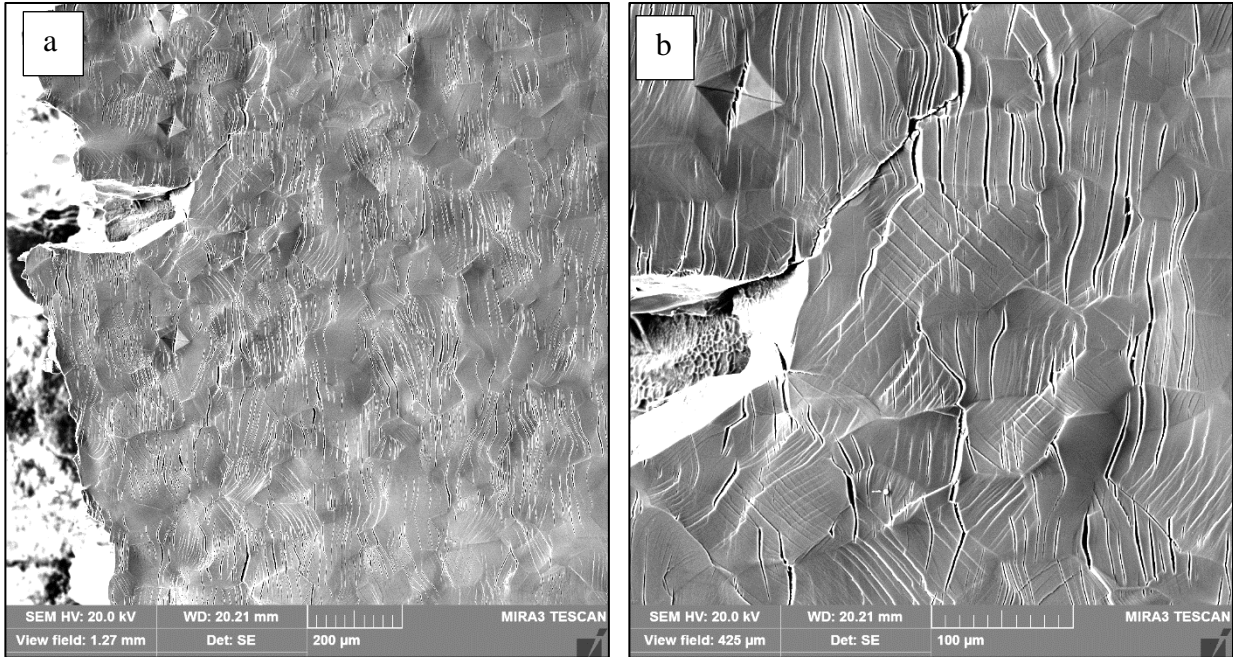


Figure 6.22 Many slip traces and cracks were observed near the fracture surface for the sample depicted in Figure 6.21. (a) Low-magnification SE SEM photomicrographs near the fracture surface and (b) high-magnification SE SEM photomicrograph near the fracture surface.

6.4 In-situ TCFA tensile test at 450 °C

A TCFA sample was heated inside SEM chamber to 450 °C at a rate of ~5 °C per minute. A tensile load was subsequently applied to the sample. Figure 6.23 shows the stress-displacement curve for the sample. The maximum stress reached was 1201 MPa before the 4th pause. After the 4th pause, a small crack initiated at a location close to the spot-welded thermocouple, as shown in Figure 6.24. The test was stopped as the crack started to propagate. Figure 6.25 shows the sequential SE SEM photomicrographs acquired during that test.

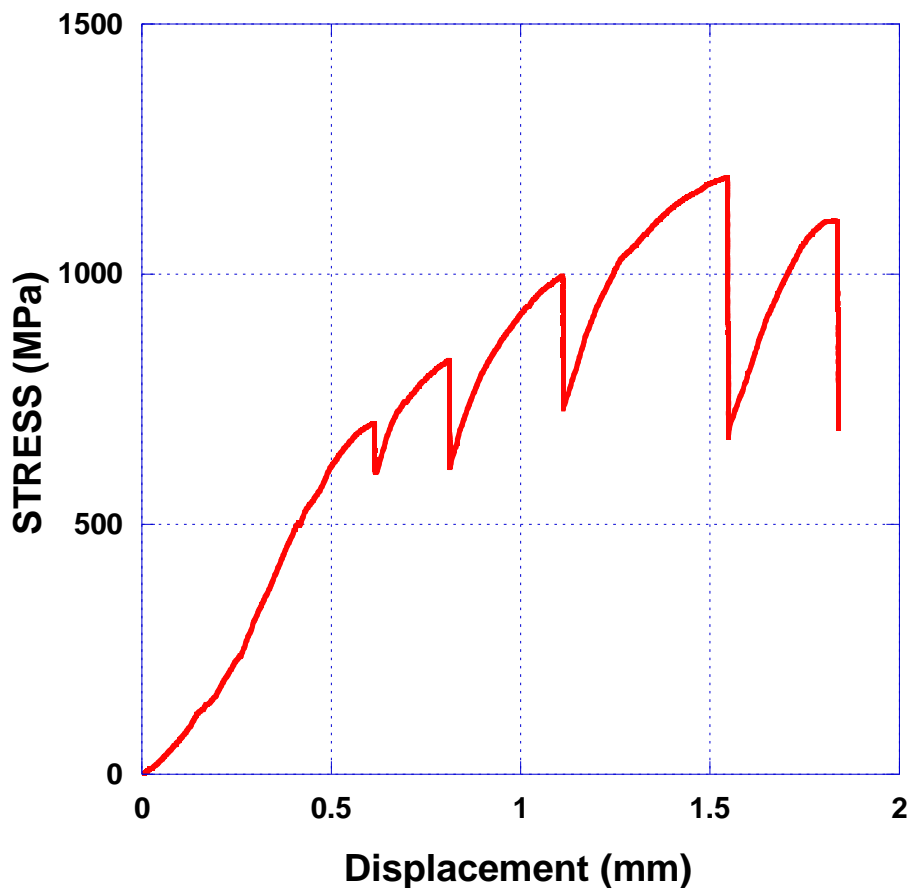


Figure 6.23 Stress-displacement of a TCFA sample tensile tested at 450 °C

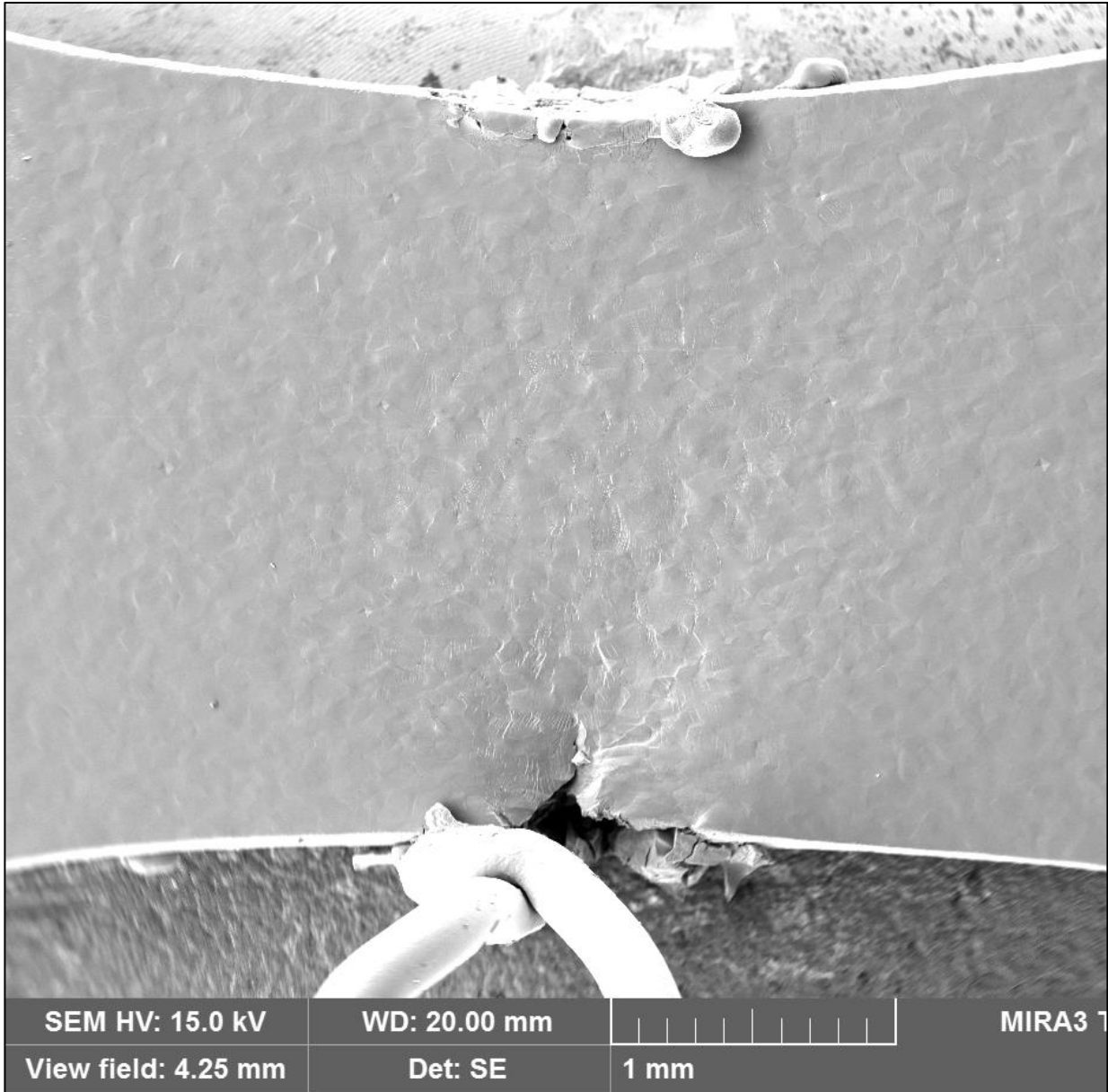


Figure 6.24 Low-magnification SE SEM photomicrograph of a TCFA sample tensile tested at 450 °C. After the 4th pause at 1201 MPa, a crack initiated in the area close to the spot-welded thermocouple. To prevent significant crack propagation, the test was stopped.

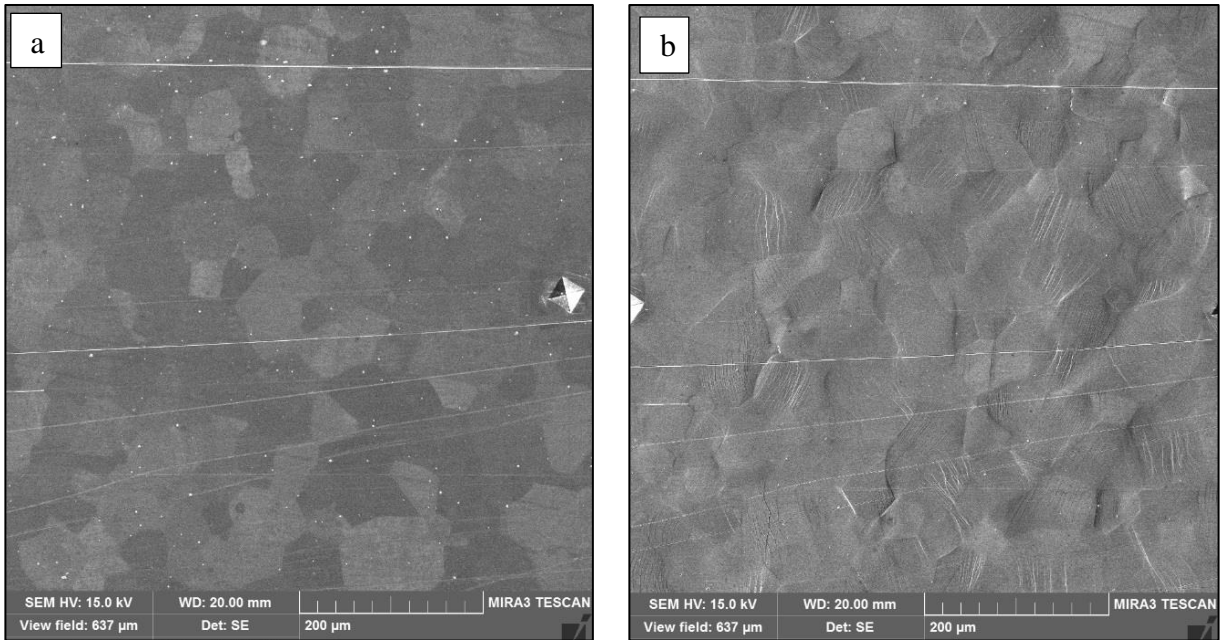
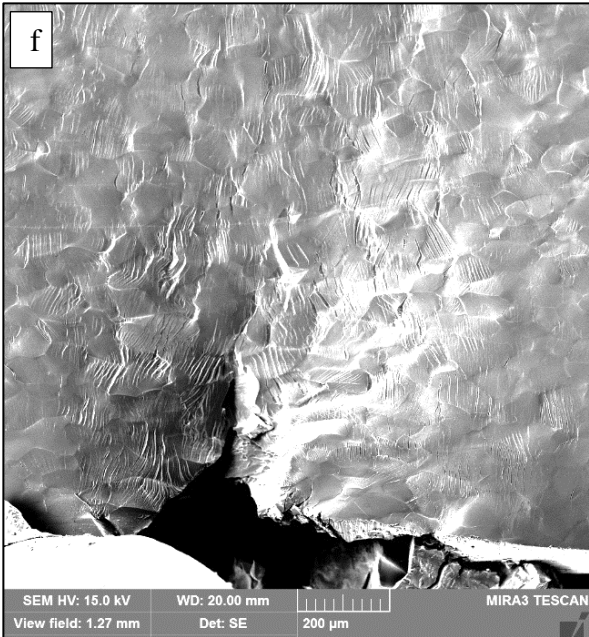
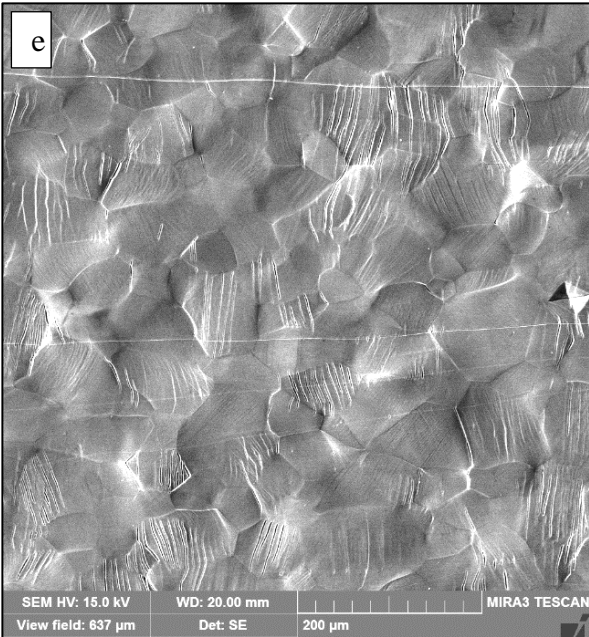
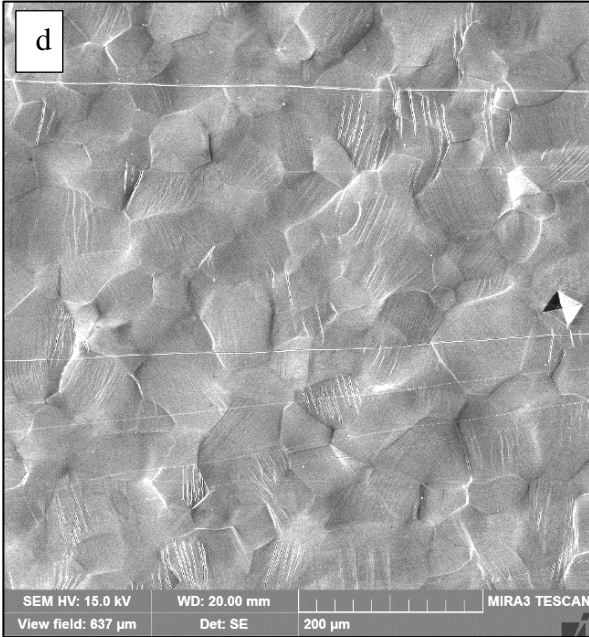
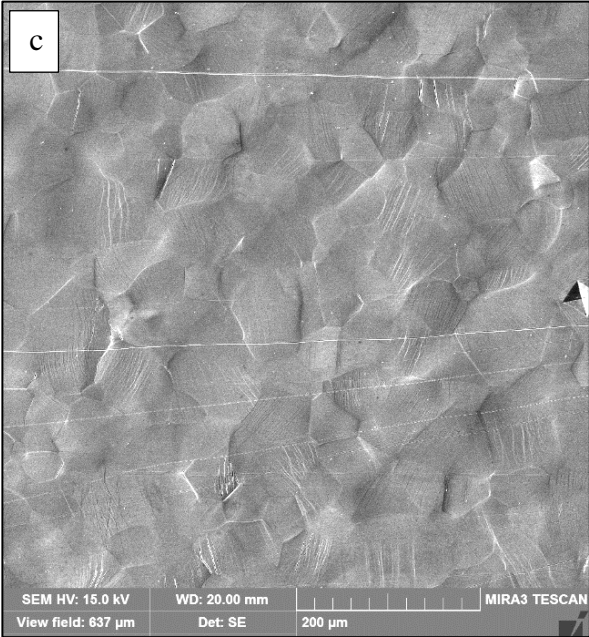


Figure 6.25 Sequential SE SEM photomicrographs taken from the same microstructural patch for a TCFA sample tensile tested at 450 °C. (a) Before the test, (b) 1st pause at 0.6 mm (700 MPa), (c) at 2nd pause, 0.8 mm (830 MPa), (d) at 3rd pause, 1.1 mm (1000 MPa), (e) at 4th pause, 1.54 mm, 1200 MPa, (f) at 5th pause (the test was stopped at this point due to crack propagation), (g) A crack started to propagate from the bottom of the sample in the area close to the spot-welded thermocouple. A low-magnification SE SEM photomicrograph of this area is shown in Figure 6.24.

Figure 6.25 (cont'd)



6.5 In-situ tensile test at 475 °C

Figure 6.26 shows the stress-displacement curve of a TCFA sample that was tensile tested at 475 °C. The stress dropped after reaching 970 MPa, and the test was stopped at 1.5 mm displacement. Figure 6.27 presents sequential SE SEM photomicrographs of the same area at different levels. No evidence of plastic deformation was observed at ~620 MPa (see Figure 6.27[b]). However, slip trace and surface cracks were observed when the test was paused at ~750 MPa. Surface cracks formed perpendicular to the tensile axis in almost all of the grains at the center of the gage length.

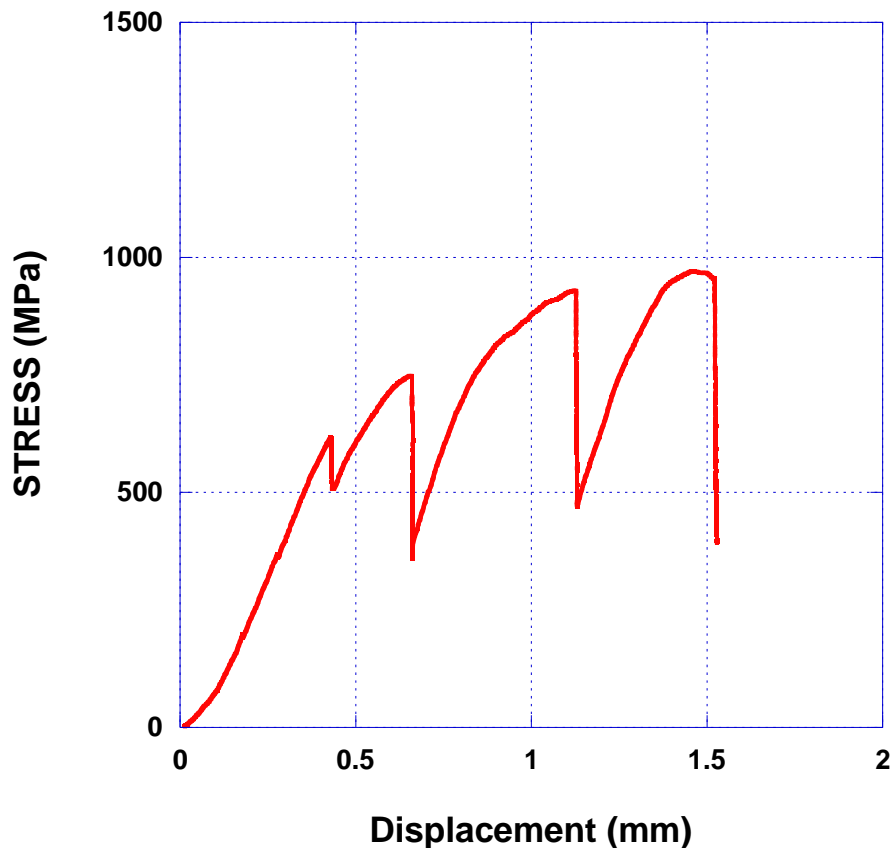


Figure 6.26 The stress-displacement curve for a TCFA sample that was tensile tested at 475 °C inside the SEM chamber.

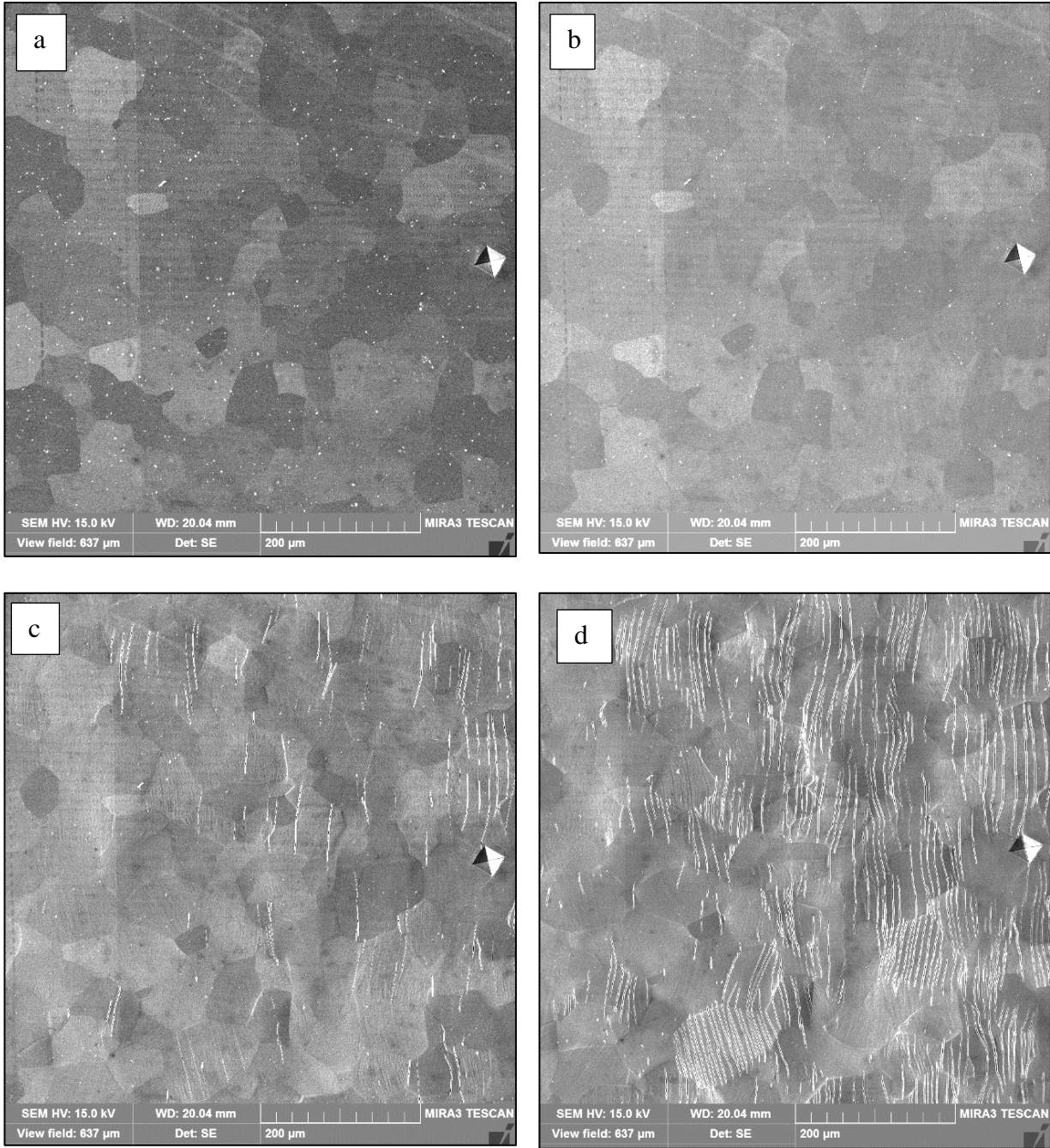
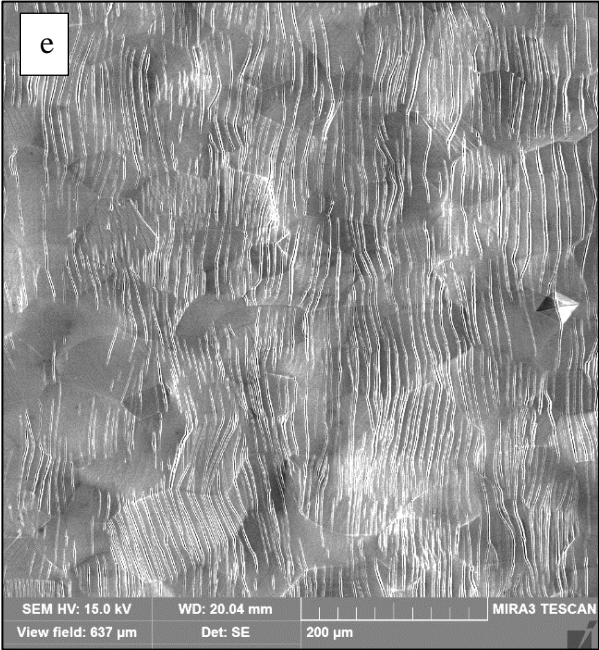


Figure 6.27 Sequential SE SEM photomicrographs of the same area taken at different intervals during the tensile experiment. (a) before the test at 475 °C, (b) 1st pause at 617 MPa, 0.43 mm displacement, no evidence of plastic deformation was observed, (c) 2nd pause, 747 MPa, 0.66 mm displacement, surface cracks occurred in some grains, (d) 3rd pause at 1.28 mm displacement, 928 MPa, (e) 4th pause at 1.5 mm displacement, 970 MPa, several slip traces and surface cracks were observed.

Figure 6.27 (cont'd)



6.6 Discussion

The peak and valley, observed in the $\tan(\delta)$ from the DMA test (see Figure 6.1), suggested that a phase transformation occurred between ~ 375 °C and 470 °C. Heat treatments have been conducted in the temperature range between 400 °C to 600 °C to investigate the effect of phase transformation on the hardness. The results confirmed that the microstructure transformed to a new phase(s) due to such heat treatments, where the Vicker's hardness exhibited an increase for all the heat-treated samples compared to the Vicker's hardness of the as-received material. The samples aged at temperatures greater than or equal to 500 °C exhibited a second phase (see Figure 6.4). The platelet morphology of the precipitates suggested that they are fine α phase precipitates (Lütjering and Williams, 2003). However, no second phase was observed in the SEM for the samples aged at 400 °C and 450 °C. This indicated that the new phase(s) formed in the nanoscale range. Nanometer scale ω precipitates have been previously observed in β Ti alloys, which formed during quenching, heat treatment, thermomechanical processing, and mechanical deformation [J. Hickman, 1969, G. Lutjering et al. 2007, J.I. Qazi et al, 2005, S. Nag et al, 2009, F. Prima et al. 2000]. As shown in Figure 2.11, the β phase-to- ω phase transformation occurs in the temperature range between 100 °C and 500 °C (Hickman, 1969). The formation of the ω phase typically results in an increase in both the strength and hardness, and a decrease in the ε_f (Hickman, 1969). The nanometer scale ω precipitates form by three mechanisms (Dubinskiy et al., 2016; Lütjering and Williams, 2003; Liu et al., 2017b; Kuan et al., 1975):

- Martensitic transformation during quenching, which is called athermal ω (ω_{ath})
- Transformation during aging by a diffusion-controlled process, which is called isothermal ω (ω_{iso})
- Deformation-induced ω phase transformation

TEM study have been performed after deformation on a sample tensile loaded at 410 °C to determine the new nanoscale phase structure. Figure 6.28 presents a TEM selected area diffraction pattern (SADP) of the $\langle 111 \rangle_{\beta}$ and $\langle 100 \rangle_{\beta}$ zone axis for the as-received TCFA, which exhibited a single phase β microstructure. The XRD of the heat-treated 400 °C sample confirmed the existence of the ω phase (see Figure 6.29). Figure 6.30 presents TEM images from a sample that was tensile tested at 410 °C. A bright field TEM image is presented in Figure 6.30 (a) and a TEM SADP is presented in Figure 6.30 (b). In Figure 6.30 (c), a TEM dark field image highlights the ω phase variant associated with the diffraction spot highlighted by the red circle in Figure 6.30 (b). In Figure 6.30(d), a TEM dark field image of the ω phase variant associated with the diffraction spot highlighted by the yellow circle in Figure 6.26(b). This phase transformation is believed to have contributed to the increased strength and the hardness of the TCFA alloy. The maximum hardens was achieved after 24 hr aging at 410 °C as shown in Figure 6.5. No significant change was observed on the measured hardness after 48 hr aging at 410 °C, which indicates that the β phase and the ω phase reached equilibrium after 24 hr at 410 °C.

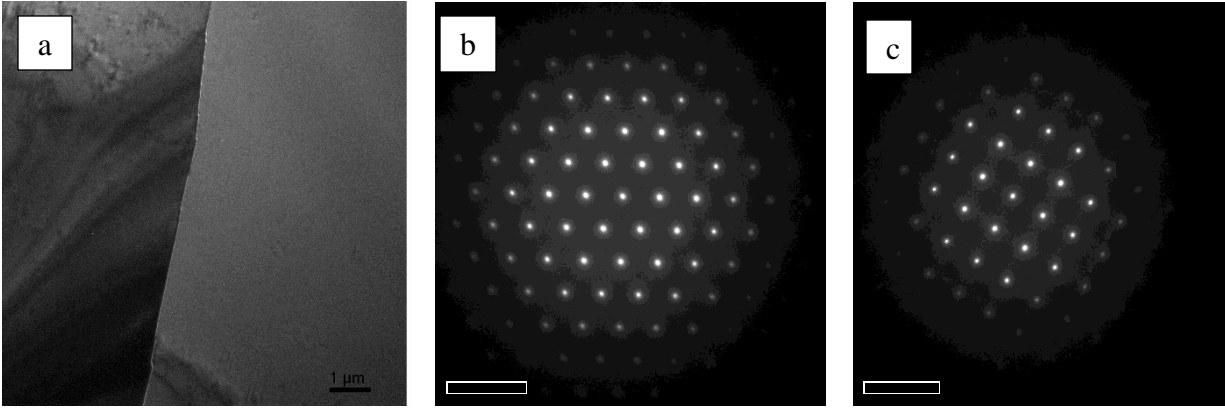


Figure 6.28 (a) Bright field TEM photomicrograph and (b) TEM SADPs of the $\langle 111 \rangle$, (c) $\langle 100 \rangle$ zone axis of β phase for the as-received TCFA alloy.

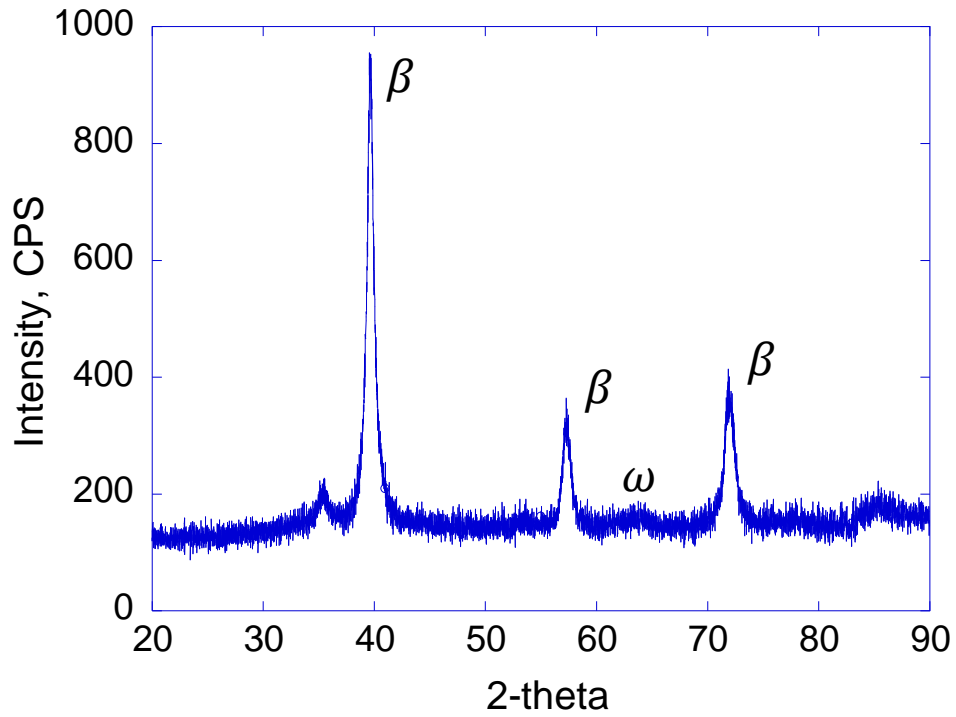


Figure 6.29 An X-ray diffraction pattern of the 400 °C heat treated TCFA sample, which exhibited an ω peak at $\sim 63^\circ$

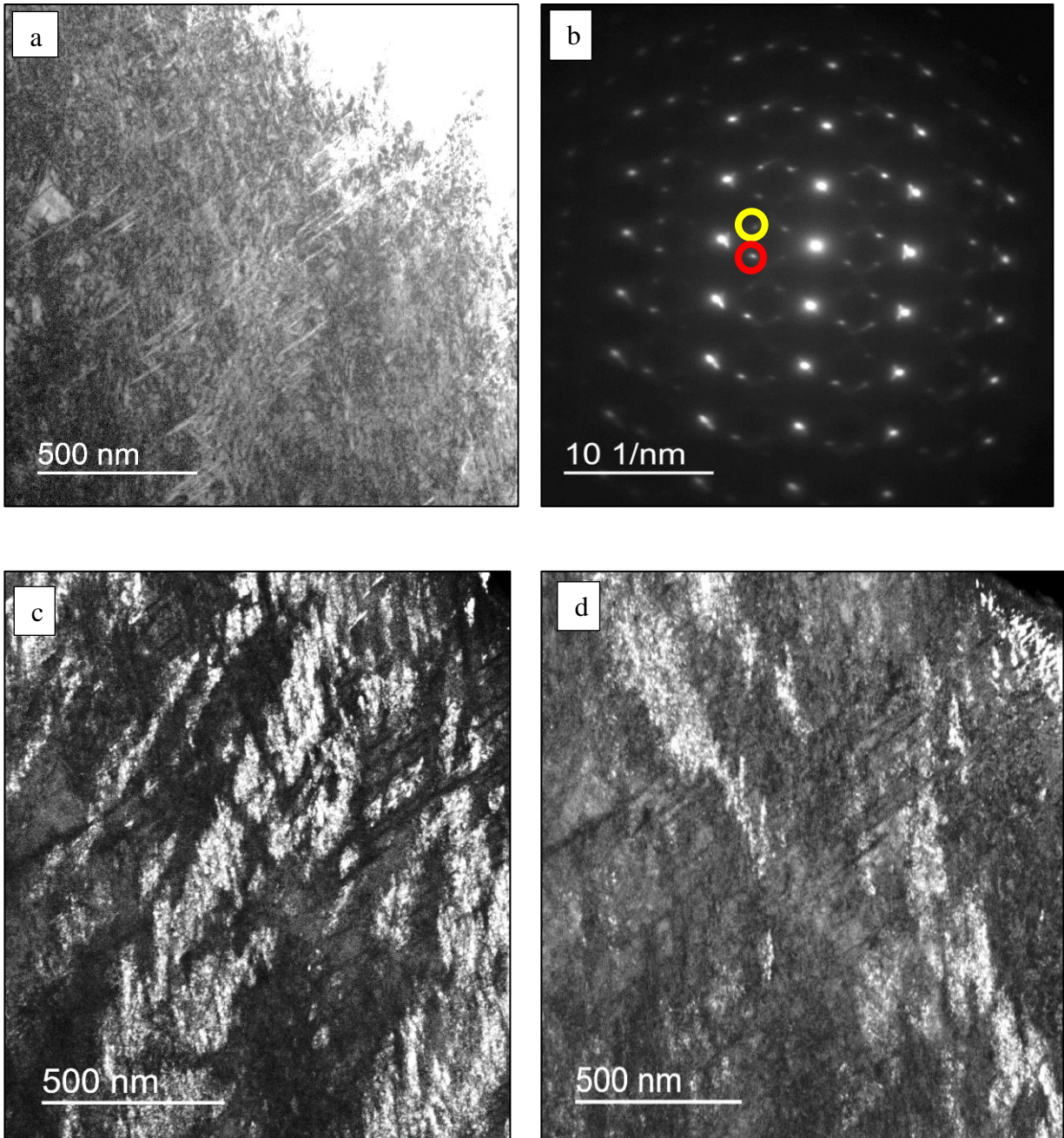


Figure 6.30 TEM photomicrographs of a TCFA sample that was tensile tested at 410°C. Some of the β phase transformed into the ω phase. (a) Bright field TEM image, (b) TEM SADP, (c) TEM Dark field image highlighting the ω phase variant associated with the diffraction spot highlighted by the red circle in (b), and (d) TEM dark field image highlighting the ω phase variant associated with the diffraction spot highlighted by the yellow circle in (b).

The results of the in-situ tensile tests are summarized in Table 6.1. The UTS decreased with an increase in temperature from RT to 300 °C. With an increase in the test temperature from 300 °C to 410 °C, the UTS increased to ~1100 MPa. Prior to applying the tensile load, the sample was heated at a rate of ~5 °C per minutes until reaching 410 °C and then it was held at 410 °C for ~ 20 minutes. It is believed that no significant change occurred in the mechanical properties in that period of time, due to the fact the aging at 410 °C, even for 2 hr, only resulted in 6% increase in the Vicker's hardness (see Figure 6.3). Hence, the abnormal UTS increase of the uninterrupted test at 410 °C should mainly be attributed to the deformation-induced phase transformation (the β phase to the ω phase). The deformation-induced ω phase transformation has been previously observed during RT loading in some β Ti alloys (Tane et al., 2013, Liu et al., 2014, 2016, 2017b).

To accelerate the transformation rate, one sample was aged for 3 hr at 410 °C, while being subjected to a nominal stress of 600 MPa. The corresponding UTS increased to ~1130 MPa, which was only 3% higher than the UTS of an uninterrupted test at 410 °C. This indicated that even 600 MPa tensile loading did not substantially trigger the isothermal transformation. This result was consistent with the aging process for 2 hrs at 400 °C, which exhibited only a 6% increase in hardness compared with the as-received sample.

The UTS value at 410 °C exhibited a substantial increase (~30% higher than UTS of uninterrupted test at 410 °C), when the sample was aged at six steps with a load level from 600 MPa to ~1300 MPa (the test was paused six times during the loading, see Figure 6.10). Each step lasted approximately 20 minutes. The greater UTS of the interrupted test compared to the uninterrupted test was mainly attributed to the ω iso phase transformation during each step, in addition to the deformation-induced ω -phase transformation, which formed during loading. For the test that was paused 17 times, and lasted for ~ 5 hrs, the UTS was 1435 MPa. This did not

exhibit a significant strength increase compared with the test that was paused 6 times (the UTS was 1400 MPa). This suggests that the ω_{iso} and the deformation-induced ω phase were saturated, similar to the heat treatment at 410 °C, where the Vicker's hardness did not exhibit significant change after increasing the aging time from 24 hrs to 48 hrs (see Figure 6.5).

Figure 6.31 presents the stress-displacement curves for tests performed at RT, 410 °C, 450 °C, and 475 °C, where the test durations were ~2 hrs. The UTS was 1220 MPa at 450 °C, which was less than the UTS at 410 °C. It should be noted that the 450 °C tested sample was not taken to failure. As shown in Figure 6.20, a crack was initiated close to the thermocouple, and therefore, the test was stopped after 4th pauses. For the tensile test that was performed at 475 °C, the UTS was 970 MPa. As shown in Figure 6.1, a phase transformation occurred at ~ 480 °C.

Table 6-1 The Summary of in situ tensile tests on TCFA alloy from RT to 475 °C

Test Temperature (°C)	UTS (MPa)	Test Duration (hr)	Number of pauses
RT	940	-	No pause
200	820	1.5	3
300	720	1.5	3
410	1100	-	No pause
410	1130	-	*1No pause
410	1400	2	6
410	1440	5	17
450	1220	1.5	*24
475	970	1.5	3

*1: Prior to the test, the sample was aged at 410 C for 3 hr while being subjected to nominal stress of 600 MPa, as described in 6.3.3

*2: The sample was not taken to fracture, as a crack initiated close to the thermocouple (see Figure 6.24)

At this temperature, it is likely that in addition to the ω phase, fine α particles were formed as the DMA curve exhibited a valley around 480 °C. More TEM investigation is needed to determine the exact phase(s) formed in the sample that was tensile tested at 475 °C. Some cracks were observed at the surface of the sample that was tested at a 410 °C and 475 °C, which might be due to oxide layer on the surface of the samples (see Figure 6.22 and Figure 6.27).

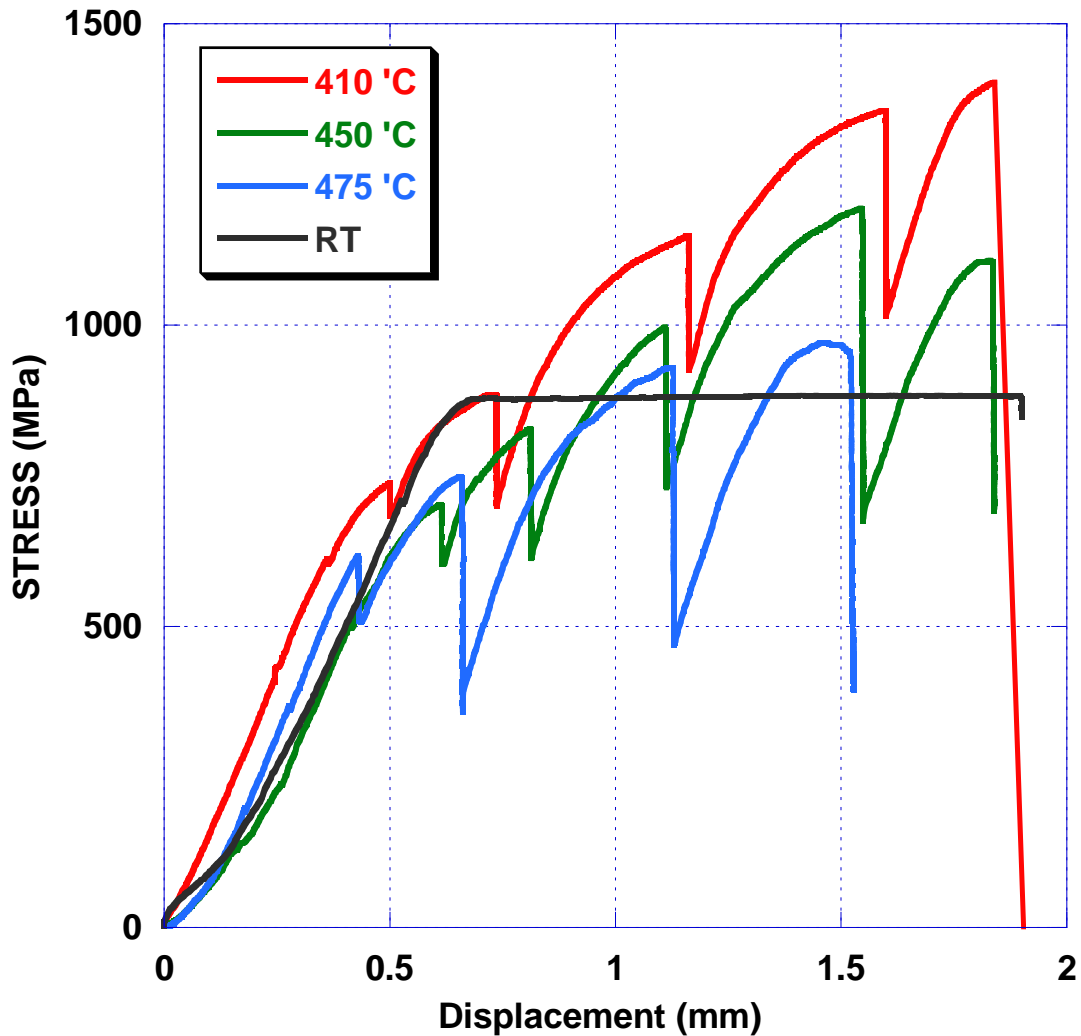


Figure 6.31 The stress-displacement curves for TCFA samples, tensile tested at RT, 410 °C, 450 °C, and 475 °C

6.7 Summary and conclusions

The transformation temperature range was estimated by the DMA and DSC, which suggested a phase transformation at $\sim 370^{\circ}\text{C}$ and another transformation at $\sim 480^{\circ}\text{C}$. Heat treatments have been conducted to verify the formation of new phase(s) by measuring the Vicker's hardness. The greatest hardness ($\sim 500\text{Hv}$) was achieved when the sample was aged at 410°C for 24 hrs. TEM revealed that the as-received TCFA consisted of a single β phase microstructure, while the ω -phase precipitates were observed in the sample deformed at 410°C . It is believed that the deformation-induced ω phase transformation played an important role in enhancing the TCFA UTS in uninterrupted tests at 410°C . Both the deformation-induced ω phase and ω_{iso} phase attributed to the high UTS for the test that was paused several times during loading. By increasing the test temperature to 450°C and 475°C , the UTS decreased to 1220 MPa and 970 MPa, respectively. The as-received TCFA UTS was ~ 940 MPa. Further investigation of the transformation mechanism will be the topic of new PhD project.

CHAPTER 7

7 SUMMARY AND CONCLUSIONS

7.1 Summary and outcomes of this work

In this work, an experimental-computational investigation was performed to aid our understanding of the relationship between crystallographic misorientation and plastic strain at the microscale and the mesoscale. A series of in-situ monotonic tensile tests were performed inside a SEM on two β Ti alloys: TCFA and TIMETAL-21S. Several algorithms were developed and implemented into MATLAB for analyzing the acquired EBSD data. The effect of reference orientation on the misorientation distribution was investigated at two length scales: microscale (i.e. grain size scale) and mesoscale. The effect of grain size and grain orientation on the misorientation were quantified as a function of plastic strain. Based on the analyzed experimental data taken from ~6,000 grains, an empirical equation was proposed to predict the level of misorientation at the grain scale as a function of the equivalent grain diameter and global plastic strain. To study the influence of loading history on misorientation, two interrupted tests were performed inside a SEM and the results were compared with those from monotonic tests. Strain field maps, obtained from a DIC-SEM RT tensile test performed, were compared with EBSD misorientation maps for the same surface microstructural patch.

The deformation behavior of β Ti alloys (TCFA, TIMETAL-21S, and TNTZ-xO) were characterized. The microstructure, texture, and YS for each of the above-mentioned alloys were evaluated and the results were compared. The effect of temperature on the active deformation modes was investigated for TCFA, and TIMETAL-21S. The effect of O content on the deformation mode and strength of TNTZ-xO was investigated. The results revealed that even a

small change in the O content has a significant effect on the UTS and the dominant deformation mechanism.

Furthermore, a series of thermomechanical processes and heat treatments were designed and performed on a low-cost Ti alloy, TCFA, which led to achieving the highest reported UTS of a Ti alloy at temperatures range between 380 °C to 480 °C. This study revealed that the β matrix transformed to the nanoscale ω phase during the TMP, which significantly enhanced the strength of TCFA.

Some the metrics developed for misorientation analysis have been implemented by EDAX-TSL (Mahwah, NJ) in their latest OIM software. Also, an international patent has been filed titled: “Ti alloy and method of forming a Ti alloy #US20170204504A1”, based on this research.

7.2 Summary and conclusions

7.2.1 Misorientation analysis

For the misorientation analysis, ten monotonic and two interrupted in-situ tensile tests were performed inside a SEM on two β Ti alloys: TCFA and TIMETAL-21S. One in-situ tensile test was performed in conjunction with DIC and EBSD. The average grain size was $\sim 50 \mu\text{m}$ and $\sim 15 \mu\text{m}$ for TCFA and TIMETAL-21S, respectively. The as-received alloys were solution treated and no significant misorientation was observed within individual grains before they were subjected to deformation. The samples were loaded to target global plastic strains of 3%, 6%, 9%, and 12%. Approximately, 600 grains were analyzed for each test. The stress-displacement curves indicated little strain hardening for both alloys. The results of the misorientation analysis are summarized here:

- (1) To study the effect of reference orientation, five metrics were investigated at the grain scale and the mesoscale: MD_{Min} , MD_{Max} , $MD_{Geo. C.}$, $MD_{Avg. Ori.}$, and MD_{All} . It was observed that regardless of the reference orientation metric, the misorientation distribution exhibited larger MD at the grain boundaries and smaller MD values within the grains, except for the MD_{Max} , where the MD values were larger within the grains. Although, the MD values were different for each metric, the MD versus plastic strain curve showed a linear relationship with different slopes and intercept values for each alloy.
- (2) The $MD_{(min)}$ values were almost constant for the undeformed material. With increasing plastic strain, the $MD_{(min)}$ values increased. The subpopulation of large grains exhibited a greater misorientation level than the small grains, where the difference became more pronounced with increased strain. This implies that the level of misorientation heterogeneity became more substantial at higher level of plastic strain. This could be explained by the fact that the large grains are surrounded by a greater number of the grains. Hence, each part of the boundary of a large grain should locally accommodate its deformation with neighboring grains to satisfy the displacement compatibility condition and to assure the deformation continuity. This leads to a variation in the local stress states throughout the grain, which results in different local slip activities.
- (3) The relationship between the $MD_{(min)}$ grain and equivalent diameter was quantified as a function of plastic strain. A numerical analysis of this data revealed that the misorientation value at the grain scale can be estimated by equation (7.1),

$$MD_{(min),grain} = (a \frac{D}{D_{avg}} + b)\epsilon_p + c \quad (7.1)$$

where D is the equivalent diameter of the grain, D_{avg} is the average grain diameter, ε_p is the global plastic strain in percent, and a , b , and c are constants, which are determined using the least square regression analysis.

- (4) To investigate the influence of the grain orientation on the $MD_{(min)}$, three crystalline orientations were chosen with respect to the loading direction (with a threshold of 20°) for both alloys, namely $\{100\}$, $\{101\}$, and $\{111\}$. For both alloys, the highest $MD_{(min)}$ was observed for the $\{100\}$ group at all the measured strains. The results suggested that the $\{100\}$ group exhibited the greatest tendency for orientation change compared to the other studied orientations, regardless of the grain size and the area fraction. This might be due to the fact that the $\{100\}$ slip systems have a higher number of rotational axes and slip systems, with relatively high Schmid factors. Similar to the grain size effect noted previously, the difference between the $MD_{(min)}$ values of each of the groups at same strain level became larger at higher strains. It can be interpreted that the level of heterogeneity increased with an increase in plastic strain.
- (5) The $MD_{(min)}$ was greater for the interrupted tests compared with the monotonic tests for both alloys at similar plastic strains. The static strain aging occurred during each pause for both alloys. The rearrangement of dislocations (due to the relaxation), pinned dislocations (due to the Cottrell atmospheres), and permanent change in the orientation and geometry at submicron scale may affect the local stress states at different regions of the grains. These factors may result in activation of new slip systems with different rotational axis, which lead to a higher misorientation dispersion for the interrupted tests.
- (6) A qualitative comparison between the DIC-SEM strain field map and the misorientation maps revealed that there is a better correlation between the hot spots in the KAM map and

the DIC-SEM strain field map compared with the correlation between the hot spots in the MD maps and the DIC-SEM strain field map. Although stress concentrations may occur in some areas and this may not be pointed out in the corresponding areas in the KAM map. In these regions, at least two slip systems should be activated simultaneously to accommodate the local plastic strains, while their net Burgers vectors were relatively small. In the current study, this inconsistency occurred in less than 10% of the studied grains.

7.2.2 Deformation behavior of TCFA and TIMETAL-21S

- (1) The TCFA UTS was ~950 MPa at RT. At 200 °C and 300 °C, the UTS decreased to ~ 820 MPa and 725 MPa, respectively. The TIMETAL-21S UTS was ~850 MPa at RT. With increasing temperature from 230 °C to 300 °C, the UTS decreased to ~ 675 MPa and 670 MPa, respectively.
- (2) Dislocation slip was the dominant deformation mechanism for both alloys. The slip trace analysis results revealed that ~ 95% of the observed traces were associated with one of three slip systems for the TCFA and TIMETAL-21S using a threshold of $\pm 4^\circ$. Although, the Schmid factor was relatively high (>0.4) for most of the observed traces, in some of the grains the Schmid factor was less than 0.2. This might indicate that the stress states were heterogeneous, locally.
- (3) The $\{123\}\langle 111\rangle$ systems exhibited the highest contribution, while the $\{110\}\langle 111\rangle$ showed the least contribution of the observed traces for both alloys. However, the normalized slip activity (the ratio of total observed slip systems divided by the total number of possible slip planes) suggested that the activity of all the systems were relatively

equal for the TCFA, while the activity of the $\{110\}\langle 111\rangle$ was slightly greater than other two slip systems in the TIMETAL-21S.

- (4) For a sanity check of this observation, slip traces analysis was performed on ~500 traces, where the $\{110\}\langle 111\rangle$ systems were considered as the only possible slip systems. In this scenario, only ~20% of traces matched. In the second scenario, both the $\{110\}\langle 111\rangle$ and $\{112\}\langle 111\rangle$ were considered, where more than 70% of traces were associated with one slip system. Hence, at least 30% of the active slip systems belonged to the $\{123\}\langle 111\rangle$ and/or MRSSP in those bcc Ti alloys.

7.2.3 Deformation behavior of TNTZ-xO

- (1) The TNTZ UTS increased with an increase in O content. The UTS value was 520 MPa, 800 MPa, and 980 MPa for 0.1O (wt.%), 0.3O (wt.%), and 0.7O (wt.%), respectively.
- (2) The TNTZ-0.1O exhibited the largest elongation-to-failure compared with the other two TNTZ-xO alloys. This was explained to be a result of the activation and cooperation of three deformation mechanisms, i.e. SIM transformation (β phase to α'' phase), $\{332\}\langle 113\rangle$ mechanical twinning, and the slip activity.
- (3) The higher content of the O suppressed both mechanical twinning and SIM transformation. Slip was the primary deformation mode for both TNTZ-0.3O and TNTZ-0.7O. The TNTZ-0.7 exhibited greater UTS and ϵ_f values. In-situ SEM tensile tests revealed the initiation of intergranular cracks at the early stage of the plastic deformation in the TNTZ-0.3O. The crack propagation and accumulation accelerated the fracture of the TNTZ-0.3O. On the other hand, no cracking occurred in the TNTZ-0.7. In addition, the SE SEM microphotographs indicated that the slip activity was more homogenous in the TNTZ-0.7O compared with the TNTZ-0.3O. This might be a consequence of a more homogenous

distribution of the O atoms throughout the TNTZ-0.7O. In-situ tensile TEM study may provide more accurate and detailed explanation for this abnormal behavior.

- (4) The slip trace analysis suggested that the $\{123\}\langle 111\rangle$ had the greatest contribution to the plastic deformation for both TNTZ-0.3O and TTNZ-0.7O, similar to the TCFA and TIMETAL-21S.

7.2.4 Enhancing the UTS of TCFA

- (1) The temperature range of the phase transformations was determined by performing DMA and DSC. The DMA test better determined the phase transformation temperature range compared with DSC test. Both methods indicated that a phase transformation occurred at $\sim 380^\circ\text{C}$. The DMA test revealed that a second phase transformation occurred at $\sim 470^\circ\text{C}$. The former phase transformation is expected to be the β to ω phase transformation, while the latter is expected to be β to α phase transformation.
- (2) Heat treatment was performed on the TCFA alloy at temperatures ranging between 400°C to 600°C for two hours in vacuum. SE SEM photomicrographs and Vickers hardness values were acquired to evaluate the effect of heat treatment on the phase transformation behavior. α phase formation occurred for the samples that were heat treated at temperatures higher than 500°C . Such a phase transformation was not evident for the sample that heat treated below 500°C . TEM investigation confirmed the existence of nanoscale ω phase precipitates for the samples that were heat treated at 400°C . The hardness values for all the heat-treated samples were significantly greater than those for the as-received sample.
- (3) The maximum hardness value was 506 Hv (the as-received hardness was 320 Hv). This value was measured after performing a heat treatment at 410°C for 24 hours.. The

maximum UTS achieved was 1450 MPa at 410 °C for TCFA. The RT UTS of the as-received TCFA alloy was 940 MPa.

7.3 Recommendations for future work

- (1) In this work, the misorientation analysis was performed on two bcc Ti alloys, which exhibited a linear relationship between the misorientation and the plastic strain for both of the studied alloys. In future work, the relationship between the misorientation and the plastic strain of hexagonal close packed structures and fcc materials should be investigated.
- (2) To gain a deeper understanding, a statistical analysis should be performed on the current data set to investigate and quantify the influence of neighboring grains on the local misorientation values at the grain boundaries as function of neighboring grain orientation and size.
- (3) Dislocation slip was the dominant deformation mode for the alloys investigated in the current work. The framework developed in this study should be used to analyze the misorientation distribution of an alloy where both twinning and slip are competitive deformation modes. Such a study will bring new insight to our understanding of the relationship between the misorientation and active deformation modes.
- (4) To gain a deeper understanding of the relationship between the experimental strain field map obtained from DIC and the misorientation value (MD), it is essential to perform statistical analyses on the strain data obtained from the DIC experiment and quantitatively compare the equivalent strain and MD values. For example, by extracting the strain from the DIC data for each grain, the equivalent strain of each grain can be compared with the MD of each grain. In addition, the distribution of the local MD can be compared with the distribution of the local strain at the grain scale. This will reveal more information regarding the relationship between the strain concentration and the local misorientation.

- (5) The slip trace analyses were conducted based on the deformation system activity on the surface of the specimen. Future work can use 3D characterization techniques, such as TEM, 3D EBSD or XRD to investigate the subsurface dislocation activity. Studying the subsurface dislocation activity may be helpful to gain a better understanding of the relationship between dislocation activity on the surface and beneath the specimen surface.
- (6) The TCFA alloy system exhibited promising tensile properties at both RT and elevated temperatures. More TEM investigation can be performed to determine the morphology and volume fraction of the ω phase as a function of TMP.
- (7) TMP on other bcc Ti alloys may result in ω phase transformation. Further work should be performed to optimize the TMP conditions for certain alloys to exhibit optimal performance for the desired applications.

BIBLIOGRAPHY

Abuzaid, W., Sangid, M.D., Sehitoglu, H., Carroll, J., and Lambros, J. (2012a). The Role of Slip Transmission on Plastic Strain accumulation across Grain Boundaries. *Procedia IUTAM* 4, 169–178.

Abuzaid, W.Z., Sangid, M.D., Carroll, J.D., Sehitoglu, H., and Lambros, J. (2012b). Slip transfer and plastic strain accumulation across grain boundaries in Hastelloy X. *Journal of the Mechanics and Physics of Solids* 60, 1201–1220.

Adams, B.L., Wright, S.I., and Kunze, K. (1993). Orientation imaging: The emergence of a new microscopy. *MTA* 24, 819–831.

Akahori, T., Niinomi, M., Fukui, H., Ogawa, M., and Toda, H. (2005). Improvement in fatigue characteristics of newly developed beta type titanium alloy for biomedical applications by thermo-mechanical treatments. *Materials Science and Engineering: C* 25, 248–254.

Allain-Bonasso, N., Wagner, F., Berbenni, S., and Field, D.P. (2012). A study of the heterogeneity of plastic deformation in IF steel by EBSD. *Materials Science and Engineering: A* 548, 56–63.

Ankem, S., and Greene, C.A. (1999). Recent developments in microstructure/property relationships of beta titanium alloys. *Materials Science and Engineering: A* 263, 127–131.

Ashby, M.F. (1970). The deformation of plastically non-homogeneous materials. *The Philosophical Magazine: A Journal of Theoretical Experimental and Applied Physics* 21, 399–424.

Bache, M.R., and Evans, W.J. (2001). Impact of texture on mechanical properties in an advanced titanium alloy. *Materials Science and Engineering: A* 319–321, 409–414.

Badji, R., Chauveau, T., and Bacroix, B. (2013). Texture, misorientation and mechanical anisotropy in a deformed dual phase stainless steel weld joint. *Materials Science and Engineering: A* 575, 94–103.

Banerjee, R., Nag, S., Stechschulte, J., and Fraser, H.L. (2004). Strengthening mechanisms in Ti–Nb–Zr–Ta and Ti–Mo–Zr–Fe orthopaedic alloys. *Biomaterials* 25, 3413–3419.

Bartali, A.E., Aubin, V., and Degallaix, S. (2009). Surface observation and measurement techniques to study the fatigue damage micromechanisms in a duplex stainless steel. *International Journal of Fatigue* 31, 2049–2055.

Bastos, A., Zaefferer, S., Raabe, D., and Schuh, C. (2006). Characterization of the microstructure and texture of nanostructured electrodeposited NiCo using electron backscatter diffraction (EBSD). *Acta Materialia* 54, 2451–2462.

Berbenni, S., Favier, V., and Berveiller, M. (2007). Impact of the grain size distribution on the yield stress of heterogeneous materials. *International Journal of Plasticity* 23, 114–142.

Bertrand, E., Castany, P., Péron, I., and Gloriant, T. (2011). Twinning system selection in a metastable β -titanium alloy by Schmid factor analysis. *Scripta Materialia* 64, 1110–1113.

- Besse, M., Castany, P., and Gloriant, T. (2011). Mechanisms of deformation in gum metal TNTZ-O and TNTZ titanium alloys: A comparative study on the oxygen influence. *Acta Materialia* 59, 5982–5988.
- Bieler, T.R., Eisenlohr, P., Roters, F., Kumar, D., Mason, D.E., Crimp, M.A., and Raabe, D. (2009). The role of heterogeneous deformation on damage nucleation at grain boundaries in single phase metals. *International Journal of Plasticity* 25, 1655–1683.
- Boehlert, C.J., Chen, Z., Chakkedath, A., Gutiérrez-Urrutia, I., Llorca, J., Bohlen, J., Yi, S., Letzig, D., and Pérez-Prado, M.T. (2013). In situ analysis of the tensile deformation mechanisms in extruded Mg–1Mn–1Nd (wt%). *Philosophical Magazine* 93, 598–617.
- Brewer, L.N., Othon, M.A., Young, L.M., and Angeliu, T.M. (2006). Misorientation Mapping for Visualization of Plastic Deformation via Electron Back-Scattered Diffraction. *Microscopy and Microanalysis* 12, 85–91.
- Brewer, L.N., Field, D.P., and Merriman, C.C. (2009). Mapping and Assessing Plastic Deformation Using EBSD. *Electron Backscatter Diffraction in Materials Science* 251–262.
- Bridier, F., Villechaise, P., and Mendez, J. (2005). Analysis of the different slip systems activated by tension in a α/β titanium alloy in relation with local crystallographic orientation. *Acta Materialia* 53, 555–567.
- Britton, T.B., Biroasca, S., Preuss, M., and Wilkinson, A.J. (2010). Electron backscatter diffraction study of dislocation content of a macrozone in hot-rolled Ti–6Al–4V alloy. *Scripta Materialia* 62, 639–642.
- Brunette, D.M., Tengvall, P., Textor, M., and Thomsen, P. (2012). *Titanium in Medicine: Material Science, Surface Science, Engineering, Biological Responses and Medical Applications* (Springer Science & Business Media).
- Buchheit, T.E., Carroll, J.D., Clark, B.G., and Boyce, B.L. (2015). Evaluating Deformation-Induced Grain Orientation Change in a Polycrystal During In Situ Tensile Deformation using EBSD. *Microscopy and Microanalysis* 21, 969–984.
- Bülbül, A., Kaçar, R., Bülbül, A., and Kaçar, R. (2017). Factors Affecting Kinetics of Strain Aging in S275JRC Steel. *Materials Research* 20, 210–217.
- Cahn, J.W., Mishin, Y., and Suzuki, A. (2006). Coupling grain boundary motion to shear deformation. *Acta Materialia* 54, 4953–4975.
- Calcagnotto, M., Ponge, D., Demir, E., and Raabe, D. (2010). Orientation gradients and geometrically necessary dislocations in ultrafine grained dual-phase steels studied by 2D and 3D EBSD. *Materials Science and Engineering: A* 527, 2738–2746.
- Callister, W.D., and Rethwisch, D.G. (2013). *Materials Science and Engineering: An Introduction*, 9th Edition: Ninth Edition (John Wiley and Sons, Incorporated).

Carroll, J.D., Clark, B.G., Buchheit, T.E., Boyce, B.L., and Weinberger, C.R. (2013). An experimental statistical analysis of stress projection factors in BCC tantalum. *Materials Science and Engineering: A* 581, 108–118.

Castany, P., Besse, M., and Gloriant, T. (2012). In situ TEM study of dislocation slip in a metastable β titanium alloy. *Scripta Materialia* 66, 371–373.

Chakkedath, A., Bohlen, J., Yi, S., Letzig, D., Chen, Z., and Boehlert, C.J. (2014). The Effect of Nd on the Tension and Compression Deformation Behavior of Extruded Mg-1Mn (wt pct) at Temperatures Between 298 K and 523 K (25 °C and 250 °C). *Metall and Mat Trans A* 45, 3254–3274.

Chakkedath, A., Escobar, D.H., Bohlen, J., Yi, S., Letzig, D., and Boehlert, C. (2016). In-Situ EBSD Observations of Recrystallization and Texture Evolution in Rolled Mg-2Zn-xCe (wt.%). *Magnesium Technology 2016* 237–237.

Chen, Z., and Daly, S.H. (2017). Active Slip System Identification in Polycrystalline Metals by Digital Image Correlation (DIC). *Exp Mech* 57, 115–127.

Chen, Y., Du, Z., Xiao, S., Xu, L., and Tian, J. (2014). Effect of aging heat treatment on microstructure and tensile properties of a new β high strength titanium alloy. *Journal of Alloys and Compounds* 586, 588–592.

Cotton, J.D., Briggs, R.D., Boyer, R.R., Tamirisakandala, S., Russo, P., Shchetnikov, N., and Fanning, J.C. (2015). State of the Art in Beta Titanium Alloys for Airframe Applications. *JOM* 67, 1281–1303.

Cottrell, A.H., and Bilby, B.A. (1949). Dislocation Theory of Yielding and Strain Ageing of Iron. *Proc. Phys. Soc. A* 62, 49.

Dastidar, I.G., Khademi, V., Bieler, T.R., Pilchak, A.L., Crimp, M.A., and Boehlert, C.J. (2015). The tensile and tensile-creep deformation behavior of Ti-8Al-1Mo-1V(wt%). *Materials Science and Engineering: A* 636, 289–300.

Dehghan-Manshadi, A., and Dippenaar, R.J. (2011). Development of α -phase morphologies during low temperature isothermal heat treatment of a Ti-5Al-5Mo-5V-3Cr alloy. *Materials Science and Engineering: A* 528, 1833–1839.

Demir, E., and Raabe, D. (2010). Mechanical and microstructural single-crystal Bauschinger effects: Observation of reversible plasticity in copper during bending. *Acta Materialia* 58, 6055–6063.

Donachie, M.J. (2000). *Titanium: A Technical Guide*, 2nd Edition (ASM International).

Dubinskiy, S., Korotitskiy, A., Prokoshkin, S., and Brailovski, V. (2016). In situ X-ray diffraction study of athermal and isothermal omega-phase crystal lattice in Ti-Nb-based shape memory alloys. *Materials Letters* 168, 155–157.

- El Bartali, A., Aubin, V., Sabatier, L., Villechaise, P., and Degallaix-Moreuil, S. (2008). Identification and analysis of slip systems activated during low-cycle fatigue in a duplex stainless steel. *Scripta Materialia* 59, 1231–1234.
- El-Dasher, B.S., Adams, B.L., and Rollett, A.D. (2003). Viewpoint: experimental recovery of geometrically necessary dislocation density in polycrystals. *Scripta Materialia* 48, 141–145.
- Espinosa, H.D., Berbenni, S., Panico, M., and Schwarz, K.W. (2005). An interpretation of size-scale plasticity in geometrically confined systems. *Proc Natl Acad Sci U S A* 102, 16933–16938.
- Esteban, P.G., Bolzoni, L., Ruiz-Navas, E.M., and Gordo, E. (2011). PM processing and characterisation of Ti–7Fe low cost titanium alloys. *Powder Metallurgy* 54, 242–252.
- Franciosi, P., Le, L.T., Monnet, G., Kahloun, C., and Chavanne, M.-H. (2015). Investigation of slip system activity in iron at room temperature by SEM and AFM in-situ tensile and compression tests of iron single crystals. *International Journal of Plasticity* 65, 226–249.
- Fu, H.-H., Benson, D.J., and Meyers, M.A. (2001). Analytical and computational description of effect of grain size on yield stress of metals. *Acta Materialia* 49, 2567–2582.
- Geetha, M., Singh, A.K., Asokamani, R., and Gogia, A.K. (2009). Ti based biomaterials, the ultimate choice for orthopaedic implants – A review. *Progress in Materials Science* 54, 397–425.
- Geng, F., Niinomi, M., and Nakai, M. (2011). Observation of yielding and strain hardening in a titanium alloy having high oxygen content. *Materials Science and Engineering: A* 528, 5435–5445.
- Gilormini, P., Bacroix, B., and Jonas, J.J. (1988). Theoretical analyses of $\langle 111 \rangle$ pencil glide in b.c.c. crystals. *Acta Metallurgica* 36, 231–256.
- Gunawarman, B., Niinomi, M., Akahori, T., Souma, T., Ikeda, M., and Toda, H. (2005). Mechanical properties and microstructures of low cost β titanium alloys for healthcare applications. *Materials Science & Engineering, C, Materials Science & Engineering. C, Materials for Biological Applications, Materials Science and Engineering C: Biomimetic and Supramolecular Systems, Materials Science and Engineering, C, Scripta Botanica Belgica* 25, 304–311.
- Hall, E.O. (1951). The Deformation and Ageing of Mild Steel: III Discussion of Results. *Proc. Phys. Soc. B* 64, 747.
- Hanada, S., and Izumi, O. (1987). Correlation of tensile properties, deformation modes, and phase stability in commercial β -phase titanium alloys. *Metall and Mat Trans A* 18, 265–271.
- Hartman, A.D., Gerdemann, S.J., and Hansen, J.S. (1998). Producing lower-cost titanium for automotive applications. *JOM* 50, 16–19.
- Hickman, B.S. (1969). The formation of omega phase in titanium and zirconium alloys: A review. *J Mater Sci* 4, 554–563.

- Hirth, J.P. (1972). The influence of grain boundaries on mechanical properties. *MT* 3, 3047–3067.
- Hosford, W.F. (2009). *Mechanical Behavior of Materials* by William F. Hosford.
- Humphreys, F.J. (2001). Review Grain and subgrain characterisation by electron backscatter diffraction. *Journal of Materials Science* 36, 3833–3854.
- Humphreys, F.J. (2004). Characterisation of fine-scale microstructures by electron backscatter diffraction (EBSD). *Scripta Materialia* 51, 771–776.
- Hwang, J., Kuramoto, S., Furuta, T., Nishino, K., and Saito, T. (2005). Phase-stability dependence of plastic deformation behavior in Ti-Nb-Ta-Zr-O alloys. *J. of Materi Eng and Perform* 14, 747–754.
- Ivasishin, O.M., Markovsky, P.E., Matviychuk, Y.V., and Semiatin, S.L. (2003). Precipitation and recrystallization behavior of beta titanium alloys during continuous heat treatment. *Metall and Mat Trans A* 34, 147–158.
- Ivasishin, O.M., Markovsky, P.E., Semiatin, S.L., and Ward, C.H. (2005). Aging response of coarse- and fine-grained β titanium alloys. *Materials Science and Engineering: A* 405, 296–305.
- Kamaya, M. (2009). Measurement of local plastic strain distribution of stainless steel by electron backscatter diffraction. *Materials Characterization* 60, 125–132.
- Kamaya, M. (2011). Assessment of local deformation using EBSD: Quantification of accuracy of measurement and definition of local gradient. *Ultramicroscopy* 111, 1189–1199.
- Kamaya, M. (2012). Assessment of local deformation using EBSD: Quantification of local damage at grain boundaries. *Materials Characterization* 66, 56–67.
- Kamaya, M., Wilkinson, A.J., and Titchmarsh, J.M. (2005). Measurement of plastic strain of polycrystalline material by electron backscatter diffraction. *Nuclear Engineering and Design* 235, 713–725.
- Kamaya, M., Wilkinson, A.J., and Titchmarsh, J.M. (2006). Quantification of plastic strain of stainless steel and nickel alloy by electron backscatter diffraction. *Acta Materialia* 54, 539–548.
- Kammers, A., and Daly, S. (2013a). Deformation Mapping at the Microstructural Length Scale. In *Experimental and Applied Mechanics, Volume 4*, C.E. Ventura, W.C. Crone, and C. Furlong, eds. (Springer New York), pp. 15–20.
- Kammers, A.D., and Daly, S. (2013b). Digital Image Correlation under Scanning Electron Microscopy: Methodology and Validation. *Exp Mech* 53, 1743–1761.
- Khademi, V., Ikeda, M., and Boehlert, C.J. (2016). The Effect of Temperature on the Tensile Deformation Behavior of Ti-13Cr-1Fe-3Al (wt. %). In *Proceedings of the 13th World Conference on Titanium*, (Wiley-Blackwell), pp. 1109–1116.

- Khorashadizadeh, A., Raabe, D., Zaefferer, S., Rohrer, G.S., Rollett, A.D., and Winning, M. (2011). Five-Parameter Grain Boundary Analysis by 3D EBSD of an Ultra Fine Grained CuZr Alloy Processed by Equal Channel Angular Pressing. *Advanced Engineering Materials* 13, 237–244.
- Kobayashi, E., Doi, H., Yoneyama, T., Hamanaka, H., Gibson, I.R., Best, S.M., Shelton, J.C., and Bonfield, W. (1998). Influence of aging heat treatment on mechanical properties of biomedical Ti–Zr based ternary alloys containing niobium. *Journal of Materials Science: Materials in Medicine* 9, 625–630.
- Kuan, T.S., Ahrens, R.R., and Sass, S.L. (1975). The Stress-induced omega phase transformation in Ti–V alloys. *MTA* 6, 1767.
- Kubin, L.P., Estrin, Y., and Perrier, C. (1992). On static strain ageing. *Acta Metallurgica et Materialia* 40, 1037–1044.
- Kuroda, D., Niinomi, M., Morinaga, M., Kato, Y., and Yashiro, T. (1998). Design and mechanical properties of new β type titanium alloys for implant materials. *Materials Science and Engineering: A* 243, 244–249.
- Lavergne, F., Brenner, R., and Sab, K. (2013). Effects of grain size distribution and stress heterogeneity on yield stress of polycrystals: A numerical approach. *Computational Materials Science* 77, 387–398.
- Lee, C.M., Ju, C.P., and Chern Lin, J.H. (2002). Structure-property relationship of cast Ti–Nb alloys. *J Oral Rehabil* 29, 314–322.
- Leyens, C., and Peters, M. (2006). *Titanium and Titanium Alloys: Fundamentals and Applications* (John Wiley & Sons).
- Li, H., Boehlert, C.J., Bieler, T.R., and Crimp, M.A. (2012). Analysis of slip activity and heterogeneous deformation in tension and tension-creep of Ti–5Al–2.5Sn (wt %) using in-situ SEM experiments. *Philosophical Magazine* 92, 2923–2946.
- Li, H., Mason, D.E., Yang, Y., Bieler, T.R., Crimp, M.A., and Boehlert, C.J. (2013). Comparison of the deformation behaviour of commercially pure titanium and Ti–5Al–2.5Sn(wt.%) at 296 and 728 K. *Philosophical Magazine* 93, 2875–2895.
- Li, H., Boehlert, C.J., Bieler, T.R., and Crimp, M.A. (2014). Analysis of the Deformation Behavior in Tension and Tension-Creep of Ti-3Al-2.5V (wt pct) at 296 K and 728 K (23 °C and 455 °C) Using *In Situ* SEM Experiments. *Metall and Mat Trans A* 45, 6053–6066.
- Li, H., Boehlert, C.J., Bieler, T.R., and Crimp, M.A. (2015). Examination of the distribution of the tensile deformation systems in tension and tension-creep of Ti-6Al-4V (wt.%) at 296 K and 728 K. *Philosophical Magazine* 95, 691–729.

- Li, S., Hao, Y., Yang, R., Cui, Y., and Niinomi, M. (2002). Effect of Nb on Microstructural Characteristics of Ti-Nb-Ta-Zr Alloy for Biomedical Applications. *Mater. Trans.* *43*, 2964–2969.
- Liqiang, W., Guanjun, Y., Huabin, Y., Jimin, C., Weijie, L., and Di, Z. (2009). Microstructure and Mechanical Properties of TiNbZr Alloy during Cold Drawing. *Rare Metal Materials and Engineering* *38*, 579–582.
- Liu, Z., and Welsch, G. (1988). Effects of oxygen and heat treatment on the mechanical properties of alpha and beta titanium alloys. *MTA* *19*, 527–542.
- Liu, H., Niinomi, M., Nakai, M., Cho, K., and Fujii, H. (2017a). Deformation-induced ω -phase transformation in a β -type titanium alloy during tensile deformation. *Scripta Materialia* *130*, 27–31.
- Liu, H., Niinomi, M., Nakai, M., Cong, X., Cho, K., Boehlert, C.J., and Khademi, V. (2017b). Abnormal Deformation Behavior of Oxygen-Modified β -Type Ti-29Nb-13Ta-4.6Zr Alloys for Biomedical Applications. *Metall and Mat Trans A* *48*, 139–149.
- Long, M., and Rack, H.J. (1998). Titanium alloys in total joint replacement—a materials science perspective. *Biomaterials* *19*, 1621–1639.
- Lütjering, G., and Williams, J.C. (2003). *Titanium* (Berlin Heidelberg: Springer-Verlag).
- Mantri, S.A., Choudhuri, D., Behera, A., Cotton, J.D., Kumar, N., and Banerjee, R. (2015). Influence of Fine-Scale Alpha Precipitation on the Mechanical Properties of the Beta Titanium Alloy Beta-21S. *Metall and Mat Trans A* *46*, 2803–2808.
- Mishra, S.K., Pant, P., Narasimhan, K., Rollett, A.D., and Samajdar, I. (2009). On the widths of orientation gradient zones adjacent to grain boundaries. *Scripta Materialia* *61*, 273–276.
- Miura, E., Yoshimi, K., and Hanada, S. (2001). Solid-Solution Strengthening by Oxygen in Nb-Ta and Nb-Mo Single Crystals. *Physica Status Solidi (A)* *185*, 357–372.
- Mohammed, M.T., Khan, Z.A., and Siddiquee, A.N. (2014). Beta Titanium Alloys: The Lowest Elastic Modulus for Biomedical Applications: A Review. *8*, 7.
- Nag, S., Banerjee, R., Srinivasan, R., Hwang, J.Y., Harper, M., and Fraser, H.L. (2009). ω -Assisted nucleation and growth of α precipitates in the Ti-5Al-5Mo-5V-3Cr-0.5Fe β titanium alloy. *Acta Materialia* *57*, 2136–2147.
- Nicaise, N., Berbenni, S., Wagner, F., Berveiller, M., and Lemoine, X. (2011). Coupled effects of grain size distributions and crystallographic textures on the plastic behaviour of IF steels. *International Journal of Plasticity* *27*, 232–249.
- Niinomi, M. (1998). Mechanical properties of biomedical titanium alloys. *Materials Science and Engineering: A* *243*, 231–236.

- Niinomi, M. (2003). Recent research and development in titanium alloys for biomedical applications and healthcare goods. *Sci. Technol. Adv. Mater.* 4, 445.
- Niinomi, M. (2008). Mechanical biocompatibilities of titanium alloys for biomedical applications. *Journal of the Mechanical Behavior of Biomedical Materials* 1, 30–42.
- Nye, J.F. (1953). Some geometrical relations in dislocated crystals. *Acta Metallurgica* 1, 153–162.
- Ogawa, M., Shimizu, T., Noda, T., and Ikeda, M. (2007). The Effect of Al Content on Tensile and Fatigue Properties of Solution-Treated and Quenched Ti-13Cr-1Fe Alloys. *Mater. Trans.* 48, 390–394.
- Peters, W.H., and Ranson, W.F. (1982). Digital Imaging Techniques In Experimental Stress Analysis. OE, OPEGAR 21, 213427.
- Qazi, J.I., Rack, H.J., and Marquardt, B. (2004). High-strength metastable beta-titanium alloys for biomedical applications. *JOM* 56, 49–51.
- Qazi, J.I., Tsakiris, V., Marquardt, B., and Rack, H.J. (2005). Effect of Aging Treatments on the Tensile Properties of Ti-35Nb-7Zr-5Ta-(0.06–0.7)O Alloys. *JAI* 2, 1–19.
- Rack, H.J., and Qazi, J.I. (2006). Titanium alloys for biomedical applications. *Materials Science and Engineering: C* 26, 1269–1277.
- Rohrer, G.S. (2001). *Structure and Bonding in Crystalline Materials* (Cambridge University Press).
- Rohrer, G.S., Li, J., Lee, S., Rollett, A.D., Groeber, M., and Uchic, M.D. (2010). Deriving grain boundary character distributions and relative grain boundary energies from three-dimensional EBSD data. *Materials Science and Technology* 26, 661–669.
- Rollett, A.D., Wagner, F., Allain-Bonasso, N., Field, D.P., and Lebensohn, R.A. (2012). Comparison of Gradients in Orientation and Stress between Experiment and Simulation.
- Sakaguchi, N., Niinomi, M., Akahori, T., Takeda, J., and Toda, H. (2005a). Effect of Ta content on mechanical properties of Ti–30Nb–XTa–5Zr. *Materials Science and Engineering: C* 25, 370–376.
- Sakaguchi, N., Niinomi, M., Akahori, T., Takeda, J., and Toda, H. (2005b). Relationships between tensile deformation behavior and microstructure in Ti–Nb–Ta–Zr system alloys. *Materials Science and Engineering: C* 25, 363–369.
- Santos, P.F., Niinomi, M., Cho, K., Nakai, M., Liu, H., Ohtsu, N., Hirano, M., Ikeda, M., and Narushima, T. (2015). Microstructures, mechanical properties and cytotoxicity of low cost beta Ti–Mn alloys for biomedical applications. *Acta Biomaterialia* 26, 366–376.
- Santos, P.F., Niinomi, M., Liu, H., Cho, K., Nakai, M., Itoh, Y., Narushima, T., and Ikeda, M. (2016). Fabrication of low-cost beta-type Ti–Mn alloys for biomedical applications by metal

injection molding process and their mechanical properties. *Journal of the Mechanical Behavior of Biomedical Materials* 59, 497–507.

Schwartz, A.J., Kumar, M., Adams, B.L., and Field, D.P. (2009). *Electron backscatter diffraction in materials science* (Springer).

Sémoroz, A., Durandet, Y., and Rappaz, M. (2001). EBSD characterization of dendrite growth directions, texture and misorientations in hot-dipped Al–Zn–Si coatings. *Acta Materialia* 49, 529–541.

Signorelli, J.W., Roatta, A., De Vincentis, N., Schwindt, C., Avalos, M., Bolmaro, R.E., and Bozzolo, N. (2017). Electron backscatter diffraction study of orientation gradients at the grain boundaries of a polycrystalline steel sheet deformed along different loading paths. *J Appl Cryst, J Appl Crystallogr* 50, 1179–1191.

Subedi, S., Pokharel, R., and Rollett, A.D. (2015). Orientation gradients in relation to grain boundaries at varying strain level and spatial resolution. *Materials Science and Engineering: A* 638, 348–356.

Sutton, M., Wolters, W., Peters, W., Ranson, W., and McNeill, S. (1983). Determination of displacements using an improved digital correlation method. *Image and Vision Computing* 1, 133–139.

Sutton, M.A., Li, N., Garcia, D., Cornille, N., Orteu, J.J., McNeill, S.R., Schreier, H.W., and Li, X. (2006). Metrology in a scanning electron microscope: theoretical developments and experimental validation. *Meas. Sci. Technol.* 17, 2613.

Sutton, M.A., Li, N., Joy, D.C., Reynolds, A.P., and Li, X. (2007a). Scanning Electron Microscopy for Quantitative Small and Large Deformation Measurements Part I: SEM Imaging at Magnifications from 200 to 10,000. *Exp Mech* 47, 775–787.

Sutton, M.A., Li, N., Garcia, D., Cornille, N., Orteu, J.J., McNeill, S.R., Schreier, H.W., Li, X., and Reynolds, A.P. (2007b). Scanning Electron Microscopy for Quantitative Small and Large Deformation Measurements Part II: Experimental Validation for Magnifications from 200 to 10,000. *Exp Mech* 47, 789–804.

Sutton, M.A., Orteu, J.J., and Schreier, H. (2009). *Image Correlation for Shape, Motion and Deformation Measurements: Basic Concepts, Theory and Applications* (Springer US).

Swygenhoven, H.V. (2002). Grain Boundaries and Dislocations. *Science* 296, 66–67.

Tahara, M., Kim, H.Y., Inamura, T., Hosoda, H., and Miyazaki, S. (2011). Lattice modulation and superelasticity in oxygen-added β -Ti alloys. *Acta Materialia* 59, 6208–6218.

Talling, R.J., Dashwood, R.J., Jackson, M., and Dye, D. (2009). On the mechanism of superelasticity in Gum metal. *Acta Materialia* 57, 1188–1198.

- Taylor, G.I., and Elam, C.F. (1926). The distortion of iron crystals. *Proc. R. Soc. Lond. A* 112, 337–361.
- Telang, A.U., Bieler, T.R., Lucas, J.P., Subramanian, K.N., Lehman, L.P., Xing, Y., and Cotts, E.J. (2004). Grain-boundary character and grain growth in bulk tin and bulk lead-free solder alloys. *Journal of Elec Materi* 33, 1412–1423.
- Wang, L., Eisenlohr, P., Yang, Y., Bieler, T.R., and Crimp, M.A. (2010). Nucleation of paired twins at grain boundaries in titanium. *Scripta Materialia* 63, 827–830.
- Weinberger, C.R., Boyce, B.L., and Battaile, C.C. (2013). Slip planes in bcc transition metals. *International Materials Reviews* 58, 296–314.
- Welsch, G., Boyer, R., and Collings, E.W. (1993). *Materials Properties Handbook: Titanium Alloys* (ASM International).
- Wilkinson, A.J., and Britton, T.B. (2012). Strains, planes, and EBSD in materials science. *Materials Today* 15, 366–376.
- Wilkinson, A.J., Britton, T.B., Jiang, J., and Karamched, P.S. (2014). A review of advances and challenges in EBSD strain mapping. *IOP Conf. Ser.: Mater. Sci. Eng.* 55, 012020.
- Wright, S.I., and Adams, B.L. (1992). Automatic analysis of electron backscatter diffraction patterns. *MTA* 23, 759–767.
- Wright, S.I., Nowell, M.M., and Field, D.P. (2011). A Review of Strain Analysis Using Electron Backscatter Diffraction. *Microscopy and Microanalysis* 17, 316–329.
- Wright, S.I., Suzuki, S., and Nowell, M.M. (2016). In Situ EBSD Observations of the Evolution in Crystallographic Orientation with Deformation. *JOM* 68, 2730–2736.
- Xing, H., and Sun, J. (2008). Mechanical twinning and omega transition by $\langle 111 \rangle \{112\}$ shear in a metastable β titanium alloy. *Appl. Phys. Lett.* 93, 031908.
- Yang, Y., Li, G.P., Cheng, G.M., Wang, H., Zhang, M., Xu, F., and Yang, K. (2008). Stress-introduced α'' martensite and twinning in a multifunctional titanium alloy. *Scripta Materialia* 58, 9–12.
- Yang, Y., Wu, S.Q., Li, G.P., Li, Y.L., Lu, Y.F., Yang, K., and Ge, P. (2010). Evolution of deformation mechanisms of Ti–22.4Nb–0.73Ta–2Zr–1.34O alloy during straining. *Acta Materialia* 58, 2778–2787.
- Yin, D.D., Wang, Q.D., Boehlert, C.J., Chen, Z., Li, H.M., Mishra, R.K., and Chakkedath, A. (2016). *In-Situ* Study of the Tensile Deformation and Fracture Modes in Peak-Aged Cast Mg-11Y-5Gd-2Zn-0.5Zr (Weight Percent). *Metall and Mat Trans A* 47, 6438–6452.

Zaafarani, N., Raabe, D., Singh, R.N., Roters, F., and Zaefferer, S. (2006). Three-dimensional investigation of the texture and microstructure below a nanoindent in a Cu single crystal using 3D EBSD and crystal plasticity finite element simulations. *Acta Materialia* 54, 1863–1876.

Zaefferer, S. (2003). A study of active deformation systems in titanium alloys: dependence on alloy composition and correlation with deformation texture. *Materials Science and Engineering: A* 344, 20–30.

Zaefferer, S., Kuo, J.-C., Zhao, Z., Winning, M., and Raabe, D. (2003). On the influence of the grain boundary misorientation on the plastic deformation of aluminum bicrystals. *Acta Materialia* 51, 4719–4735.

Zhou, Y.L., Niinomi, M., and Akahori, T. (2004). Effects of Ta content on Young's modulus and tensile properties of binary Ti–Ta alloys for biomedical applications. *Materials Science and Engineering: A* 371, 283–290.